UNIVERSITY OF OKLAHOMA

GRADUATE COLLEGE

ADVANCED TURBULENCE MODELING STRATEGIES WITHIN THE HYBRID RANS-LES FRAMEWORK

A DISSERTATION

SUBMITTED TO THE GRADUATE FACULTY

In partial fulfillment of the requirements for the

Degree of

Doctor of Philosophy

Mechanical Engineering

By

Tausif Jamal
Norman, OK
2020

ADVANCED TURBULENCE MODELING STRATEGIES

WITHIN THE HYBRID RANS-LES FRAMEWORK

A DISSERTATION APPROVED FOR THE SCHOOL OF AEROSPACE AND MECHANICAL ENGINEERING

BY THE COMMITTEE CONSISTING OF

Dr. D. Keith Walters, Chair

Dr. Edgar O'Rear

Dr. Jivtesh Garg

Dr. Hamidreza Shabgard

Dr. Prakash Vedula

Dr. Keisha B. Walters

ABSTRACT

Reynolds Averaged Navier-Stokes (RANS) models still represent the most common turbulence modeling technique used in Computational Fluid Dynamics (CFD) today. RANS models are preferred primarily due to their relatively low computational demand and ease of use. The general RANS framework utilizes the ensemble averaged form of the Navier Stokes equations in which all turbulent scales are modelled, and hence requires reduced computational effort compared to scale resolving methods. Despite their popularity, RANS models have been found to perform poorly in flows with separated shear layers, unsteady wakes, and temporally evolving flows. There has been ongoing progress towards high-fidelity methods such as Large Eddy Simulation (LES) to more accurately represent these flow features. LES models apply filters to the equations of fluid motion to resolve the large turbulent structures that are responsible for energy transfer. The smaller scales however, are represented using a sub-grid scale (SGS) model. LES models perform well in separated shear layers where large eddies dictate the energy and momentum transfer, due to the small time and length scales associated with near wall flow. The costs associated with LES are a major limiting factor in their adoption in industrial and academic research. This has led to the development of Hybrid RANS-LES (HRL) models which offer improved performance over RANS models while being relatively inexpensive compared to LES models. The hybrid modeling approach aims to provide the best of both worlds. In hybrid models, LES models are used far away from the wall to resolve large scale structures primarily responsible for the transfer of momentum and energy, while the wall bounded turbulence is treated using a RANS model. However, HRL models suffer from inherent drawbacks associated with their handling of RANS to LES transition in addition to a high degree of grid sensitivity. The present study proposes advanced turbulence modeling strategies within the hybrid RANS-LES class of

models. Major contributions include: (i) evaluation of RANS and hybrid RANS-LES models for separated and non-stationary flows, (ii) development of time-filtering techniques for the dynamic Hybrid RANS-LES (DHRL) model to improve predictive capabilities for non-stationary periodic and non-periodic flows, and (iii) a new variant of the DHRL model for complex turbulent flows to address a known weakness in the DHRL formulation.

First, the performance of the DHRL model is evaluated against popular RANS and HRL models for flow over a three-dimensional axisymmetric hill. DHRL model results indicate superior prediction of mean flow statistics and turbulent stresses. However, some discrepancy in Reynolds stress prediction and the lack of a smooth LES-mode away from the wall is observed. Second, static and dynamic time filters are implemented to extend the DHRL model from an ensemble averaged framework to a non-stationary framework. Results once again indicate superior model performance when compared to other models investigated. The model consistently reproduces results similar to pseudo-spectral LES and DNS data for mean flow and second moment statistics. Some underprediction in the outer layer is observed due to the model remaining partially in RANS mode, a known potential source of error for the DHRL model. Third, the dynamic time filtering (DTF) proposed in the previous study is extended via the incorporation of double exponential filtering for applications in flows with non-periodic and/or monotonically time-varying statistics. Results indicate an improvement in performance for high frequency oscillations in a pulsating channel and a good agreement with DNS data for temporally varying mixing layer. Discrepancies in temporal evolution of flow statistics is observed due to the imposed initial fluctuation, however the results indicate that it is able to accurately simulate the appropriate flow physics, and fine tuning of the initial fluctuations would significantly improve predictive capabilities. Additionally, benchmark DNS data for medium and low frequency oscillation is added to supplement the

existing DNS for high frequency oscillations. Finally, the performance of a new variant of the DHRL model with an improved blending parameter is investigated for the test cases of fully developed channel, three-dimensional axisymmetric hill, and pulsating channel. The new model variant introduces a blending parameter that smoothly transitions the model from RANS-to-LES in regions where RANS tends to significant overpredict turbulent stresses. Results indicate an improvement over the baseline model for all the cases previously investigated.

ACKNOWLEDGEMENTS

I also extend my gratitude to my committee members, who have been very flexible and accommodating especially through these trying times.

I would also like to thank my co-workers and co-authors for their expertise and help throughout my graduate program and research.

I also thank my friends who have always been supportive of my goals and experienced the hardships and the simplicity of student-life together. I am extremely glad and blessed to have such wonderful friends.

I am grateful to my parents who have worked relentlessly throughout their lives in hopes that someday I would achieve my goals.

I thank my wife for sticking by my side through all these years of graduate school and for making it more enjoyable. I am glad that we got to experience graduate school together.

Finally, I would like to thank my advisor, mentor, and one of the most important influences in my life, Dr. D.K. Walters. He has always set an example for his students. His work ethic, tenacity, intellectual curiosity, and kindness are unmatched. Throughout my professional and personal development, he has always been there to guide me. Taking the opportunity to work under him as a freshman almost a decade ago was one of the best decisions in my life and I will forever cherish the experience. I am extremely grateful to him for his support and patience. Without him, I would never be here.

TABLE OF CONTENTS

TITLE PAGE i

ACKNOWLEDGEMENTS vii

LIST OF FIGURES xv

NOMENCLATURE xix

CHAPTER I

INTRODUCTION 1

CHAPTER II

LITERATURE REVIEW 7

2.1 Flow over Three-Dimensional Axisymmteric Hill 7

2.2 Non-stationary Pulsating Channel Flow.....11

2.3 Non-stationary Temporally Evolving Channel Flow 13

CHAPTER III

TURBULENCE MODELING AND NUMERICAL APPROACHES..... 15

3.1 Turbulence Modeling Approaches 14

3.1.1 Reynolds Averaged Navier-Stokes (RANS) Models……..15

3.1.1.1 Spalart Allmaras (SA) Model.....16

3.1.1.2 Shear Stress Transport (SST) Model.....17

3.1.2 Large Eddy Simulation (LES)……..…..18

3.1.2.1 Monotonically Integrated Large Eddy Simulation (MILES)……...19

3.1.2.2 Detached Eddy Simulation (DES).....19

3.1.2.3 Delayed Detached Eddy Simulation (DDES).....21

3.1.2.4 SST Multiscale Model.....22

3.1.2.5 Dynamic Hybrid RANS-LES (DHRL)……....23

3.2 Numerical Approach ……...25

3.2.1 Optimization-based Gradient RE-construction (OGRE) Scheme.....25

CHAPTER IV

NUMERICAL SIMULATION OF A THREE-DIMENSIONAL AXISYMMETRIC HILL: PERFORMACNE EVALUATION OF RANS AND HYBRID RANS-LES TECHNIQUES..... 27

4.1 Introduction 27

4.2 Numerical Setup.....28

4.3 Computational Domain.....29

4.5 Results and Discussion..... 32

4.5.1 Distribution of Pressure Coefficient on the centerline z/H = 0.....32

4.5.2 Recirculation Zone behind the Hill.....37

4.5.3 Streamwise Velocity Distribution at x=3.69H.....40

4.5.4 Spanwise Velocity Distribution at x=3.69H.....43

4.5.5 Profiles of Friction Velocity at x=3.63H.....46

4.5.6 Streamwise and Spanwise Velocity Distribution at x=3.63H.....48

4.5.7 Resolved Turbulent Kinetic Energy (TKE) and Resolved Reynolds Stress <u'v> distribution at x= 3.63H.....51

4.5.8 Contours of resolved Turbulent Kinetic Energy.....54

4.5.9 Structure of Flow behind the Hill.....56

4.6 Conclusions.....58

CHAPTER V

STATIC AND DYNAMIC TIME FILTERING TECHNIQUES FOR HYBRID RANS-LES SIMULATION OF NON-STATIONARY TURBULENT FLOWS.....61

5.1 Introduction 61

5.2 Novel Time-Filtering Approaches 63

5.2.1 Exponential Time Averaging (ETA).....63

5.2.2 Exponential Time Averaging (ETA) with static filters.....65

5.2.3 Dynamic Time Filtering (DTF) 66

5.3 Numerical Setup 67

5.3.1 Forcing Functions and Parameters.....67

5.3.2 Data Analysis.....68

5.3.3 Computational Domain and Boundary Conditions.....68

5.4 Results and Discussion 71

5.4.1 Static-Filter Results.....71

5.4.1.1 AC-DC Components.....71

5.4.1.2 Time Varying Mean Velocity.....72

5.4.2 Dynamic Time Filtering Results.....78

5.4.2.1 Steady Pressure Driven Flow (Re_τ = 350 & 590) 78

5.4.2.2 Pulsating Channel Flow 79

5.4.2.3 AC-DC Mean Velocity Components.....80

5.4.2.4 Time Varying Mean Velocity.....83

5.4.2.5 Behavior of Blending Parameter (**α**) for the DHRL model variants 88

5.4.2.6 Reynolds Stresses.....90

5.4.2.7 Comparison of ($\overline{u_i'u_i'}$) and Reynolds Shear Stress ($\overline{u_1'u_2'}$).....92

5.4.2.8 Stream-wise Velocity Fluctuations.....99

5.4 Conclusions.....102

CHAPTER VI

NUMERICAL SIMULATION OF NON-STATIONARY TURBULENT FLOWS USING DOUBLE EXPONENTIAL DYNAMIC TIME FILTERING TECHNIQUE.....104

6.1 Introduction 104

6.2 Modeling Approaches.....106

6.2.1 Direct Numerical Simulation (DNS).....106

6.2.2 Double Exponential Dynamic Time Filtering (DDTF).....106

6.3 Solver & Data Analysis.....108

6.4 Pulsating Channel Flow.....109

6.4.1 Direct Numerical Simulation Setup.....109

6.5 Results and Discussion.....110

6.5.1 Direct Numerical Simulation Validation.....110
6.5.2 Double Dynamic Filtering Validation.....112
6.5.3 Steady Channel Flow.....112
6.5.4 Pulsating Channel Flow.....113
6.5.4.1 AC-DC Mean Velocity Components.....113
6.5.4.2 Time Varying Mean Velocity.....116
6.6 Turbulent Mixing Layer 121
6.6.1 Computational Domain and Grid Generation.....121
6.6.2 Problem Setup.....122
6.6.3 Results and Discussion.....123
6.6.3.1 Flow and Turbulence Statistics.....123
6.6.3.2 Temporal Evolution and Turbulence Statistics.....125
6.7 Conclusions.....126

CHAPTER VII

A NEW VARIANT OF THE DYNAMIC HYBRID RANS-LES MODEL FOR COMPLEX TURBULENT FLOWS.....129
7.1 Introduction 129
7.2 Development of a new Dynamic Hybrid RANS-LES (DHRL) Model.....132
7.2.1 Governing Equations and Turbulence Modeling Approach.....132
7.2.2 Baseline Dynamic Hybrid RANS-LES (DHRL) 133
7.2.3 New Dynamic Hybrid RANS-LES (DHRL) Model.....137
7.3 Test Cases.....141

7.3.1 Fully Developed Turbulent Channel Flow.....142

7.3.1.2 Results and Discussion..... 142

7.3.2 Three Dimensional Axisymmteric Hill.....147

7.3.2.1 Results and Discussion..... 148

7.3.2.2 Distribution of Pressure Coefficient on the centerline z/H = 0.....148

7.3.2.3 Streamwise and Spanwise Velocity Distribution at x= 3.69H.....149

7.3.2.4 Streamwise and Spanwise Velocity Distribution at x=3.63H.....150

7.3.2.5 Turbulent Kinetic Energy ($\frac{1}{2}\overline{u'_\iota u'_\iota}$) and Reynolds Shear Stress ($u'v'$) at x=3.63H 152

7.3.3 Pulsating Channel Flow.....154

7.3.3.1 Results and Discussion..... 154

7.3.3.2 Time Varying Mean-Velocity.....154

7.3.3.3 AC and DC Comparison Reynolds Stresses.....159

7.3.3.4 Comparison of $\overline{u_i'u_i'}$.....159

7.3.3.5 Comparison of Reynolds Shear Stress ($\overline{u_1'u_2'}$).....164

7.3.3.6 AC and DC Component of Blending Parameter.....168

7.4 Conclusions….....169

CHAPTER VIII

CONCLUSIONS & FUTURE WORK..... 171

8.1 Conclusions.....171

8.2 Future Work.....173

LIST OF REFERENCES…….174

LIST OF FIGURES

CHAPTER IV

Figure 1: Side-view of the hill 30
Figure 2: Isometric view of the domain 30
Figure 3: Close up view of the refined mesh around the hill 32
Figure 4: Cell density of the refined grid around the hill 32
Figure 5: Contours of Cp by Simpson et al 33
Figure 6: Contours of Cp for 4.5m grid 34
Figure 7: C_P profiles along the centerline z/H = 0 36
Figure 8: Separation-bubble size comparison 39
Figure 9: $< \bar{u} > / U_{in}$ at x= 3.69H 41
Figure 10: $< \bar{w} > / U_{in}$ at x= 3.69H 44
Figure 11: Profiles of Friction Velocity 47
Figure 12: Plots of (a) $< \bar{u} > / U_{in}$ and (b) $< \bar{w} > / U_{in}$ at x= 3.63H 49
Figure 13: Plots of (a) $< \bar{u} > / U_{in}$ and (b) $< \bar{w} > / U_{in}$ at x= 3.63H 50
Figure 14: Plots of (a) Resolved TKE/U_{in}^2, (b) Resolved Reynolds Stress $(u'v')/U_{in}^2$ at x= 3.69H. 52
Figure 15: Plots of (a) Resolved TKE/U_{in}^2, (b) Resolved Reynolds Stress $(u'v')/U_{in}^2$ at x= 3.69H 53
Figure 16: TKE/U_{in}^2 at x= 3.69H 55
Figure 17: Vortex structure 57

CHAPTER V

Figure 1: Side-view of (a) coarse grid, (b) fine grid, and (c) isometric-view of the domain 69
Figure 2: U^+ vs log (Y^+) for steady channel flow 70
Figure 3: (a) AC, and (b) DC component of streamwise velocity for high frequency case 72
Figure 4: U^+ vs log (Y^+) for high-frequency case 75
Figure 5: U^+ vs log (Y^+) for medium-frequency case 76

Figure 6: U^+ vs log (Y^+) for low-frequency case.....77
Figure 7: U^+ vs log (Y^+) for steady channel flow at (a) Re_τ=350 and (b) flow at Re_τ=590.....79
Figure 8: Streamwise velocity components (a) High Frequency AC and (b) DC; (c) Medium Frequency AC and (d) DC; (e) Low Frequency AC and (f) DC.....82
Figure 9: U^+ vs log (Y^+) for high-frequency case.....85
Figure 10: U^+ vs log (Y^+) for medium-frequency case.....86
Figure 11: U^+ vs log (Y^+) for low-frequency case.....87
Figure 12: Variation of blending parameter for steady-channel flow for baseline DHRL model....88
Figure 13: Distribution of blending function.....89
Figure 14: Mean and Fluctuating Components of resolved Reynolds stresses for high-frequency oscillation.....91
Figure 15: Plots of resolved ($\overline{u_i'u_i'}$) vs y^+ for high-frequency oscillations.....93
Figure 16: Plots of resolved ($\overline{u_i'u_i'}$) vs y^+ for medium-frequency oscillations 94
Figure 17: Plots of resolved ($\overline{u_i'u_i'}$) vs y^+ for low-frequency oscillations 95
Figure 18: Plots of resolved ($\overline{u_1'u_2'}$) vs y^+ for high-frequency oscillations 96
Figure 19: Plots of resolved ($\overline{u_1'u_2'}$) vs y^+ for medium-frequency oscillations 97
Figure 20: Plots of resolved ($\overline{u_1'u_2'}$) vs y^+ for low-frequency oscillations 98
Figure 21: Contours of stream-wise velocity fluctuation at y+=10 for high-frequency oscillations at 8 equidistant times in one cycle.....100
Figure 22: Contours of stream-wise velocity fluctuation at y+=10 for low-frequency oscillations at 8 equidistant times in one cycle.....101

CHAPTER VI

Figure 1: AC & DC component of streamwise velocity 111
Figure 2: U^+ vs log (Y^+) for steady channel flow at Re_τ=350.....113
Figure 3: AC & DC component of streamwise velocity 115
Figure 4: U^+ vs log (Y^+) for high-frequency case.....118
Figure 5: U^+ vs log (Y^+) for medium-frequency case.....119
Figure 6: U^+ vs log (Y^+) for low-frequency case.....120
Figure 7: Computational domain.....121

Figure 8: Computational mesh distribution…….....122
Figure 9: Initial velocity profile comparison.....123
Figure 10: Profiles of (a) Mean-velocity, (b) $\overline{u'}$, (c) $\overline{v'}$, (d) $\overline{w'}$, and (e) $\overline{u'v'}$.....124
Figure 11: Profiles of centerline values of (a) $\overline{u'}$, (b) $\overline{v'}$, (c) $\overline{w'}$, and (d) $\overline{u'v'}$.....126

CHAPTER VII

Figure 1: Illustration of new blending function γ using different coefficients.....138
Figure 2: Distribution of original RANS dependent blending function α and the and new RANS independent blending function γ, for turbulent channel flow simulation.....140
Figure 3: For turbulent channel flow, distribution of original DHRL blending function α and proposed new blending α_{eff} function to be implemented for modified DHRL model.....141
Figure 4: Profiles of normalized mean-velocity for Re_τ = 350.....143
Figure 5: Profiles of blending parameter for Re_τ = 350.....144
Figure 6: Profiles of resolved (a) $\overline{u_i'u_i'}$, and (c) $\overline{u'v'}$ for Re_τ = 350.....145
Figure 7: Profiles of normalized mean-velocity for Re_τ = 590.....146
Figure 8: Profiles of blending parameter for Re_τ = 590.....146
Figure 9: Profiles of (a) mean-velocity, (b) $\overline{u'u'}$, (c) $\overline{v'v'}$, (d) $\overline{w'w'}$, and (e) $\overline{u'v'}$.....147
Figure 10: C_P profiles along the centerline z/H = 0.....149
Figure 11: Plots of (a) $< \bar{u} > / U_{in}$, (b) $< \bar{w} > / U_{in}$ at x= 3.69H.....150
Figure 12: Plots of (a) $< \bar{u} > / U_{in}$ and (b) $< \bar{w} > / U_{in}$ at x= 3.69H.....151
Figure 13: Plots of (a) Resolved TKE$/U_{in}^2$, (b) Resolved Reynolds Stress $(u'v')/U_{in}^2$ at x= 3.69H.....153
Figure 14: U^+ vs log (Y^+) for high-frequency case.....156
Figure 15: U^+ vs log (Y^+) for medium-frequency case.....157
Figure 16: U^+ vs log (Y^+) for low-frequency case.....158
Figure 17: AC and DC Components of resolved Reynolds stresses for high-frequency oscillations……...160
Figure 18: Plots of resolved ($\overline{u_i'u_i'}$) vs y^+ high-frequency oscillations.....161
Figure 19: Plots of resolved ($\overline{u_i'u_i'}$) vs y^+ medium-frequency oscillations.....162
Figure 20: Plots of resolved ($\overline{u_i'u_i'}$) vs y^+ low-frequency oscillations.....163

Figure 21: Plots of resolved ($\overline{u_1'u_2'}$) vs y^+ high-frequency oscillations.....165
Figure 22: Plots of resolved ($\overline{u_1'u_2'}$) vs y^+ medium-frequency oscillations.....166
Figure 23: Plots of resolved ($\overline{u_1'u_2'}$) vs y^+ low-frequency oscillations.....167
Figure 24: Plots of the blending parameter……...168

NOMENCLATURE

c	Chord Length
ρ	Air Density
μ	Dynamic Viscosity
ν	Kinematic Viscosity
U_∞	Free Stream Velocity
Re_τ	Reynolds Number based on friction velocity
RANS	Reynolds Averaged Navier-Stokes
SA	Spalart-Allmaras Model
DNS	Direct Numerical Simulation
LES	Large Eddy Simulation
HRL	Hybrid RANS-LES
DES	Detached-Eddy Simulation
DDES	Delayed Detached-Eddy Simulation
ETA	Exponential Time-Averaging
DTF	Dynamic Time Filtering
DDTF	Doube-Exponential Dynamic Time Filtering
TKE	Turbulent Kinetic Energy
y^+	Non-dimensional Wall Distance
U^+	Non-dimensional Velocity
u_τ	Friction Velocity
ω	Specific Dissipation Rate
δ	Half Channel Height
α	Blending Parameter for the DHRL model

α_{eff}	Alternate Blending Parameter for the DHRL model
U_{in}	Inlet Velocity
$\overline{u'}$	Mean Streamwise Fluctuating Velocity
$\overline{v'}$	Mean Wall-Normal Fluctuating Velocity
$\overline{w'}$	Mean Spanwise Fluctuating Velocity
$R_{11} = \overline{u'u'}$	Streamwise Reynolds Stress
$R_{22} = \overline{v'v'}$	Wall-Normal Reynolds Stress
$R_{33} = \overline{w'w'}$	Spanwise Reynolds Stress
$R_{12} = \overline{u'v'}$	Reynolds Shear Stress
$R_{ii} = \overline{u_i'u_i'}$	Trace of Reynolds Stress

CHAPTER I

INTRODUCTION

From the flow of streams to moving clouds, turbulence is ubiquitous. We encounter turbulence on a daily basis and rarely stop to think about it. For example, when we use a spoon to stir our tea, we are using turbulence to our advantage by enhancing the diffusion of thermal energy. Although humankind has tried to describe the behavior of fluids since the time of Aristotle and Archimedes in ancient Greece [59], it wasn't until the mid-1700's that the first solutions to the equations governing inviscid fluid dynamics were formulated by Leonhard Euler. Following Euler's work, a significant breakthrough came about when Sir Isaac Newton's law of viscosity was adopted in order to relate stress in a fluid to the velocity gradient. Eventually Claude-Louis Navier and George Gabriel Stokes are ultimately credited to have derived the fundamental equations governing fluid flow although they arrived at the derivation independently in the mid-1800's [60].

Since its inception, the Navier-Stokes equations have been validated on numerous occasions over the past 200 years, however, exact analytical solutions still elude us. One of the major hurdles towards obtaining a successful solution to the Navier-Stokes equations is the presence of non-linearities associated with turbulent flows. Modern fluid dynamics revolves around solving turbulent flow problems using iterative methods and approximate models using high performance computing (HPC). This branch of engineering is known as computational fluid dynamics (CFD). Like any technology-based innovation, the evolution in CFD research has tracked the progress in computer development over the decades. As computational power has

grown over the years, our ability to solve problems that seemed impossible only a few years ago, are now possible. This advancement in computing has fostered the development of numerical tools that allow engineers to leverage CFD in day-to-day design and analysis instead of physically testing products and new designs. Modern CFD codes have been implemented to effectively tackle some of the most difficult engineering problems known to man. For example, in the biomedical industry, blood flows in arteries can be simulated using CFD to understand and visualize serious medical conditions such as Hypertrophic Cardiomyopathy (HCM). In the aerospace industry, CFD reduces the need to physically build test components. Parts are designed using Computer Aided Design (CAD) software and tested using CFD to allow preliminary evaluation of their performance.

One of the critical technology barriers for consistently implementing accurate and efficient CFD techniques is turbulence modeling. Turbulence modeling is the development of advanced physics based mathematical models that predict effects associated with turbulence. Richard Feynman, the famous Nobel Laureate for Physics, once described turbulence as "the most important unsolved problem of classical physics." The presence of a large range of scales of motion, high Reynolds numbers, strong three-dimensionality, time dependence, and non-linearities makes turbulence notoriously difficult to predict. One of the earliest attempts at successfully developing a mathematical model for turbulence was carried out by Joseph Valentin Boussinesq in 1877 who suggested that turbulence was, in a sense, similar to the molecular diffusion process and proposed the Boussinesq eddy viscosity hypothesis. In 1925, Ludwig Prandtl proposed a relatively simple method for calculating eddy viscosity by estimating the mixing length analogous to the concept of mean-free path of a gas in thermodynamics. Later in 1945, Prandtl

proposed a model where the eddy viscosity was dependent upon turbulent kinetic energy using a differential equation.

Modern turbulence modeling approaches can be broadly categorized into three different classes: Reynolds Averaged Navier-Stokes (RANS), Large Eddy Simulation (LES), and Direct Numerical Simulation (DNS). RANS solves only the ensemble or time-averaged equations of fluid motion and models all scales of fluctuating motion, LES solves the Navier-Stokes equations for some scales while DNS explicitly solves the Navier-Stokes equations for all scales of motion. The theoretical accuracy of each of these methods is directly proportional to the range of resolved scales, as is the computational expense. Hence, DNS is the most accurate numerical method available today, but it is prohibitively expensive and cannot be employed to solve complex flow problems without the use of supercomputers. Even LES can be too expensive for engineering purposes based on the resolution of the method, requiring several days or even weeks of runtime on typical High-Performance Computing (HPC) architectures. Although not as accurate as DNS or LES, a RANS solution can be obtained using a laptop for most everyday engineering problems with some degree of accuracy. Recently, an emerging class of models, Hybrid RANS-LES (HRL), have been developed to provide a reasonable compromise between the accuracy of LES and the efficiency of RANS. The concept of HRL modeling is still relatively new, with the first model versions introduced in the late 1990s. As the name suggests, the HRL modeling strategy is based on using RANS to model smaller dissipative scales in near-wall regions while larger energy carrying scales are resolved using LES in regions farther from the wall.

The two most common methods of combining RANS and LES are zonal and non-zonal methods. The zonal approach effectively divides the computational domain into regions where RANS or LES models are applied separately. For example, near-wall regions are typically assigned

to a RANS model, while LES model is applied to regions away from the wall where large eddies persist. One of the major difficulties associated with zonal modeling is the treatment of RANS-to-LES transition zones. Since RANS does not support turbulent fluctuations, an internal forcing mechanism or turbulence generator is often required to resolve the correct stress and velocity in the interface before reaching the LES zone. The non-zonal approach seeks to smoothly transition RANS-to-LES based on flow statistics. Some of the most well known non-zonal models are the Detached Eddy Simulation (DES), Delayed Detached Eddy Simulation (DDES), and Improved Delayed Detached Eddy Simulation (IDDES). Although these non-zonal HRL models have been successfully validated and utilized in the aerospace industry for complex flow simulations, most HRL models have strict grid generation requirements and can suffer from non-physical RANS-to-LES transition resulting in modeled stress depletion (MSD). Research focused on improving these models to facilitate high-fidelity CFD solutions for complex scientific and engineering problems is therefore active and, is a major focus of the present work.

The primary goal of this research is to develop, implement, and validate advanced turbulence modeling strategies within the hybrid RANS-LES modeling framework. Also highlighted are some of the key deficiencies with traditional hybrid RANS-LES models while analysing the performance of the baseline and a new variant of the Dynamic Hybrid RANS-LES (DHRL) model for complex turbulent flows. The DHRL model performance is evaluated against Reynolds-Averaged Navier-Stokes (RANS), Monotonically Integrated Large Eddy Simulation (MILES), Detached Eddy Simulation (DES), Delayed Detached Eddy Simulation (DDES), Multiscale LES model, and benchmark LES, DNS, and experimental studies for canonical test cases such as fully turbulent channel flows, flow over a three-dimensional axisymmetric hill, and non-stationary pulsating channel flow. Results obtained from the simulations in terms of mean

flow statistics, pressure distribution, Reynolds stress distribution, and turbulence characteristics are presented and discussed in detail for each test case.

The main objectives of this research are:

1. Evaluation of the performance of the dynamic hybrid RANS-LES (DHRL) model for simulating the flow over a 3D axisymmetric hill including comparison to numerical results from RANS, DES, DDES, Multiscale LES model, and experimental data. Results obtained from the simulations in terms of mean flow statistics, pressure distribution, and turbulence characteristics are presented and discussed in detail. Some of the HRL model performance along with the DHRL model was also compared to benchmark numerical simulations.
2. Development of static and dynamic time-filtering techniques for non-stationary periodic and non-periodic turbulent flows. The present study investigates the performance of the DHRL model with two temporal filtering techniques: Exponential Time Averaging (ETA) with static filter and Dynamic Time Filtering (DTF). These techniques are compared against an industry standard RANS model, MILES, and two conventional HRL models. Model performance is evaluated based on comparison to previously documented DNS and LES results.
3. Development of double exponential averaging to enhance trend predictive capabilities of the dynamic time filtering technique for non-stationary flows including flows with monotonically varying statistics. In this study, the performance of the DHRL model with a double exponential dynamic time filtering (DDTF) methodology is evaluated against a RANS model, a conventional HRL model, implicit LES, and the DHRL model with DTF for a pulsating channel and a

temporally-varying turbulent mixing layer. Model performance is evaluated based on comparisons to existing experimental and Direct Numerical Simulation (DNS) results.

4. Development of a new DHRL model variant with improved RANS-to-LES blending. The alternate blending parameter is developed using a new statistical term that is sensitized to indicate the presence of resolvable LES content in regions of the flow where RANS stress is significantly overpredicted. Three variants of the new DHRL model are validated for fully turbulent channel flow, flow over a three-dimensional axisymmetric hill, and non-stationary flow in a pulsating channel against RANS, HRL, DNS and experimental data.

CHAPTER II

LITERATURE REVIEW

Literature review for the three main test cases evaluated in this study is presented below.

2.1 Flow over three-dimensional axisymmetric hill

Flow over a three-dimensional axisymmetric hill is a challenging test case for Computational Fluid Dynamics (CFD) using Reynolds-Average Navier-Stokes (RANS) and Hybrid RANS-LES (HRL) models. As the flow approaches the hill, it is first decelerated near the foot of the hill and then accelerated upwards. Flow eventually separates just downstream of the crest of the hill in response to the adverse pressure gradient caused by the curvature of the hill. The separation region behind the hill is characterized by the presence of intermittent wakes, separation bubbles, vortices, and regions of spatially varying turbulence intensity. The separated flow forms two sets of counter-rotating vortices with high levels of flow unsteadiness and turbulent kinetic energy (TKE). This type of unsteady behavior is quite commonly observed in hydrodynamics, energy extraction, dispersion of air pollutants, and in aviation applications [38]. It is because of these highly unsteady flow features, conventional Reynolds-Averaged Navier-Stokes (RANS) models fail to accurately capture the flow physics. Also, the prediction of separation location and size of the separation bubble are sensitive to changes in Reynolds number (Re) and turbulent fluctuations. Although, Direct Numerical Solution (DNS) can provide an accurate description of the flow physics, it is computationally not feasible. Previously documented studies [7-10] have

focused on the use of variants of Detached Eddy Simulation (DES), LES and hybrid RANS-LES (HRL) techniques in an attempt to accurately model this type of flow.

Experimental studies of flow over an axisymmetric hill were carried out by Ishihara et al. [1]. Results indicated that flow separation occurred at the top of the hill followed by reattachment at the foot of the hill. This phenomenon was also accompanied by a low frequency motion in the wall layer downstream of the hill. Simpson et al. [2] carried out experiments using Laser-Doppler Velocimetry (LDV) at $Re=1.3x10^5$ with an approach turbulent boundary layer height of $\delta = H/2$. Results from the experiments indicated that the flow was symmetric about the centerline, while complex vortical separations were observed on the leeward side of the hill. These structures merged into two large vortices on the outer regions of the hill and were responsible for the production of large amounts of turbulence. The experimental results also showed the presence of low frequency motion, similar to the observations made by Ishihara et al. [1], which contributed to turbulent diffusion. Further experiments were carried out by Byun et al. [9] using 3D fibre-optic LDV techniques for two different hill heights ($\delta = H$ and $\delta = H/2$). Although the shapes of the bumps were different, the study once again confirmed the presence of two vortical structures on the leeside of the hill formed by the separated flow. The study also suggested the use Unsteady-RANS (URANS) and LES to capture the physics of the separated region especially the effects of low-frequency vortex shedding.

Several numerical simulations of detached flows with fixed separation locations, such as flow over a backward facing step have been performed with varying degrees of success [3,4]. Because of the slowly changing gradients caused by the curvature of the hill, accurate prediction separation and reattachment is a daunting task for both RANS and HRL models alike. Recently, Chitta et al. [5] successfully employed a four-equation transition sensitive and rotation-curvature

corrected eddy viscosity (RANS) model [6] to significantly improve the CFD results compared to more traditional RANS model forms. The new model improved prediction of pressure distribution over the hill surface and accurately captured the formation of a pair of separation bubbles on the leeward side of the hill. There remained, however, discrepancies regarding the height of the recirculation bubble and maximum pressure values downstream of the hill.

RANS and LES studies were carried out by Temmerman et al. [7] at $Re=1.3x10^4$ with an incoming boundary layer height of $\delta=H/2$. The results indicated the presence of a horseshoe vortex upstream of the hill which was not previously mentioned in the experimental results. The investigation also revealed the inability of RANS models to capture non-local turbulence features associated with large-scale structures. According to numerical simulations performed by Persson et al. [8], RANS models display poor predictive capability especially in the wake region when compared to detached eddy simulation (DES), and LES models. DES results, however, depended strongly on the value of freestream turbulent viscosity. For a high level of inflow viscosity, RANS-like results were observed, while improved accuracy was obtained with a lower incoming turbulent viscosity. The DES results were found to be less accurate than LES regardless of the inlet value of turbulent viscosity. Patel et al. [9] used LES with a Localized Dynamic sub-grid Kinetic-energy Model (LDKM) to simulate the flow around the hill. The results indicated good quantitative agreement with measured data in terms of near-wall mean flow statistics and the model correctly resolved two counter-rotating vortex pairs downstream on the lee-side. Although promising, some discrepancies were observed in the outer regions of the flow. Despite some drawbacks, the authors concluded that because LDKM was able resolve the complex near-wall flow with reasonable accuracy, the model is sufficient for this class of flows.

Davidson et al. [10] documented simulations using Hybrid RANS-LES (HRL) and LES models. For the HRL model, an unsteady RANS (URANS) was employed to resolve flow for $y^+ \leq 40$ (y^+ = dimensionless wall distance) before switching to an LES formulation farther from the wall. Results indicated that the HRL model with forcing at the RANS-LES interface had improved predictive capabilities, while the resolved turbulence from the HRL model with no forcing was gradually dissipated. LES, on the other hand, was less accurate than either of the HRL models. Garcia et al. [11] performed a comprehensive study of the flow behavior, using the dynamic Smagorinsky model [12]. The study provided detailed analysis of the structure and behavior of the flowfield around of the hill. Although the velocity and pressure profiles were close to experimental data, the results indicated some differences. According to simulation results, flow reversal tapered leading to separation followed by the presence of two foci and two saddle points in the separation region. However, experimental data shows the separation location to be further downstream and the presence of two foci and only one saddle point in the separated zone. Although, Byun, Simpson, and Ma et al. [13-15] did conjecture that to satisfy topological rules, three foci and three saddle points should have been observed in the separation zone. The study did, however, an explanation for the presence of a high turbulent region upstream of the separation zone which influences the location of separation. Also, the authors pointed out that the simulations predicted separated flow at all times during the simulations as opposed to the speculated intermittent attachment and re-attachment based on the bimodal velocity in the experiments [1]. Overall, the study provided a useful insight into to structure and behavior of the flow around the hill and is considered a benchmark for evaluation of hybrid RANS-LES and LES models.

2.2 Non-stationary pulsating channel flow

Turbulent flows in engineering applications such as flow over airfoils, immersed bodies, stenosed arteries, heat exchangers, and in gas turbine engines are often accompanied by imposed unsteadiness, large-scale vortex shedding, and the interaction of different scales of motion. Because of their significance, these types of flows are of considerable interest to the computational fluid dynamics (CFD) community as a test for newly developed turbulence models and numerical methods. Often these problems are notoriously difficult to model and may require high fidelity numerical methods with large computational resources. The pulsating channel flow is one such problem. The presence of unsteady turbulent boundary layers, complex interaction between the mean and time-dependent components of the flow, and regions of spatially and temporally varying statistical quantities presents a unique set of challenges for existing and newly developed turbulence models.

Unsteady turbulent boundary layers can either be oscillating (zero temporal mean) or pulsating (non-zero temporal mean). Experimental results suggest that, for a purely oscillating case, the flow remains stable for Re_s (Reynolds number based on Stokes thickness) less than 400. As Re_s is increased, the flow is intermittent between laminar and turbulent until $Re_s = 800$ [16], after which the flow becomes fully turbulent. On the other hand, for a pulsating channel flow with low frequency oscillations, turbulence has time to relax to the local equilibrium. With an increase in pulsating frequency, the ratio between the intensity of streamwise fluctuation and turbulent kinetic energy shows signs of phase dependence indicating that production and dissipation are also out of phase.

Since the early 1960's, several experiments have been carried out in an attempt to describe the physics of oscillating and pulsating boundary layer flows. Sarpkaya [17] studied the response

of coherent turbulent structures in an oscillating pipe using Laser Induced Fluorescence (LIF), while Gündoğdu and Çarpinlioğlu [18,19] performed detailed studies describing the theory of pulsatile flow in a channel for laminar, transitional, and turbulent regimes. Both studies suggested further investigations into oscillatory, pulsatile, and non-canonical flows to ensure a better understanding of the underlying physics involved in turbulent processes. Experiments in a reciprocating wind tunnel using LDV (Laser Doppler Velocimetry) and hot wire anemometry were carried out by Hino et al. [16]. The authors concluded that in the acceleration phase, turbulence is generated by instabilities close to the wall but is not allowed to grow. As the flow begins to decelerate, large amounts of turbulence are generated near the wall. They also found that the turbulent energy-spectrum closely follows the Kolmogorov spectrum in the acceleration phase while following a steep power law for the deceleration phase denoting a large amount of dissipation from high frequency turbulent oscillations.

Spalart et al. [20] performed DNS calculations for the turbulent solution to Stokes' second problem. Results indicated that the oscillating boundary layer behaves as a function of both, the Reynolds number and the phase angle. For Re<600, the flow undergoes a preliminary transition to a pre-turbulent state followed by a second transition between Re 600-800 which is similar to the observations made in [16]. LES calculations using a fourth-order finite difference scheme and commutative filter suggested by Vasilyev et al. [21] was carried out by Lund [22]. According to the author, explicit filtering improved the accuracy of LES. Such improvements include a better description of the logarithmic region, near wall anisotropy of the velocity fluctuations, and the shear stress estimation of the sub-grid scale model. He concluded that mesh refinement and explicit filtering both improve results since numerical results are damped out by both mechanisms, but they do so with a considerable increase in cost.

RANS (Reynolds Averaged Navier-Stokes), LES, and DNS calculations of pulsating flows were carried out extensively by Scotti et al. [23,24]. Results indicated that eddy viscosity models significantly overestimated the Reynolds stresses, turbulent kinetic energy and dissipation. LES model results indicated that high frequencies are damped before reaching the log layer, with the cut-off frequency being proportional to the mean turbulent intensity. LES data also agreed with experimental observations that turbulent fluctuations tend to appear towards the end of the acceleration phase and the phase difference between the turbulent quantities in the generation region was more dependent on the driving frequency while away from the generation regions the phase difference remained fairly constant.

2.3 Non-stationary temporally evolving channel flow

Similar to the non-stationary pulsating channel flow, the temporally evolving non-stationary flows introduce their own set of challenges. These types of flows require high fidelity numerical methods to accurately capture flow behavior such as laminar to turbulent transition, growth and suppression of turbulent fluctuation, and temporally evolving gradients. Because of these complex flow features, traditional numerical and turbulence modeling techniques are often unable to accurately resolve the flow statistics.

Ansari et al. [25] performed DNS of a turbulent mixing layer using low-gradient laminar (ML1) and high-gradient laminar (ML2) initial velocity profiles. The ML1 simulations indicated the presence of vortex roll up and streamwise vortices observed in experimental studies. These vortical structures were responsible for enhancing the intensity of the turbulent fluctuations and scalar mixing in agreement with experimental observations. However, the simulations predicted higher normal RMS when compared to experiments indicating the presence of large-scale coherent structures for the ML1 flow. The ML2 simulations allowed a longer turbulent development than

the ML1 while lacking the high-energy large-scale structures observed in the ML1 simulations. The ML2 simulations were in close agreement with experimental observations. It was concluded that two-dimensional vortex roll-ups and streamwise vortices both contribute to growth of mixing layers. The authors concluded that the long-time character of the laminar boundary layer and turbulent boundary layer mixing layers are similar and that both layers reach a universal self-similar rate.

CHAPTER III

TURBULENCE MODELING AND NUMERICAL APPROACHES

3.1 TURBULENCE MODELING APPROACHES

Computational Fluid Dynamics simulations were performed using unsteady three-dimensional finite-volume computational fluid dynamics (CFD) for a single-phase incompressible fluid. The SA, *k-ω* SST, MILES, SA-DES, SA-DDES, SST Multiscale, and the dynamic hybrid RANS-LES (DHRL) model were used to model the effects of turbulence via the use of eddy-viscosity or turbulent-viscosity which models the effect of turbulent mixing as an increase in the effective diffusion rate of momentum. The following section provides brief descriptions of the models with their relevant equations.

3.1.1 Reynolds Averaged Navier-Stokes (RANS) Models

RANS modeling framework revolves around solving the Navier-Stokes equations for mass, momentum, and energy for an average description of the flow, while the effects of complex turbulent interactions are modeled via additional transport equations based on statistical quantities. For RANS models, the instantaneous velocity field is decomposed into the sum of mean and fluctuating components as shown in the following equation.

$$u(x,t) = \bar{u}(x,t) + u'(x,t) \tag{1}$$

where $\bar{u}(x,t)$ is the mean-velocity and $u'(x,t)$ is the fluctuating velocity. Once substituted into the Navier-Stokes equations and ensemble-averaged, the RANS equations are obtained. The

RANS mass and momentum conservation equations for a compressible single species fluid are given below :-

$$\frac{\partial \bar{\rho}}{\partial t} + \frac{\partial (\bar{\rho}\bar{u}_i)}{\partial x_i} = 0 \tag{2}$$

$$\frac{\partial}{\partial t}(\bar{\rho}\bar{u}_i) + \frac{\partial}{\partial x_j}(\bar{\rho}\bar{u}_i\bar{u}_j) = -\frac{\partial \bar{p}}{\partial x_i} + \frac{\partial}{\partial x_j}(\sigma_{ij} + \tau_{ij}) \tag{3}$$

where σ_{ij} is the viscous stress tensor and τ_{ij} is the Reynolds stress tensor defined as:

$$\sigma_{ij} = \mu\left[\left(\frac{\partial \overline{u_i}}{\partial x_j} + \frac{\partial \overline{u_j}}{\partial x_i}\right) - \frac{2}{3}\delta_{ij}\frac{\partial \overline{u_k}}{\partial x_k}\right] \tag{4}$$

$$\tau_{ij} = -\left(\overline{\rho u_i u_j} - \bar{\rho}\bar{u}_i\bar{u}_i\right) \tag{5}$$

where the overbar symbol ($\bar{}$) signifies an ensemble average.

The use of transport equations to model all scales of turbulent motion makes RANS models very efficient. Coupled with low computational requirement and the relative ease to use, RANS models have remained an industry standard since their inception.

3.1.1.1 Splart-Allmaras (SA) Model

The Spalart-Allmaras or the SA model [26] is a one-equation model that solves a transport equation for the kinematic eddy (turbulent) viscosity. The SA model was designed specifically for aerospace applications involving wall-bounded flows and has been shown perform well for boundary layers subjected to adverse pressure gradients. The transport equation for the modified viscosity ($\tilde{\nu}$) is given by:

$$\frac{D\rho\tilde{\nu}}{Dt} = G_\nu - Y_\nu + \frac{1}{\sigma_{\tilde{\nu}}}\left[\frac{\partial}{\partial x_j}\left\{(\mu + \rho\tilde{\nu})\frac{\partial \tilde{\nu}}{\partial x_j}\right\} + C_{b2}\rho\frac{\partial \tilde{\nu}}{\partial x_j}\frac{\partial \tilde{\nu}}{\partial x_j}\right] + S_{\tilde{\nu}} \tag{6}$$

$$G_\nu = C_{b1}\rho\tilde{S}\tilde{\nu} \tag{7}$$

$$Y_\nu = C_{\omega 1} \rho f_\omega \left(\frac{\tilde{\nu}}{d}\right)^2 \quad (8)$$

where G_ν is the production term, and Y_ν is the destruction term in the near-wall region due to wall blocking and viscous damping, $\sigma_{\tilde{\nu}}$ and C_{b2} are the constants, ν is the molecular kinematic viscosity, $S_{\tilde{\nu}}$ is a user-defined source term, and *d* is the distance to the nearest wall.

3.1.1.2 Shear Stress Transport (SST) *k-ω* RANS Model

The Shear Stress Transport (SST) *k-ω* RANS model developed by Menter [27] is a two-equation eddy viscosity model that solves for turbulent kinetic energy *(k)* and specific dissipation rate (*ω)*. The model was developed to combine the near-wall benefits of the standard *k-ω* and the free-stream performance of the *k-ε* model. The SST *k-ω* is one of the most widely used RANS turbulence models for industrial and academic CFD simulations. The model has demonstrated improved performance compared against other two-equation models for a wide range of flows including turbulent boundary layers, jets, and adverse pressure gradients. The key model equations are shown below:-

$$\frac{D\rho k}{Dt} = \tau_{ij}\frac{\partial u_i}{\partial x_j} - \beta^* \rho \omega k + \frac{\partial}{\partial x_j}\left[(\mu + \sigma_k \mu_t)\frac{\partial k}{\partial x_j}\right] \quad (9)$$

$$\frac{D\rho\omega}{Dt} = \frac{\gamma}{\nu_t}\tau_{ij}\frac{\partial u_i}{\partial x_j} - \beta\rho\omega^2 + \frac{\partial}{\partial x_j}\left[(\mu + \sigma_\omega \mu_t)\frac{\partial \omega}{\partial x_j}\right] + 2(1 - F_1)\rho\sigma_{\omega 2}\frac{1}{\omega}\frac{\partial k}{\partial x_j}\frac{\partial \omega}{\partial x_j} \quad (10)$$

$$\nu_t = \frac{a_1 k}{max(a_1\omega, SF_2)} \quad (11)$$

$$F_1 = tanh\,(arg_1^4) \quad (12)$$

$$F_2 = tanh\,(arg_2^2) \quad (13)$$

$$arg_1 = min\,(max\left(\frac{\sqrt{k}}{0.09wy}; \frac{500\nu}{y^2\omega}\right); \frac{4\rho\sigma_{\omega 2}k}{CD_{k\omega}y^2}) \quad (14)$$

$$arg_2 = max\left(2\frac{\sqrt{k}}{0.09wy}; \frac{500\nu}{y^2\omega}\right) \quad (15)$$

where ν_t is the kinematic turbulent or eddy viscosity, and F_1 is the switching function. For $F_1 = 1$, the model operates in a *k*-ω form, while for a value of $F_1 = 0$, an approximation to the *k*-ε model form is obtained.

3.1.2 Large Eddy Simulation (LES)

Similar to the RANS approach, the LES modeling framework decomposes the flowfield based on scales of motion. Using filters, large energy carrying structures are explicitly resolved, while small dissipative scales of motion are modeled using sub-grid scale models. Eq. (16) shows the decomposition of the velocity field used in the LES modeling approach.

$$u(x,t) = \hat{u}(x,t) + u'(x,t) \tag{16}$$

where $\hat{u}(x,t)$ is the filtered velocity and $u'(x,t)$ is the unresolved velocity. By substituting Eq. (16) into the Navier-Stokes equations, the filtered Navier-Stokes equations for mass and momentum for a single-phase, single-species compressible fluid with negligible body forces are obtained :

$$\frac{\partial \hat{\rho}}{\partial t} + \frac{\partial}{\partial x_j}\left(\hat{\rho}\widehat{u_j}\right) = 0 \tag{17}$$

$$\frac{\partial}{\partial t}\left(\hat{\rho}\widehat{u_i}\right) + \frac{\partial}{\partial x_j}\left(\hat{\rho}\widehat{u_i}\widehat{u_j}\right) = -\frac{\partial \hat{p}}{\partial x_i} + \frac{\partial}{\partial x_j}\left(\sigma_{ij} + \tau_{ij}\right) \tag{18}$$

where the hat overbar symbol (^) signifies an undefined filtering operation. The viscous and sub-filter stress tensors are defined as:

$$\sigma_{ij} = \mu\left[\left(\frac{\partial \widehat{u_i}}{\partial x_j} + \frac{\partial \widehat{u_j}}{\partial x_i}\right) - \frac{2}{3}\delta_{ij}\frac{\partial \widehat{u_i}}{\partial x_k}\right] \tag{19}$$

$$\tau_{ij} = -\left(\widehat{\rho u_i u_j} - \hat{\rho}\widehat{u_i}\widehat{u_j}\right) \tag{20}$$

Closure of the filtered Navier-Stokes equations require modeling of the sub-filter stress tensor τ_{ij}. Use of sub-grid scale models or RANS models are two different approaches to modeling the sub-filter stress tensor.

3.1.2.1 Monotonically Integrated Large Eddy Simulation (MILES)

Proposed by Fureby et al. [28], the Monotonically Integrated Large Eddy Simulation (MILES) approach utilizes the inherent dissipative nature of finite volume methods to numerically model the effect of sub-grid scales of motion on the resolved scales. In the MILES approach for an incompressible fluid, the sub-filter term shown in Eq. (20) reduces to:

$$\tau_{ij} = \widehat{u_i u_j} - \widehat{u_i}\widehat{u_j} = 0 \tag{21}$$

For the present study, the MILES approach was implemented by simply running the simulation with no turbulence model and using a low-dissipation upwind-biased numerical scheme (OGRE).

3.1.2.2 Detached Eddy Simulation (DES)

Proposed by Spalart et al., the Detached Eddy Simulation (DES) [29] is a hybrid RANS-LES model that locally blends RANS and LES models based on the distance to the nearest wall. In near-wall regions where the turbulent length scale is smaller than local grid scale, the model operates in RANS mode, while in regions away from wall that are dominated by large scale structures for which the turbulent length scales are larger than the local grid scale, an LES model is used to resolve the flowfield. The initial DES model proposed by Spalart modified the wall distance, d, in the destruction term of the SA model to be implemented as a RANS-to-LES blending parameter given by:

$$\tilde{d} = min\,(d, C_{DES}\Delta) \tag{22}$$

where d is the distance to the nearest wall, C_{DES} is a constant of calibration, and Δ corresponds to the local grid scale. In regions of relatively tight grid spacing, the modified destruction term has the effect of lowering eddy viscosity. This allows the DES model to act like a sub-grid scale model when the local grid scale is smaller than the distance to the nearest wall which is the case outside the boundary layer.

Further implementations of the DES model with other RANS models were carried out by Menter et al. [30,31] by modifying the turbulent length scales. Although not investigated in this study, the SST-DES model is one such example. The SST-DES model includes such a modification to the dissipation term of the turbulent kinetic energy equation, Eq. (6), of the SST- *k-ω* RANS model shown below:

$$\frac{D\rho k}{Dt} = \tau_{ij}\frac{\partial u_i}{\partial x_j} - \beta^*\rho\omega k F_{DES} + \frac{\partial}{\partial x_j}[(\mu + \sigma_k\mu_t)\frac{\partial k}{\partial x_j}] \tag{23}$$

$$F_{DES} = max\left(\frac{L_t}{C_{DES}\Delta}, 1\right) \tag{24}$$

$$C_{DES} = 0.61 \tag{25}$$

$$\Delta = max(\Delta x, \Delta y, \Delta z) \tag{26}$$

$$L_t = \frac{\sqrt{k}}{\beta^*\omega} \tag{27}$$

where F_{DES} is the switching function used for RANS-to-LES transition, and L_t is the modeled turbulent length scale from the SST- *k-ω* RANS model. In regions of the flow where the turbulent length scale is larger than the local grid scale, i.e. $L_t > C_{DES}\Delta$, the model operates in LES mode, while in near-wall regions where turbulent length scale is smaller than the local grid scale, i.e. $L_t < C_{DES}\Delta$, the model operates in RANS mode. This model behaves similar to a *k*-equation sub-grid scale LES model with the dissipation equation remaining decoupled from the turbulent kinetic energy equation in the LES part of the spectrum.

Past studies have highlighted the relative effectiveness of DES based models in predicting unsteady flows with complex wakes and separated shear layers when compared to traditional RANS models. However, because of strict grid generation requirements and relative sensitivity to changes in grid resolution, more advanced methods such as DDES have been developed.

3.1.2.3 Delayed Detached-Eddy Simulation (DDES)

The Delayed Detached Eddy Simulation (DDES) [32] was formulated to address some of the issues with the DES framework. For a traditional grid with high aspect ratio cells near the wall and in the boundary layer, the grid spacing in the flow direction is large such that $\Delta = \max(\Delta x, \Delta y, \Delta z) \gg d$ (distance to nearest wall) and the model remains in RANS mode. Outside the boundary layer where $\Delta \ll d$, the model effectively transitions to LES. For complex geometries where $\Delta \sim d$, LES mode can be activated inside the boundary layer where the grid is not refined enough to sustain the resolved turbulence. The DDES model attempts to correct this issue by delaying the RANS to LES transition. The DES length scale $\tilde{d}$ is redefined by the following equation :

$$\tilde{d} = d - f_d \max(0, d - C_{DES}\Delta_{max}) \tag{28}$$

$$f_d = 1 - \tanh((8r_d)^3) \tag{29}$$

$$r_d = \frac{\tilde{\nu}}{\sqrt{\frac{\partial \overline{u_i}}{\partial x_j}\frac{\partial \overline{u_i}}{\partial x_j}\kappa^2 d^2}} \tag{30}$$

$$\tilde{\nu} = \nu_t + \nu \tag{31}$$

where ν_t is the eddy viscosity, ν is the molecular kinematic viscosity, $U_{i,j}$ are the velocity gradients, κ is Von Kármán constant, and d is the distance to the nearest wall. The RANS-to-LES transition is carried out by r_d which equals 1 in a logarithmic layer, and falls gradually towards 0 at the edge of the boundary layer. Also, the addition of ν in the numerator corrects the very near-wall behavior by ensuring that r_d remains greater than 0.

3.1.2.4 SST Multiscale Model

Proposed by Nichols and Nelson [33,34], the SST Multiscale model is an alternative to the DES approach for constructing a hybrid RANS-LES model. Instead of using a single turbulent length scale, the SST Multiscale model uses an additional turbulent length scales usually associated with algebraic turbulence models. Relevant model equations are presented below:

$$L_T = max\ (6.0\sqrt{\frac{\nu_{t_{RANS}}}{\Omega}}, l_T) \tag{32}$$

$$l_T = k_{RANS}^{\frac{3}{2}} / \varepsilon_{RANS} \tag{33}$$

$$k_{LES} = k_{RANS} f_d \tag{34}$$

$$f_d = \frac{1+tanh\left(2\pi(\Lambda-0.5)\right)}{2} \tag{35}$$

$$\Lambda = \frac{1}{1+(\frac{L_T}{L_g})^{4/3}} \tag{36}$$

$$L_g = max\ (\Delta x, \Delta y, \Delta z) \tag{37}$$

$$\nu_{tLES} = min\ (0.084 L_g \sqrt{k_{LES}}, \nu_{tRANS}) \tag{38}$$

$$\nu_t = \nu_{tRANS} f_d + (1 - f_d)\nu_{tLES} \tag{39}$$

In the above, L_T is the effective turbulent length scale, $\sqrt{\frac{\nu_{t_{RANS}}}{\Omega}}$ is the length scale derived from algebraic models, l_T is the turbulent length scale of the two-equation RANS model, $\nu_{t_{RANS}}$ is the eddy viscosity from the unfiltered RANS model, Ω is the local mean flow vorticity, f_d is a switching function, L_g is the local grid scale, Δx, Δy, and Δz denote the local grid spacing, ν_{tLES} is the sub-grid eddy viscosity, and ν_t is the effective viscosity. The damping function f_d is used to smoothly transition between RANS and LES modes.

3.2.5 Dynamic Hybrid RANS-LES model

The dynamic hybrid RANS-LES (DHRL) model is a hybrid RANS-LES modeling framework developed by Walters et al. [35,36] for coupling any RANS model with any LES model. For an incompressible Newtonian fluid, the filtered Navier-Stokes momentum equation solved in a typical LES framework can be written as:

$$\frac{\partial \hat{u}_i}{\partial t} + \hat{u}_j \frac{\partial \hat{u}_i}{\partial x_j} = -\frac{1}{\rho}\frac{\partial \hat{P}}{\partial x_i} + \frac{\partial}{\partial x_j}\left(2\nu \hat{S}_{ij}\right) - \frac{\partial}{\partial x_j}(\tau_{ij}) \tag{40}$$

$$\tau_{ij} = \widehat{u_i u_j} - \hat{u}_i \hat{u}_j \tag{41}$$

where (ˆ) is an undefined filtering operation, and τ_{ij} is the sub-filter stress term. Analogous to the Reynolds Stress term ($-\overline{u_i' u_j'}$) in a RANS modeling approach, the sub-filter stress (τ_{ij}) term is a direct consequence of the filtering operation. In the DHRL framework, this term is modeled as a weighted sum of the sub-grid stress and the Reynolds stress obtained from a RANS model. The appropriate stress is computed using,

$$\tau_{ij} = \alpha {\tau_{ij}}^{SGS} + (1 - \alpha){\tau_{ij}}^{RANS} \tag{42}$$

$$\alpha = \overline{u_i^{"} u_j^{"}}\,\overline{S_{ij}} \Big/ \left(\tau_{ij}^{RANS}\overline{S_{ij}} - \overline{\tau_{ij}^{SGS}}\,\overline{S_{ij}}\right) \tag{43}$$

where α is the blending parameter. Based on local flow statistics, the sub-filter stress now transitions between a modeled Reynolds stress (${\tau_{ij}}^{RANS}$) and an LES sub-grid stress (${\tau_{ij}}^{SGS}$). The resolved and modeled stresses contain an overbar ($\bar{}$) signifying ensemble or Reynolds-averaged quantities. Since the baseline version of the DHRL modeled was developed for stationary flows, the Reynolds-averaged quantities were obtaining by using a running time average for a large number of time-steps which is statistically analogous to an infinite time average.

The DHRL model used in this study incorporates the SST *k-ω* model as its RANS component and MILES as the LES component. Since MILES does have an explicitly defined sub-grid stress model but depends on numerical dissipation to model the effects of the small scales, we know that:

$$\overline{\tau_{ij}^{SGS}} = 0 \tag{44}$$

and Eqs. (42) and (43) simplify to:

$$\tau_{ij} = (1-\alpha){\tau_{ij}}^{RANS} \tag{45}$$

$$\alpha = \overline{u_i^{"} u_j^{"}}\,\overline{S_{ij}} \Big/ \tau_{ij}^{RANS}\overline{S_{ij}} \tag{46}$$

where,

$${\tau_{ij}}^{RANS} = \frac{2}{3}k\delta_{ij} - 2\,\nu_t\overline{S_{ij}} \tag{47}$$

and Eq. (40) can now be written as:

$$\frac{\partial \hat{u}_i}{\partial t} + \hat{u}_j\frac{\partial \hat{u}_i}{\partial x_j} = -\frac{1}{\rho}\frac{\partial \hat{P}}{\partial x_i} + \frac{\partial}{\partial x_j}\left(2\nu\hat{S}_{ij}\right) - \frac{\partial}{\partial x_j}\left((1-\alpha){\tau_{ij}}^{RANS}\right) \tag{48}$$

Based on the ratio of resolved to modeled production, the value of α is limited between 1 and 0. In regions where sufficient turbulent fluctuations can be resolved, i.e. $\overline{u_i^{"}u_j^{"}S_{ij}} \geq \tau_{ij}^{RANS}\overline{S_{ij}}$, the model recovers pure LES as $\alpha \to 1$. In regions where $\overline{u_i^{"}u_j^{"}S_{ij}} \ll \tau_{ij}^{RANS}\overline{S_{ij}}$, the model recovers pure RANS as $\alpha \to 0$. Further details regarding the development of the DHRL model are discussed in Chapter VII.

Compared to other HRL models, one major improvement of the DHRL modeling framework is the lack of any explicit grid terms in the blending parameter α. This allows the model to remain relatively insensitive to changes in grid resolution as shown in previous studies.

3.2 NUMERICAL APPROACH

This research uses a low- dissipation numerical scheme for simulation of all the turbulent flow for which at least a portion of the turbulence spectrum is resolved. The representative low-dissipation scheme used is discussed below.

3.2.1 Optimization-based Gradient RE-construction (OGRE) Scheme

The low-dissipation numerical scheme used in this study is the Optimization-based Gradient RE-construction (OGRE) scheme [37]. OGRE is a face variable reconstruction method that utilizes iterative least-square gradient computation to minimize 2nd order dissipation on cartesian and structured grids. The left and right face states are calculated using Mach-number-weighted averaging, while a slope limiter preserves local monotonicity. OGRE calculates an initial gradient using a weighted least-squares method of the form:

$$\frac{\partial \widehat{\phi}}{\partial x_i} = \sum_{n=1:N} \omega_{i,n}(\phi_n - \phi_0) \tag{49}$$

where ϕ is any primary variable, ω_i is the weight co-efficient, ϕ_n is the neighboring cell variable value of variable ϕ, ϕ_0 is the current cell variable value, and N is the summation over neighboring cells. A modified gradient is then calculated using identical weight coefficients as:

$$\frac{\partial \phi}{\partial x_i} = \sum_{n=1:n} \omega_{i,n} \left[(\phi_n - \phi_0) + 0.5 \left(\frac{\partial \hat{\phi}}{\partial x_i}\Big|_0 - \frac{\partial \hat{\phi}}{\partial x_i}\Big|_n \right) r_{j,0n} \right] \tag{50}$$

The initial cell gradient for a given cell and its neighbor are denoted by $\frac{\partial \hat{\phi}}{\partial x_i}\Big|_0$ and $\frac{\partial \hat{\phi}}{\partial x_i}\Big|_n$ and the direction vector pointing to each neighboring cell centroid is given by $r_{j,0n}$. It has been shown for several previously documented numerical simulations that OGRE effectively reduces numerical dissipation in Cartesian and structured regions of meshes even for non-uniform aspect ratios and wall-normal cell stretching. From spectral analysis, the OGRE scheme has a been shown to eliminate up to the 3rd order dissipative error contribution for perfectly structured grids.

CHAPTER IV

NUMERICAL SIMULATION OF A THREE-DIMENSIONAL AXISYMMETRIC HILL: PERFORMANCE EVALUATION OF RANS AND HYBRID RANS-LES TECHNQIUES

4.1 INTRODUCTION AND OBJECTIVES

The unsteady flow over a three-dimensional axisymmetric hill is of considerable importance to the Computational Fluid Dynamics (CFD) community because of the complex flow features associated with it. The incoming fully developed boundary layer is attached in the windward side with a small recirculation bubble at the foot of the hill. The flow separates at the apex of the hill and re-attaches close to the foot of the hill. Because of the separation, several key flow features dominate the separation region such as intermittent wakes, separation bubbles, vortices, and regions of varying turbulence intensities. This type of unsteady behavior is commonly associated in hydrodynamic applications, energy extraction, dispersion of air pollutants, and in aviation applications. These highly unsteady flow features are represented poorly using conventional Reynolds-averaged Navier-Stokes (RANS) models. Although Direct Numerical Solution (DNS) is capable of providing accurate descriptions of the flow physics, it is prohibitively

expensive. Most recent studies have focused on the use of Detached Eddy Simulation (DES), LES and hybrid RANS-LES (HRL) techniques to accurately model this type of flow.

This study aims to demonstrate the predictive capabilities of a dynamic Hybrid-RANS LES (DHRL) model in resolving the flow around a 3D axisymmetric hill. The DHRL model proposed by Bhushan and Walters [35,36] is based on the concept of rigorous separation of Reynolds stress and sub-grid stress. The model attempts to improve on the shortcomings of traditional HRL models such as explicit grid dependence, delayed break down of shear layers, and modeled stress depletion in attached boundary layers. This study also aims to demonstrate the importance of using a low-dissipation numerical scheme for practical simulation of turbulent flow for which at least a portion of the turbulence spectrum is resolved.

4.2 NUMERICAL SETUP

Numerical simulations were carried out in Loci-CHEM [39,40] which is a finite volume flow solver capable of modeling chemically reacting flows. CHEM employs density-based algorithms, implicit numerical methods, and high-resolution approximate Riemann solvers to solve chemically reacting viscous turbulent flows. The convective terms are discretized using a traditional upwind-biased second-order Roe flux formulation and with a low dissipation face variable scheme also known as the Optimization-based Gradient RE-construction (OGRE) scheme.

For the present simulations, low Mach number ideal gas flow was used to simulate flow in the incompressible regime. Velocity inlet and pressure outlet boundary conditions were applied in the upstream and downstream directions respectively, while the hill, bottom wall, and side walls were specified as no-slip wall boundaries. To match the experiments, a fully-developed turbulent boundary layer profile was enforced on the inlet plane and atmospheric pressure was considered

at the pressure outlet boundary. The incoming streamwise velocity profile was defined by the power law approximation

$$u_x = \begin{cases} U_0 \left(\frac{y}{\delta}\right)^{\frac{1}{n}} & y \leq \delta \\ U_0 & (3.2H - \delta) \geq y \geq \delta \\ U_0 (\frac{3.2H - y}{\delta})^{\frac{1}{n}} & 3.2H \geq y \geq (3.2\mathrm{H} - \delta) \end{cases} \quad (50)$$

where the inlet velocity is $U_0 = 27.5\, m/s$, the boundary layer height is equal to one-half of the hill height ($\delta = H/2$), the exponent $n = \log(Re)$, and y is the wall-normal distance. A Reynolds number of $Re_\theta \approx 7300$ was approximated by using $n = 7$, similar to the study carried out by Persson et al. [8]. Other inlet variables were calculated based on inlet freestream turbulence intensity and turbulent-to-molecular viscosity ratio of 0.1% and 10, respectively. Turbulent kinetic energy and specific dissipation rate for fully developed duct flow were specified at the inlet. For further details on inlet boundary conditions, readers are referred to [3,8-10] and Ansys Fluent User Guide [41].

4.3 COMPUTATIONAL DOMAIN

Fig. 1 shows the shape of the hill is defined by Simpson et al. [7] given by:

$$\frac{y(r)}{H} = -\frac{1}{6.04844}\left[J_0(\Lambda) I_0(\Lambda \frac{r}{a}) - I_0(\Lambda) J_0(\Lambda \frac{r}{a})\right] \quad (51)$$

where Λ=3.1926, height of the hill is given H=78mm, and a=2H=156mm which is the radius of the circular base of the hill. J_0 and I_0 are the Bessel function of first kind, and the modified Bessel function of the first kind respectively. Figure 2 shows an isometric view of the computational domain with the hill mounted at the bottom of a channel. The domain extends up to 32H in the stream-wise direction, 11.6H in the cross-stream direction and 3.2H in the wall-normal direction.

The inlet, outlet and the cross-stream boundaries are located at 12.8H, 19.2H, and 5.8H, respectively, from the center of the hill.

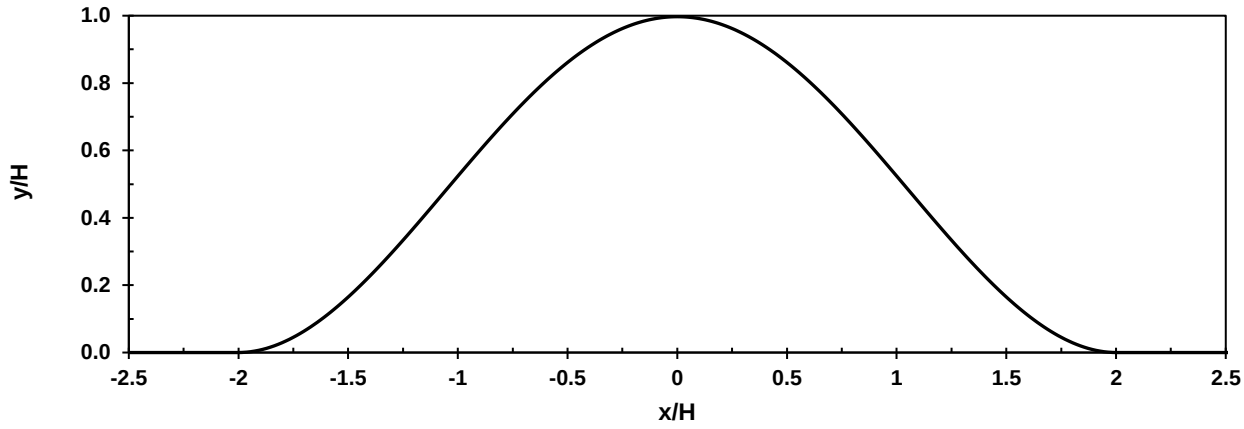

Figure 1. Side-view of the hill

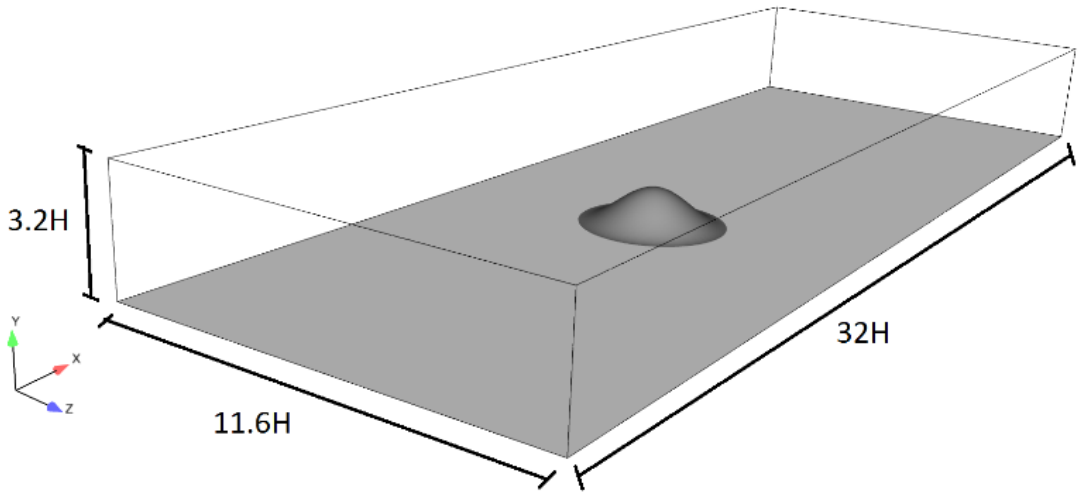

Figure 2. Isometric view of the domain

Table 1. Comparison of computational domain sizes used in past numerical studies

STUDY	DIMENSION (x, y, z)	GRID SIZE (approximate)
Present Study and [42]	32H x 3.2H x 11.6H	$1x10^6$ (Coarse Grid), $2.5x10^6$ (Medium grid), and 4.5 $x10^6$ (Fine grid)
Chitta et al. [5]	32H x 3.2H x 11.6H	6.85 $x10^6$
Davidson et al. [10]	19.8H x 3.2H x 11.7H	1.72 $x10^6$
Garcia et al. [11]	20H x 3.2H x 11.7H 13H x 3.2H x 11.7H	134.5 $x10^6$ (GVR group) $36.7x10^6$ (LL group)
Persson et al. [8]	12H x 3.2H x 10H 48.6H x 3.2H x 10H	$1x10^6$, 2.09 $x10^6$, and 4.03 $x10^6$
Patel et al. [9]	9.5H x 3.2H x 10H	5.08 $x10^6$

Three multi-block structured grids were generated containing 1 million (coarse grid), 2.5 million (medium grid) and, 4.5 million cells (fine grid) in Ansys. The boundary layer was resolved such that the non-dimensional wall distance or y^+ of the first cell height was less than unity throughout the domain based on the flow conditions. The cell spacing away from the hill was gradually increased to reduce computational expense as shown figures 2 and 3. The cell distribution of each grid is provided in Table 1. The fine grid was used for all numerical simulations after results from a grid independence study were considered.

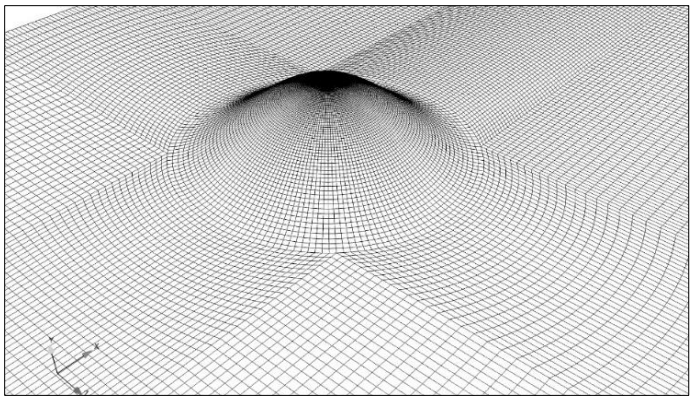

Figure 3. Close up view of the refined mesh around the hill

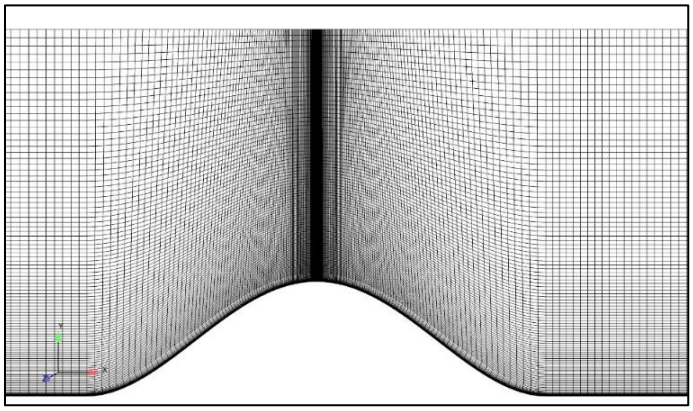

Figure 4. Cell density of the refined grid around the hill

4.5 RESULTS AND DISCUSSION

Results obtained from all the models are discussed and validated against experimental data and other numerical data in the following section.

4.5.1 Distribution of Pressure Coefficient on the Centerline z/H = 0

Figures 5 and 6 compare the C_p distribution on the surface on the hill between experiments and numerical simulations respectively. C_p is the dimensionless ratio of relative pressures given by Eq. (52):

$$C_p = \frac{P - P_\infty}{\frac{1}{2}\rho {U_\infty}^2} \tag{52}$$

where P is the static pressure at a given location, P_∞ static freestream pressure, ρ is the density, and U_∞ is the freestream velocity.

Both, the experimental results and numerical simulations, have been displayed using the same scale. As the flow approaches the hill, incoming boundary layer causes a small recirculation zone at the foot of the hill at x/H = -2 because of the stagnation zone at the foot of the hill. The presence of this recirculation region is not mentioned in the experimental results but was identified by Persson et al. [8] and by Chitta et al. [5]. After reattachment, the flow is accelerated towards the top of the hill where the lowest pressure is recovered. All the models predict the mean flow characteristics closely up to the top of the hill. The major differences in predictions are in the size and shape of the low-pressure region on the leeward side which causes a variation in the size and location of the separation bubble. The SST k-ω, SA-DDES, and SST Multiscale models predict lower pressure gradients and predict a late pressure recovery, while the SA-DES and the DHRL model predicts a sharp C_p recovery and a smaller separation bubble.

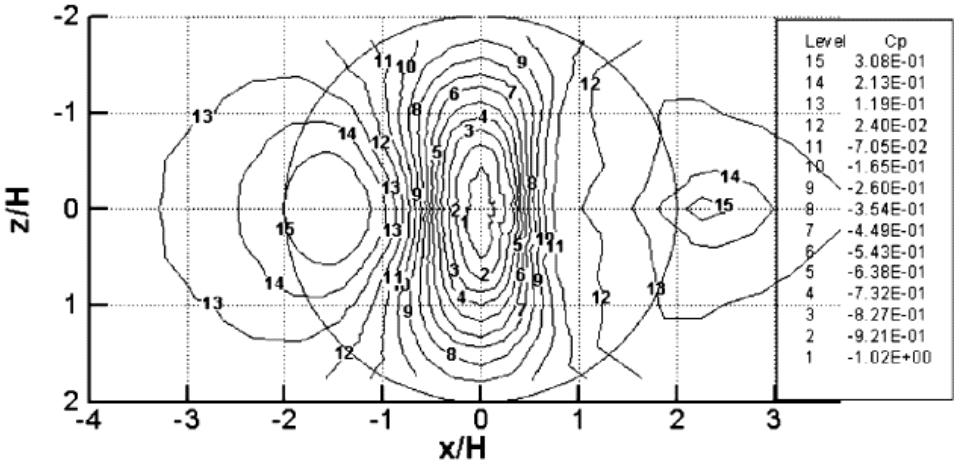

Figure 5. Contours of Cp by Simpson et al. [2]

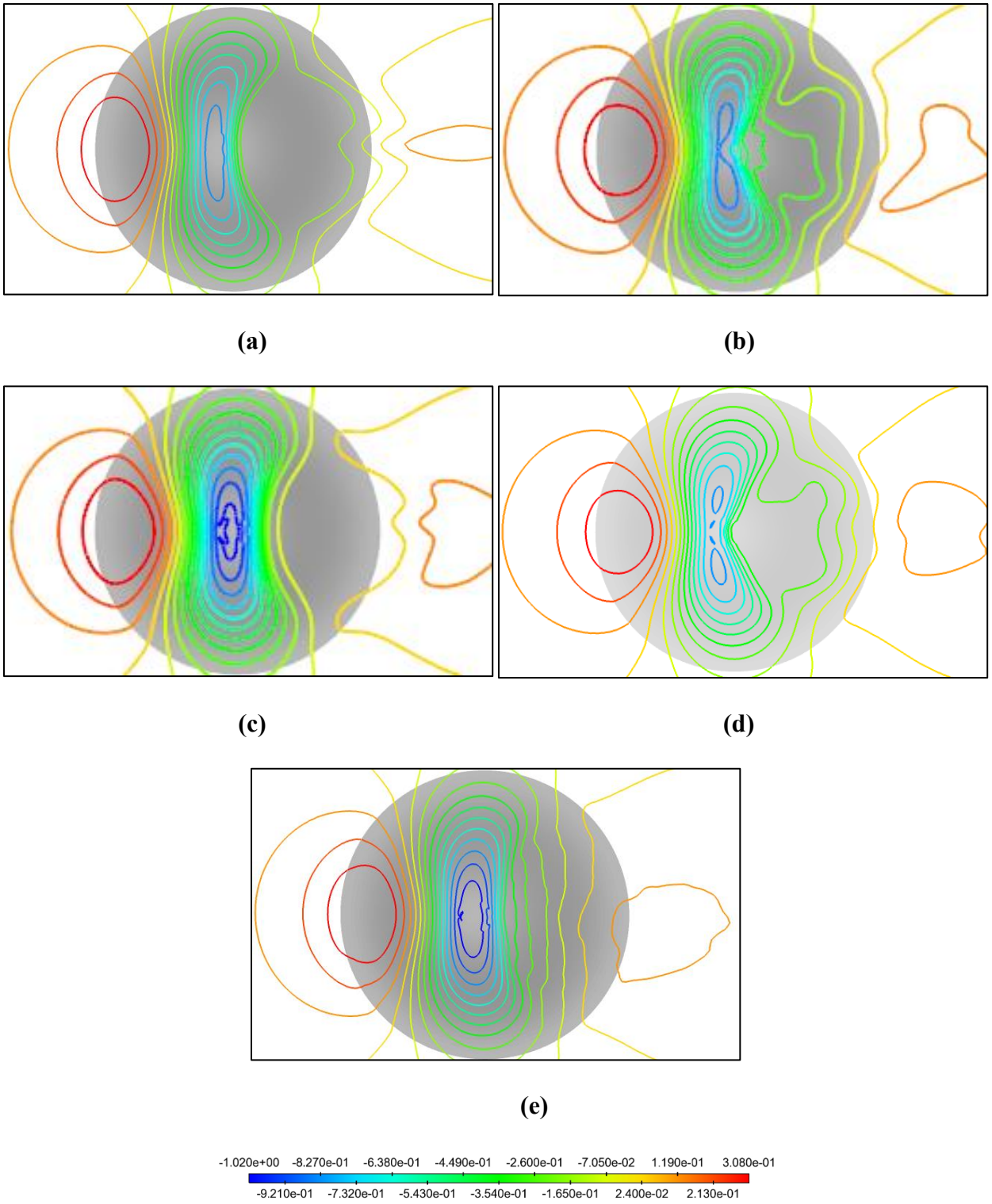

Figure 6. Contours of Cp for 4.5m grid using (a) SST Model, (b) SA DES Model, (c) SA DDES Model, (d) SST Multiscale Model, and (e) DHRL Model.

Figure 7 shows the variation of pressure coefficient on the centerline z/H = 0 for all the models considered in this study. As the flow approaches the foot of the hill on the windward side, a stagnation region is observed at -2 < z/H < -1.5 which is represented by an increase in C_p . As the flow moves further up the hill, because of streamline curvature, C_p starts to decrease sharply. Lowest mean pressure is recorded at x/H=0 at the top of the hill followed by flow separation indicated by the inflex in the C_p plot around x/H~0.8. Reattachment takes place between x/H=1.85 and 2.25 when mean-pressure eventually recovers. All the models accurately predict the C_p values on the windward side (x/H < 0), and leeward side (x/H ≥ 3). In both these regions a RANS solution is predicted by all the HRLs. The SST *k-ω* and the SA-DDES models over-predict mean-pressures on the windward side at the stagnation region (x/H=-1.5). For x/H > -1, all the models behave similarly as the flow is accelerated towards the top of the hill. Only the SA-DDES and the DHRL models predict correct inflexion point at x/H = 0 and x/H= 1 which enables them to recover accurate mean-pressures and predict smaller recirculation bubble. The SST *k-ω*, SA-DES, and SST Multiscale models predict inflexion before x/H=1 and separate early. Also, the models do not recover pressure fast enough leading to exaggerated recirculation zones. Overall, the DHRL model predictions are superior to the other models. The model accurately predicts peak pressure zones with slight deviations in the inflexion regions along. The DHRL model also predicts the smallest recirculation zone with a reattachment location that is close to experimental observations.

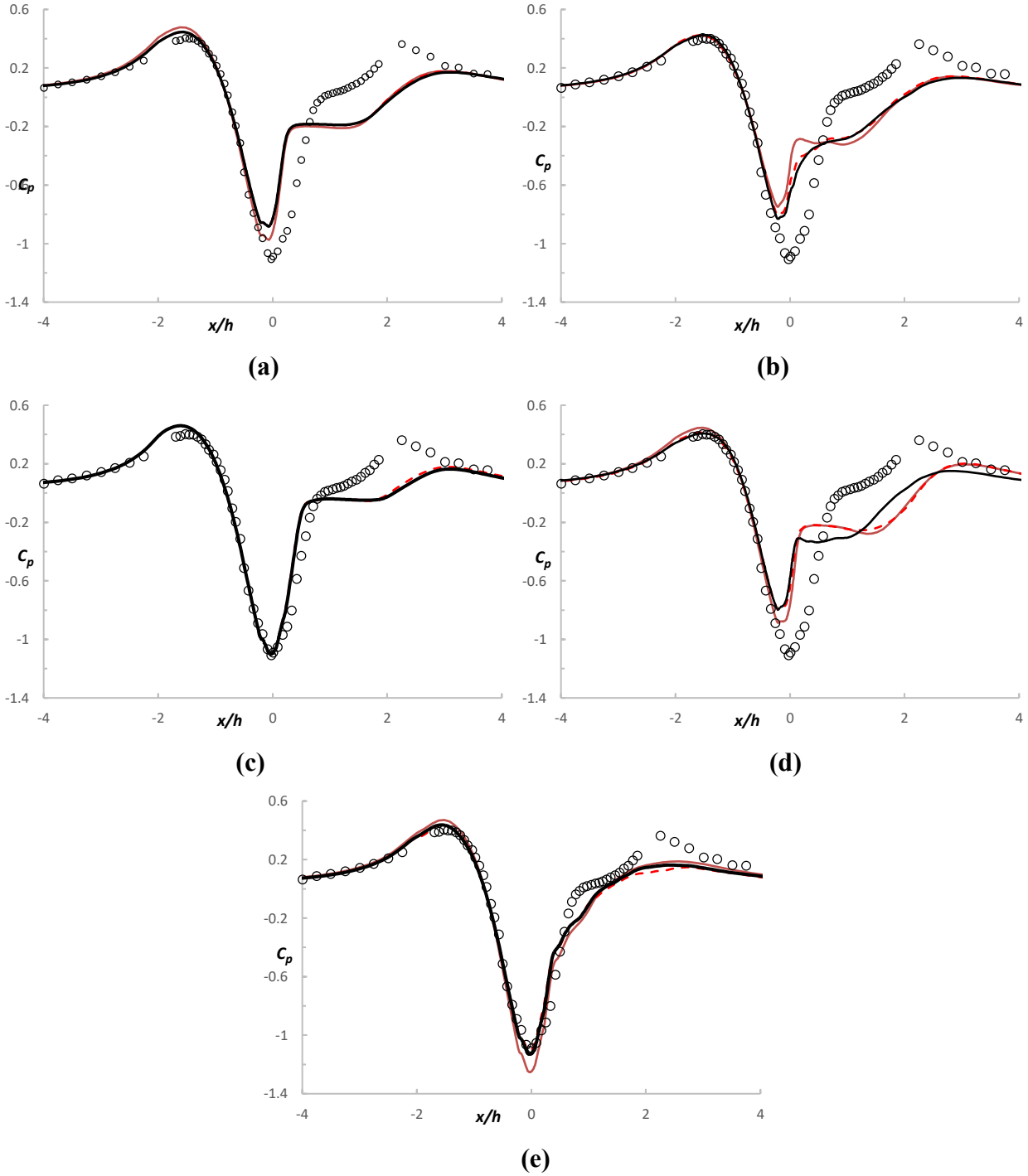

Figure 7. C_P profiles along the centerline z/H = 0. (a) SST, (b) SA-DES, (c) SA-DDES, (d) SST Multiscale, and (e) DHRL Model. ∘ Simpson et al. [2]; —coarse grid, – – medium grid, and ····· fine grid.

4.5.2 Recirculation Zone Behind the Hill

Figure 8 (a) thru (h) compares the separation and reattachment location of the flow for experimental observations and for each of the models considered in this study. For flows past bluff bodies, the size and shape of the obstruction plays a very important role in the location of boundary layer separation and reattachment. The SST k-ω RANS model predicts separation past the apex of the hill with a large recirculation region. Because of the lowered stress prediction, the reattachment location is delayed resulting in a large separation bubble. For the traditional HRL models, the RANS-LES transition takes place inside the boundary layer on the windward side of the hill. As the models switch to an LES form, eddy viscosity is lowered and the near wall momentum in the boundary layer is reduced. In the boundary layer around the apex of the hill, the models operate in LES. Since this region is dominated by small scale vortex shedding, the grid is too coarse to resolve enough fluctuations that would balance the lack of modeled stress. This phenomenon manifests itself as modeled-stress depletion (MSD) and is readily observable for the SA-DES and SST-Multiscale model. Both these models separate early followed by large recirculation zone and delayed reattachment. In the recirculation zone, the flow is characterized by large scale vortex shedding and unsteady boundary layer separations. In this region, the SA-DES and SST Multiscale models initially switch to LES before reverting back to a RANS form. Since RANS models are shown to underpredict shear stress in separated flows, the prediction of the separation bubble is grossly overestimated. The SST k-ω model separates later and predict massive separation bubbles. The separation location of the SA-DDES model is also delayed as the DDES was formulated to address this very issue of early transition caused by modeled stress depletion. The model effectively delays separation but ultimately over-predicts the recirculation bubble size caused by predicted stress. Overall, the DHRL model prediction of the recirculation zone is closest to

experimental observations [2], with reattachment taking place just beyond the foot of the hill at x/H ~2.25. The DHRL model predicts RANS behavior till the apex of the hill followed by a transition to LES mode in the separated region. Since the DHRL model does not include any grid scale parameters in the RANS-LES blending, the model appears to be relatively insensitive to changes in aspect ratio between the boundary layer and the freestream regions. Figure 9 (h) highlights the ability of the DHRL model to resolve the separation region accurate for the coarse grid (1 million cell) using the DHRL model. The location of flow separation and the recirculation height recovered is comparable to the fine grid.

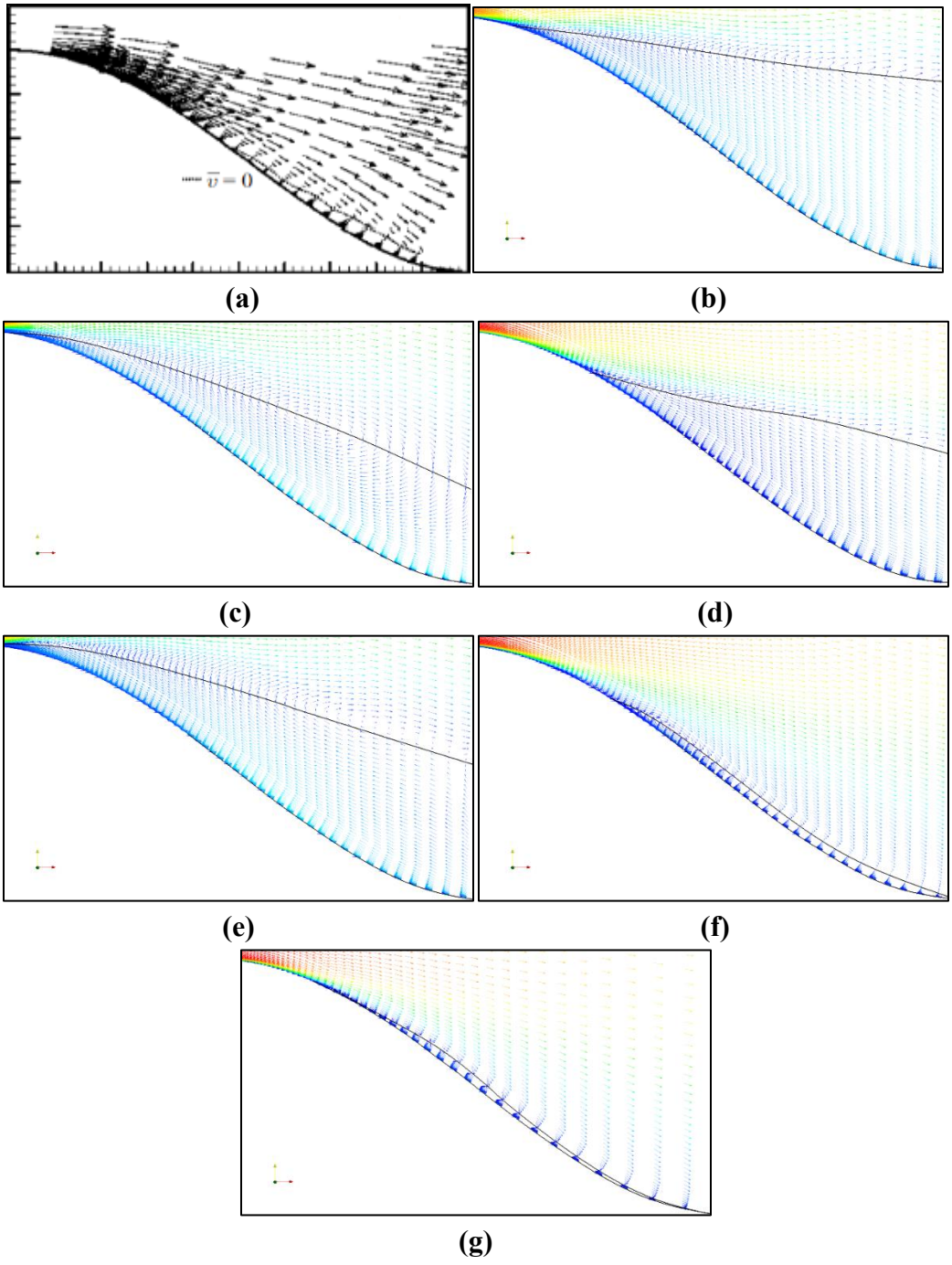

Figure 8. Separation-bubble size comparison (a) Byun et al. [9], (b) SST, (c) SA DES, (d) SA DDES, (e) SST Multiscale, (f) DHRL, and (g) DHRL Model for coarse grid (1 million cell grid).

4.5.3 Streamwise Velocity Distribution at x= 3.69H

Normalized streamwise velocity distribution profiles are shown in Figure 9. All the models considered in this study show velocity defects closer to the center of the hill, i.e. at z=0, especially in the boundary layer. This streamwise location is past the reattchement location for the experimental case where the turbulent boundary has re-formed. Major discrepancies in this region is caused by the over exaggerated separation bubble size predicted by some of the models. The SST *k-ω* model first underpredicts the value of $\bar{u}/U_{in}$ for z/H < -0.33, then overpredicts the value of $\bar{u}$ for z/H ≥ -0.33. The SA-DES model predictions are an improvement over the SST *k-ω* model. The model qualitatively captured the velocity field with considerable accuracy for z/H ≥ -0.81. Major disagreements with experimental data occur directly behind the hill for 0 ≤ z/H ≤ -0.16 where velocity is under-predicted. For z/H ≤ -1.79, the model over-estimates the near-wall velocity which leads to large separation region. The SA-DDES does not improve results when compared to the SA-DES model. In fact, the SA-DDES model considerably over-estimates the near-wall. The model, however, does provide improved predictions when compared to the SST *k-ω* model for z/H < -0.33. The SST Multiscale model predictions are on par with the SA-DES model. The model predicts velocity defect for z/H ≤ 0.33 and predictions are closer to experimental results. Finally, The DHRL model produces the least velocity defect especially in the near-wall regions however, some defects are present in the outer layer where the flow is separated z/H ≤ -0.33. Predictions improve considerably at stations farther away from the hill, z/H ≥ -0.81. Some of the inaccuracy near wall can be attributed to delayed transition from RANS to LES and vice versa.

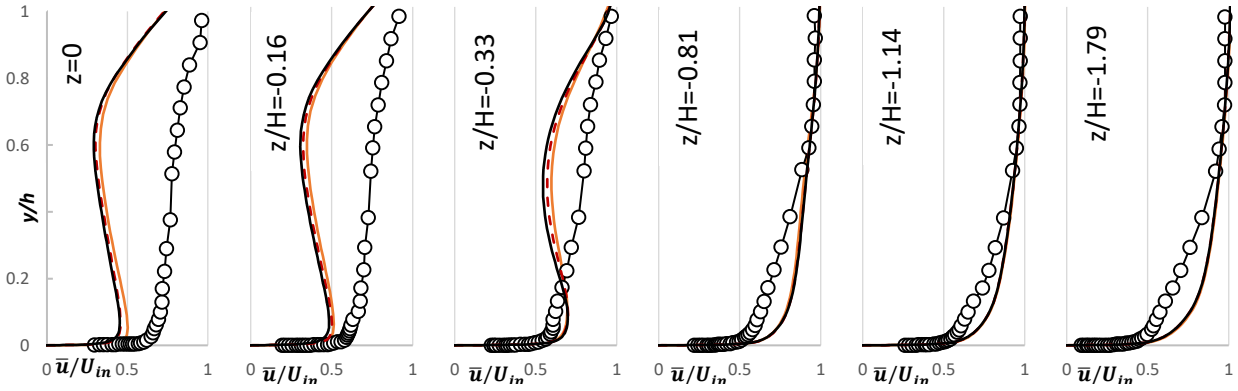
z=0
z/H=-0.16
z/H=-0.33
z/H=-0.81
z/H=-1.14
z/H=-1.79
y/h
$\overline{u}/U_{in}$

(a)

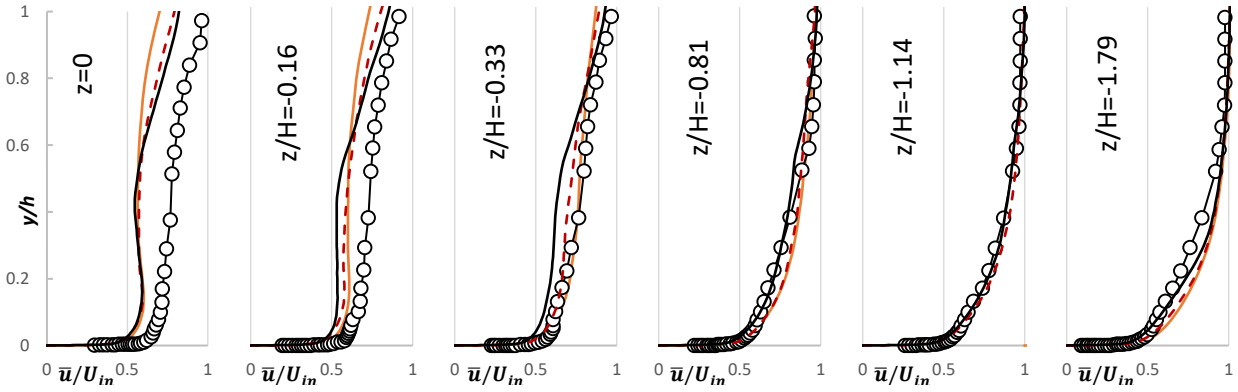
z=0
z/H=-0.16
z/H=-0.33
z/H=-0.81
z/H=-1.14
z/H=-1.79
y/h
$\overline{u}/U_{in}$

(b)

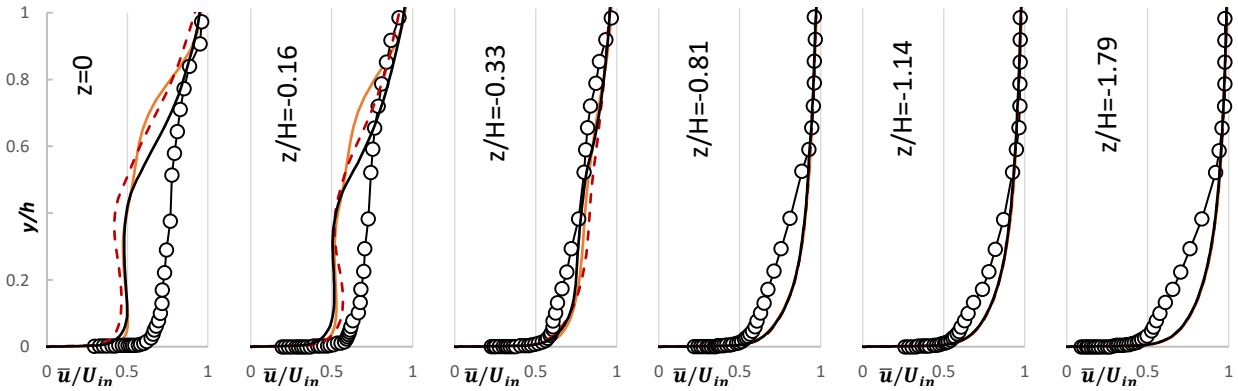
z=0
z/H=-0.16
z/H=-0.33
z/H=-0.81
z/H=-1.14
z/H=-1.79
y/h
$\overline{u}/U_{in}$

(c)

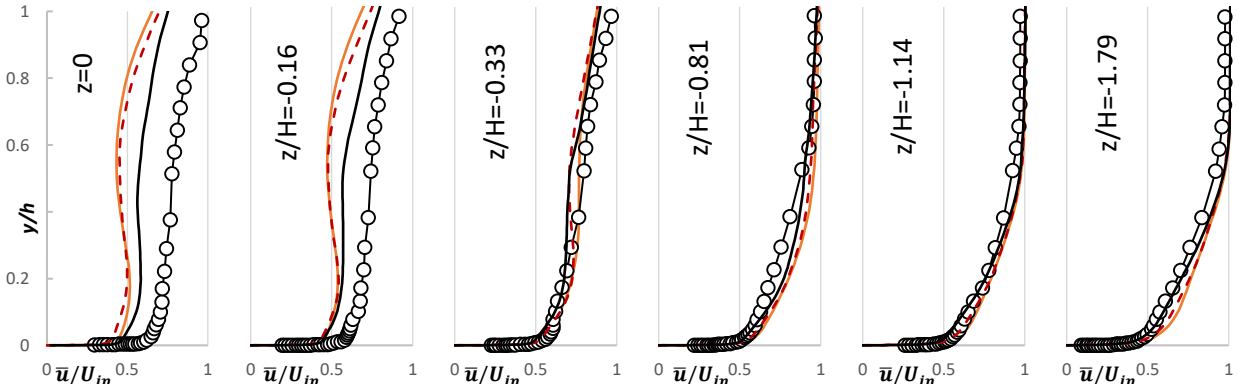

(d)

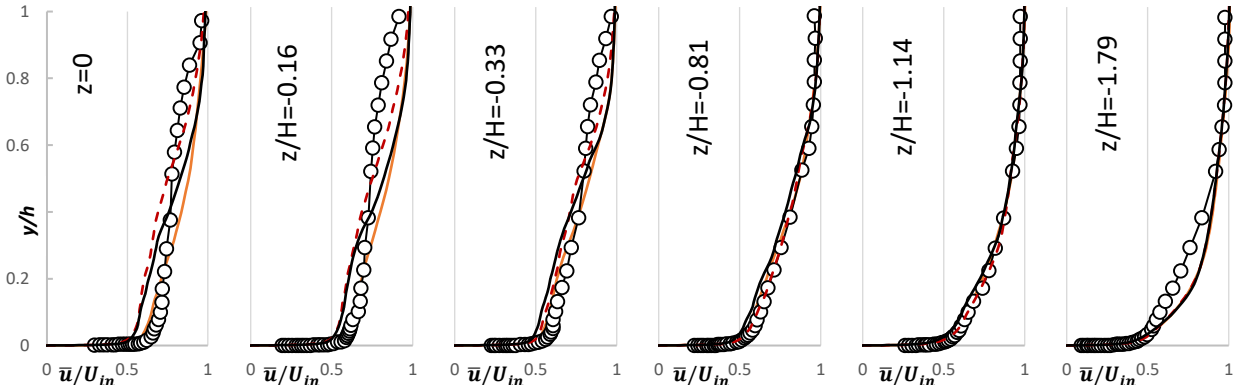

(e)

Figure 9. $<\bar{u}>/U_{in}$ at x= 3.69H for (a) SST, (b) SA-DES, (c) SA-DDES, (d) SST Multiscale, and (e) DHRL Model. —o— Simpson et al. [2]; —— coarse grid, - - - medium grid, and ····· fine grid.

4.5.4 Spanwise Velocity Distribution at x= 3.69H

Figure 10 shows the distribution of normalized spanwise velocity behind the hill. As mentioned in the last section, some of the discrepancies in velocity is due to the exaggerated separation bubble predicted by some of the models. The SST *k-ω* model predicts the wrong direction of flow in the boundary layer for $0.16 \leq z/H \leq 0.81$. For $z/H > 0.81$. Similar to the stream-wise component, the SA-DES model improves the velocity prediction significantly from the SST *k-ω* model. The model captures the flow behavior qualitatively but fails to predict the magnitude with accuracy. Predictions are improved for $z/H > 1.14$ where the effects of turbulent fluctuations are dampened. The SA-DDES model predicts large velocity defects in the near wall region with flow going in the opposite direction for $z/H \leq 0.33$. The outer region of the flow is predicted with considerable accuracy and very little disagreement with experimental observation is noticed. The SST Multiscale model behaves like the SST *k-ω* and adopts a similar behavior in the boundary layer. The model overestimates the separation bubble size shows significant velocity defects in the near-wall regions. Finally, The DHRL model predicts the correct direction of the flow in the boundary layer and predictions are closest to experimental results.

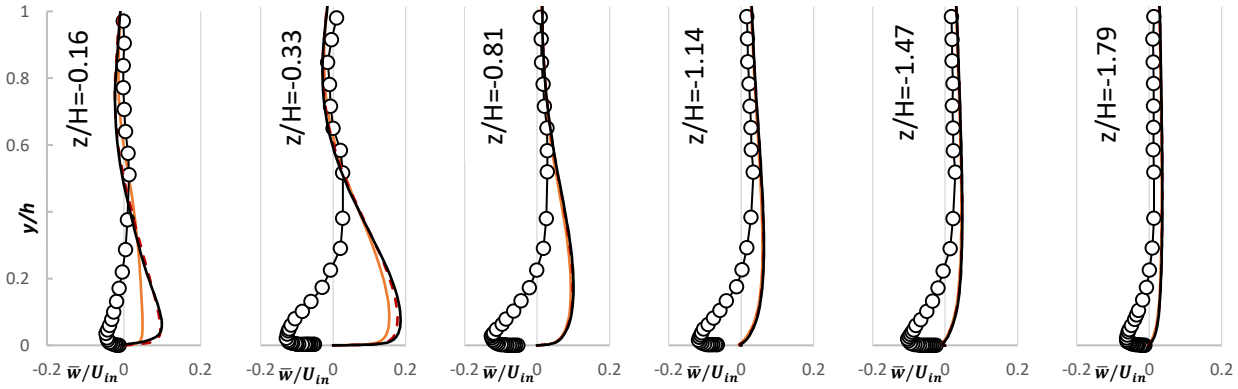
z/H=-0.16
z/H=-0.33
z/H=-0.81
z/H=-1.14
z/H=-1.47
z/H=-1.79
y/h
$\bar{w}/U_{in}$

(a)

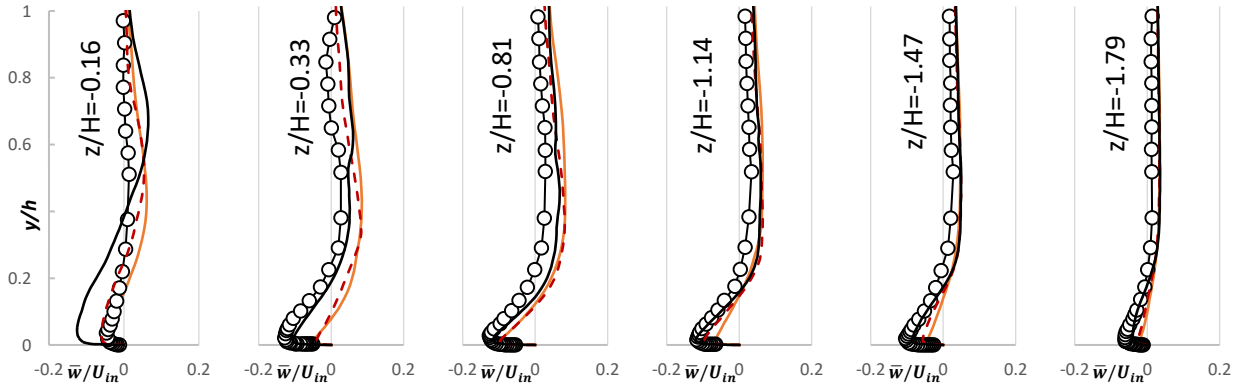
z/H=-0.16
z/H=-0.33
z/H=-0.81
z/H=-1.14
z/H=-1.47
z/H=-1.79
y/h
$\bar{w}/U_{in}$

(b)

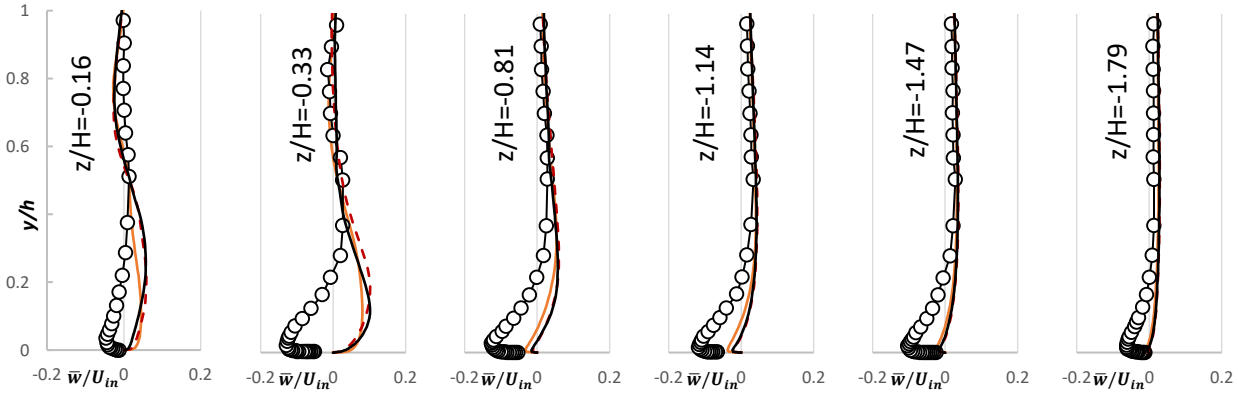
z/H=-0.16
z/H=-0.33
z/H=-0.81
z/H=-1.14
z/H=-1.47
z/H=-1.79
y/h
$\bar{w}/U_{in}$

(c)

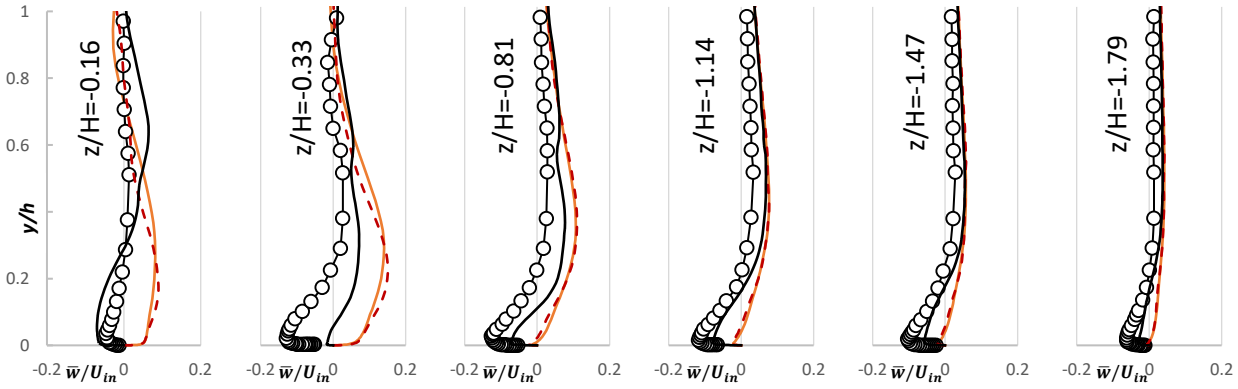

(d)

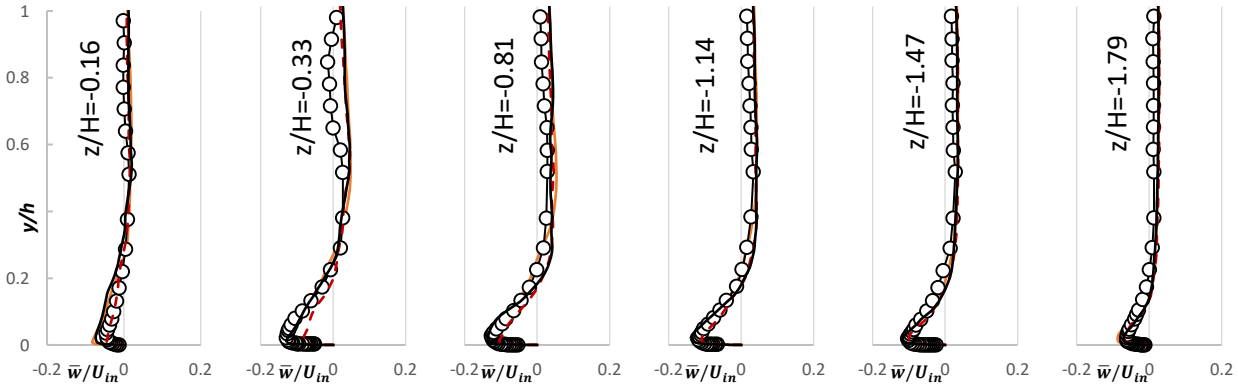

(e)

Figure 11. $< \bar{w} > / U_{in}$ at x= 3.69H for (a) SST, (b) SA-DES, (c) SA-DDES, (d) SST Multiscale, and (e) DHRL Model. —o— Simpson et al. [2]; —— coarse grid, - - - medium grid, and ····· fine grid.

4.5.5 Profiles of Friction Velocity at x=3.63H

Figure 11 compares the spanwise variation of normalized friction velocity (u_τ/U_o) at x/H=3.63 along several stations in the z-direction. According to experimental data, at z/H=0, peak value of friction velocity is observed due to the strong downwash of the vortices and eventually smooths out towards the outer edge of the hill. From numerical simulations, none of the models accurately resolves peak friction velocity. The SST Multiscale model recovers the peak values but overpredicts friction velocity along the z-direction. The DHRL model provides most agreement with experimental data for z/H ≤ -0.5 and z/H ≥ 0.3 but fail to predict peak friction velocity values at z/H=0. From figure 10 (e), it is clear that the DHRL model underpredicts velocity in the near-wall region for z/H=0. This ultimately leads to inaccurate mean-stress prediction hence the absence of the peak friction velocity. According to the study conducted by Persson et al. [8], RANS models predict reduced mean-stress at z/H=0 where experimental stress attains peak value. Since the DHRL model primarily operates in the RANS framework at the wall, an alternative would be to use an improved RANS model within the DHRL framework. Chitta et al. [5] demonstrated that using a four-equation transition and rotation-curvatures sensitized model which improves the near-wall mean-flow predictive capability.

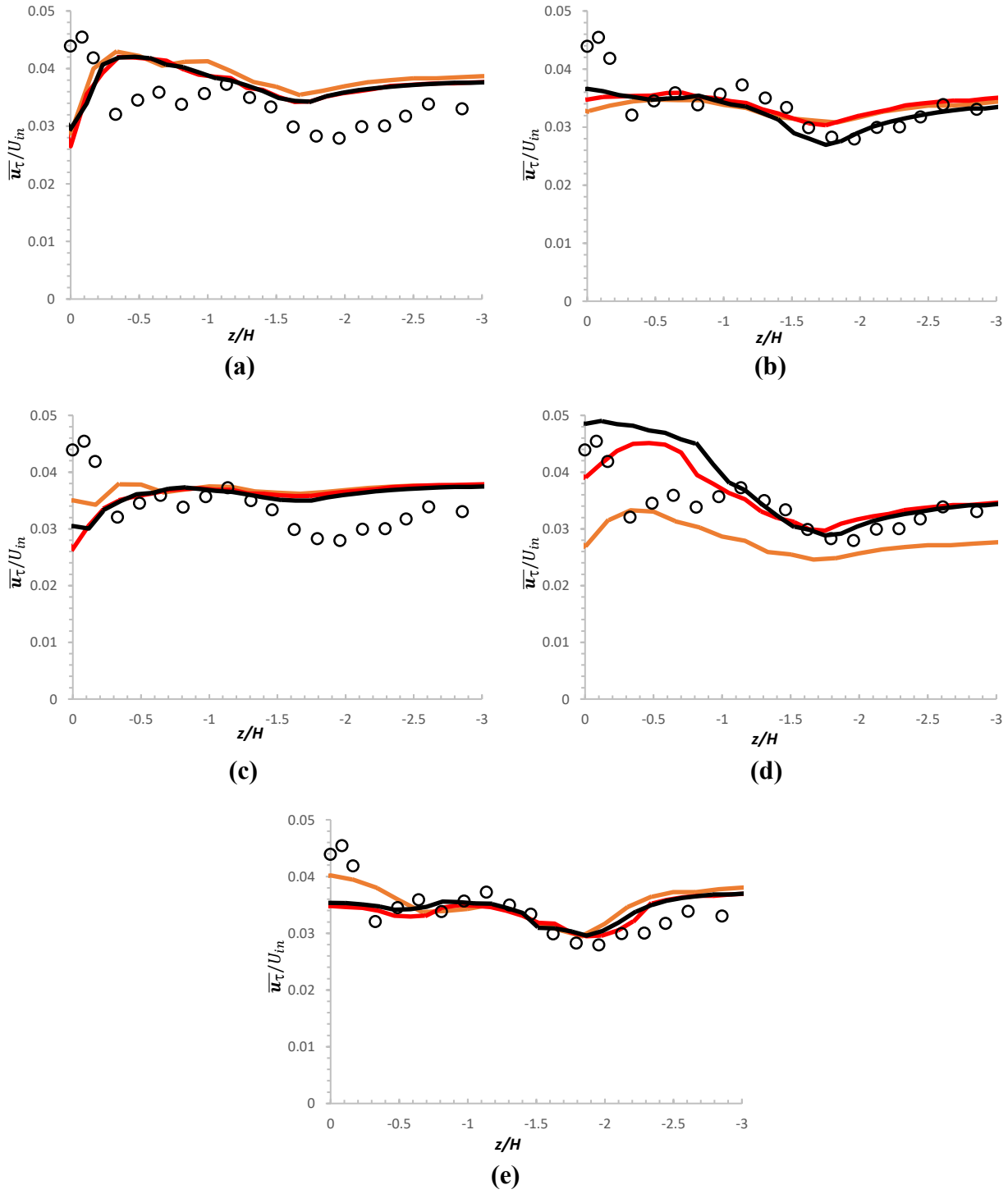

Figure 11. Profiles of friction velocity. (a) SST, (b) SA-DES, (c) SA-DDES, (d) SST Multiscale, and (e) DHRL Model. Φ Simpson et al. [2] with ±3% experimental error; — coarse grid, – – medium grid, and ····· fine grid.

4.5.6 Streamwise and Spanwise Velocity Distribution at x= 3.63H

To highlight the relative performance and cost-effectiveness of the DHRL model, comparisons against benchmark numerical studies performed by Garcia et al. [11] and two of the best performing HRL models (SA-DES and SST Multiscale) from the previous sections are made in the following sections. Figures 13 and 14 show the distribution of streamwise and spanwise velocity profiles for the SA-DES, SST Multiscale, and DHRL model at x=3.63H evaluated against the experimental data [15] and provided by Garcia et al. [11]. The SA-DES model and the SST-Multiscale models show poor agreement with experimental and benchmark data for $x/H < 1.10$ and $z/H < 1.10$. However, predictions are substantially improved for $x/H \geq 1.10$ and $z/H \geq 1.10$. Compared to SA-DES and SST Multiscale models, the DHRL model predictions are considerably more accurate. For streamwise velocity, some discrepancies arise in the location directly behind the hill (z/H=0), while predictions for the spanwise velocity are in close agreement with experimental data and numerical simulations.

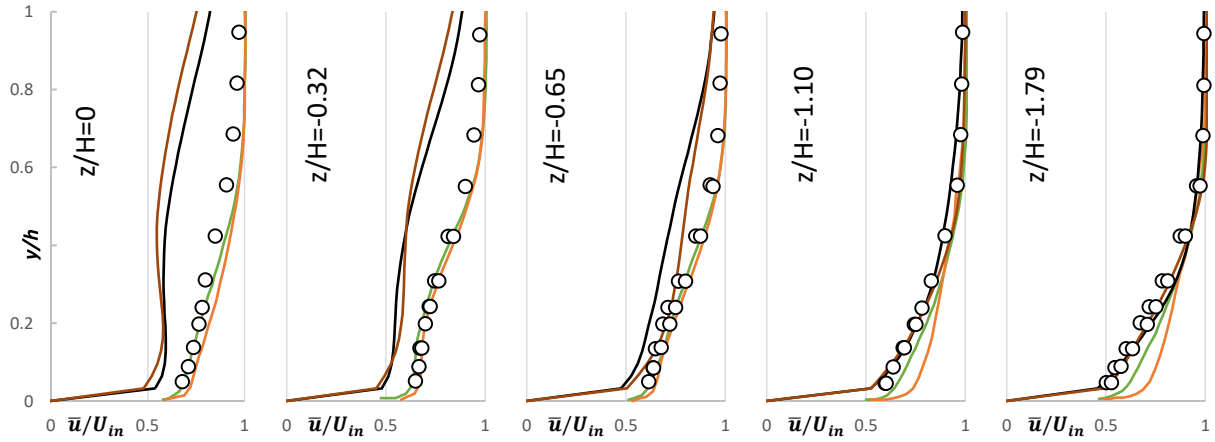

(a)

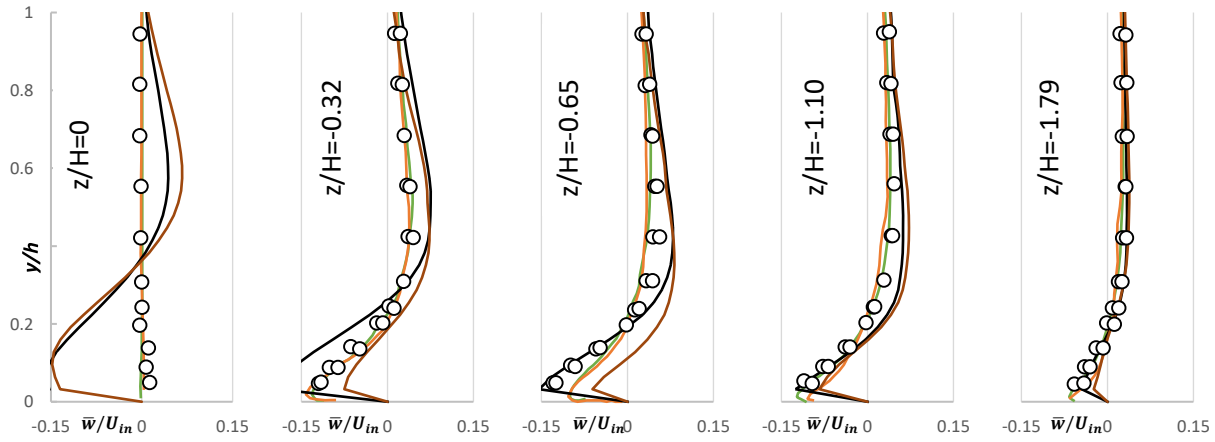

(b)

Figure 12. Plots of (a) $< \bar{u} > /U_{in}$ and (b) $< \bar{w} > /U_{in}$ at x= 3.63H. Ma et al. [15], LL and GVR [11], SST Multiscale , and SA-DES model

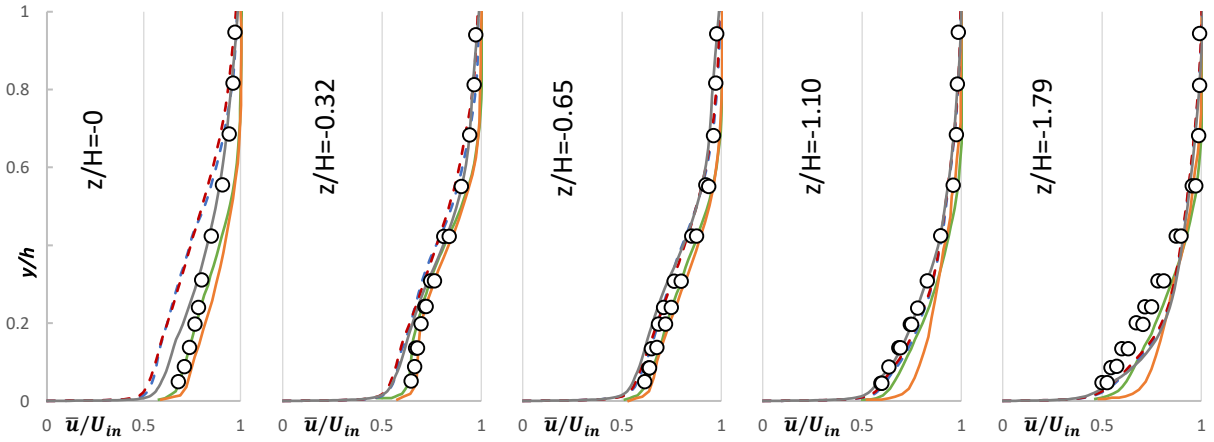

(a)

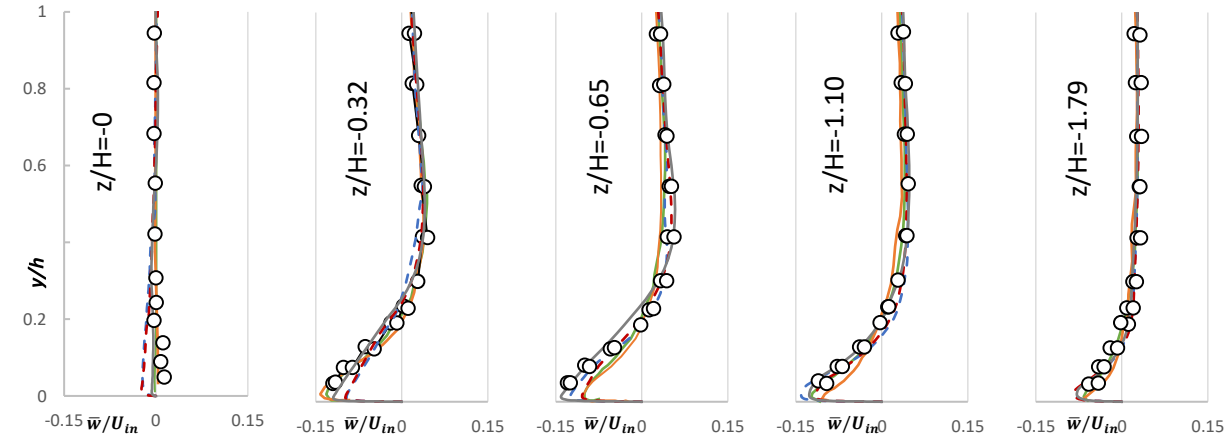

(b)

Figure 13. Plots of (a) $< \bar{u} > /U_{in}$ and (b) $< \bar{w} > /U_{in}$ at x= 3.63H. Ma et al. [15], LL and GVR [11], DHRL coarse grid, DHRL medium grid, and DHRL fine grid

4.5.7 Resolved Turbulent Kinetic Energy and Resolved Reynolds Stress distribution at x= 3.63H

Figures 14 and 15 compare resolved Turbulent Kinetic Energy (TKE) and Reynolds Stress plots for some of the HRL models considered in this study (SA-DES and SST Multiscale) and the DHRL model against experimental and benchmark numerical data. The SA-DES and SST Multiscale models overestimate resolved TKE considerably for $z/H \leq -0.65$ due to the presence of large separation bubble. Predictions are somewhat improved for z/H= -1.10 before both models recover little resolved fluctuation for z/H = -1.79. The SA-DES and Similar behavior is observed the Reynolds stress profiles. Most of the unsteady interactions are in the separated region and eventually decay when unsteady content is no longer adequately resolved. The DHRL model results are a significant improvement over its HRL counterparts. The DHRL model effectively recovers the resolved TKE qualitatively with slightly higher magnitudes for $z/H \leq -0.65$. However, resolved TKE predictions are less accurate resolved away from the centerline, i.e. for z/H=0, in the spanwise direction. This overprediction is caused due to lack of dissipative scales in the flow in these regions of high aspect ratio cells. The predicted Reynolds stress profiles are also in good agreement with experimental and numerical data.

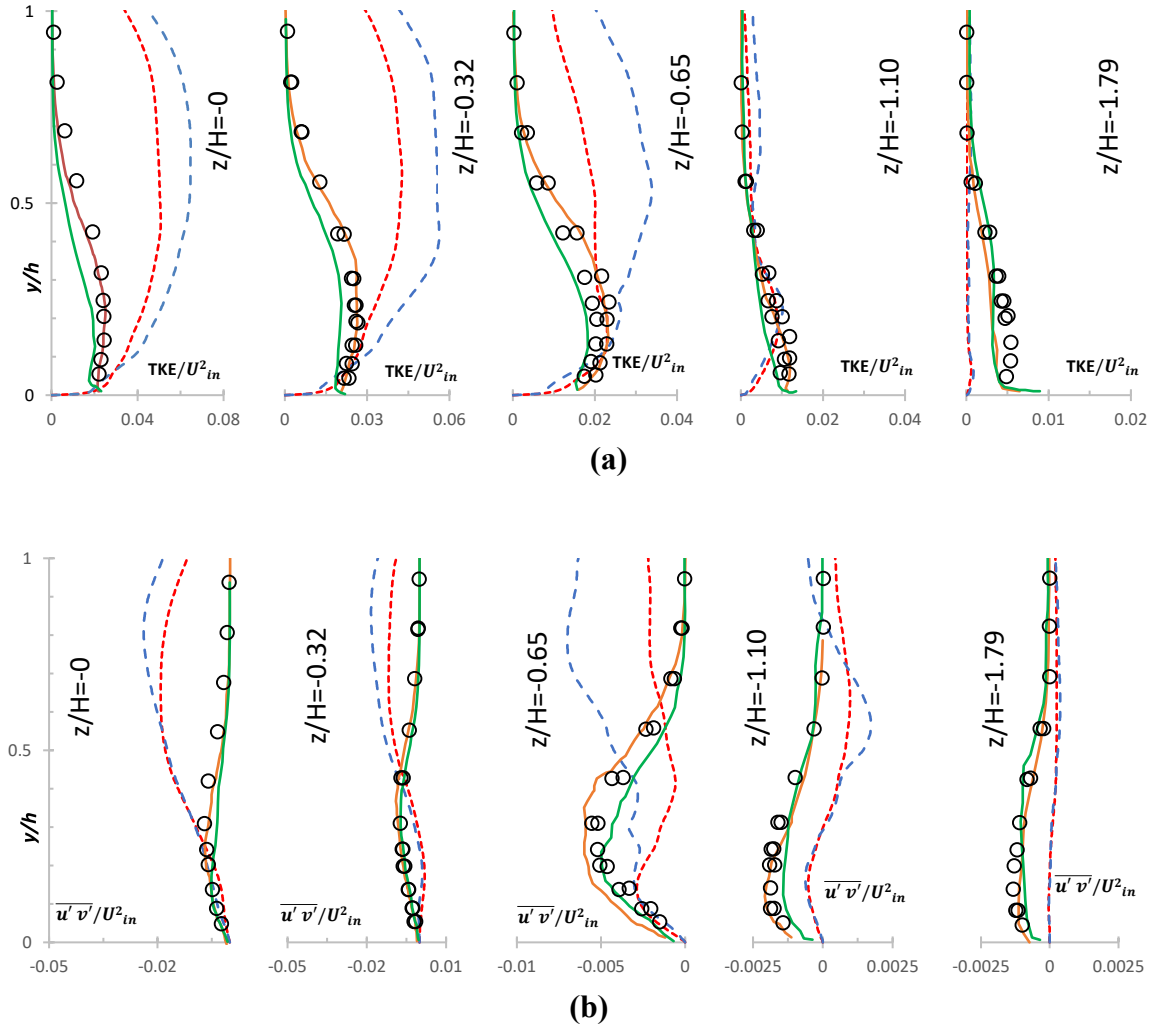

Figure 14. Plots of (a) Resolved TKE/$U_{in}{}^2$, (b) Resolved Reynolds Stress ($\overline{u'v'}$)/$U_{in}{}^2$ at x= 3.69H. ○ Ma et al. [15], — LL and — GVR [11], - - SA-DES, and - - SST-Multiscale model

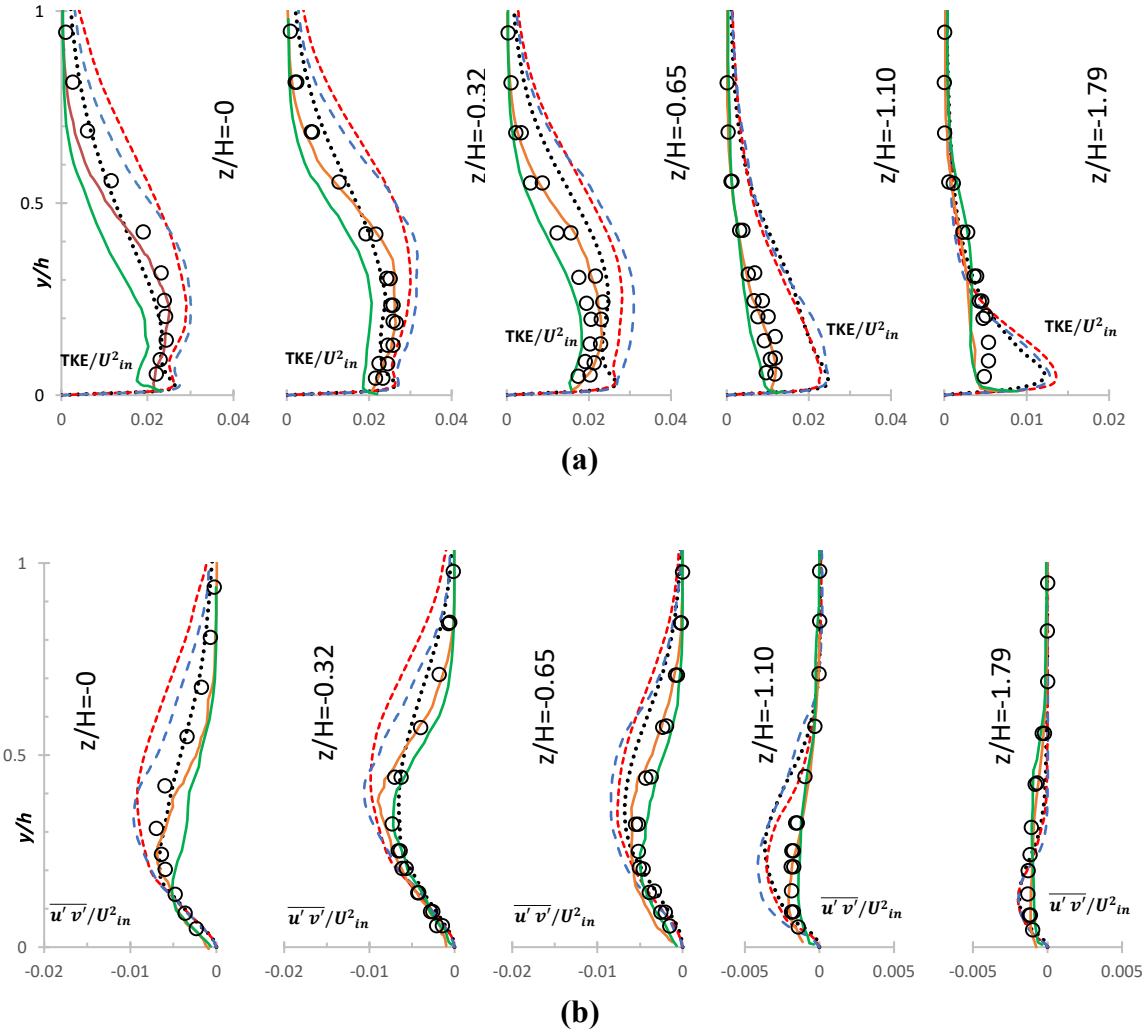

Figure 15. Plots of (a) Resolved TKE/$U_{in}{}^2$, (b) Resolved Reynolds Stress ($\overline{u'v'}$)/$U_{in}{}^2$ at x= 3.69H. ○ Ma et al. [15], — LL and — GVR [11], ····· DHRL coarse grid, - - DHRL medium gird, and - - DHRL fine grid

4.5.8 Contours of Turbulent Kinetic Energy

Figure 16 compares contours of resolved TKE for the SA-DES, SST Multiscale and DHRL model against experimental data and numerical simulations carried out by Garcia et al. [11]. As the flow passes the crest of the hill, flow instabilities are initiated due to the adverse pressure gradient on the leeside of the hill. Eventually, the flow separates and thus a region of enhanced turbulent production is formed in the separated shear layer. Fig. 16 (a) shows the distribution of TKE and flow transport velocity vectors of TKE due to turbulent diffusion. The variation in the magnitudes of the turbulent diffusion vectors signify unsteadiness in the flow. Large amounts of TKE generated near the wall around x/H~0.3 and it is interesting to note that this location is quite upstream from the actual separation location which occurs around x/H~0.7. Similar behavior is exhibited by the LL group in the study performed by Garcia et al. [11]. The authors attribute this behavior to large production of TKE associated with thin shear layer. Overall the DHRL model performance is superior to the other HRL models and somewhat comparable to the GVR simulations.

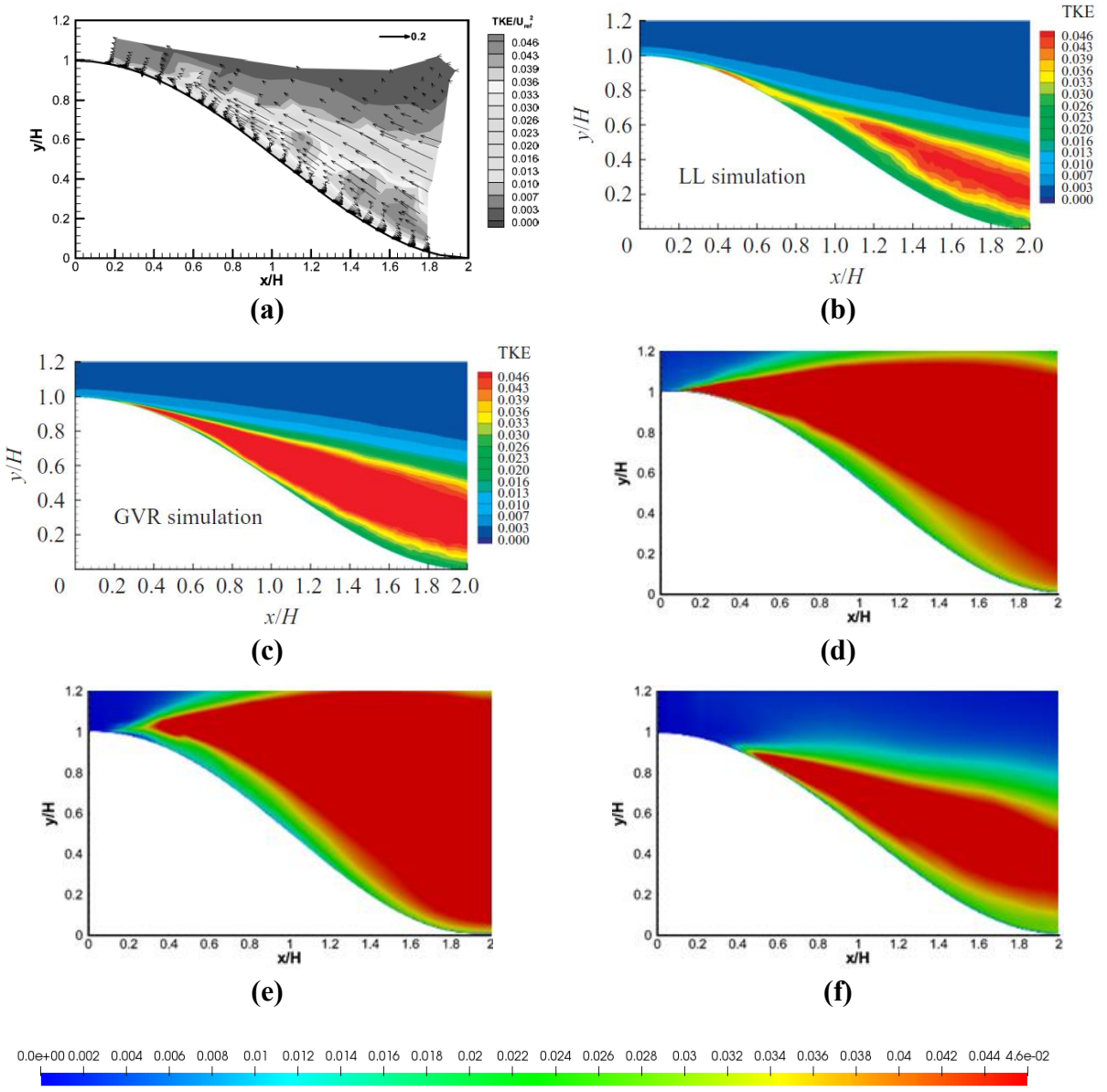

Figure 16. $TKE/U_{in}{}^{2}$ at x= 3.69H for (a) Byun et al. [14], (b) GVR and (c) LL [11], (d) SA-DES, (e) SST Multiscale, and (f) DHRL Model

4.5.9 STRUCTURE OF FLOW BEHIND THE HILL

The flow past the hill is complex due to the presence of strong spanwise and streamwise currents. The wake region is characterized by the presence of complex structures such as recirculation bubbles and vortices. The vortices are formed as a low-pressure region is created behind the hill as flow is accelerated flow around the sides and over the hill. This recirculation zone consists of two vortices or one counter rotating vortex pair (CRVP) that produces large amounts of turbulence along z/H=0 with low frequency motions, effectively contributing to turbulent mixing. Similar to the experimental observations [2] and numerical data from the GVR [11], the DHRL model clearly resolves two CRVPs on the center and two CRVPs along the edges of the hill. The coarse grid results also show the presence of two CRVPs except for some of the finer structures that are lost due to added numerical dissipation caused by the coarseness of the grid.

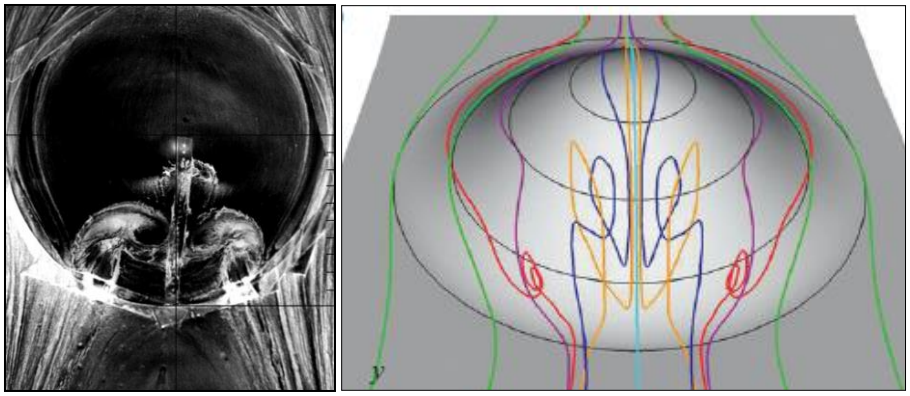

(a) **(b)**

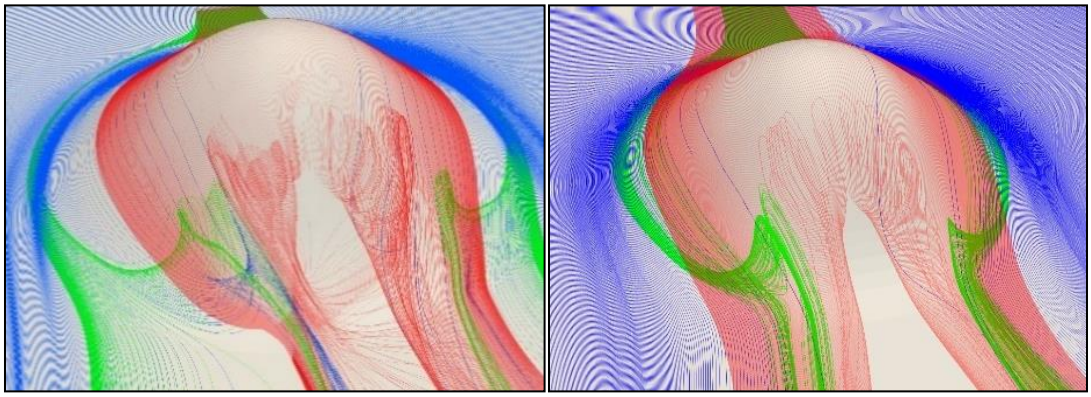

(c) **(d)**

Figure 17. Vortex structure. (a) Oil Flow Visualization [2], (b) Garcia [11], (c) DHRL, and (d) DHRL Model for coarse grid

4.6 CONCLUSIONS

This study investigated the predictive capabilities of a dynamic Hybrid-RANS LES (DHRL) model against a RANS SST k-ω model, SA-Detached-Eddy Simulation (DES), SA-Delayed Detached-Eddy Simulation (DDES) and, SST Multiscale model for the canonical case of flow over a 3D axisymmetric hill. The flowfield around the hill contains complex 3D structures such as unsteady separations, reattachment zones, counter rotating vortices, regions of spatially varying pressure gradients. For highly separated flows such as this, RANS methods have often produced unsatisfactory results, while LES simulations are often deemed too expensive for practical application. The DHRL formulation provides a suitable balance between accuracy and cost of computation. Results obtained from numerical simulations using SST k-ω model, SA-DES, SA-DDES, SST Multiscale model, and DHRL model were compared to experimental data provided by Simpson, Byun, and Ma et al. [2,13-15] and benchmark LES data obtained by Garcia et al. [11].

Coefficient of pressure distribution, separation bubble size, normalized streamwise and spanwise velocity, and normalized friction velocity profiles were first evaluated behind the hill at x/H = 3.69 against experimental observations made by Simpson and Byun et al. [2,13-14]. As expected, the SST k-ω model results were poor compared to experimental data. The model predicted early flow separation followed by a large recirculation zone on the leeward side of the hill. The failure of the SST k-ω model can be attributed to the fact that the RANS models remove most of the energy containing the large eddies present in the flowfield as an outcome of the Reynolds-Averaging process. The HRL (SA-DES, SA-DDES, and the SST Multiscale) models provided improved description of the flow field by suffer from grid sensitivity leading to modeled stress depletion (MSD). Among the traditional HRL models, SA-DES and the SST Multiscale

models predicted the velocity profiles with some accuracy away from z/H = 0, but failed to capture the correct spanwise velocity, pressure distribution, and friction velocity. The DHRL model predictions were closer to experimental data. The model profiles were captured with considerable accuracy and, the pressure distribution was in close agreement with experimental results. The DHRL model also predicted a smaller recirculation zone with delayed separation.

Since the SA-DES and SST Multiscale model predicted velocity and friction velocity profiles with the most accuracy among the traditional HRL models, data obtained from both models and the DHRL model was compared at x/H=3.63 are against benchmark LES data provided by Garcia et al.[11] and experiments carried out by Byun and Ma et al. [14,15]. Although both HRL models performed relatively well and captured velocity profiles away from z/H=0 with considerable accuracy, there were major disagreements with experimental and benchmark data for resolved Turbulent Kinetic Energy (TKE) and Reynolds Stress. Because of the exaggerated separation region, large amount of TKE was predicted above the wall near the centerline z/H = 0. The DHRL model predicted velocity profiles and turbulent statistics with greater accuracy. The streamwise and spanwise velocity predictions were close to experimental data and in some cases superior to benchmark numerical data for z/H ³ -0.65. The model predicted resolved TKE and Reynolds with relatively well however, major disagreements for resolved TKE occurred for z/H ³ -0.65. Because cells in this region are stretched rapidly to reduce computational cost, fluctuations smaller than grid scale are removed from the spectrum. This effectively reduces TKE dissipation leading to large overpredictions relatively close to the wall. Overall, the DHRL model outperformed the traditional HRL models and highlighted some of the advantages of the DHRL modeling framework. It must be mentioned that DES and DDES results can be improved significantly by following strict grid generation guidelines as suggested by Spalart et al. [43].

In conclusion, the DHRL model improved overall performance versus the other model forms investigated and showed relative insensitivity to mesh refinement level when compared to RANS and the other HRLs in this study. There was some deviation of DHRL model from experimental results for friction velocity and some near-wall statistics, but that can be attributed to the limitation of the RANS model used in this study. A transition sensitive, rotation and curvature corrected model such as the k-kL-ω-v^2 [6] model, proposed by Chitta et al., could be a more suitable RANS model for this case. Throughout the study, the DHRL model predicted the flow with accuracy even with a coarser grid. In some cases, the DHRL model was able to capture importance flow physics with considerable accuracy for a fraction of the computing cost when compared to benchmark data. There were some discrepancies due to a part of the spectrum that was lost due to the coarseness of the mesh but the overall performance of the DHRL model for this type of complex flow is a testament to the robustness and superiority of the DHRL modeling framework over conventional HRL modeling techniques.

CHAPTER V

STATIC AND DYNAMIC TIME FILTERING TECHNIQUES FOR HYBRID RANS-LES SIMULATION OF NON-STATIONARY TURBULENT FLOWS

5.1 INTRODUCTION AND OBJECTIVES

Because of the complexities associated with simulating non-stationary pulsating flows, explicit filtering operations can be used to improve predictive capabilities of LES models. It is a common assumption that the finite difference operators coupled with a sub-grid-stress model for an implicitly filtered LES, acts as a low pass filter by damping out high wavenumber flow structures. Though practical enough for most problems, there are drawbacks to this technique. One such issue is the contamination of the solution due to the lack of control over high frequency oscillations in the wave spectrum. Since there is no explicitly defined filter, high-frequency oscillations can interfere with the resolved portion of the spectrum and affect the dynamics of turbulence across a wide range of scales. This problem is easily mitigated by using an explicit filtering operation. Although a very useful alternative, the cost of using explicitly filtered LES is considerably higher than implicit LES.

An alternative approach is to make use of finite time filtering, in which turbulent statistics are obtained based on values of the dependent variables at previous time steps. The temporal filter

size reflects the extent of the filtering operator into the past. Ideally, for the purpose of computing turbulence statistics, the temporal filter size will be significantly larger than the characteristic time scale of fluid turbulence, and significantly smaller than the characteristic time scale of any imposed unsteadiness (non-stationarity) of the flow field. Different choices for the filter type are available, but one such filter that is particularly attractive due to its ease of implementation is the exponential time filter or exponential time average (ETA), which allows the filtered value at any given time step in the simulation to be obtained solely as a function of the time step size, the filter size, the instantaneous value of the dependent variable at the current time step, and the filtered value of the dependent variable at the previous time step. As such, the ETA method is adopted in this study as a potential method for extending the DHRL model to non-stationary flows.

The objective of this study is to investigate the performance of the dynamic hybrid RANS-LES (DHRL) [35-36] model with a suitable time filtering technique for non-stationary flows. Two different filtering approaches are investigated: Exponential Time-Averaging (ETA) with a static filter and a Dynamic Time-Filtering (DTF) technique. Initially, the predictive capabilities of three static filters with ETA incorporated in the DHRL model are evaluated against LES data from [24], MILES and baseline DHRL models. The results indicate that a smaller filter width is suitable for low-forcing while, a large filter with is more appropriate with high forcing frequency. This suggest that for flows with a large difference in turbulent time scale and forcing time scale, i.e. low-frequency oscillation, a smaller filter width is ideal. Although useful, the ETA with static filter relies heavily on user estimation to determine the appropriate filter width. For more complex flows, ETA with static filters may not be suitable. To address the issue of user dependence and to account for the changes in turbulent and forcing time-scales, the Dynamic Time Filtering (DTF) technique is proposed. As the name suggests, the DTF technique adjusts the filter width based on turbulent

statistics to resolve non-stationary flows accurately without the need of a user defined filter width. Performance of the DHRL model with the DTF are compared against the LES study conducted by Scotti et al. [24], Monotonically Integrated LES (MILES), a RANS model (SST *k*-ω), two conventional hybrid RANS-LES models (SST multiscale and SST-based detached eddy simulation), the baseline DHRL model, and the DHRL model with the static ETA methods. Results show that DTF shows improvement over the baseline ETA model throughout the entire forcing frequency spectrum for pulsating channel flow while having no detrimental effects when used in stationary channel flow.

5.2 NOVEL TIME-FILTERING APPROACHES

In order to extend the DHRL modeling framework to non-stationary flows, an alternative averaging technique is required. A relatively straightforward approach is to adopt causal time filtering. For the present study, the ETA and the DTF techniques would utilize exponential time averaging instead of Reynolds-Averaging.

5.2.1 Exponential Time Averaging

Exponential time averaging (ETA) is a 1st order infinite impulse response filter originally used in statistical applications such as stock market analysis [44]. The technique has previously been adopted for use in CFD applications, for example Pruett et al. [45] analyzed the use of exponential time averaging for the development of time-filtered large eddy simulation methods.

For an arbitrary time-dependent variable ϕ, the exponential time averaged value $\bar{\phi}$ is defined as:

$$\bar{\phi}(t) = \frac{1}{\Delta_f}\int_{-\infty}^{t} exp\left(\frac{\tau - t}{\Delta_f}\right)\phi(\tau)d\tau \tag{53}$$

where the filtered value of $\bar{\phi}$ is obtained as a weighted average of all previous values of ϕ, with the most recent values most heavily weighted. The filter size Δ_f determines how rapidly the weighting drops off as time is integrated into the past. The equivalent differential form is:

$$\frac{d\bar{\phi}}{dt} = \frac{1}{\Delta_f}(\phi - \bar{\phi}) \tag{54}$$

where above is a causal filter with the key advantage that the rate of change of the filtered value at time t is calculable based only on values of ϕ and $\bar{\phi}$ at time t. A discrete analog is obtained by substituting a first-order backward difference approximation for the temporal derivative, with the result:

$$\bar{\phi}(t) = \beta\phi(t) + (1 - \beta)\bar{\phi}(t - \Delta t) \tag{55}$$

where,

$$\beta = \frac{\Delta t}{\Delta t + \Delta_f} \tag{56}$$

During a CFD simulation, successive values of a filtered variable can be computed at each time step based only on the filtered value at the previous time step and the instantaneous value at the current time step. In the limit of zero filter size, the filtered value is equal to the instantaneous value. The running time-averaging operation used for stationary flow is formally similar to the above with the difference that the smoothing factor β is given by Eq. (56).

$$\beta = \frac{\Delta t}{t} \tag{57}$$

The filtering operation defined in Eq. (53) and numerically implemented by Eq. (55) was used to obtain a non-stationary approximation to the Reynolds-averaging operation.

It is apparent, however, that the filtering operation defined by Eq. (53) is not an exact equivalent to the infinite ensemble average implied by Reynolds averaging, even under conditions of ergodicity and zero numerical error. It is proposed, however, that the exponential time filter is a sufficiently accurate approximation of the Reynolds average that it can be used to provide an effective basis for application of the DHRL framework to non-stationary flowfields.

5.2.2 Exponential Time Averaging (ETA) with static filters

As an initial approach to determining an appropriate filter-width relevant for this particular problem, three different filter widths based on the time of one pulsation cycle (T) was chosen as shown in Table 3. It must be remembered that the filter width for any particular simulation using static filters is uniform in space and constant in time, and that filtering and differentiation operations commute.

Table 1. Time filtering method used in the simulations for each frequency

Model	**Time Averaging Method**	**Filter Width (Δ_f)**
SST- *k-ω*	Infinite	N/A
SST Multiscale	Infinite	N/A
MILES	Infinite	N/A
DHRL	Infinite	N/A
DHRL1	Exponential	1/2 Cycle Static Filter ($\Delta_f = \pi/\omega \ or \ T/2$)
DHRL2	Exponential	1/4 Cycle Static Filter ($\Delta_f = \pi/2\omega \ or \ T/4$)
DHRL3	Exponential	1/8 Cycle Static Filter ($\Delta_f = \pi/4\omega \ or \ T/8$)

5.2.3 Dynamic Time Filtering (DTF)

Similar to the ETA method outlined above, but with a spatially and temporally varying filter size, the Dynamic Time Filter (DTF) is selected based on an approximation of the large-eddy time scale of the turbulence. The goal of the dynamic filtering is to use a sufficiently large filter size, where and when needed, to obtain a reasonable approximation of Reynolds-averaged statistics, while limiting any tendency of the filter to smooth large-scale or imposed unsteady flow features.

For the current DHRL implementation, the filter width Δ_f used in Eq. (58) is computed at each mesh location and at each time step as:

$$\Delta_f = \psi / \sqrt{max\left(\bar{S}_{ij}\bar{S}_{ij}, C_\mu \omega^2\right)} \tag{58}$$

where ψ is a calibration constant, $\bar{S}_{ij}$ is the mean rate of strain, ω is the specific dissipation rate, and C_μ is a constant with value 0.09. It is evident that the filter width is assumed to be inversely proportional to a large-eddy time scale, which is in turn assumed to be the proportional to the greater of the mean strain rate or the specific dissipation rate from the *k-ω* SST RANS model. Initially, a calibration constant ψ = 50 was chosen and is used for this study. Investigation of the influence of the value of the calibration coefficient is reserved for future studies.

5.3 NUMERICAL SETUP

The pulsating channel simulations were carried out using the CFD code Loci-CHEM [39,40]. Loci-CHEM is a three-dimensional density-based finite-volume solver using implicit numerical methods and high-resolution approximate Riemann solvers. Since the current study

involves incompressible flow, all simulations were run with Mach Number on the order 0.1 based on average streamwise velocity. All post processing and data reduction was done using ParaView.

5.3.1 Forcing Functions and Parameters

A forcing function based on a time-dependent pressure gradient was applied as a source term in the streamwise momentum equation. The forcing term is given by:

$$\frac{dP_f}{dx} = \Delta P_0[1 + A\,cos(\omega t)]/\,L_x \tag{59}$$

where $\frac{dP_f}{dx}$ is the time-dependent pressure gradient in the source term, A is the non-dimensional amplitude of oscillation, ω is the forcing frequency, and $\Delta P_0/L_x$ is the steady pressure gradient.

Table 2 and Eqs. (60-64) provide a list of variables used for boundary condition calculations. Re_τ is the Reynolds number based on mean friction velocity, δ is the channel half-height, and ω^+ is the forcing frequency in wall units. For additional variables and definitions, the readers are referred to [24].

Table 2. Parameters used in the simulations

Variable	High Frequency	Medium Frequency	Low Frequency
Re_τ	350	350	350
ω^+	0.04	0.01	0.0016
A	200	50	8

$$Re_\tau = \frac{u_\tau \delta}{\nu} \tag{60}$$

$$\omega^+ = \frac{\omega \nu}{{u_\tau}^2} \tag{61}$$

$$u_\tau = \sqrt{\frac{\tau_{wall}}{\rho}} \tag{62}$$

$$u^+ = \frac{u}{u_\tau} \tag{63}$$

$$y^+ = \frac{y u_\tau}{\nu} \tag{64}$$

5.3.2 Data Analysis

As discussed above, neither exponentially filtered averages nor infinite-time averages of statistics reflect a true ensemble average for the present study. Planar averaging or phase averaging must be employed to accurately compare data to DNS and LES studies [24]. In the present work, instantaneous statistics of variables are planar averaged in post-processing using the averaging operation:

$$\langle f \rangle(y,t) = \frac{1}{L_z L_x} \int_0^{L_z} \int_0^{L_x} f(x,y,z,t)\, dx\, dz \tag{65}$$

where $\langle f \rangle$ is the planar averaged value of any arbitrary flow variable f, x and z are the streamwise and spanwise coordinate directions respectively, and y is the wall-normal direction.

5.3.3 Computational Domain and Boundary Conditions

Figure 1 shows the computation domain used in this study, which is identical to [46,47]. The domain extends to $L_x = 3\pi\delta$ in the x-direction, $L_y = 2\delta$ in the y-direction, and $L_z = \pi\delta$ in the z-direction. Periodic boundary conditions were specified in the streamwise (x) and spanwise (z) directions, while a no-slip boundary condition was specified on the top and bottom walls.

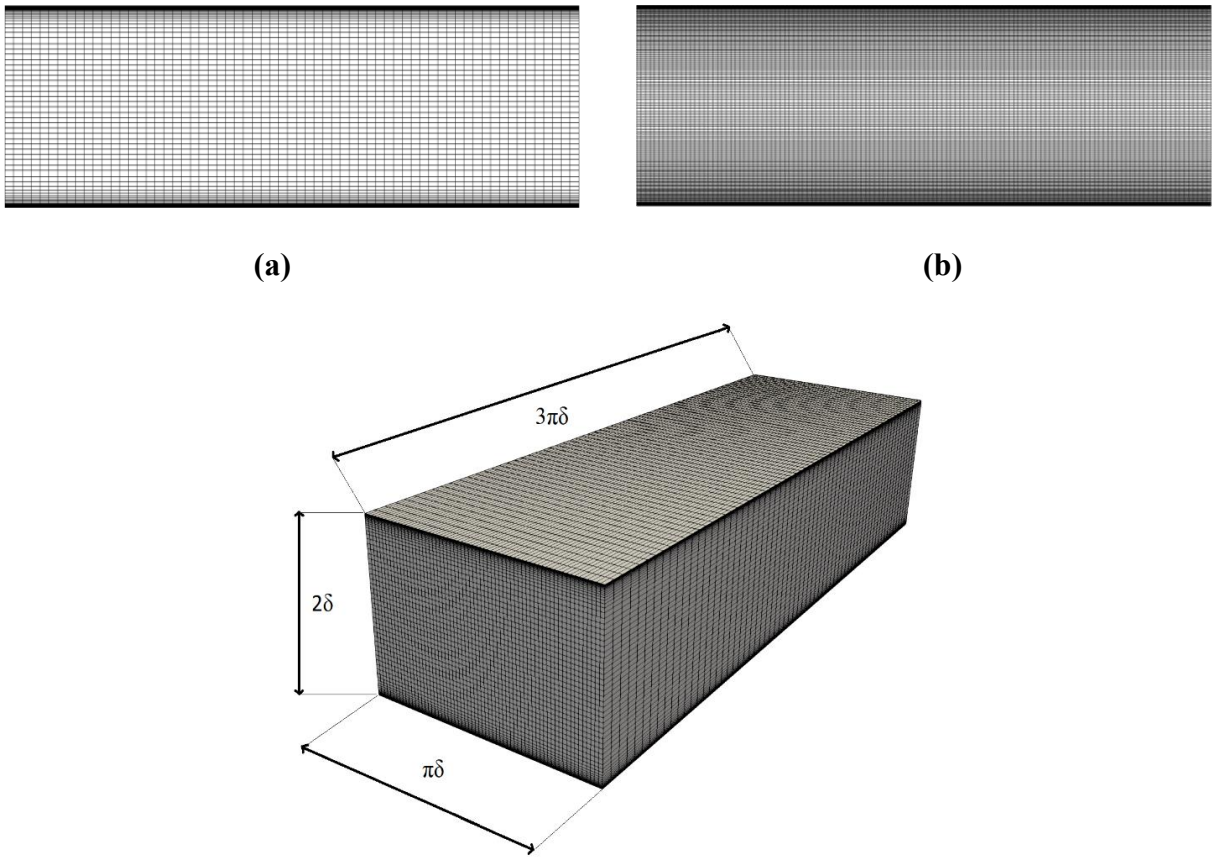

Figure 1. Side-view of (a) coarse grid, (b) fine grid, and (c) isometric-view of the domain

Grid Generation & Sensitivity Study

The boundary layer was constructed such that the non-dimensional wall distance or y^+ was maintained at less than unity for the first cell, while cells were stretched normal to the wall to reduce computational expense. To validate computational grids for the present study, steady channel flow simulations at $Re_\tau = 350$ were carried out using MILES and SST *k-ω* model for two grid resolutions, 64x64x64 (coarse grid) and 128x128x128 (fine grid) respectively. Simulations were run for at least 40 cycles with a time step size of 10^{-5} seconds for the 64x64x64 grid and 10^{-6} seconds for the 128x128x128 grid. Convergence was determined by ensuring that key variables reached limit cycle behavior.

Table 3. Grid sizes used in the grid sensitivity study

Mesh Type	Coarse Grid	Fine Grid
Mesh Size	64x64x64	128x128x128

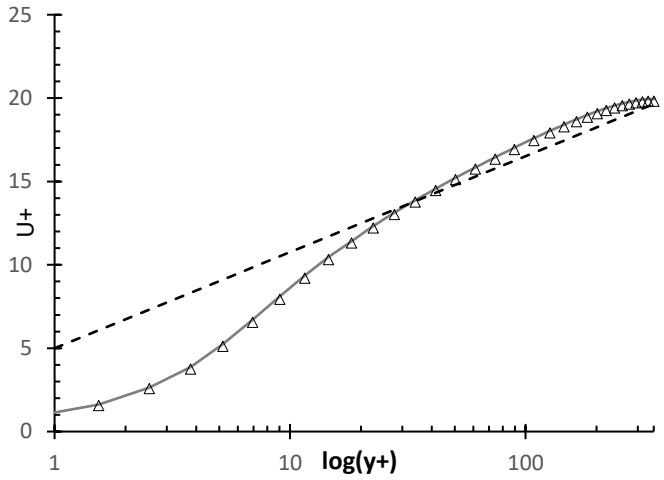

Figure 2. U^+ vs log (Y^+) for steady channel flow. △SST *k-ω* Model Coarse, — SST *k-ω* Model Fine, and - - - Log-Law.

Figure 2 shows the variation of normalized friction velocity (u^+) against dimensionless wall distance (y^+), given by Eqs. (46) and (47) respectively, for a steady channel flow at $Re_\tau = 350$ using the SST *k-ω* model and MILES with both 64x64x64 and 128x128x128 grids. The results indicate minimal difference in the profiles of the SST *k-ω* model suggesting that the model behavior is very nearly independent of the grid resolution. Based on the results of Figure 2, all numerical simulation data presented in this study was obtained from simulations performed using the 64x64x64 grid based on the grid sensitivity study and to for comparison with LES data in [24].

5.4 RESULTS AND DISCUSSION

5.4.1 Static-Filter Results

This section will investigate the performance of the three proposed static filters with exponential time-averaging (ETA) against LES, MILES and baseline DHRL model.

5.4.1.1 AC-DC Components

In order to better understand the response of the mean flow to the time-varying pressure gradient forcing, results for pulsating flow are decomposed into a time-mean component (DC) and a time fluctuating component (AC). Figure 3 shows the variation of normalized friction velocity (u^+) versus dimensionless wall distance (y^+) for the AC and DC components of the flow for the high frequency case. Results are shown for MILES and for the DHRL model with the stationary formulation (DHRL) and the three ETA versions with varying filter size (DHRL1, DHRL2, DHRL3). According to Figure 3 all models are in close agreement with DNS and LES data [24] for the AC component. The models behave almost identically in the outer layers of the flow with minor disagreements with the experimental data in the buffer layer. For the DC component shown in Figure 3, laminar (MILES), DHRL1, DHRL2 and, DHRL3 models overpredict the velocity in the buffer layer and the outer layer while the DHRL model provides the best agreement with experimental data.

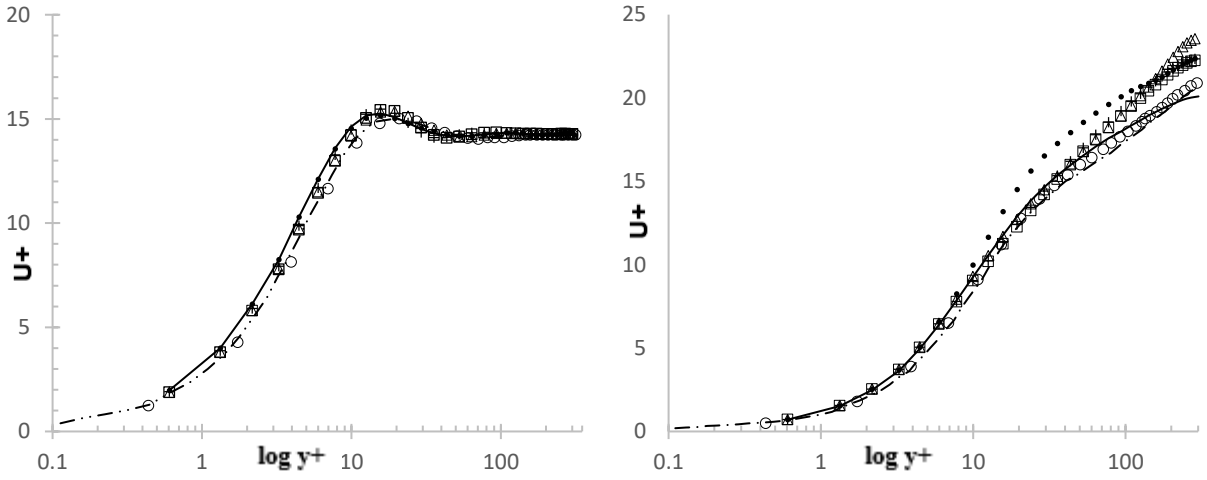

(a) **(b)**

Figure 3. (a) AC, and (b) DC component of streamwise velocity for high frequency case.

○LES [24], – · – · DNS [24], • MILES, ── DHRL, + DHRL1, ▫ DHRL2, and △ DHRL3

5.4.1.2 Time Varying Mean Velocity

Figures 4, 5, and 6 show the variation of normalized mean velocity (u^+) versus dimensionless wall distance (y^+) at 8 equidistant phases during a pulsation cycle. In each figure, t/T=0.75 and t/T=0.25 mark the beginning of the acceleration and deceleration phases respectively. For the high frequency case, the presence of a distinct logarithmic layer can be observed. At different phases during the cycle, the log layer is moved upwards and downwards by the changing core velocity while the outer layer remains virtually unaffected by the flow. MILES and all DHRL variants reproduce the velocity profiles with reasonable accuracy. Overall, the DHRL model, provides the best agreement with experimental data. MILES overpredicts the velocity in the log layer and the DHRL models with ETA (DHRL1, DHRL2, and DHRL3) overpredict velocity in the outer layers as seen from Figures 4, 5, and 6.

The effects of the forcing term are much more prominent in the velocity profiles of the medium frequency case. A distinct logarithmic layer is present only during a part of the cycle when the velocity is maximum. Also, a strong coupling of the logarithmic and outer layer can be seen in the deceleration phase of the cycle. In the acceleration phase, DHRL1, DHRL2, and DHRL3 models slightly overpredict velocity in the log layer with major defects in the outer-layer. As the flow starts to decelerate, the DHRL1 and DHRL2 model predictions improve with minor deviations in the log-layer but the DHRL3 model consistently predicts a minor velocity defect in the buffer and log-layers. Overall, the baseline DHRL model consistently provides the most accurate predictions. The DHRL ETA variants with the larger filter widths, i.e. DHRL1 and DHRL2, are in better agreement with experimental data than DHRL3 suggesting that the use of larger filter widths is most effective for high frequency oscillations. A similar behavior is

At low frequency, the entire channel is affected by slow modulations originating from the imposed forcing function. Throughout the acceleration phase, the DHRL models with ETA predict velocity with accuracy while, MILES and DHRL models overpredict the velocity. As the flow starts to decelerate causing enhanced mixing, DHRL2 and DHRL3 models follow experimental data closely while all the other models show large disagreements with experimental data. As the flow continues to slow down, DHRL1 recovers the correct velocity while MILES and DHRL models continue overpredicting velocity. Throughout the cycle, the explicitly filtered models provide reasonable agreement in the inner parts of the flow while slightly overpredicting velocity in the outer layers.

The results in Figure 4 support the previous suggestion that, for high frequency pulsating flow, the DHRL model formulated for stationary flow performs the best. In this case the velocity

component due to the oscillating pressure gradient are treated as part of the fluctuating (rather than mean) velocity. However, as the frequency decreases, this description is less accurate. For the low frequency case shown in Figure 6, the stationary version of the model (DHRL) shows significant discrepancy with the LES results of [9]. The best agreement is obtained with the DHRL ETA variants with the two smallest temporal filter widths (DHRL2 and DHRL3). When the difference between the forcing time scale and the turbulence time scale becomes large, i.e. when there is significant temporal scale separation, the use of exponential time filtering is more appropriate. In that case, the periodic component of the velocity due to the oscillating pressure gradient is more appropriately treated as a time-dependent contribution to the mean flow rather than as a fluctuating component. Taken as a whole these results are encouraging. They suggest that the appropriate filter size may perhaps be computed based on the turbulent time scale rather than the imposed unsteadiness. Since this time scale varies spatially in the flow, it may require a dynamic filtering operation in which the temporal filter size is not spatially uniform.

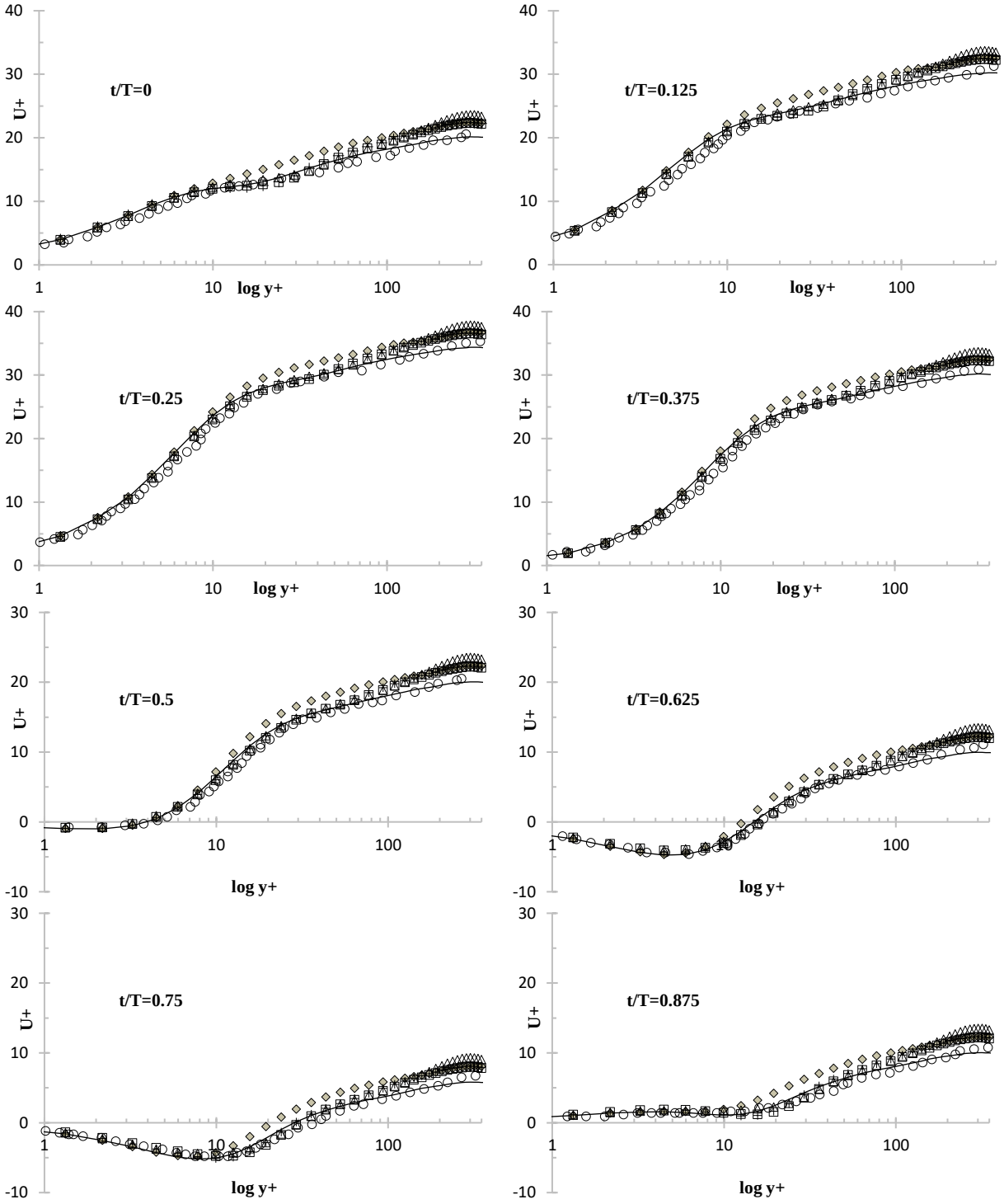

Figure 4. U^+ vs log (Y^+) for high-frequency case. ○ LES [24], ◆ MILES, ── DHRL, + DHRL1, □DHRL2, and △ DHRL3

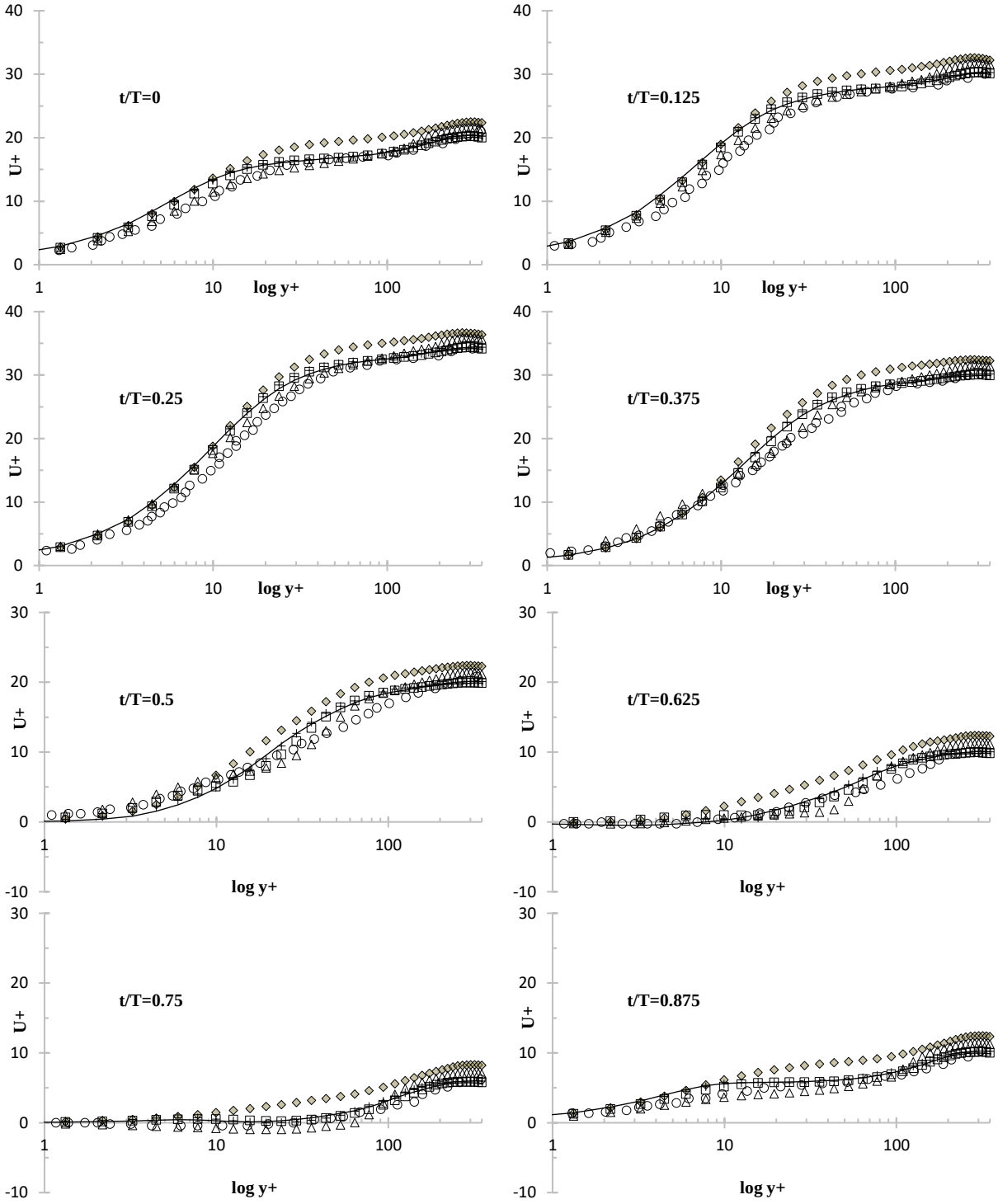

Figure 5. U^+ vs log (Y^+) for medium-frequency case ○ LES [24], ◈ MILES, ── DHRL, + DHRL1, □DHRL2, and △ DHRL3

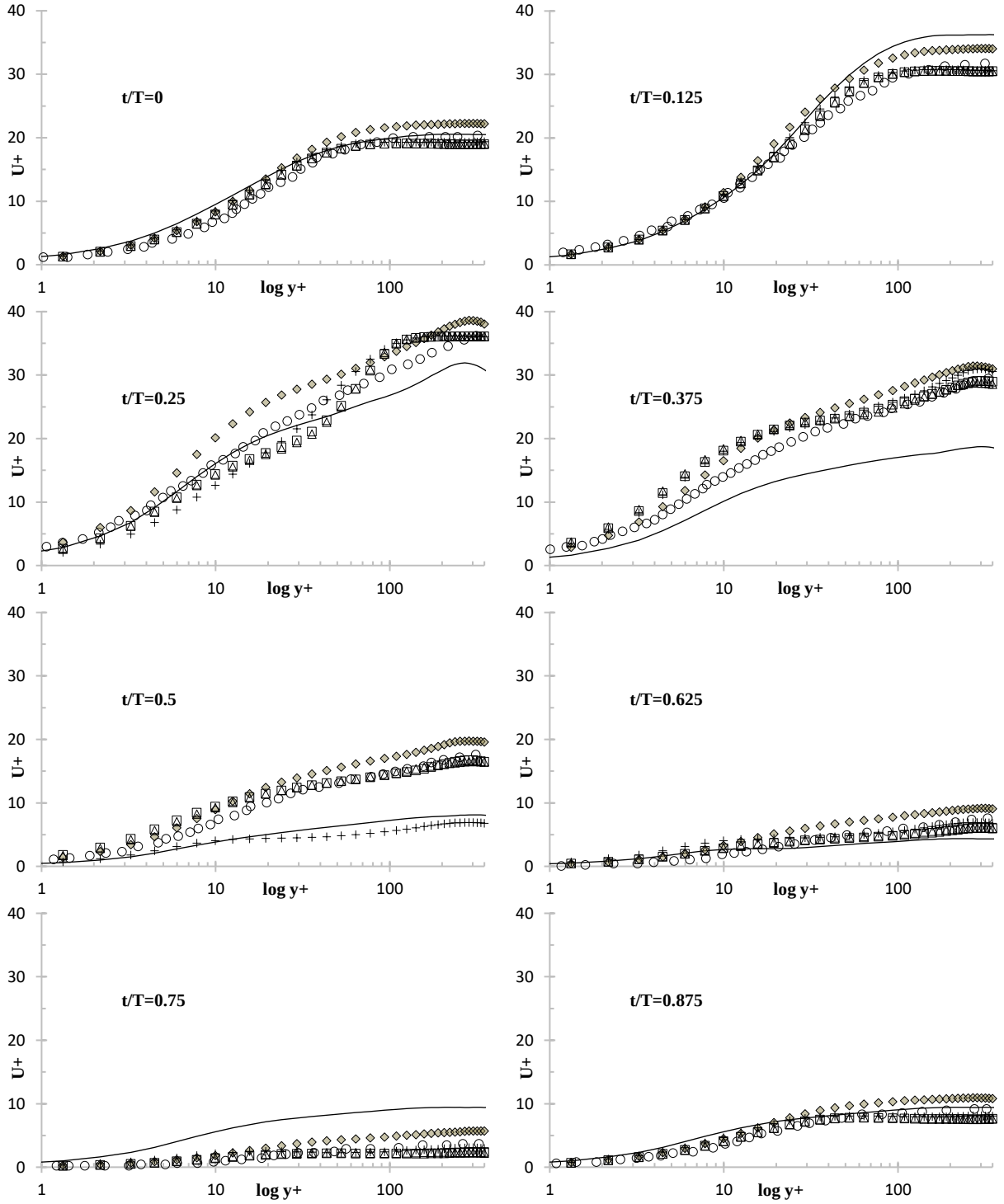

Figure 6. U^+ vs log (Y^+) for low-frequency case. ○ LES [24], ◈ MILES, ── DHRL, + DHRL1, ▫DHRL2, and ▵ DHRL3

5.4.2 Dynamic Time Filtering Results

This section will investigate the performance of the DTF with exponential time-averaging against LES, MILES, SST *k-ω*, Multiscale, DHRL, and DHRL ETA models.

5.4.2.1 Steady Pressure Driven Flow (Re_τ = 350 & 590)

Simulations of steady pressure-driven channel flow were carried out for Re_τ=350 and Re_τ=590 to verify the effect of using the DTF technique with DHRL model for a stationary flow. Results from all the models are in qualitative agreement with LES data from [24]. For both cases, all the models predict the behavior in the viscous sub-layer with considerable accuracy with major velocity defects appearing in the log-layer. The SST Multiscale model undergoes RANS-LES transition too close to the wall and underpredicts velocity in the log-layer for both cases. For Re_τ = 590, MILES overpredicts velocity in the log-layer as LES is under-resolved in this region for the coarse grid, resulting in the well-known "log-layer mismatch". The baseline DHRL model underpredicts velocity in the outer layer for Re_τ = 350, a behavior that can be attributed to increased modeled stress from the underlying RANS model. The DHRL model with DTF behaves like the baseline DHRL model up to the log layer but remains in LES mode in the middle region of the channel to predict the velocity profile with greater accuracy.

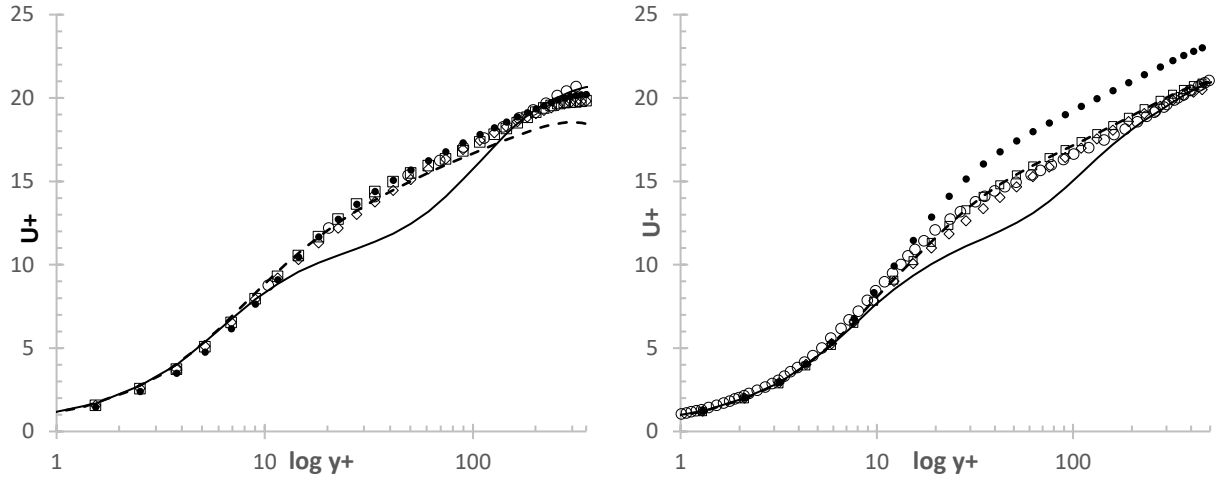

(a) **(b)**

Figure 7. $U^+ \; vs \; log \; (Y^+)$ for steady channel flow at (a) Re_τ=350 and (b) flow at Re_τ=590. (a) ○ Scotti et al. [24]; (b) ○ Moser et al. [48]; •MILES, - - - DHRL, ◘ DHRL DTF, ◇ SST *k-ω*, and —— SST Multiscale Model

5.4.2.2 Pulsating Channel Flow

In the previous section, the ETA with static filtering is a potentially attractive solution for applying the DHRL model for these types of problems. Despite improving the predictive capabilities of DHRL, ETA required considerable user input when considering an appropriate time filter width to be used in the averaging process. The filter widths were chosen arbitrarily to be based on forcing frequency. The DTF method eliminates user input by automatically selecting and dynamically altering the filter width based on local turbulent statistics. Users still have the option to alter the calibration constant (ψ), allowing some measure of tunability, however for the present study a constant value of 50 was chosen based on preliminary numerical investigations. Table 4 lists the naming convention for different models used in this study along with filtering methods and sizes used in this study.

Table 4. Time filtering method used for each model

Model	Time Averaging Method	Time Filtering Method
SST *k-ω*	Infinite	N/A
MILES	Infinite	N/A
SST MULTISCALE	Infinite	N/A
DHRL	Infinite	N/A
DHRL ETA	Exponential	1/4 Cycle Static ETA ($\Delta_f = \pi/2\omega \; or \; T/4$)
DHRL DTF	Exponential	Dynamic Time Filtering (DTF)

5.4.2.3 AC-DC Mean Velocity Components

Figure 8 shows the normalized result for the three pulsating frequencies investigated. For the AC component in the high frequency case, all models are in close agreement with LES data with minor mismatch in the log-layer. For the DC component, all the models follow LES data in [24] closely in the buffer layer with the majority of the models overpredicting velocity in the log-layer. The SST Multiscale model transitions to LES in the log-layer and revert to RANS in the outer layer, while the DHRL model with infinite time-averaging and the DHRL model with DTF follow LES data closely.

For the AC component in the medium frequency case, all the models show significant velocity defect in the buffer layer all the way up to the log layer. MILES and the DHRL models underpredict velocity throughout the cycle but successfully capture the overall trend of the LES data. The SST *k-ω* and the DHRL model with DTF follow LES values closely in the log and outer-layer with some defects in the near wall regions. SST Multiscale model initially overpredicts velocity in the near-wall regions before switching to switch to LES in the log-layer and underpredicting velocity. Most of the models are in better agreement with LES data for the DC

part of the flow. All the baseline hybrid models show velocity defects in the log layer. However, the DHRL model with DTF predicts accurate mean velocity throughout the channel with only minor defects in the log-layer. The DHRL model with DTF behaves very similarly to the SST k-ω model throughout the flow. It appears that the DTF technique allows the DHRL model to remain in RANS mode in the outer regions of the flow where the baseline DHRL model is more LES dominant. The SST Multiscale model behavior is quite similar to that of the baseline DHRL model. Both predict near wall velocity reasonably well, but transition to LES in the log-layer and underpredict velocity.

In the low frequency case, the overall behavior of all the models for AC and DC parts of the flow are similar to the medium frequency case. The baseline hybrid models predict near-wall velocity with reasonable accuracy, then underpredict velocity in the log and outer-layers of the flow. The SST k-ω and the DHRL model with DTF are in best agreement with LES data. However, there is some velocity defect for the DHRL model with DTF in the outer layer caused by increased resolved turbulence production.

The analysis of the AC and DC components suggest that the DTF technique helps the DHRL model to accurately capture the flow physics throughout the imposed frequency spectrum and consistently provide superior results compared to the baseline DHRL model with infinite time-averaging.

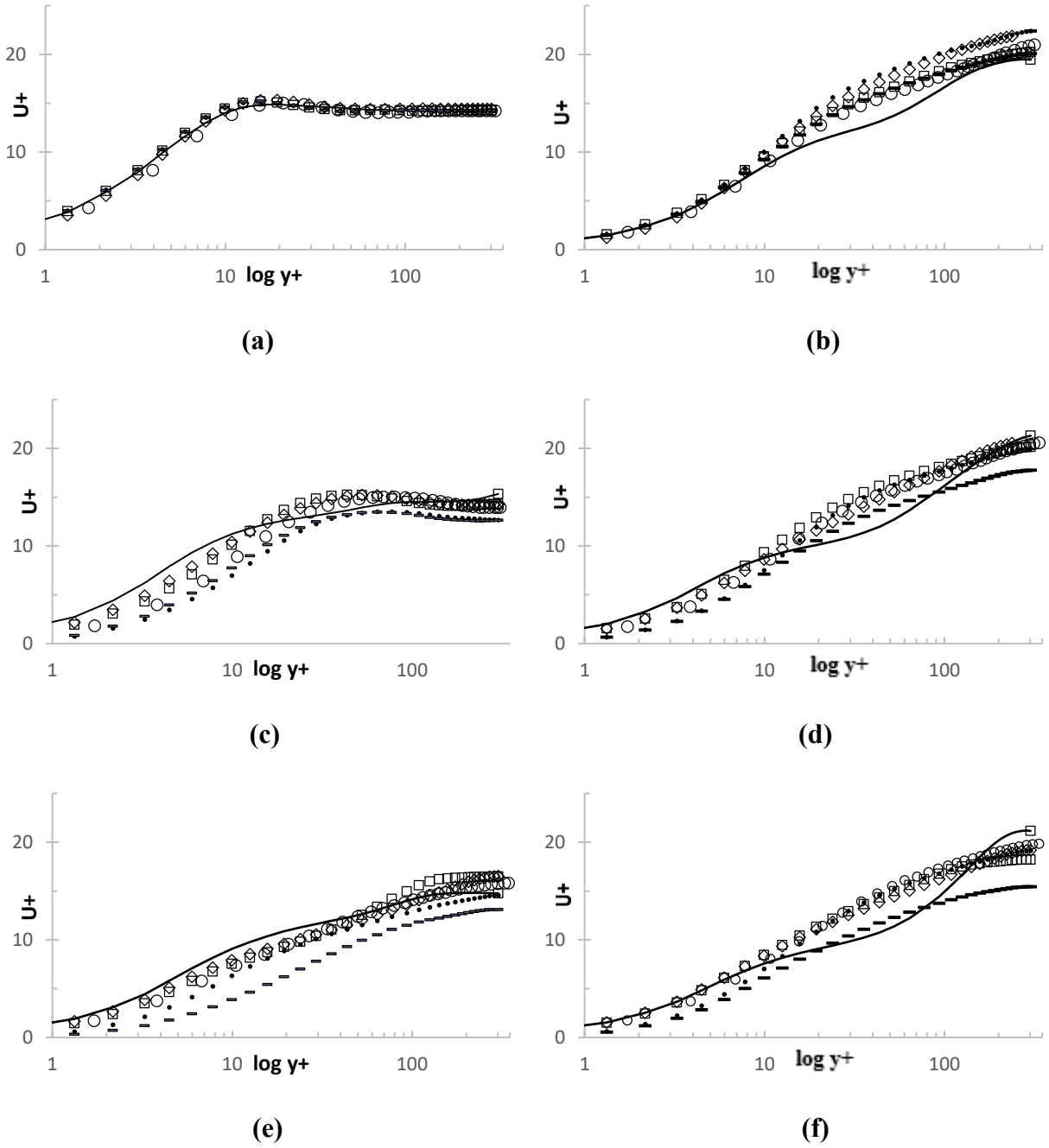

Figure 8. Streamwise velocity components (a) High Frequency AC and (b) DC; (c) Medium Frequency AC and (d) DC; (e) Low Frequency AC and (f) DC. ○ LES [24]; •••MILES, − − − DHRL, ▫ DHRL DTF, ◇ SST *k-ω*, and ── SST Multiscale Model

5.4.2.4 Time-Varying Mean Velocity

Figures 9, 10, and 11 show mean velocity versus wall distance at 8 equidistant times during a single pulsation cycle. Results are shown for all models in table 2.

For all three of the forcing frequencies investigated, most of the models accurately capture the flow in the near-wall regions with major disagreements only appearing within the log-layer or wake region. For high frequency oscillations, all of the models predict the flow in the viscous sub-layer and the buffer layer accurately. SST k-ω shows significant velocity defects in this region only in the acceleration phase. In the log-layer, the SST Multiscale model underpredicts velocity throughout the cycle. In the outer layer, the baseline DHRL model continues to follow LES data, while the DHRL model with ETA overpredicts velocity. In Figure 4 it was shown that all the ETA models overpredicted velocity in the outer layer with defects that increased as filter width was decreased. The DHRL model with DTF corrects this issue by dynamically adjusting the filter width based on turbulent statistics instead of relying on a user-defined filter width.

For the medium frequency case, the effects of the forcing frequency on the velocity profile appear to be more significant. As mentioned earlier, the presence of a distinct log-layer can be observed only for some parts of the cycle. Similar to the high frequency case, most models capture the velocity profile trend of the LES data with some accuracy. In the acceleration phase, all the models overpredict velocity close to the wall. The SST Multiscale model undergoes RANS-LES transition just outside the buffer layer. In the log-layer, the SST Multiscale model underpredicts velocity while the DHRL model variants slightly overpredict velocity. In the deceleration phase, a similar trend is observed. The SST Multiscale model underpredicts velocity for majority of the flow, while the RANS model overpredicts velocity. Once again, all of the DHRL model variants show improved predictive capabilities when compared to the other models in the study.

For low frequency oscillations, the velocity profile exhibits slow modulations throughout the cycle. All three models show some defects in the log-layer but capture the correct velocity in the outer layer. The baseline DHRL model shows significant defect towards the end of the acceleration phase, but the DHRL models with ETA and DTF consistently follow LES data. All models without any filtering method predict incorrect velocity profiles towards the end of acceleration phase due to enhanced mixing as the flow starts to decelerate. Appropriate filtering techniques apparently enable the DHRL model with ETA and DTF to resolve turbulence more effectively. As flow continues to decelerate, the DHRL model with DTF resolves the mean velocity profile with reasonable accuracy with minor defects appearing in the outer layer.

Overall, the results from Figures 9, 10 and 11 suggest that the DHRL model with DTF provides improved predictive capability when compared to ETA with a static filter size. For the high frequency case, the DHRL model with DTF behaves almost identically to the baseline DHRL model. Since for this case the turbulent time scale and characteristic mean time scale due to the imposed pulsation frequency are similar, the velocity component due to the oscillating pressure gradient is treated in the model as a part of the fluctuating velocity. As the forcing frequency is reduced, the separation between the turbulent time scales and the forcing frequency becomes larger. For these frequencies, the DHRL model with DTF dynamically adjusts the filter width based on the turbulent statistics.

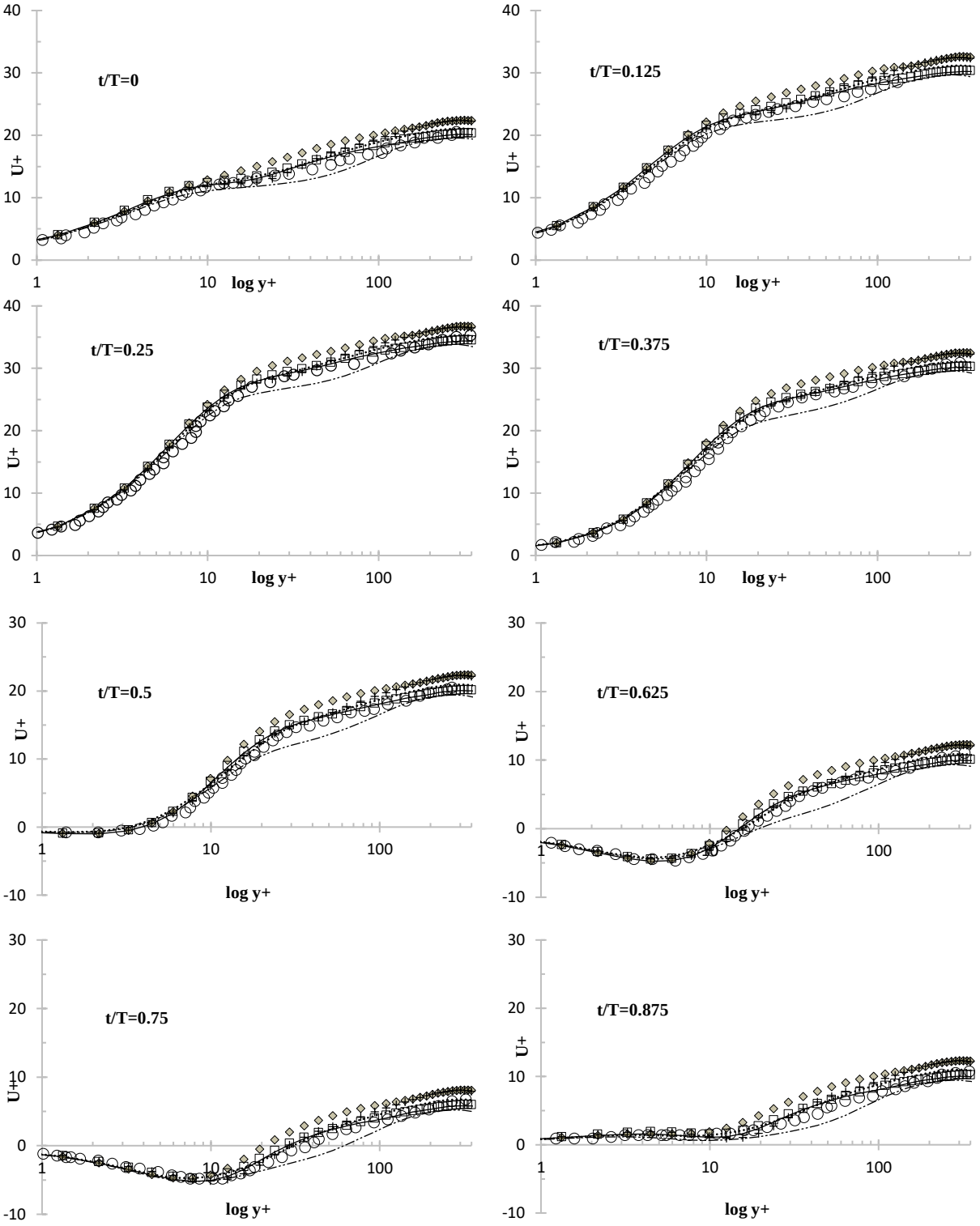

Figure 9. U^+ *vs* $log\ (Y^+)$ for high-frequency case. ○ LES [24]; ◇MILES, ── DHRL, □ DHRL DTF, + DHRL ETA , ••• SST *k-ω*, and ─··─ SST Multiscale Model

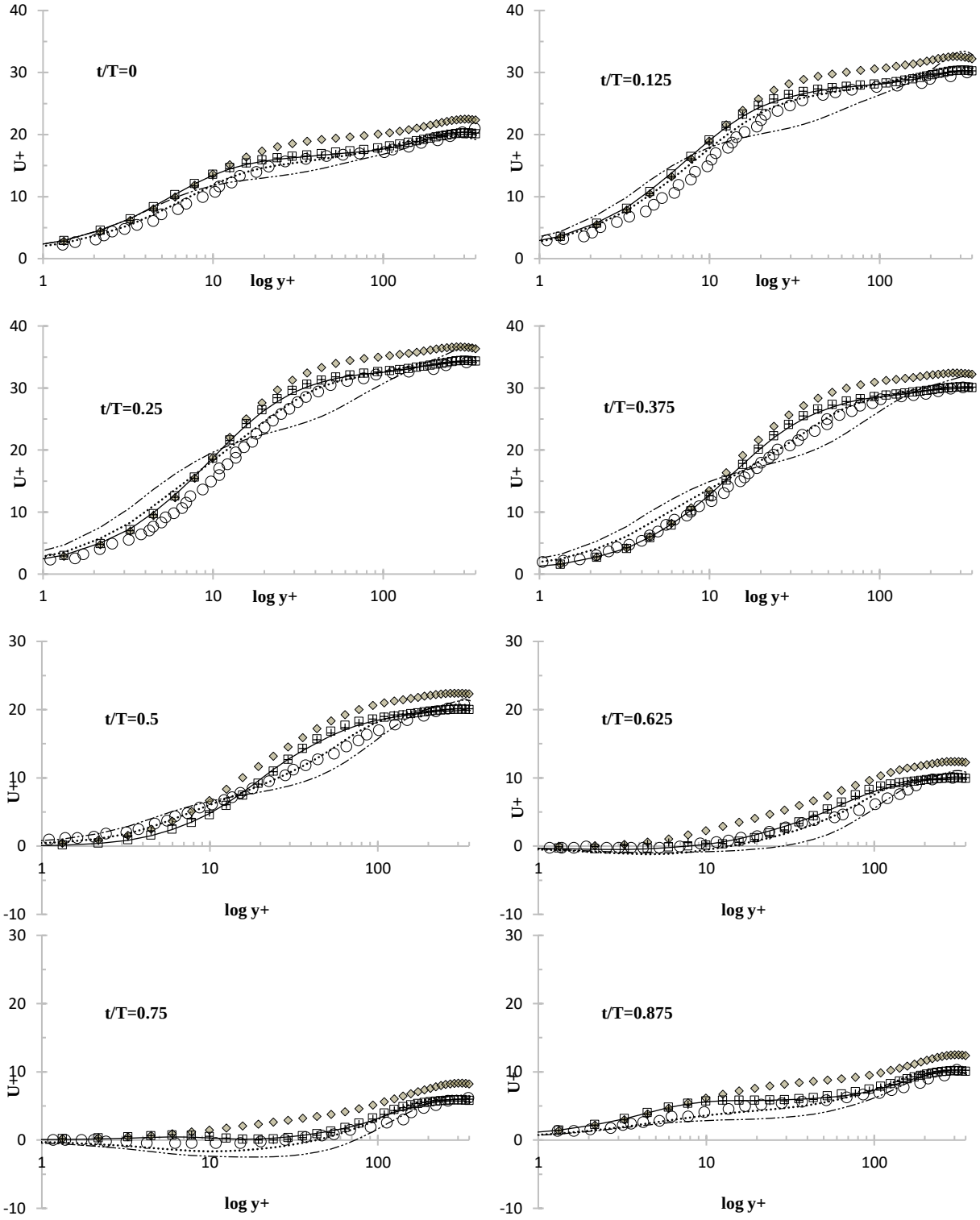

Figure 10. u^+ *vs* $log\ (y^+)$ for medium-frequency case. ○ LES [24]; ◈MILES, ── DHRL, ▫ DHRL DTF, + DHRL ETA, ••• SST *k-ω*, and ─··─ SST Multiscale Model

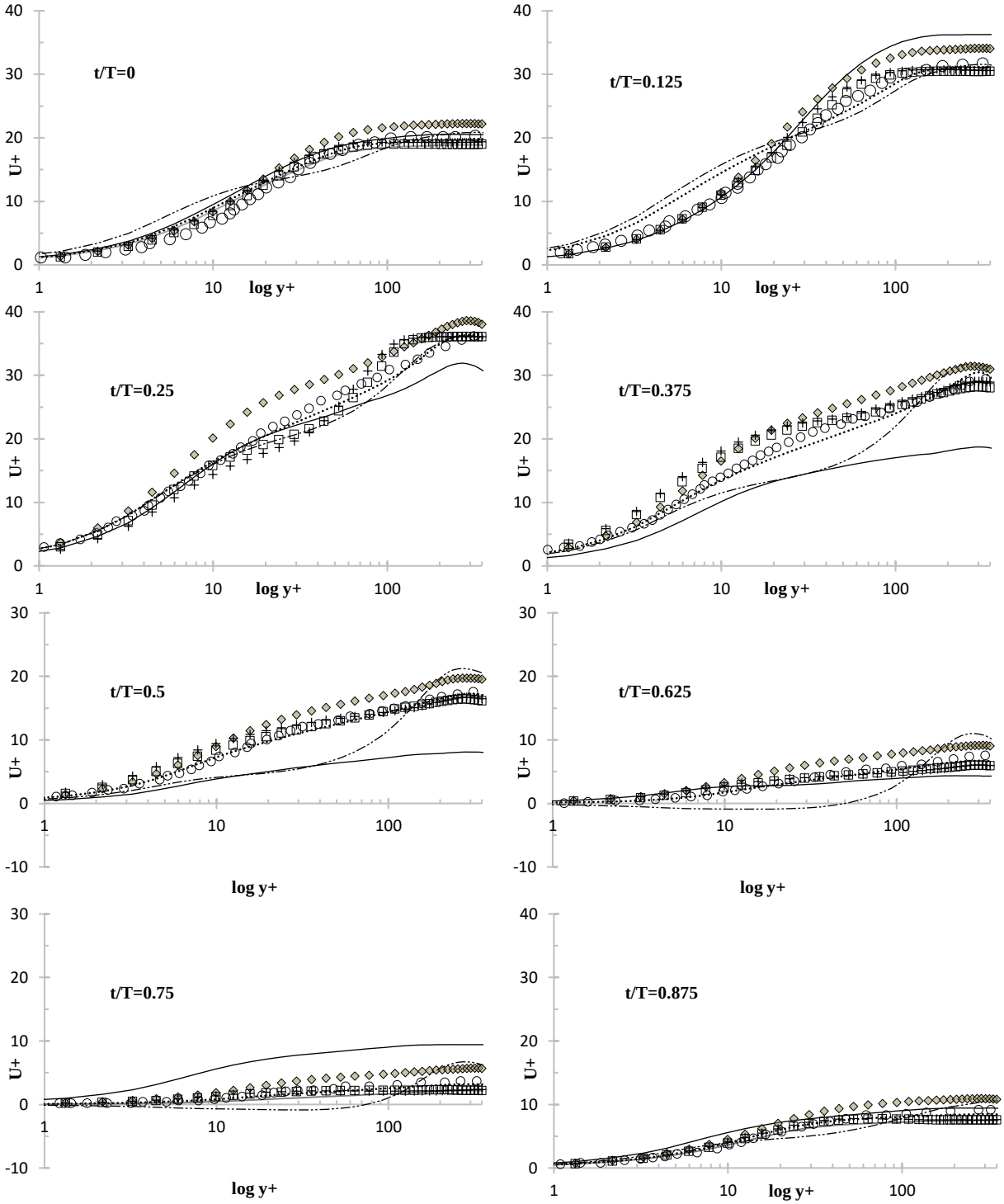

Figure 11. U^+ *vs* $log\ (Y^+)$ for low-frequency case. ○ LES [24]; ◇MILES, ── DHRL, □ DHRL DTF, + DHRL ETA, ••• SST *k-ω*, and ─··─ SST Multiscale Model

5.4.2.5 Behavior of the blending parameter (α) for the DHRL model variants

Figure 12 shows the variation of the blending parameter (α) for steady-channel flows at Re_τ=350 and Re_τ=590. For channel flows in relatively coarse grids, MILES is generally underresolved in the log-layer (log-layer mismatch). The DHRL model supplements the lack of resolved stress contribution in this region by adding a modeled stress component to improve predictions. Ideally, for turbulent channel flows, it is preferable for the DHRL model to be in a LES-biased mode with small RANS contributions. However, in coarse grids at low Reynolds numbers, the baseline DHRL model operates in a RANS-biased state throughout the height of the channel in response to the lack of significant resolved fluctuations. Although mean-flow features are well predicted by the RANS model, Reynolds stress are significantly underpredict due to the lack of resolved fluctuations.

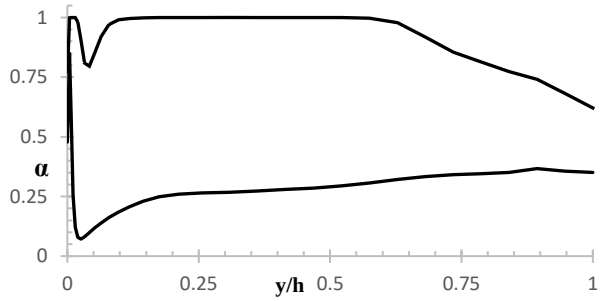

Figure 12. α for baseline DHRL model —Re_τ=350 and --- Re_τ=590

Figure 13 shows the distribution of AC and DC components of the blending parameter (α) for all the DHRL model variants throughout the forcing frequency spectrum. The baseline DHRL model treats the velocity fluctuations due to the oscillating pressure gradient as part of the mean-flow throughout the forcing spectrum. This behavior is appropriate for high frequency oscillations since the imposed pulsation time-scale and the turbulent time-scales are of similar order. Hence, the AC component of the flow is appropriately described by the DHRL model in RANS-biased

mode. However, for lower frequency oscillations, the baseline formulation is unable to adequately separate the time-dependent velocity from turbulent fluctuations leading to increased RANS contribution and severe velocity defects. The implementation of the ETA and the DTF improves predictions as the models can effectively distinguish between the time-dependent components of the flow and turbulent fluctuations. Both models effectively adjust the relative RANS-LES contributions and significant improvements are observed for medium and low frequency oscillations. Overall, the DHRL DTF model performance is closer to the desirable behavior throughout the forcing spectrum and it provides the best agreement to LES data.

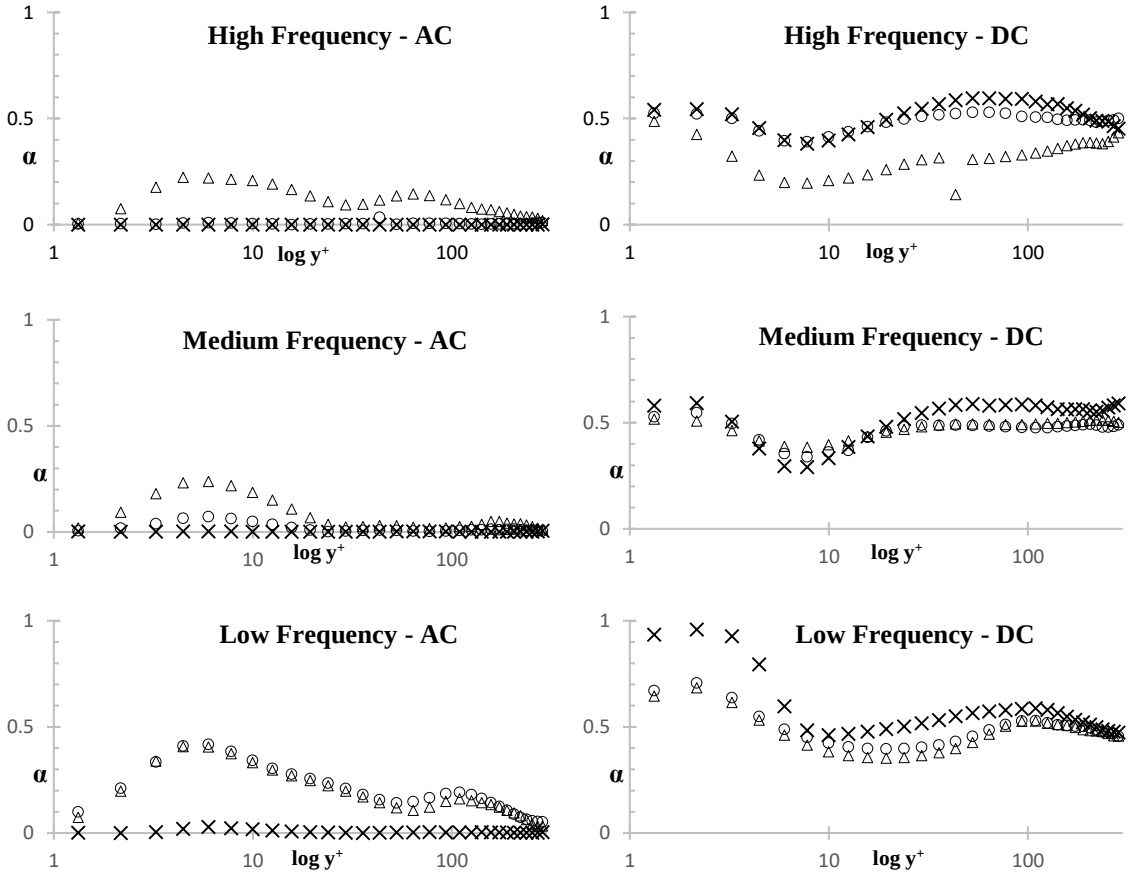

Figure 13. Distribution of α for Baseline DHRL model X ; DHRL ETA△; DHRL DTF ○

5.4.2.6 Reynolds Stresses

Figure 14 compares AC and DC components of Reynolds-stresses for high frequency oscillations of some of the models investigated against DNS and LES calculations in [9]. MILES, baseline DHRL, and the DHRL DTF models are in qualitative agreement with DNS and LES data while, the DHRL ETA and SST Multiscale predictions are poor in comparison. MILES overpredicts the DC component of the Reynolds stresses but underpredicts the AC component. The baseline DHRL and the DHRL-DTF models provide relatively accurate descriptions of the $\overline{u_1'u_1'}$ and $\overline{u_1'u_2'}$ components. Some defects are observed in the buffer and log-layers however, predictions are comparable to LES results in the outer regions of the flow.

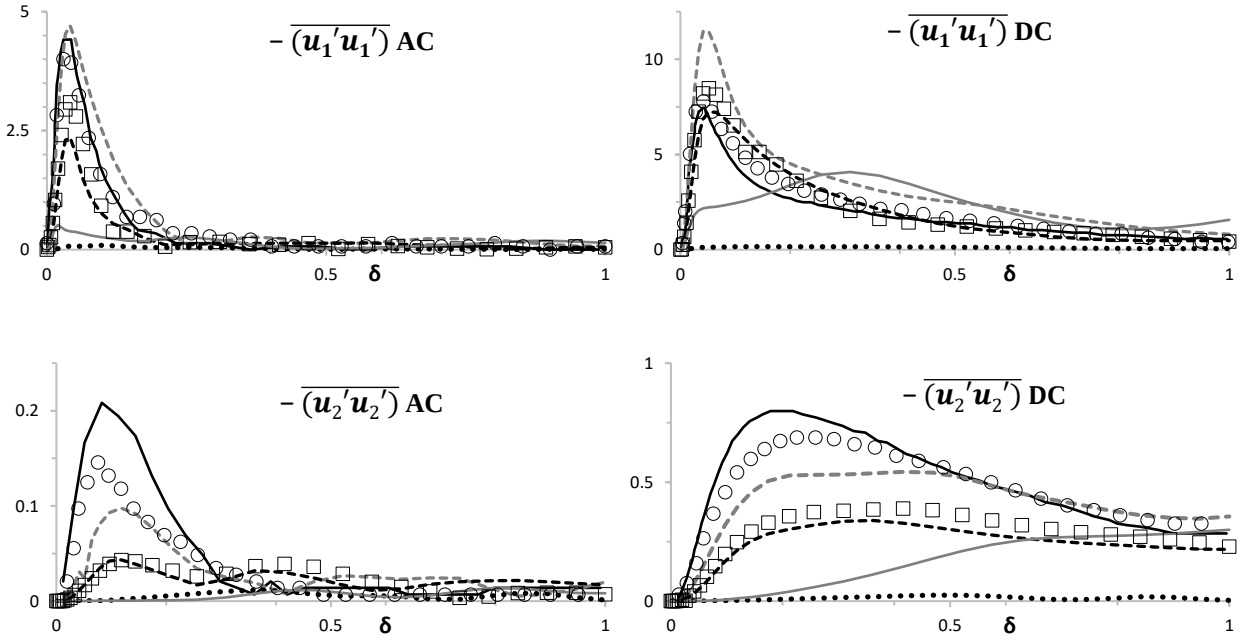

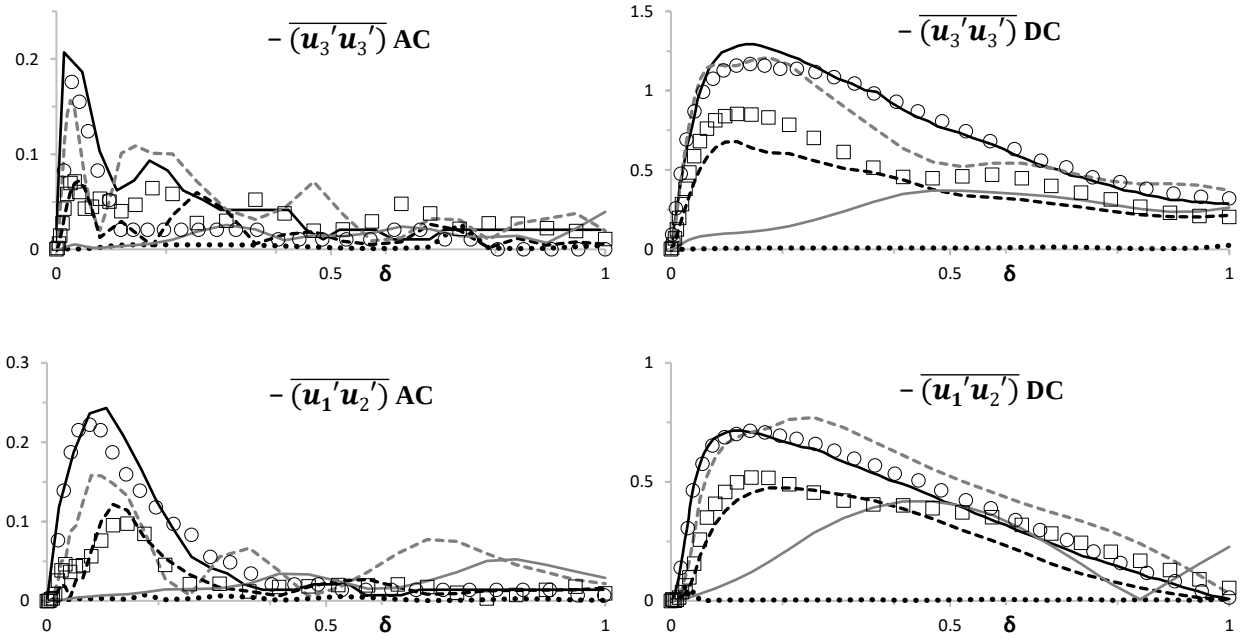

Figure 14. AC and DC components of resolved Reynolds stresses for high-frequency oscillations. —DNS [24], ○LES [24], – – – MILES, --- DHRL, •••• DHRL ETA, ▫ DHRL DTF RESOLVED, and — SST MULTISCALE

5.4.2.7 Comparison of $\overline{u_i'u_i'}$ and Reynolds Shear Stress ($\overline{u_1'u_2'}$)

Figures 15-17 compare the Reynolds stress predictions of the models investigated against the LES study carried out by Scotti et al. [24]. At start of the cycle for high frequency oscillations, the resolved stresses are well correlated with LES observations. All the models expect the DHRL ETA and SST Multiscale exhibit a similar behavior to the LES model. Once the flow reaches the maximum velocity (at t/T=0.25) and starts to decelerate, the DHRL model variants show some velocity defects. Once the acceleration phase begins (at t/T=0.75), comparisons are significantly improved once again. Similar behavior can be observed for the medium frequency except for t/T=0.375 where all the DHRL variants underpredict stresses. For low frequency oscillations, the

DHRL model variants predictions are close to LES only during the deceleration phase where turbulence production is enhanced.

Results for Reynolds shear stress, shown in figures 18-20, indicates that MILES performance is superior to all the models investigated in this study. Although MILES overpredicts stresses during the deceleration phase, results from the acceleration phase is well correlated to LES data. Since the DHRL model tends to remain RANS-biased for Re_τ=350, all the DHRL variants underpredict stresses. Correlations during the acceleration phase is poor as the model fails to accurately predict increased momentum and energy transfer between *u* and *v* components of the velocity. Similar to the low-frequency oscillations, some improvements in the predictive capabilities of the DHRL model variants are observed in the deceleration phase due to enhanced turbulence production.

Overall, the DHRL-DTF models provide the best descriptions of the flow. Both models track the general behavior of the LES model reasonably well for the high and medium-frequency oscillations with major defects appearing for low-frequency oscillations.

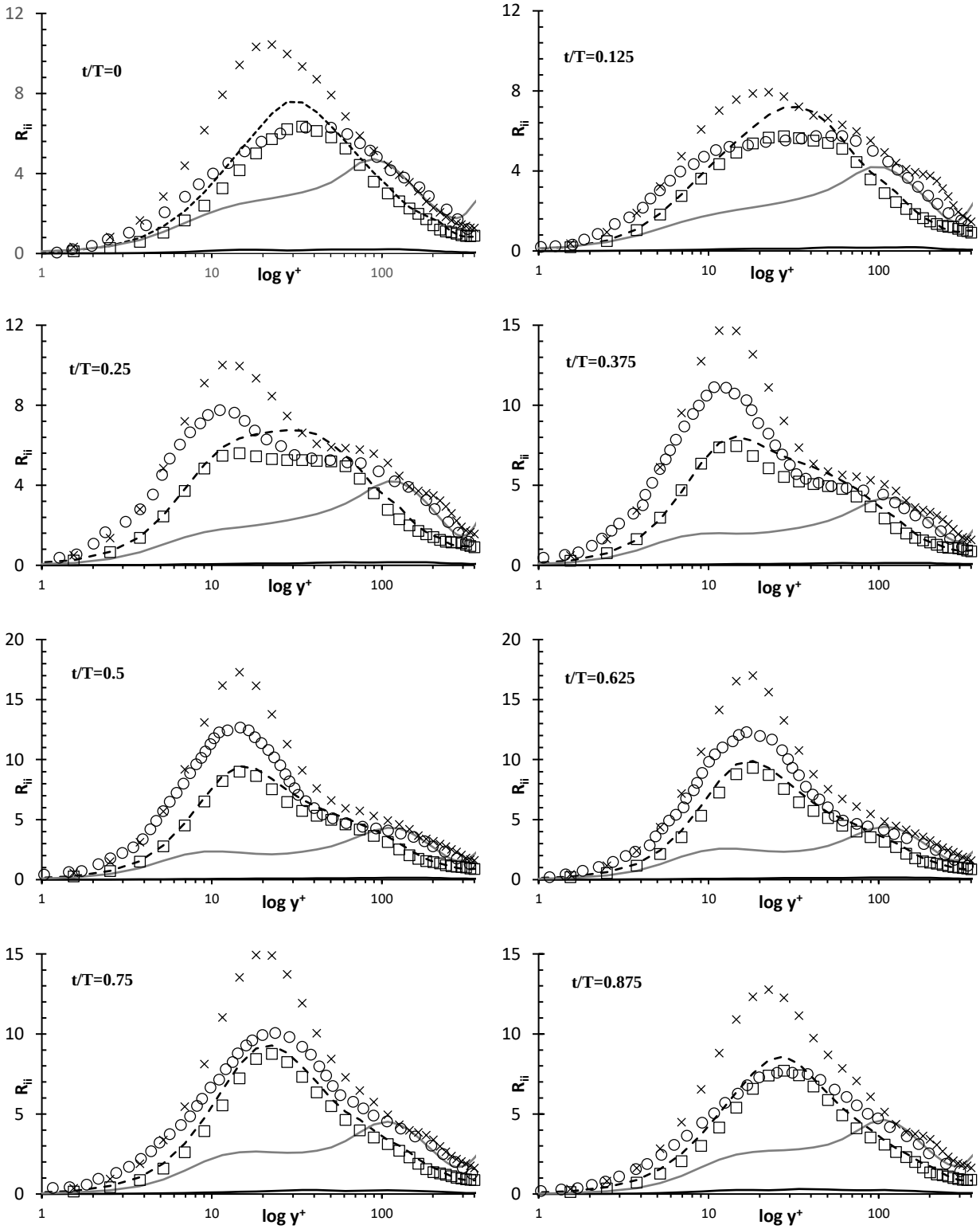

Figure 15. Plots of resolved ($\overline{u_i'u_i'}$) vs y^+ for high-frequency oscillations . ○ LES [24], x MILES, --- DHRL, ▬ DHRL ETA, ▫ DHRL DTF, and ▬ SST MULTISCALE

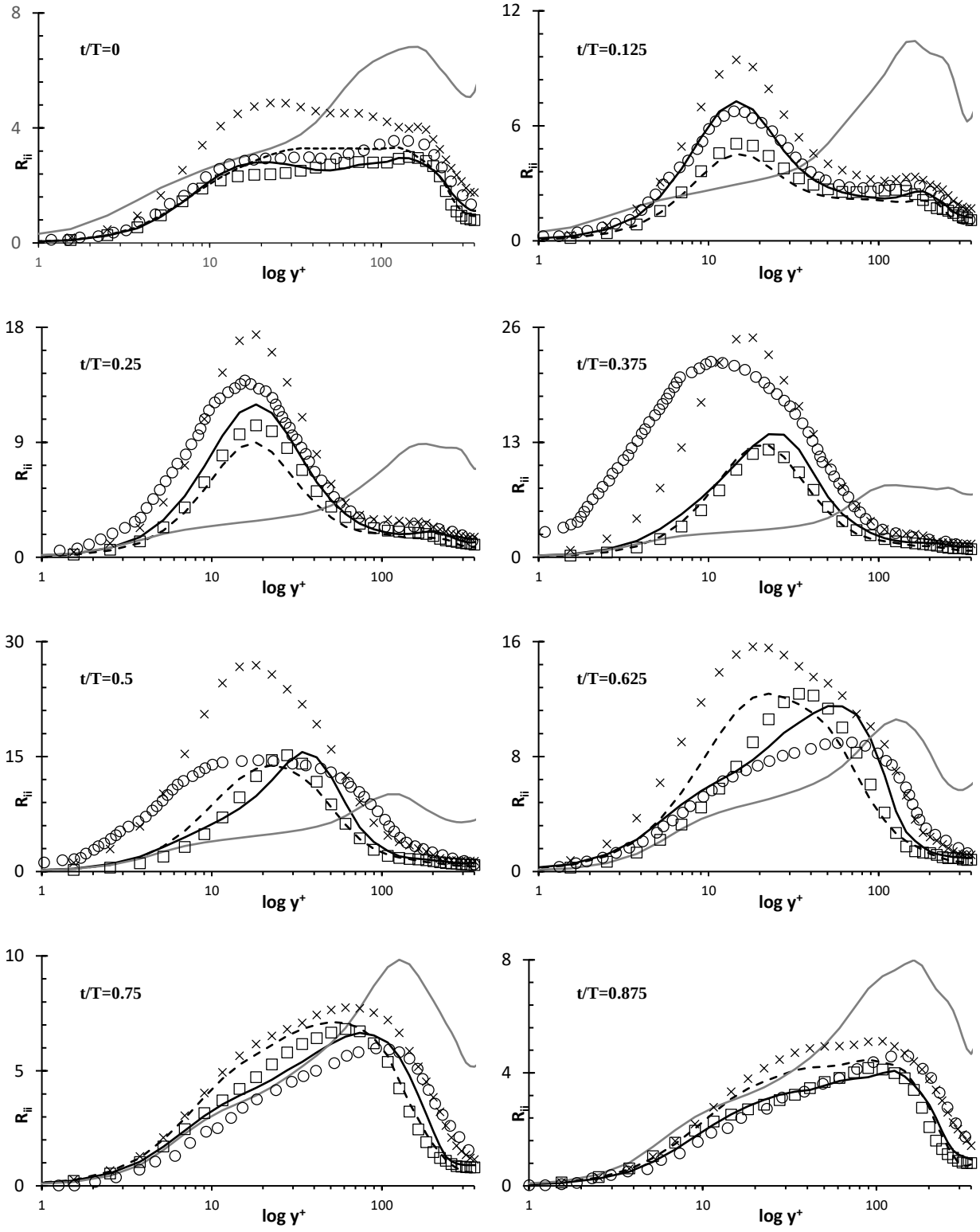

Figure 16. Plots of resolved ($\overline{u_i'u_i'}$) vs y^+ for medium-frequency oscillations . ○ LES [24], x MILES, --- DHRL, ▬ DHRL ETA, ▫ DHRL DTF, and ▬ SST MULTISCALE

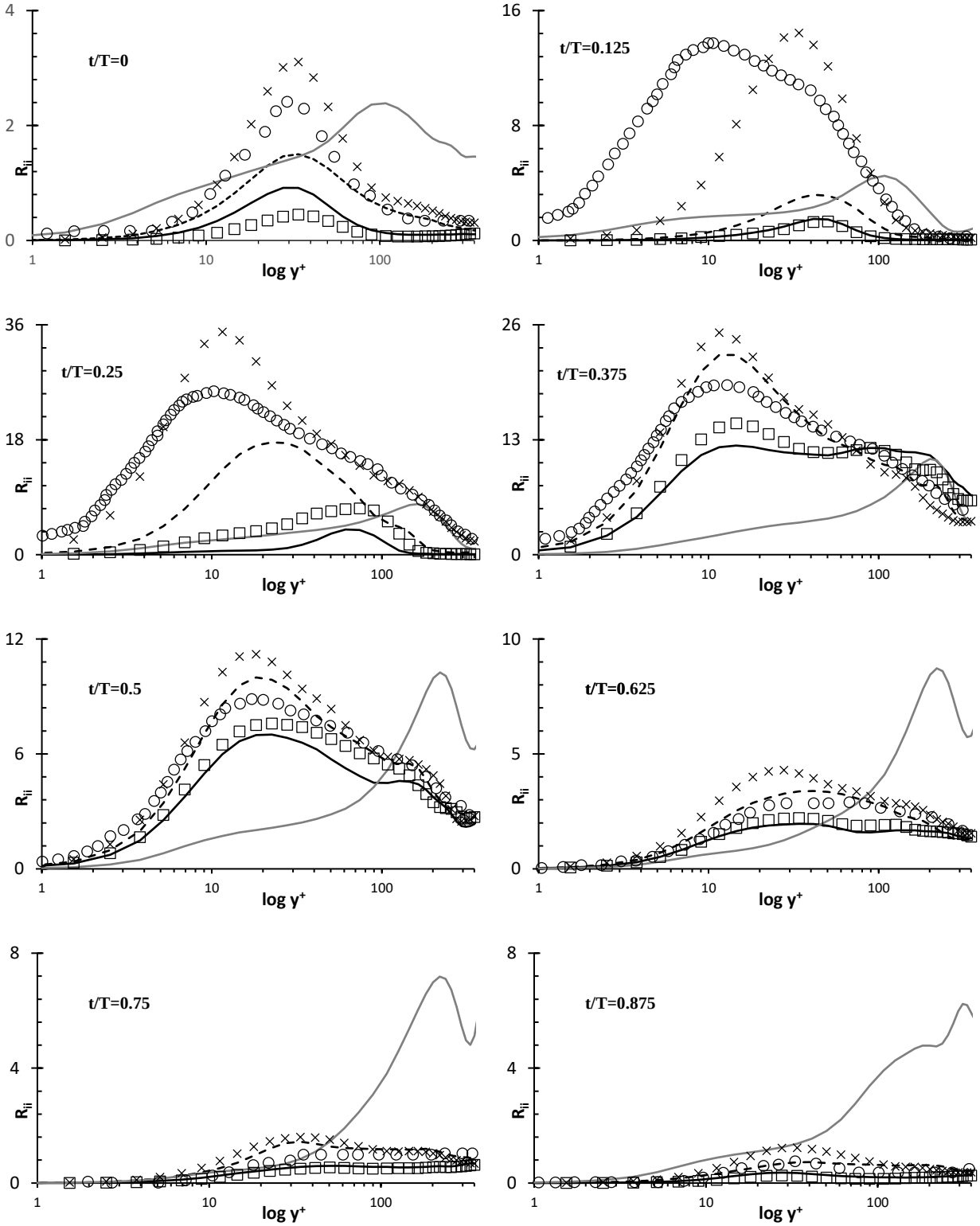

Figure 17. Plots of resolved ($\overline{u_i'u_i'}$) vs y^+ low-frequency oscillations. ○LES [24], ˣ MILES, -- - DHRL, ▬DHRL ETA, ▫ DHRL DTF, and ▬ SST MULTISCALE

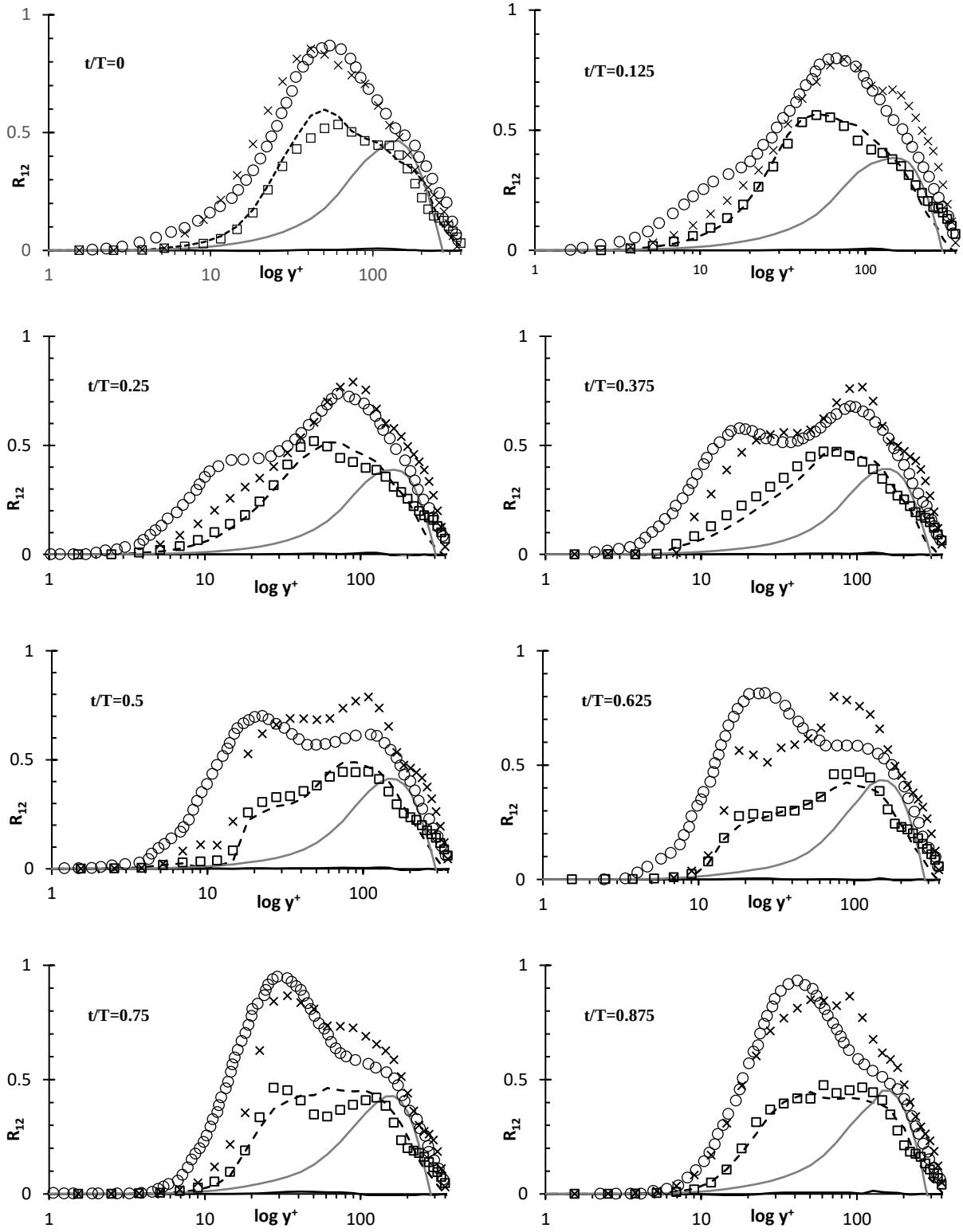

Figure 18. Plots of resolved ($\overline{u'v'}$) vs y^+ for high -frequency oscillations. ○LES [24], x MILES, --- DHRL, —DHRL ETA, □ DHRL DTF, and — SST MULTISCALE

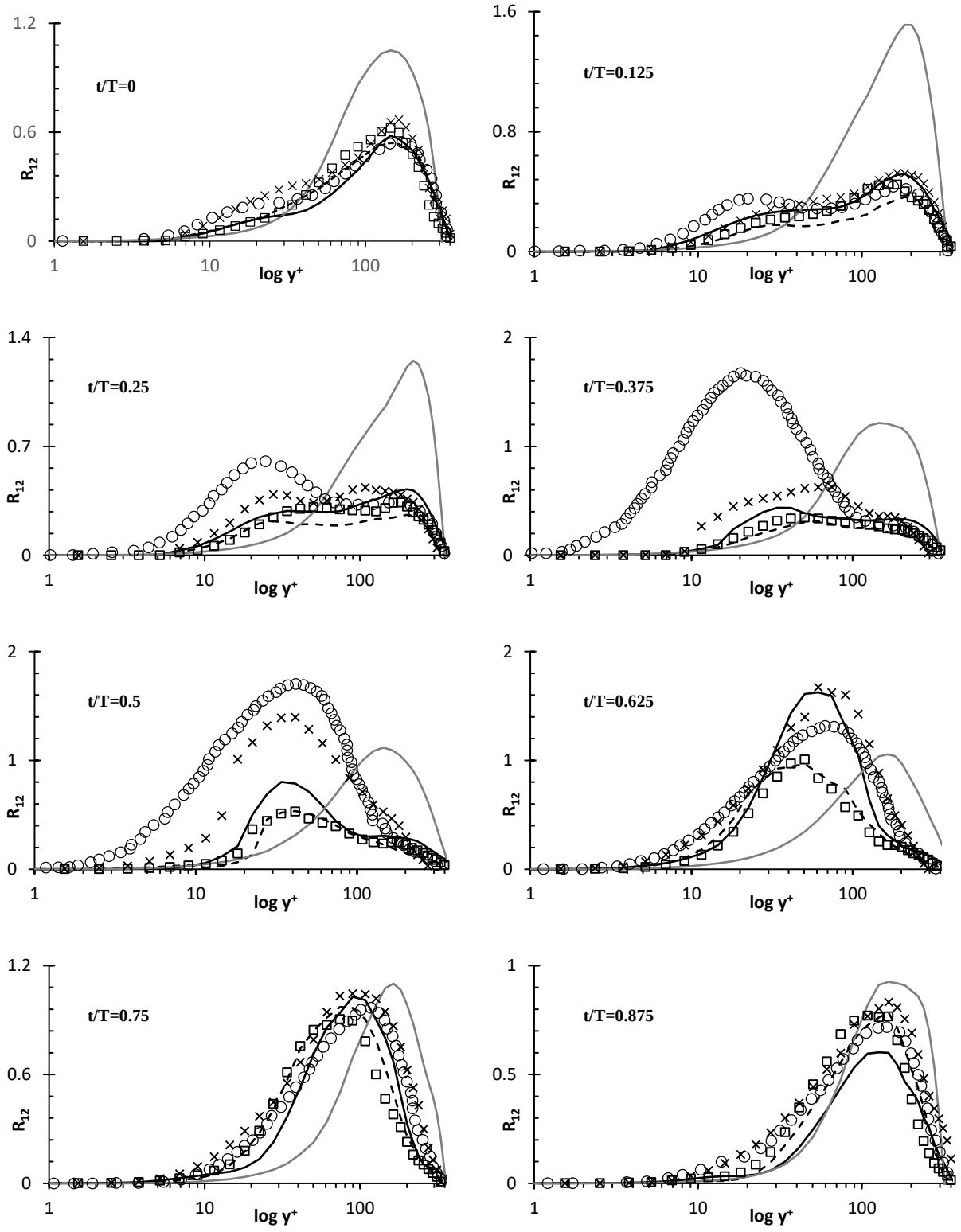

Figure 19. Plots of resolved ($\overline{u'v'}$) vs y^+ medium-frequency oscillations. ○LES [24], x MILES, --- DHRL, —DHRL ETA, □ DHRL DTF, and — SST MULTISCALE

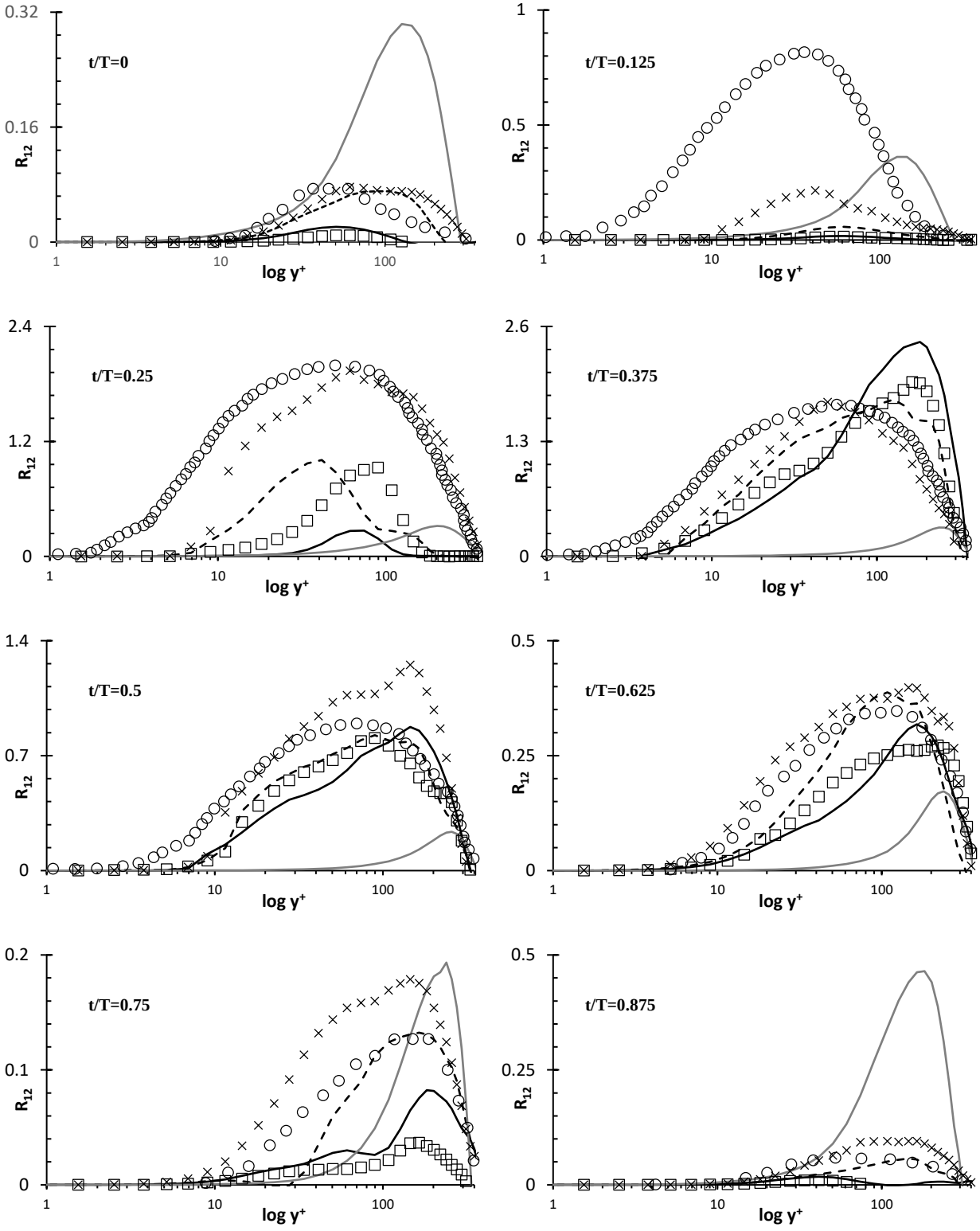

Figure 20. Plots of resolved ($\overline{u'v'}$) vs y^+ low-frequency oscillations. ○LES [24], × MILES, -- - DHRL, —DHRL ETA, ▫ DHRL DTF, and — SST MULTISCALE

5.4.2.8 Stream-wise Velocity Fluctuations

Figures 21 and 22 show contours of stream-wise velocity fluctuations for high and low-frequency oscillations at $y^+=10$. In [24], t/T=2/8 signifies zero contribution from the forcing function which is identical to t/T=0 used in this study.

For high-frequency oscillation, as the imposed forcing starts to accelerate the flow, large streaky structures can be observed. This behavior is consistent with energy transfer between *u* and *v* components. As the effect of forcing is reduced, these streaks slowly disappear and, in the deceleration phase the flow is fully turbulent. The DHRL model with DTF, baseline DHRL model, and MILES resolve velocity fluctuations with considerable accuracy. On the other hand, the DHRL model with ETA filters out most of the small-scale fluctuations but retains the overall features of the flow.

For low-frequency oscillations, the separation between the acceleration and deceleration phases is more apparent. At the beginning of the acceleration phase when forcing is small, the flow is nearly quiescent with streaks of fluctuations appearing in some parts of the flow. As the flow reaches maximum velocity and starts decelerating, these streaks transition to turbulence and the entire channel is filled with turbulent structures. Towards the end of the deceleration phase, the flow starts to gradually relaminarize and very little turbulent fluctuations can be observed during the beginning of the acceleration phase. All the DHRL variants and MILES predict the flow features with considerable accuracy. It is interesting to note that the DHRL DTF and ETA models have some observable phase lag towards the end of the acceleration phase. This can be attributed to the limitation of the exponential averaging technique in responding to changing trends. A potential solution to this issue would be to use double exponential averaging which can react to changing trends more accurately.

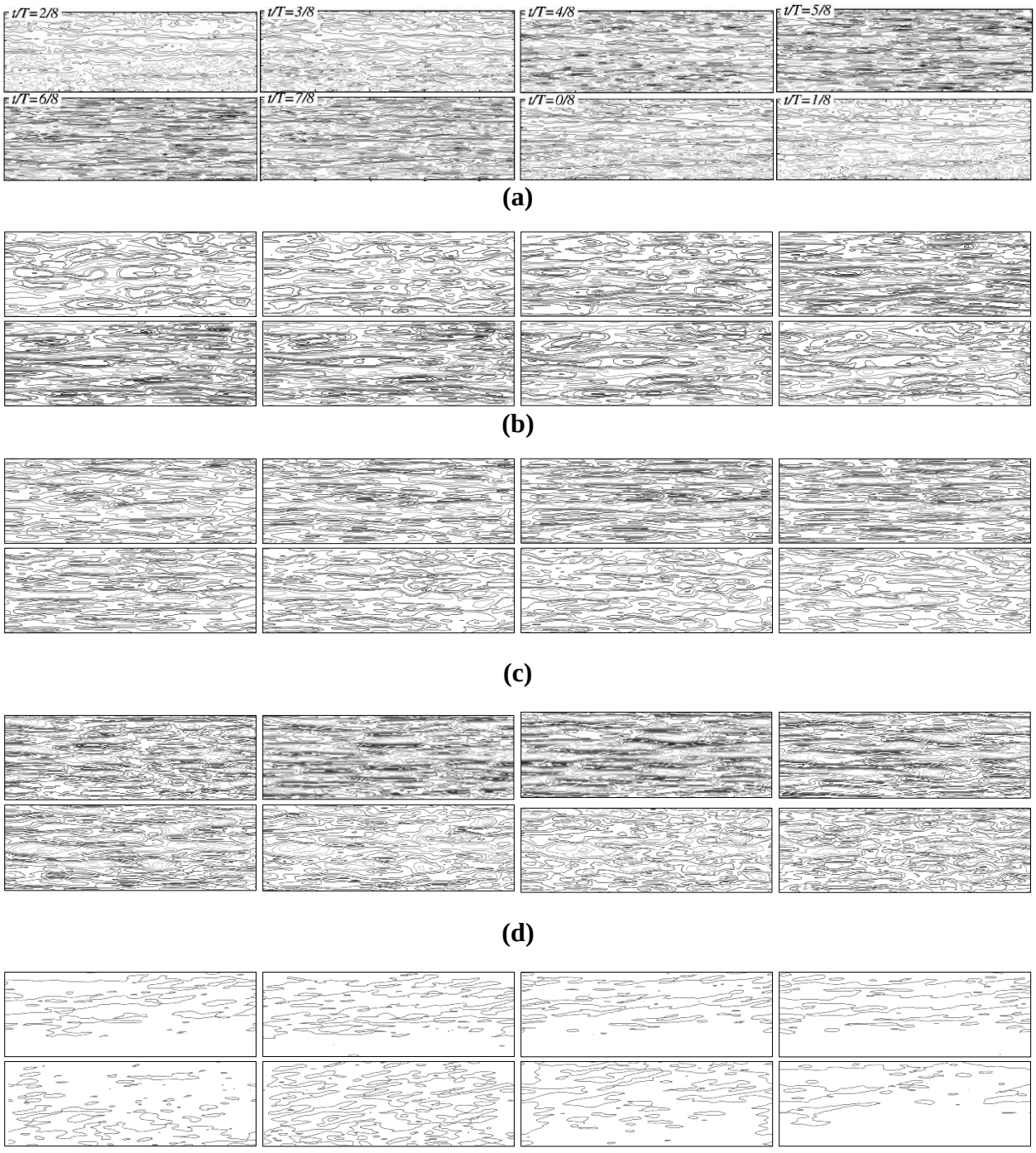

Figure 21. Contours of stream-wise velocity fluctuation at y+=10 for high-frequency oscillations at 8 equidistant times in one cycle. (a) Scotti et al. [24], (b) DHRL DTF, (c) DHRL Baseline, (d) MILES, and (e) DHRL ETA 2

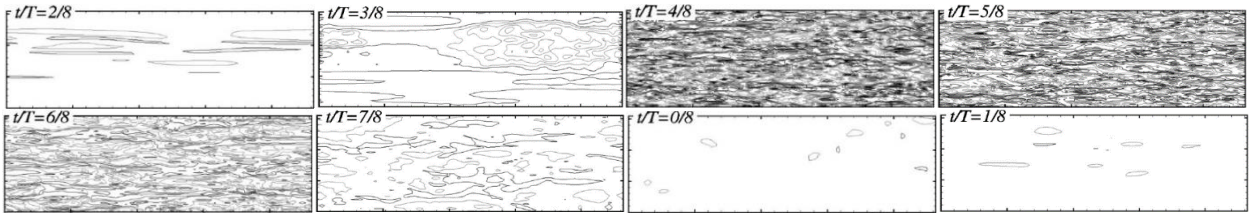

(a)

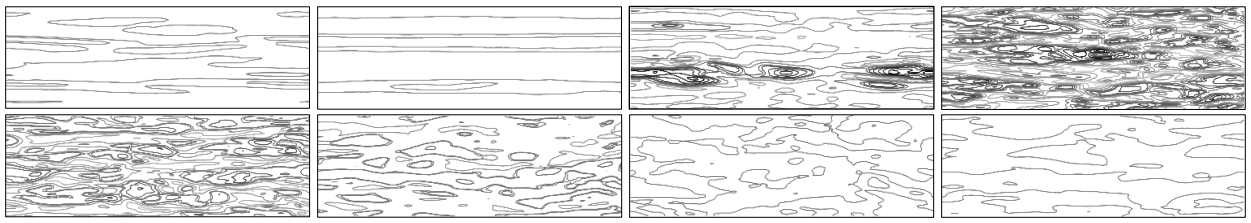

(b)

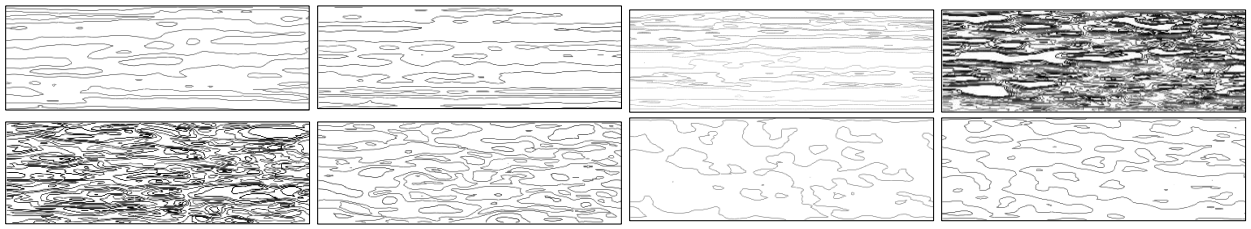

(c)

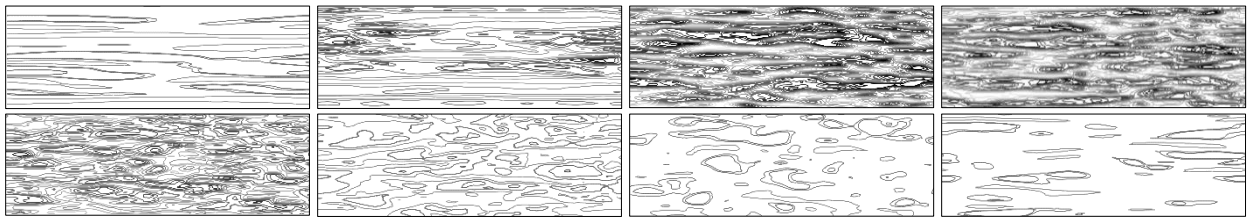

(d)

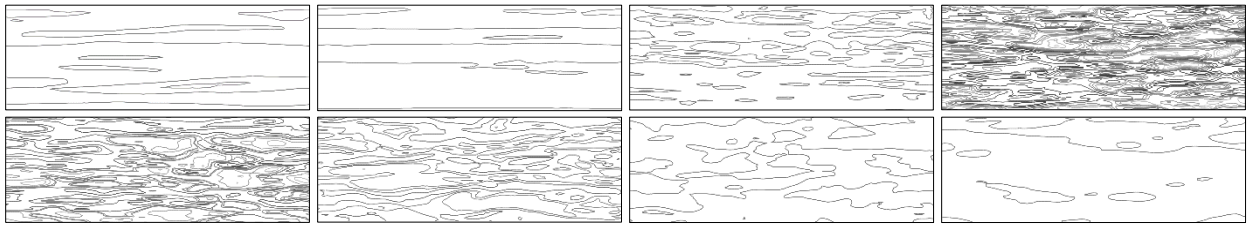

(e)

Figure 22. Contours of stream-wise velocity fluctuation at y+=10 for low-frequency oscillations at 8 equidistant times in one cycle. (a) Scotti et al. [24], (b) DHRL DTF, (c) DHRL Baseline, (d) MILES, and (e) DHRL ETA 2

5.4 CONCLUSIONS

This study investigates the performance of a Dynamic Hybrid RANS-LES (DHRL) model with two newly proposed time-filtering techniques: The Exponential Time Averaging (ETA) with static filter width and, the Dynamic Time-Filtering (DTF). Both techniques offer attractive solutions to solving non-stationary flows using the (DHRL) framework. Results for the DHRL-ETA and DHRL-DTF are compared against Large-Eddy Simulation (MILES), a fully turbulent RANS (SST k-ω) model, a conventional hybrid RANS-LES (SST Multiscale) model, the baseline DHRL model, and previously published Large Eddy Simulation (LES) and Direct Numerical Simulation (DNS) study performed by Scotti et al. [24] for a pulsating channel.

Results using the ETA with static filters highlighted some key improvements of the model when compared to baseline DHRL model and MILES. As the difference between the turbulent time-scales and forcing time-scales is increased, i.e. forcing frequency is reduced, smaller filter widths improve the DHRL ETA model performance compared to the baseline model and MILES. Since all three variants of the DHRL ETA model perform best for a particular forcing frequency, the choice of appropriate filter width is user-dependent and for flows with changing turbulent time-scale to forcing time-scale, the use ETA with static filters may not be ideal. To address this limitation of the DHRL-ETA and to derive appropriate filter widths from flow physics, the Dynamic Time Filtering (DTF) technique is proposed. As the name suggests, the DTF technique dynamically adjusts the filter width based on turbulent statistics to improve predictions. To better validate the DTF technique, numerical simulations for steady channel flow at $Re_\tau = 350$ and $Re_\tau = 590$ were also performed. The DHRL DTF model performance was almost identical to the baseline DHRL model performance showing that the model does not suffer from any detrimental effects when used in stationary flows. Results from Pulsating Channel flow highlighted some key

improvements for the DTF technique. Velocity plots indicated that the RANS model predicts near-wall behavior with considerable accuracy but shows velocity defects in the outer regions of the flow for some forcing frequencies. The DES and the HRL models effectively capture near-wall effects but underpredict velocity in the log-law region for high and medium frequency oscillations. For low forcing frequency, the DES adopts a RANS-like behavior, while the HRL model continues to show large velocity defects away from the wall. The DHRL model with DTF more consistently provides accurate results throughout the forcing frequency spectrum with minimal defects when compared to the LES [24] model data. Analysis of Reynolds Stress indicated some limitations of the DTF technique that will likely be improved by implementing a better RANS-LES blending parameter or using a more refined grid.

In conclusion, the ETA and DTF techniques appear to substantially improve the predictive capability of the DHRL model. In addition, the DTF method requires less user input and dynamically adjusts filter width based on local turbulent statistics. Further work is required to validate this method for other complex non-stationary flows in order to propose further improvements. Future work will include implementation of the DTF method in a new DHRL model variant with improved RANS to LES blending function and the incorporation of a potentially more accurate exponential averaging technique.

CHAPTER VI

NUMERICAL SIMULATION OF NON-STATIONARY TURBULENT FLOWS USING DOUBLE EXPOENTIAL DYNAMIC TIME FILTERING TECHNIQUE

6.1 INTRODUCTION AND OBJECTIVES

Non-stationary turbulent flows are often observed in nature and in industrial applications. Examples include maneuvering marine and aerospace vehicles as well as flow in engines during transient operation. These types of flows are generally accompanied by complex physics such as time-varying unsteadiness, interactions of various scales of motion, changing pressure gradients, vortex shedding, and flow transition. Because of their importance, these types of flows are of significant interest in Computational Fluid Dynamics (CFD) as a test for validating turbulence models and numerical methods. However, due to their complexity, these problems often require substantial computational resources and high-fidelity numerical methods to solve. The pulsating flow in a channel and the temporally evolving mixing layers are canonical examples of such problems, representing non-stationary wall-bounded and free shear flow, respectively.

Recently, RANS and hybrid RANS-LES studies of pulsating channel flow were carried out by Jamal and Walters [46,47] using static-exponential (ETA) and dynamic-exponential (DTF) time-filtering techniques to validate the performance of the dynamic Hybrid RANS-LES (DHRL) model. The approach relied on obtaining one-point statistics to improve the performance of the

blending parameter used in the DHRL model for non-stationary flows. Both the studies highlighted the improved performance of the DHRL model with the ETA and the DTF against traditional RANS and hybrid RANS-LES models throughout the frequency spectrum. The studies also highlighted the superior performance of the DTF technique over the already improved ETA in resolving the flow accurately. The authors concluded that appropriate selecting of filter widths is necessary to accurately resolve the pulsatile behavior of the flow. For high frequency oscillations, a larger filter width is suggested as it is more appropriate to treat the high frequency oscillations as a part of the fluctuating velocity since their timescales are close to the characteristic large-eddy time scale of the turbulence. As the frequency of the forcing is reduced, significant scale-separation between the turbulence and the imposed oscillations make it more ideal to reduce filter width in order to treat the imposed fluctuations as a time-dependent contribution to the mean velocity.

The main objective of this study is to propose a novel time-filtering technique for periodic and non-periodic statistically non-stationary flows within the dynamic hybrid RANS-LES (DHRL) framework. The new Double-exponential Dynamic Time Filtering (DDTF) technique is compared and validated against the baseline Dynamic Time Filtering (DTF) technique for flow in a pulsating channel and for a temporally-varying mixing layer. The performance of the DHRL model with the DDTF technique is validated against a RANS model (SST k-ω), the SST multiscale hybrid RANS-LES model, the DHRL model with DTF, and against previously published pseudo-spectral LES [24] and DNS [25] results. Results indicate that the DDTF technique shows an improvement over the DTF technique for the high-frequency pulsating channel case and the mixing layer. Some drawbacks are observed for medium and low frequency pulsations in the outer layer of the flow which can be attributed to under-resolved LES. Additionally, results from DNS are presented for flow in a pulsating channel case for high, medium, and low frequency oscillations. This effort adds

to the existing DNS study conducted by Scotti et al. [24] for high frequency oscillations and validates the performance of the studies performed in [46,47].

6.2 MODELING APPROACHES

Numerical simulations of pulsatile flow in a channel and temporally-varying mixing layer were performed for a single phase fluid using a pseudo-spectral solver and unsteady three-dimensional finite-volume Computational Fluid Dynamics (CFD). The following sections discuss the various modeling techniques and numerical methods used in this study.

6.2.1 Direct Numerical Simulation

The DNS studies in this research were performed using the parallel pseudo-spectral solver, *ParaSpectra* [49,50]. The solver discretizes incompressible Navier-Stokes equations using FFT along the homogenous streamwise and spanwise directions and Chebyshev polynomials in the wall normal direction. The solver is parallelized using a hybrid OpenMP/MPI approach to effectively utilize the distributed and shared memory across and within nodes of HPC systems. The solvers scale up to 16K processors on up to 1 billion grid points. The solver has been extensively validated for LES of channel, mixing layer and jet flows, and for DNS of channel flow at Ret =180 and 590.

6.2.2 Double-Exponential Dynamic Time Filtering (DDTF)

For any arbitrary time-dependent variable ϕ, the exponential time averaged value of the variable is given by,

$$\bar{\phi}(t) = \frac{1}{\Delta_f}\int_{-\infty}^{t} \exp\left(\frac{\tau - t}{\Delta_f}\right)\phi(\tau)d\tau \tag{66}$$

where $\bar{\phi}$ is the time-averaged filtered value obtained from a weighted average of all previous values of ϕ. An equivalent differential form for Eq.66 is given by,

$$\frac{d\bar{\phi}}{dt} = \frac{1}{\Delta_f}(\phi - \bar{\phi}) \tag{67}$$

where Δ_f is the filter width used to determine how quickly the weighting decays as time is integrated into the past. Using a first order backward difference approximation for the temporal derivative yields

$$\bar{\phi}(t) = \beta\phi(t) + (1-\beta)\bar{\phi}(t-\Delta t) \tag{68}$$

which alternatively can be written as,

$$\bar{\phi}(t) = \bar{\phi}(t-\Delta t) + \beta(\phi(t) - (t-\Delta t)) \tag{69}$$

where $\phi(t)$ is the value of the variable at time *t*, $\bar{\phi}(t-\Delta t)$ is the exponential average at previous time-step, and β is a smoothing factor that controls the rate at which data enters the calculation.

Although the performance of the DTF was significantly improved over the static ETA, evidence of temporal lag was observed in the outer layers of the mean flow. In the DTF implementation, the filter width is dependent on flow statistics. Analogous to a feedback loop, when the flow statistics change, the filter width changes in response. The effect of this can been seen in the AC component analysis in [46,47] where the model significantly overpredicts velocities in the log to outer layer transition region. Since moving and exponential average are backward-looking indicators, the double exponential moving average was developed by Patrick Mulloy [51] in 1994 in an attempt to mitigate some of the lag associated with traditional averaging methods. The double exponential average of a variable ϕ is defined as,

$$\breve{\phi}(t) = 2\bar{\phi}(t) - \bar{\bar{\phi}}(t) \tag{70}$$

where $\breve{\phi}$ is the double exponentially averaged variable, $\bar{\phi}$ is the exponentially averaged variable, and $\bar{\bar{\phi}}$ is the exponential average of the exponentially-averaged variable. For additional details, readers are referred to [51].

6.3 SOLVER & DATA ANALYSIS

DNS calculations of pulsating channel flow were carried out using the pseudo-spectral solver *ParaSpectr*a, while density-based finite-volume simulations were carried out using Loci-CHEM [39,40]. Loci-CHEM uses high-resolution approximate Riemann solvers and implicit numerical methods. For the present study, all simulations were run with a Mach number close to 0.1 based on average streamwise velocity to simulate incompressible flow conditions. Postprocessing was carried out using Tecplot and ParaView.

For statistically non-stationary flows, neither infinite-time-averaging nor exponential averaging is exactly equal to a true ensemble average. Hence, for the present study, instantaneous variables are planar averaged along statistically homogeneous directions during post processing:

$$\langle f \rangle(y,t) = \frac{1}{L_x L_z} \int_0^{L_z} \int_0^{L_x} f(x,y,z,t)\, dx\, dz \tag{71}$$

where $\langle f \rangle$ is the planar averaged value of any arbitrary flow variable f, x and z are the streamwise and spanwise coordinate directions respectively, and y is the wall-normal direction. Alternatively, phase averaging used by Scotti et al. [24] is equivalent to an ensemble average for non-stationary flows.

6.4 PULSATING CHANNEL FLOW

Simulation setup and results from fully developed and pulsating channel flow are discussed in this section.

6.4.1 Direct Numerical Simulation setup

Direct Numerical Simulations (DNS) for flow in a pulsating channel was performed using the pseudo-spectral solver *ParaSpectra* [49,50]. Initially, simulations for a steady channel flow at Re_τ = 350 were run until a stable converged solution was obtained, then the time-dependent pressure gradient term was added to simulate the pulsatile nature of the flow. Table 1 shows some of the parameter used by Scotti et al. [24] and the present study.

Table 1. Flow parameters

Flow Parameters	**Scotti et al. (2001) [24]**			**Present Study**		
	Frequency					
	High	**Medium**	**Low**	**High**	**Med.**	**Low**
$Re_{\tau,0}$	350			350		
Domain size	3πh×2h×πh			3πh×2h×πh		
Grid	128×129×192			192×129×192		
u_τ	-			0.048276		
ν	-			1.38×10^{-4}		
ρ	-			1		
α	200	50	8	200	50	8
Forcing	$\frac{dP}{dx} = \frac{dP_0}{dx}[1 + \alpha\cos(\omega t)]$					
ω^+	0.04	0.01	0.0016	0.04	0.01	0.0016
Re_s	100	200	500	100	200	500

Variables for each forcing frequency were obtained using the following relationships given by Eqs. (30-32):

$$Re_\tau = \frac{u_\tau \delta}{\nu} \tag{72}$$

$$Re_s = U_0\sqrt{\frac{2}{\omega\nu}} \tag{73}$$

$$\omega^+ = \frac{\omega\nu}{{u_\tau}^2} \tag{74}$$

where, Re_τ is the Reynolds number based on mean friction velocity, Re_s is the Reynolds number based on Stokes length, and ω^+ is the forcing frequency expressed in wall units.

6.5 RESULTS AND DISCUSSION

In this section simulation results from DNS and DHRL-DDTF are validated against the numerical study performed by Scotti et al. [24].

6.5.1 Direct Numerical Simulation Validation

DNS results were validated first for the alternating (AC) and mean (DC) components of the mean flow. Figure 1 shows the variation of AC and DC components of the normalized velocity (u^+) against dimensionless wall distance (y^+) for high, medium, and low frequency-imposed oscillations. These components were obtained via a decomposition of the normalized-planar-averaged velocity at eight equidistant times in one cycle by applying Fast Fourier Transform at each wall normal location.

For the DC component in high-frequency oscillations, the *ParaSpectra* results are in close agreement with the LES and DNS study performed by Scotti et al. [24]. Some disagreement can be observed in the outer layer where the *ParaSpectra* results underpredict velocity when compared to the previous LES and DNS results. Comparison of medium-frequency and low-frequency performance between the pseudo-spectral LES and the DNS results from *ParaSpectra*. Although DNS data from Scotti et al. [24] is not available for the medium and low-frequency cases, the behavior of *ParaSpectra* is identical to the DNS simulation behavior. Both the previously validated

LES model and *ParaSpectra* DNS are in close agreement for the majority of the inner layer, while some differences appear in the buffer-log layer transition and which carries into the outer layer. It can be concluded that the DNS data presented in this study is in good agreement with DNS and the LES performed by Scotti el al.

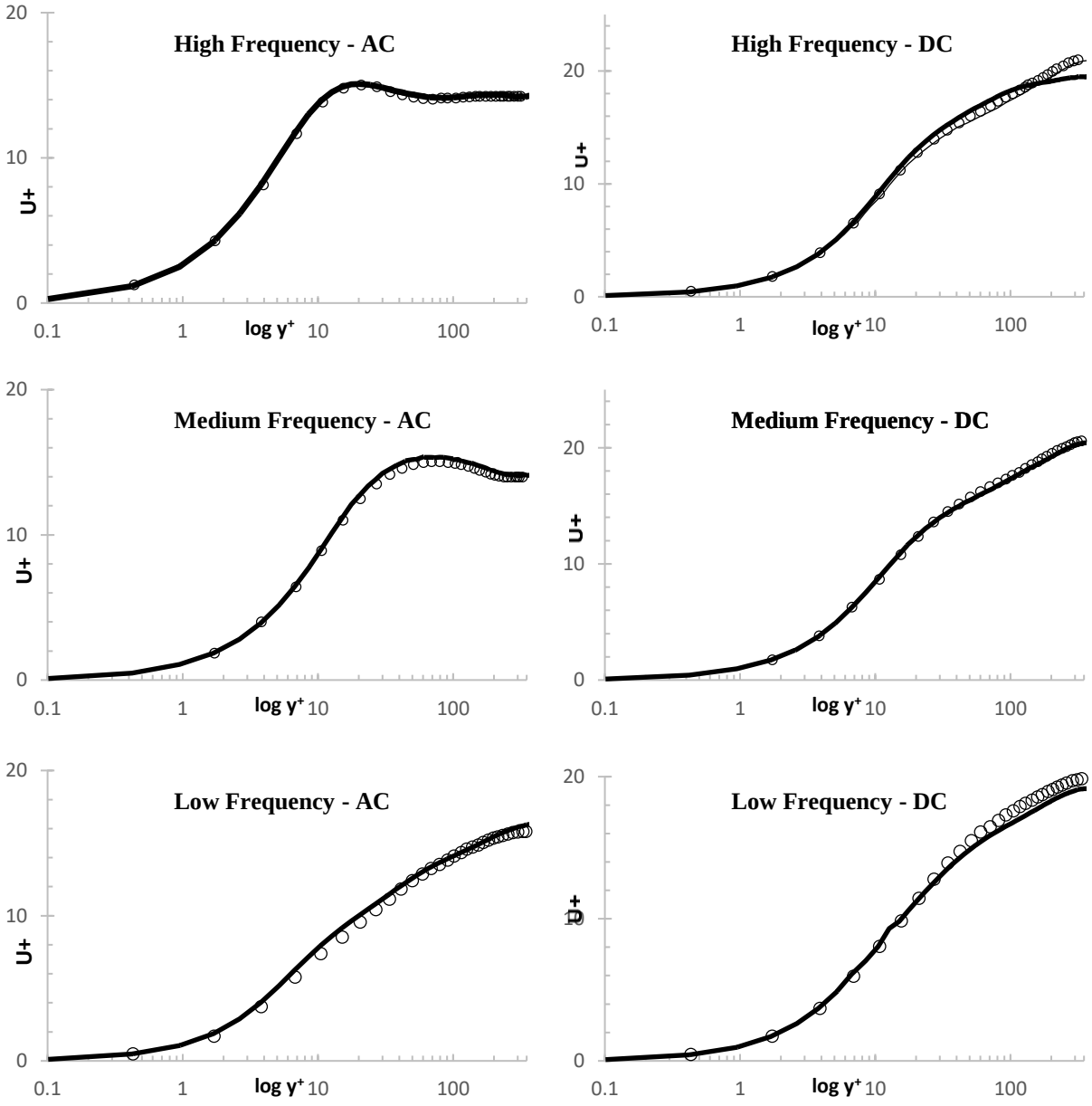

Figure 1. AC & DC component of streamwise velocity; ── DNS Scotti et al. [24] (only high-frequency), ○LES Scotti et al. [4], ▪▪▪ DNS *ParaSpectra*

6.5.2 Double Dynamic Filtering Validation (DDTF)

This section presents validation of the performance of the DHRL model with the Double Dynamic Time Filtering (DDTF) technique. Results presented below are compared against DNS and LES data from [24]; SST *k*-ω, SST multiscale, and DHRL DTF data from [47].

6.5.3 Steady Channel Flow

Figure 2 shows the distribution of normalized-friction-velocity (u^+) against dimensionless wall distance (y^+) for a steady channel flow at $Re_\tau = 350$. Similar to the approach taken in [47], the DHRL DDTF was first validated for a statistically stationary case in order to observe any detrimental effects arising from its use. Results indicate that all the models compared in this study are in close agreement with LES data [24] in the viscous sub-layer. Halfway through the buffer layer, the SST multiscale modle transitions to LES and underpredicts velocity in the log-layer. Since the closely packed cells in the boundary layer region grow to larger aspect ratio cells in the buffer layer, the SST multiscale model incorrectly transitions to LES due to modeled stress depletion. Throughout the majority of the log-layer, all the models are in fair agreement with each other and with the log-law. The SST *k*-ω model underpredicts velocity near the center of the channel, this behavior is commonly observed for RANS models. Interestingly, both the DHRL model variants also follow this trend. Although there is enough resolved fluctuations to support LES mode in this region, the modeled RANS stresses are relatively high. So, the DHRL models remains in a RANS biased state and underpredicts mean velocity.

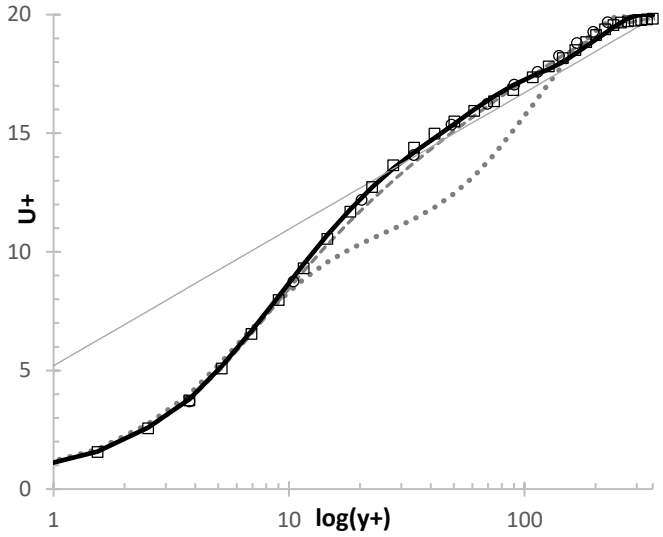

Figure 2. U^+ vs log (Y^+) for steady channel flow at Re_τ=350; — log-law, ○ Scotti et al. [24], □ DHRL DTF, – – – SST *k-ω*, • • • SST Multiscale Model, and ▪ ▪ ▪ DHRL DDTF

6.5.4 Pulsating Channel Flow

In [47], the DTF was presented as a potential solution for using the DHRL model to solve statistically non-stationary flow problems. Since the selection of a relevant time scale for different problems may be difficult, the DTF technique approximated the filter width to be proportional to the large-eddy time-scale. This also alleviated issues that stemmed from using a temporally static filter in [46]. Although the DTF was a significant improvement in terms of performance and user-independence, lag due to exponential averaging persisted during parts of pulsation cycle. Since a faster response to the filter width is desired, the double dynamic filtering is presented as a potential solution.

6.5.4.1 AC-DC Mean Velocity Components

AC and DC mean velocity components are compared for all the model results in this study to [24,47]. Figure 3 shows the variation of normalized-friction-velocity (u^+) against dimensionless wall distance (y^+) for the three pulsating frequencies investigated.

For the high frequency oscillations, all the models are in good agreement with LES [24] for the AC component, however large differences appear in the DC component of the flow. Although the behavior in the viscous sub-layer is identical for all models, differences between the models can be observed in the buffer layer. The SST multiscale model transitions to LES early as was the case for the steady channel flow at $Re_\tau = 350$ shown in Fig. 2. The DHRL DDTF outperforms the DHRL DTF throughout the length of the channel. The DDTF reacts quicker to changes in the velocity gradient and is in close agreement with LES.

For medium frequency oscillations. Significant deviations from the LES and *ParaSpectra* DNS is observed for the AC component, in the viscous sub-layer, buffer, and in the log-layer. The SST multiscale model once again transitions to LES early and underpredicts velocity. The SST k-ω model slightly overpredicts velocity in the buffer layer, then underpredicts velocity in the log layer, before finally recovering the correct velocity in the outer layer. The DDTF is an improvement over the DTF in the buffer layer with both model tracking each other closely in the log and outer layers of the flow.

For low-frequency oscillations, significant defects for the DTF and DDTF model are observed in both AC and DC components. For the majority of the channel, the DDTF is an improvement over the DTF. However, the DDTF severely underpredicts velocity in the outer-layer for the DC component similar to the SST k-ω behavior in Fig. 2.

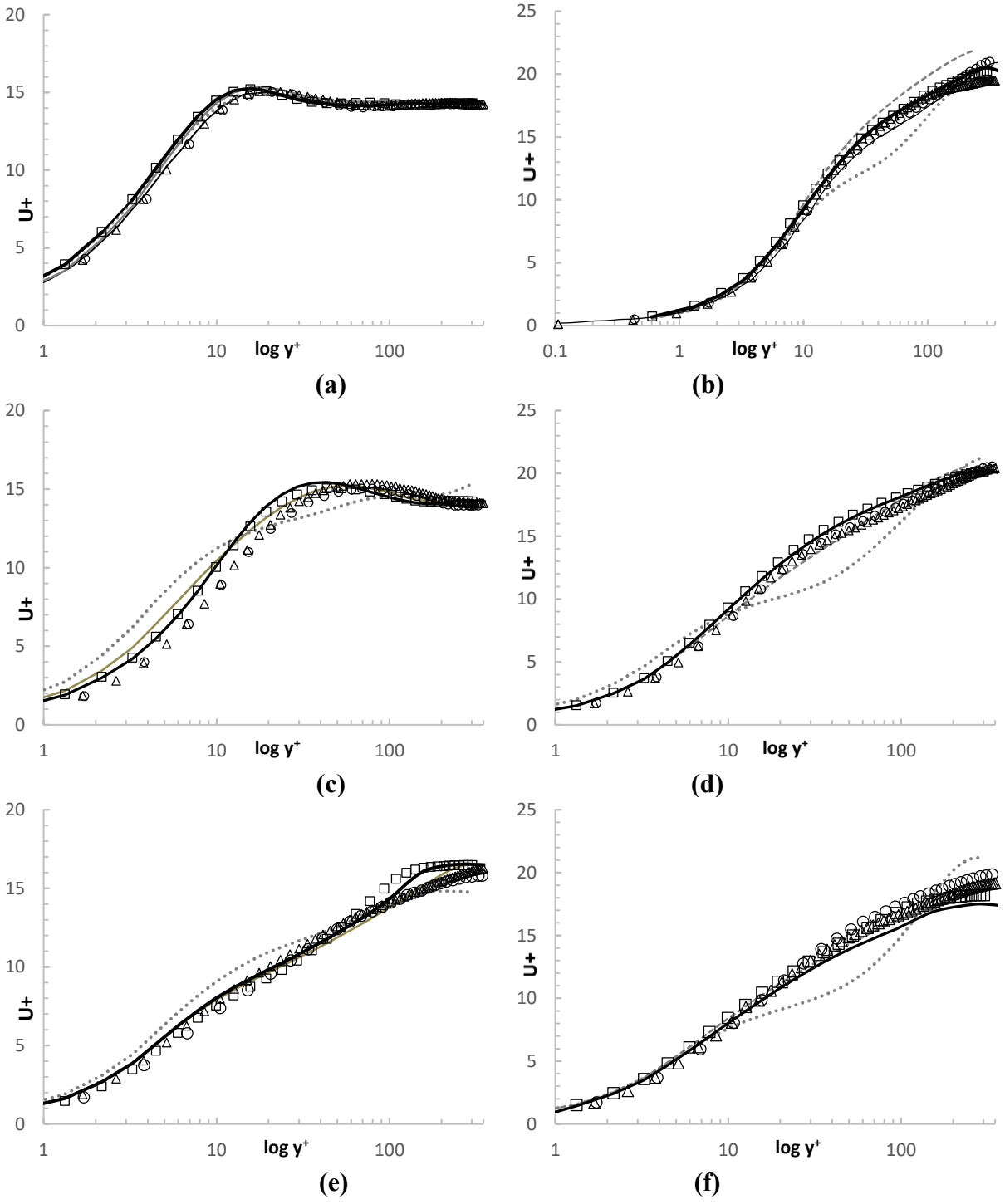

Figure 3. AC & DC component of streamwise velocity (a) High Frequency AC, (b) High Frequency DC, (c) Medium Frequency AC, (d) Medium Frequency DC, (e) Low Frequency AC, (f) Low Frequency DC, ── DNS Scotti et al. [24], ○ Scotti et al. [24]; ▫ DHRL DTF, ▬ ▬ ▬ SST *k-ω*, ▪ ▪ ▪ SST Multiscale Model, △ DNS *ParaSpectra* , ▪▪▪ DHRL DDTF

6.5.4.2 Time-Varying Mean Velocity

Figures 4, 5, and 6 compare the normalized-friction-velocity (u^+) against dimensionless wall distance (y^+) at equidistant phases during each pulsation cycle and results are compared against previously available DNS and LES [24], and *ParaSpectra* DNS performed in this study. In the figures, t=0 signifies $\frac{dP(t)}{dx} = 0$, and the start of the forcing. To be consistent with the description in [24], (g) in each cycle marks the beginning of the acceleration phase, and (c) marks the beginning of the deceleration phase.

One of the ever-present characteristics of the pulsating channel flow is the upward and downward modulation of the log-layer. The log-layer is markedly distinct for the high frequency oscillations and disappears during significant parts of the medium and low-frequency cycles. As mentioned in [47], this modulation of the log-layer adversely affects traditional HRL models. There is also some outer layer defect observed for the DHRL models for the lower frequency oscillations. For high frequency oscillations, all the models are in close agreement with LES and DNS data except the SST multiscale hybrid RANS-LES model. The model transitions to LES in the log and underpredicts velocity before recovering it in the outer layer. The presence of a distinct log-layer can be observed throughout the entire pulsation cycle.

It is during the medium frequency oscillations that the effects of forcing become more apparent. The log-layer disappears during parts of the deceleration phase before reappearing in the acceleration phase. Once again, the SST multiscale model transitions to LES early and underpredicts velocity. At the start of the deceleration phase, the model overpredicts velocity in the buffer layer before grossly underpredicting velocity at the start of the acceleration phase. The other models show increased defects for the majority of the cycle, especially in the buffer layer.

The SST *k-ω*, the DHRL DTF and the DHRL DDTF models overpredict velocity in the buffer layer before providing improved predictions in the log-layer. The DDTF can observed to react to the changes in log-layer profile better, however during parts of the deceleration phase, peaks in velocity are observed for both the DHRL variants.

Past studies [46,47] highlighted the difficulties associated with the accurate prediction of flow behavior for the low-frequency forced oscillations. Both, the SST *k-ω* and the SST multiscale models perform poorly in the buffer layer during the acceleration phase. The DHRL model variants are in best agreement with LES [24] and DNS data except for an abnormal increase in velocity at the start of the deceleration phase. The DHRL DDTF damps out the spike effectively however, the model is prone to underpredicting velocity in the outer layer

Overall, the results for figures 8, 9, and 10 indicate some of the improvements of the DDTF formulation. The DHRL model with DDTF provides an improved response to changes in velocity throughout the frequency spectrum. For the high frequency case, the DDTF model improves the existing DHRL DTF performance by predicting more accurate flow physics. However, less significant improvement is observed for the medium and low frequency oscillations. Although the DDTF technique is an overall improvement over the DTF technique, velocity defects in the outer layer underscores some of the gains in performance. Future publications will address this issue using a more robust blending parameter that enables the model to remain in LES mode and provide improved prediction of flow physics.

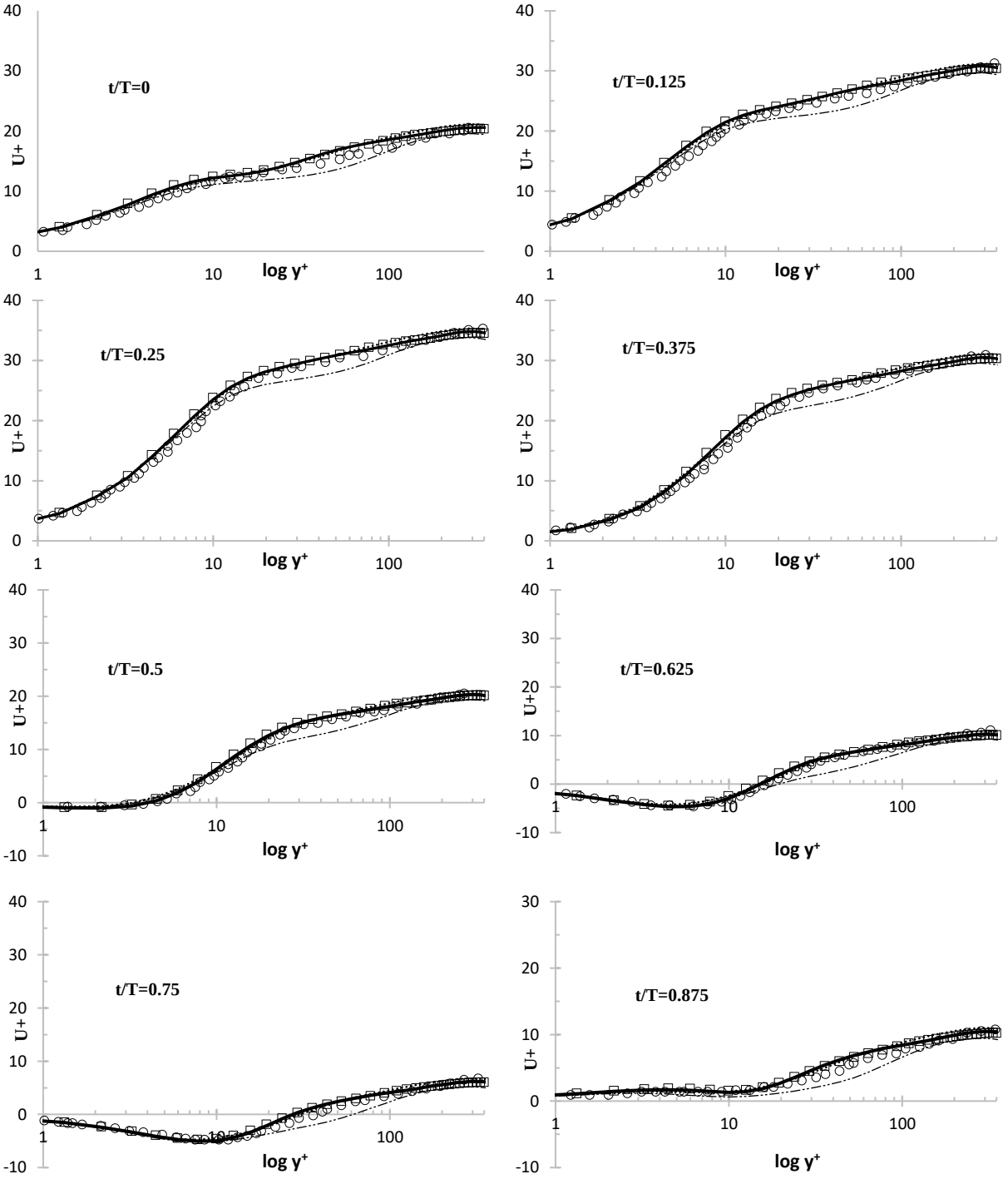

Figure 4. U^+ vs log (Y^+) for high-frequency case. ○ Scotti et al. [24]; ── DHRL, ▫ DHRL DTF,+DHRL ETA , ••• SST *k-ω*, ▪▪▪ DHRL DDTF, and ─··─ SST Multiscale Model

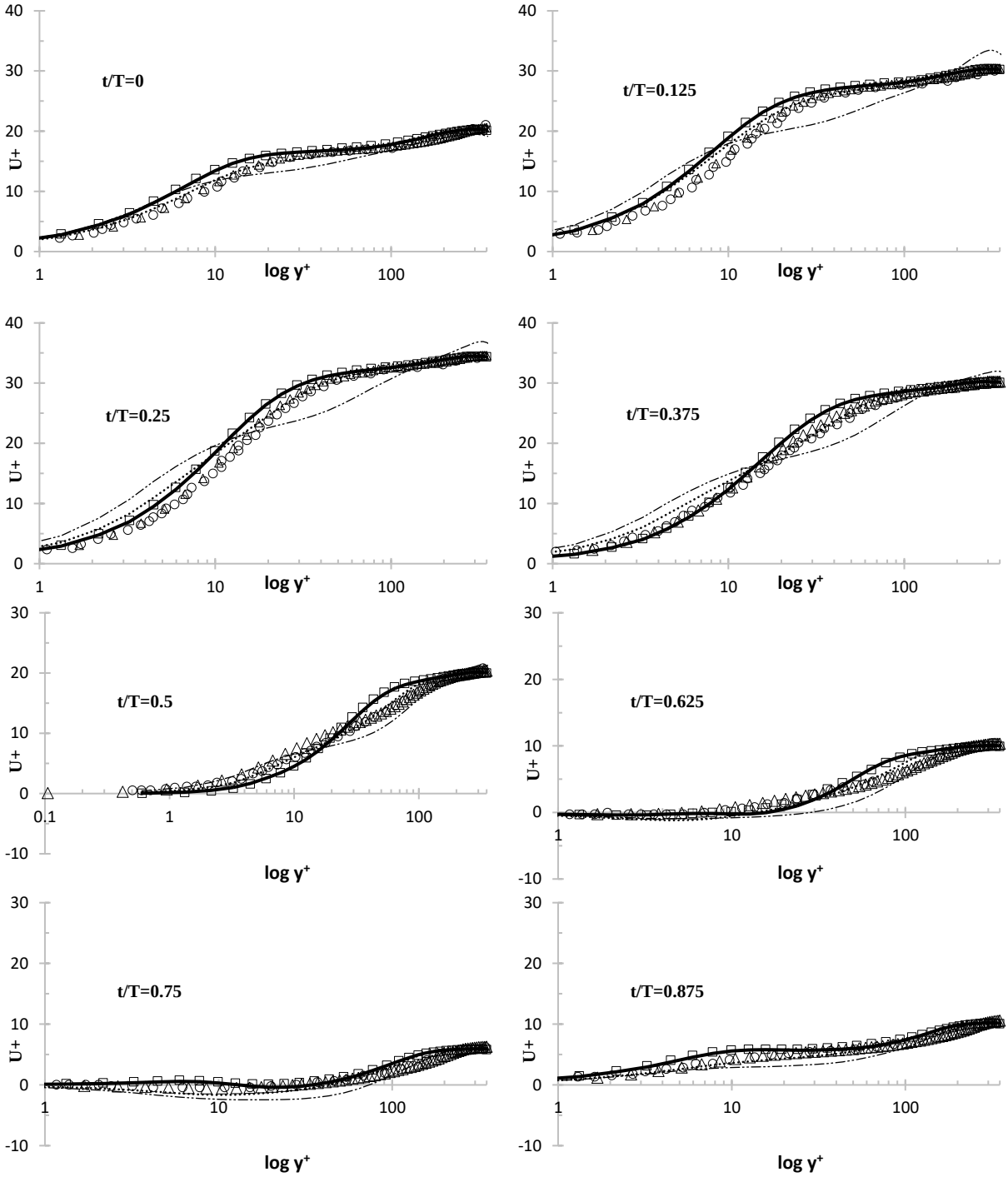

Figure 5. U^+ vs log (Y^+) for medium-frequency case. ○ Scotti et al. [24]; ── DHRL, ▫ DHRL DTF,+ DHRL ETA , ••• SST *k-ω*, △ DNS *ParaSpectra*, ▪▪▪ DHRL DDTF, and ─··─ SST Multiscale Model

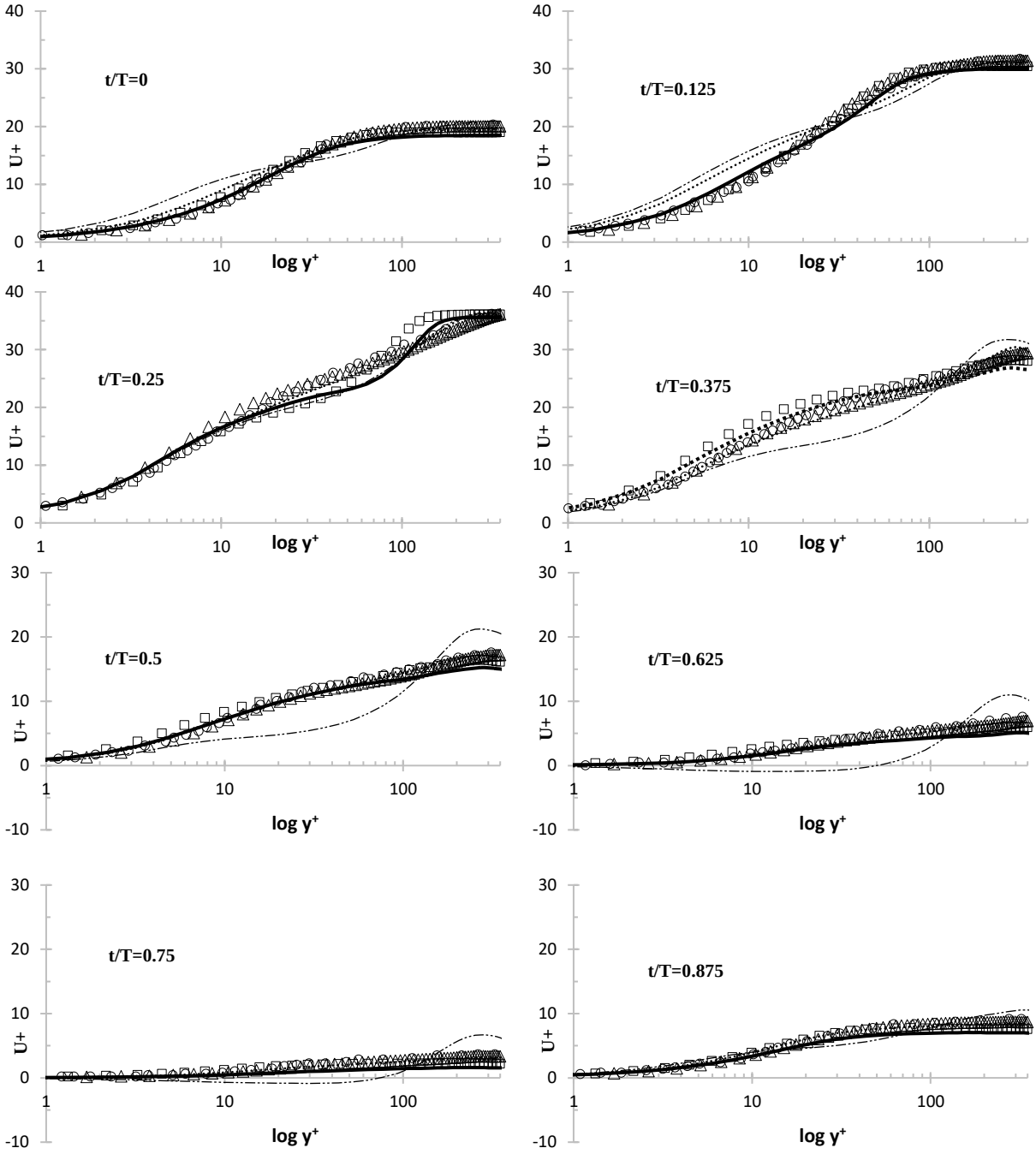

Figure 6. U^+ vs log (Y^+) for low-frequency case. ○ Scotti et al. [24]; ── DHRL, ▫ DHRL DTF, + DHRL ETA, ••• SST *k-ω*, ▵ DNS *ParaSpectra*, ▪▪▪ DHRL DDTF, and ─··─ SST Multiscale Model

6.6 TURBULENT MIXING LAYER

The temporally evolving, planar, turbulent mixing layer is simulated for an initial Reynolds number of Re_{δ_i}=220 defined by the following equation:

$$Re_{\delta_i} = \frac{\Delta U_0 \delta_i}{\nu} = 220 \tag{75}$$

where, δ_i is the initial vorticity thickness, ΔU_0 is the velocity difference between the two streams, and ν is the kinematic viscosity.

6.6.1 Computational Domain and Grid Generation

Figure 7 shows the computational domain used in the present study. Detailed domain dimensions are provided in the DNS study [25] which allowed the development of three-dimensional eigenmodes to initiate instabilities that would assist the flow transition to turbulence. Cells were grown outward from the channel centerline by resolving the initial vorticity thickness, δ_i with 10 cells with a growth ratio of 1.4. The streamwise and spanwise boundaries were specified as periodic boundaries while the vertical boundaries were specified with a symmetry boundary condition. For further details about the recommended domain size, readers are referred to [25].

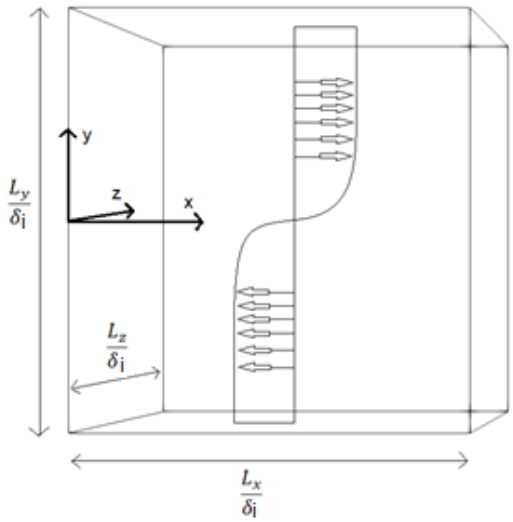

Figure 7. Computational domain

Table 2. Grid resolution comparison

Study	Grid Resolution
DNS [25]	512 x 256 x 257
Present Study	128 x 86 x 64

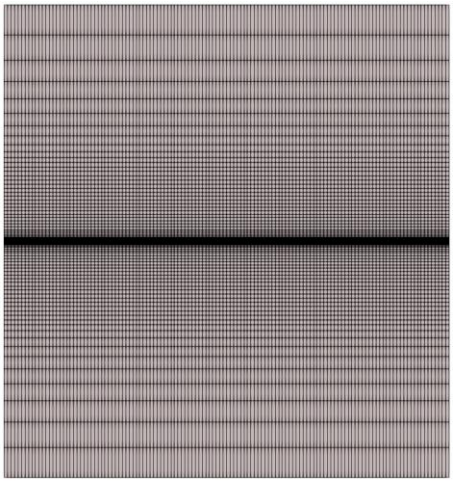

Figure 8. Computational mesh distribution

6.6.2 Problem Setup

Flow was initialized using the profile given by Eq. (34), where $U_1(y)$ is the initial profile, U_0 is the initial freestream velocity, and δ_i is the initial vorticity thickness of each layer. Additionally, an infinitesimal, divergence-free perturbation was included with the velocity profile to mimic experimental noise. Figure 13 compares the initial velocity profiles used in the present study against DNS [25].

$$\frac{U_1(y)}{U_0} = tanh\left[\left(\frac{y}{\delta_i}\right)\right] \tag{76}$$

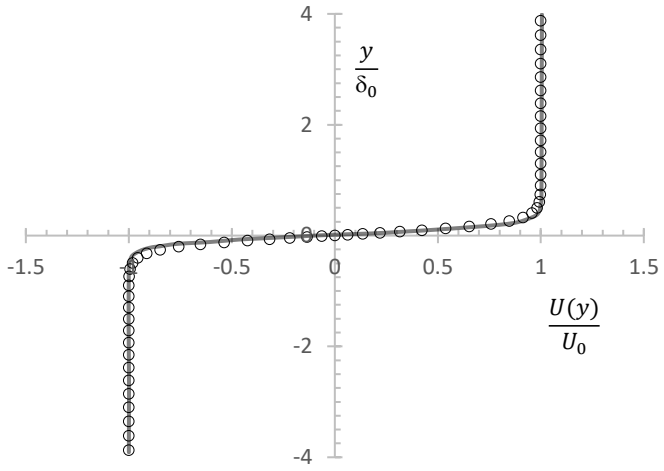

Figure 9. Initial velocity profile comparison — DNS Ansari [8] ○ DHRL DDTF

6.6.3 Results and Discussion

In this section DHRL-DDTF results are validated against the MILES and DNS study performed by Ansari [25]. Similar to the pulsating channel case, mean-statistics were obtained using planar-averaging of instantaneous data.

6.6.3.1 Flow and turbulence statistics at t'=400

Figure 10 compares the predicted distribution of mean-velocity, fluctuating velocity, and Reynolds shear stress at t'=400 in terms of initial momentum thickness, δ_m [52]. Also included for comparison are DNS results from Rogers et al. [52] and experimental data from Bell et al. [53]. Overall, the DHRL-DDTF model captures the complex flow features with considerable accuracy for all the statistics investigated in this section, however some deviation for DNS data can be observed the normal velocity fluctuation.

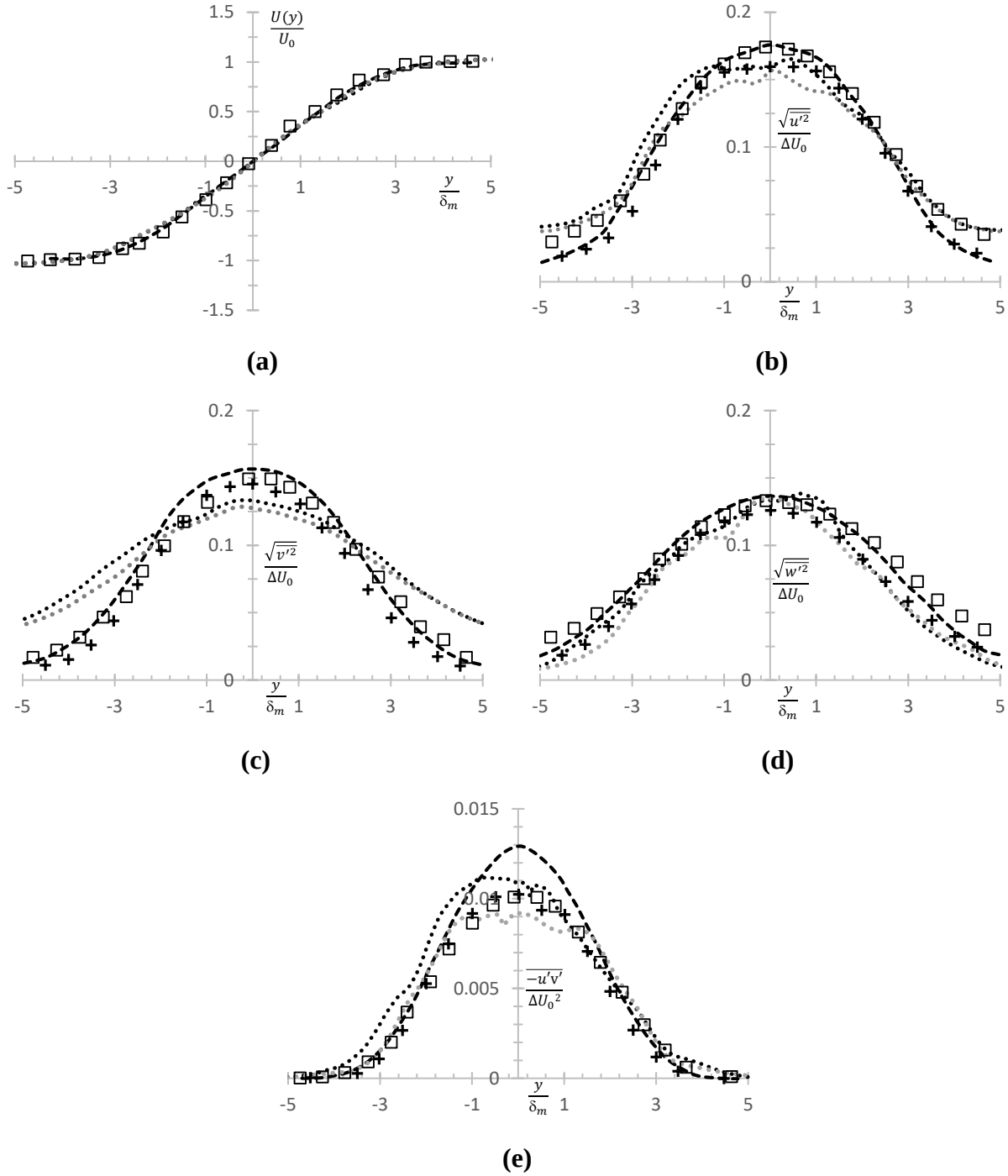

Figure 10. Profiles of (a) Mean-velocity, (b) $\overline{u'}$, (c) $\overline{v'}$, (d) $\overline{w'}$, and (e) Reynolds shear stress - $\overline{u'v'}$; ▬ ▬ DNS, Ansari [25], + DNS Rogers and Moser [52], ▫ DNS Bell and Mehta [53], • • • MILES, and ⋯ DHRL DDTF

6.6.3.2 Temporal evolution and turbulence statistics

Figure 11 shows the temporal evolution of the flow in terms of mean velocity fluctuations and Reynolds shear stress as a function of non-dimensional time given by Eq. (77):

$$t' = \frac{t\Delta U_0}{\delta_i} \tag{77}$$

where t is physical time, ΔU_0 is the velocity difference between the two streams, and δ_i is the initial vorticity thickness.

It is clear that the DHRL-DDTF model and MILES undergoes a slightly more rapid transition to turbulence initially when compared to the DNS. Peak values of streamwise and normal rms velocity fluctuations occur between $225<t'<275$ for both, DNS and simulations. Some differences in the prediction of self-similarity regions can also be observed. The DNS data shows self-similar behavior for $t'>300$, while the simulations exhibit self-similar behavior around $t'=250$. Both DNS and the MILES and DHRL-DDTF simulations show a decline in centerline values for $t'>350$ suggesting that the largest eddies are no longer uncorrelated with themselves [8]. Both DHRL-DDTF and MILES exhibit similar behavior with some differences appearing in the prediction of Reynolds shear stress, where the DHRL-DDTF model shows slightly better agreement with DNS. Overall predictions are in qualitative agreement with DNS data and further fine-tuning of the initial perturbation would likely help replicate the initial laminar to turbulence transition more appropriately. It has been observed by [52] that the initial perturbation dictates the evolution of the flow. Hence, optimization of the initial disturbance would possibly yield more accurate data and help validate the performance of the DHRL-DDTF model more accurately.

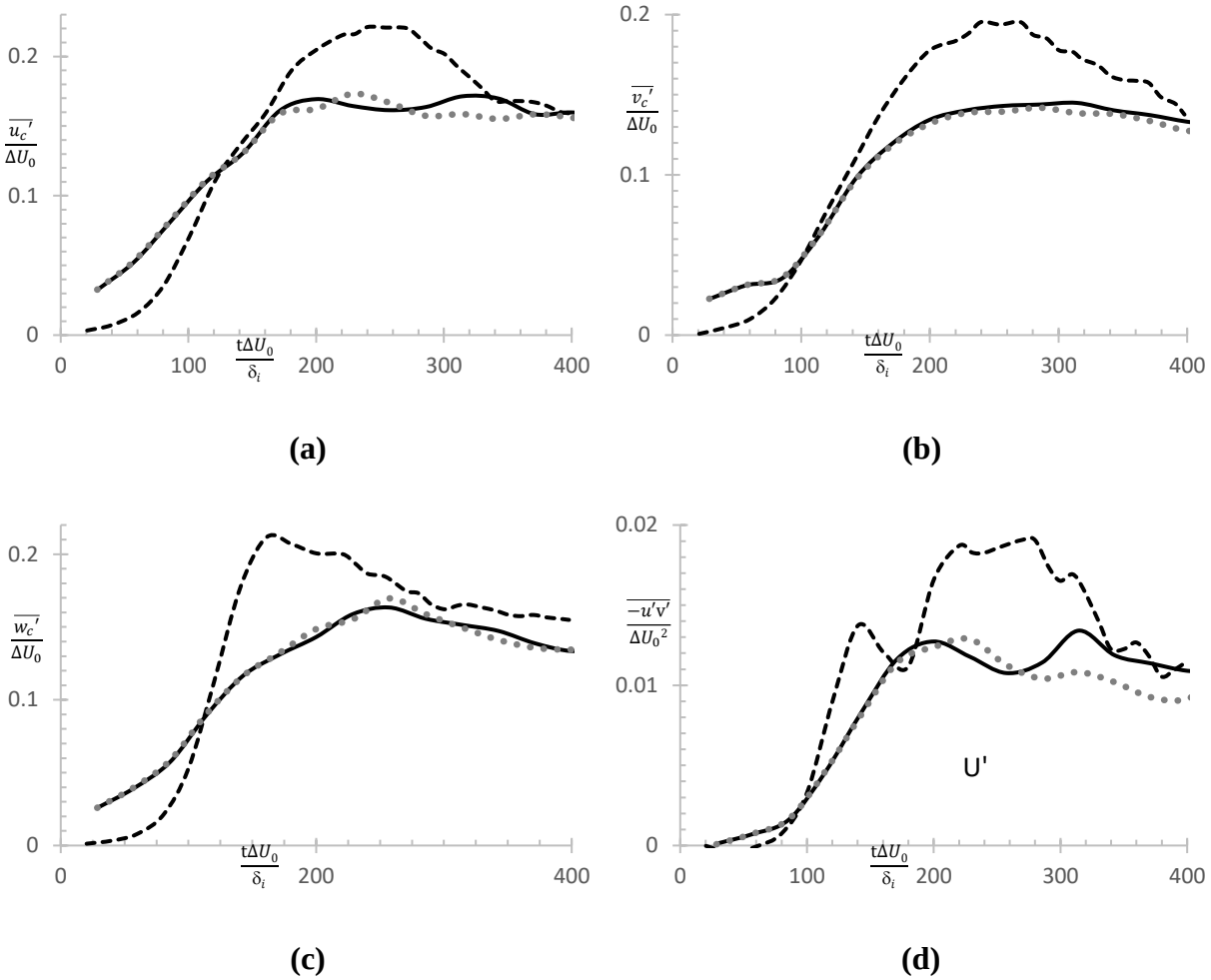

Figure 11. Profiles of centerline values of (a) $\overline{u'}$, (b) $\overline{v'}$, (c) $\overline{w'}$, and (d) Reynolds shear stress -$\overline{u'v'}$; – – – DNS Ansari [25] ··· MILES, and — DHRL DDTF

6.7 CONCLUSIONS

This study investigates the performance of a newly proposed Double Dynamic Time-Filtering (DDTF) technique implemented in the DHRL model for two statistically non-stationary flows: a) pulsating channel flow, and b) temporally-varying mixing layer. Additional Direct Numerical Simulations (DNS) are performed to supplement non-existing datasets for medium and low frequency-imposed oscillation for a pulsating channel flow. The DHRL-DDTF performance

is compared against a fully turbulent RANS (SST k-ω) model, a conventional hybrid RANS-LES (SST Multiscale) model, the DHRL model with Dynamic Time Filtering (DTF), and previously published numerical simulations performed by Scotti et al. [24] for a pulsating channel. Additionally, the DHRL-DDTF model performance is further investigated against MILES and DNS study by Ansari [25] for a temporally varying mixing layer.

The DNS study was performed using the pseudo-spectral solver *ParaSpectra* [49,50] to simulate the flow in a pulsating channel. Since previous DNS studies were not extended beyond high-frequency oscillation, the DNS performed in this study aims to supplement the existing dataset. Apart from a minor disagreement in the outer layer for the high-frequency oscillations , DNS data presented in this study using *ParaSpectra* were in close agreement with prior DNS and LES studies conducted by Scotti et al. [24].

Following the validation of the DNS data, the newly proposed DDTF technique was validated for pulsating channel and temporally evolving turbulent channel flow. For the pulsating channel case, results indicate that RANS (SST k-ω) and the traditional hybrid RANS-LES model (SST multiscale) models fail to accurately describe all the flow features for medium and low-frequency oscillations. The SST multiscale model captures near wall behavior reasonably well but suffers from early RANS-LES transition due to changes in grid density in the buffer and log-layer. The RANS model also exhibits velocity defects in the buffer layer for the medium and low frequency cases and tends to underpredict velocity in the outer layer as can be seen in Fig. 6. The DHRL model with DDTF more consistently provides accurate results throughout the forcing frequency spectrum and improves on the predictions of the DHRL model with DTF. The DDTF effectively incorporates trends in its velocity predictions and damps out some of sharp variations

in velocity for the low-frequency oscillations. However, the model consistently underpredicts velocity in the outer layer.

For the temporally evolving mixing layer, the DHRL-DDTF model is in good agreement with DNS data for turbulence statistics at t'=400 but the model does not accurately predict the rate of transition to turbulence accurately. The temporal evolution of turbulence statistics is in qualitative agreement with DNS. The deviation from DNS can reduced by fine tuning the initial disturbance provided so that the evolution from transition to turbulence is more consistent with DNS.

In conclusion, the results presented in this study highlight an improvement of the DDTF technique over the existing modeling techniques. The newly proposed DDTF technique improves the performance of the DHRL model for periodic and non-periodic statistically non-stationary flows while suffering from no detrimental effects when used in stationary-flows. Future effort will be focused on the implementation of the DDTF method in a new DHRL model with improved RANS to LES blending function along with variety of initial imposed fluctuations.

CHAPTER VII

A NEW VARIANT OF THE DYNAMIC HYBRID RANS-LES MODEL FOR COMPLEX TURBULENT FLOWS

7.1 INTRODUCTION AND OBJECTIVES

Reynolds-averaged Navier-Stokes (RANS) models still represent the state-of-the-art for practical, engineering-level Computational Fluid Dynamics (CFD) simulations of industry relevant problems. Although RANS models have existed for over half a century, they are still preferred because of their inherent efficiency and robustness. RANS models have been validated for an extensive number of cases and tend to perform well in terms of accuracy and computational expense for simple wall-bounded turbulent flows. The RANS framework is based on solution of the equations of fluid motion governing the ensemble-averaged flowfield. Effects of complex time-dependent fluctuations in the flowfield are included via prescription of the unclosed terms in the ensemble-averaged equations. These terms are modeled as functions of the averaged flowfield and known local quantities such as wall distance, and often require the solution of additional transport equations for r model variables. Since RANS models only resolve the mean flowfield and rely on significant levels of empiricism in their construction, these models tend to perform rather poorly for complex three-dimensional problems or for cases where the details of the geometry lead to

complex flow physics such as separated shear layers and flows with rotation and curvature. With increasing demands and reliance on CFD for complex engineering designs in a range of industries, there is an increasing demand for improved modeling techniques that extend beyond classical RANS.

Since Direct Numerical Simulation (DNS) of complex, high Reynolds number turbulent flow is generally considered to be prohibitively expensive, LES is often viewed as the natural successor to RANS models. LES models apply filters to the equations of fluid motion to resolve the large turbulent structures. The smaller scales however, are represented using a sub-grid scale (SGS) model. This approach removes a significant amount of empiricism associated with RANS models since large-scale, geometry dependent, and energy containing flow structures are fully resolved both spatially and temporally. This, however, comes at a considerable computational cost when compared to RANS, and the cost increases with increasing Reynolds number. Even with substantial improvements in computational power over the last several decades, LES is still uncommon in industry and remains widely used primarily in highly specialized research environments. Nevertheless, modern research is definitely headed in that direction [54].

Recent developments in hybrid RANS-LES (HRL) modeling have paved a way for improved predictive capabilities over RANS while being more computationally efficient than LES. The fundamental premise of HRL models is to use a RANS-type model for wall-bounded turbulence in the boundary layer, while using an LES-type model to resolve large scale structures far from the wall. The two most common implementations of the HRL framework are zonal and non-zonal modeling. For zonal modeling, pre-specified regions in a flowfield are treated with RANS or LES based on the physics of the flow. Non-zonal methods on the other hand use some type of blending based on local flow variables to dictate RANS-to-LES transition. The Detached

Eddy Simulation (DES) by Spalart [29] is possibly the most well-known example of a non-zonal method. The DES model incorporates a modification to the one-equation Spalart-Allmaras (SA) model [26] to switch between RANS in wall-bounded regions and LES away from the wall by dynamically adjusting the contribution of modelled stress in the momentum equation. Although these models have had considerable success in predicting complex flow features where traditional RANS models have failed, HRL models suffer from some key weaknesses [4]. Since traditional HRL formulations contain grid metrics in their RANS-to-LES switching functions, one of the most common and recurring issues associated with HRL methods is modeled stress depletion (MSD). For some flows, sudden changes in grid size or aspect ratio triggers a non-physical RANS to LES transition inside the boundary layer or in regions where the grid is not refined enough to compensate for lowered modeled stress. Although potential solutions for MSD were proposed by Menter-Kuntz [31] and by Spalart [32] through the SST-DES model and the DDES models, the inclusion of grid metrics in the HRL model formulation can still lead to unsatisfactory model performance in complex flows. To alleviate some of these issues, Walters and Bhushan [35,36] proposed an alternate HRL modeling approach. The Dynamic Hybrid RANS-LES (DHRL) modeling framework was developed to combine any RANS model with any LES model using a more physics-based approach compared to traditional HRL models. The model transitioned from RANS-to-LES using the ratio of resolved to modeled stress production ensuring a continuity of total turbulence production. Some of the key characteristics of the DHRL modeling framework are: i) relative insensitivity to changes in grid resolution due to the lack of explicit grid metrics in the RANS-LES switch, ii) ability to combine any RANS and LES model, and iii) recovery of RANS model for steady flows. The DHRL model has shown improved predictions compared to traditional HRL models for a variety of flow problems [55-57].

This study proposes a new Dynamic Hybrid RANS-LES model for complex turbulent flows. Since the baseline DHRL model uses the ratio of resolved to modeled turbulent stress in RANS-to-LES blending, it was observed that for some types of flows the RANS component of the DHRL model can significantly overpredict turbulent stress in regions where appreciable levels of LES fluctuation could be sustained. As a representative example, for the flow in a vortex cell [58], the RANS component of the DHRL modeled overpredicted turbulent stress inside the cell/cavity. Although significant velocity fluctuations were observed inside the cell, the DHRL model remained in RANS mode. A new statistical variable is introduced in this study and implemented into a modified blending function to facilitate model transition from RANS to LES based on the presence of appreciable levels of resolved turbulence. Initially, three variants of the transition parameter are investigated for a variety of cases with increasing levels of complexity; i) fully developed turbulent channel flow, ii) flow over a three-dimensional axisymmetric hill, and iii) non-stationary turbulent flow in a pulsating channel. Results indicate that the new model successfully addresses some of the shortcomings of the baseline DHRL model for each of the test cases investigated. Major improvements include a better resolution of the mean-flow statistics in the log-layer and improved prediction of second-moment statistics.

7.2 Development of a new Dynamic Hybrid RANS-LES (DHRL) model

The following sections discuss the development of the new DHRL model.

7.2.1 Governing Equations and Turbulence Modeling Approach

Recall, the governing equations for mass and momentum for a single-phase, single-species compressible fluid with negligible body forces are given by Eq. (78 and 79).

$$\frac{\partial \hat{\rho}}{\partial t} + \frac{\partial}{\partial x_j}\left(\hat{\rho}\tilde{u}_j\right) = 0 \tag{78}$$

$$\frac{\partial}{\partial t}(\hat{\rho}\tilde{u}_i) + \frac{\partial}{\partial x_j}(\hat{\rho}\tilde{u}_i\tilde{u}_j) = -\frac{\partial \hat{p}}{\partial x_i} + \frac{\partial}{\partial x_j}(\sigma_{ij} + \tau_{ij}) \tag{79}$$

where the hat overbar symbol (^) signifies an undefined filtering operation. Variables in the equations are expressed in terms of either filtered or mass-weighted filtered variables as shown in the Eq. (80):

$$\tilde{u}_i = \widehat{\rho u_i}/\hat{\rho} \tag{80}$$

For example, if the filter were defined as a Reynolds average, then $\tilde{u}_i$ would represent the Favre-averaged velocity. The viscous and turbulent stress tensors are defined as:

$$\sigma_{ij} = \mu\left[\left(\frac{\partial \tilde{u}_i}{\partial x_j} + \frac{\partial \tilde{u}_j}{\partial x_i}\right) - \frac{2}{3}\delta_{ij}\frac{\partial \tilde{u}_k}{\partial x_k}\right] \tag{81}$$

$$\tau_{ij} = -\left(\widehat{\rho u_i u_j} - \hat{\rho}\tilde{u}_i\tilde{u}_j\right) \tag{82}$$

Since the filtering operation is not defined, the above equations are formally valid for either LES or RANS. Closure of the equations requires modeling of the turbulent stress tensor τ_{ij}.

7.2.2 Baseline Dynamic Hybrid RANS-LES (DHRL) model

The baseline Dynamic Hybrid RANS-LES (DHRL) modeling framework was developed by Walters and Bhushan [35,36] to allow for a more physics-based blending of any RANS model with any LES model. Recall, that for an incompressible single species fluid, the Navier-Stokes equation can be written as :

$$\frac{\partial \hat{u}_i}{\partial t} + \hat{u}_j\frac{\partial \hat{u}_i}{\partial x_j} = -\frac{1}{\rho}\frac{\partial \hat{P}}{\partial x_i} + \frac{\partial}{\partial x_j}(\sigma_{ij} + \tau_{ij}) \tag{83}$$

where (^) is an undefined filtering operation, σ_{ij} represents the viscous stress, and τ_{ij} is the sub-filter stress term given by the following equation.

$$\tau_{ij} = \widehat{u_i u_j} - \hat{u}_i \hat{u}_j \tag{84}$$

In the DHRL framework, the instantaneous velocity is decomposed into three components: Reynolds averaged ($\overline{u_i}$), resolved fluctuating ($u_i^{"}$), and unresolved fluctuating (u_i') as shown in Eqs. (85-86) :

$$u_i = \overline{u}_i + u_i^{"} + u_i' \tag{85}$$

$$\hat{u}_i = \overline{u}_i + u_i^{"} \tag{86}$$

where the filtered velocity, $\hat{u}_i$, is computed by the LES model as the solution to the momentum equation. The first two terms in Eq. (85) are directly computed via the solution of the momentum equation. The contribution of the third term is modeled using the sub-filter stress term. Substituting Eq. (85) in Eq. (84) and assuming negligible correlation between resolved and unresolved velocity fluctuations, the sub-filter stress can be approximated as.

$$\tau_{ij} = (\widehat{\hat{u}_i \hat{u}_j} - \hat{u}_i \hat{u}_j) + \widehat{u_i' u_j'} \tag{87}$$

In the DHRL framework, $\widehat{\hat{u}_i \hat{u}_j} - \hat{u}_i \hat{u}_j$ is modeled as a linear function of the sub-grid stress obtained from an LES model and $\widehat{u_i' u_j'}$ is modeled as a linear function of the Reynolds stress obtained from a RANS model. Following the concept of scale similarity, the sub-filter stress is expressed as a weighted average of the modelled sub-grid stress and the modelled Reynolds stress.

$$\tau_{ij} = \alpha {\tau_{ij}}^{SGS} + (1 - \alpha) {\tau_{ij}}^{RANS} \tag{88}$$

Assuming that the turbulent resolved scales and Reynolds stress are uncorrelated in the RANS-LES transition region, Reynolds averaging Eq. (87) and substituting in Eq.(85) yields:

$$\tau_{ij}{}^{RANS} - \overline{\tau_{ij}} = \left(\overline{u_i u_j} - \overline{u_i}\,\overline{u_j}\right) - \left(\overline{\widehat{u_i}\widehat{u_j}} - \overline{\widehat{u_i}}\,\overline{\widehat{u_i}}\right) = \overline{\widehat{u_i}\widehat{u_i}} - \overline{u_i u_j} = \overline{u_i'' u_j''} \tag{89}$$

which can be interpreted as the difference between the Reynolds average of the modeled stress and the Reynolds stress predicted by the RANS model i.e., the Reynolds average of the resolved velocity components. Finally, combining Eqs. (88 & 89) and taking scalar product of the result with the Reynolds averaged strain rate yields an expression for the blending parameter :

$$\alpha = \overline{u_i^{"} u_j^{"} S_{ij}} \Big/ \left(\tau_{ij}^{RANS}\overline{S_{ij}} - \overline{\tau_{ij}^{SGS} S_{ij}}\right) \tag{90}$$

where α is used to switch between LES and RANS based on the ratio of resolved turbulence production $(\overline{u_i^{"} u_j^{"} S_{ij}})$ to modeled turbulent stress production $\left(\tau_{ij}^{RANS}\overline{S_{ij}} - \overline{\tau_{ij}^{SGS} S_{ij}}\right)$ from the RANS and sub-grid scale model. Hence, transition is solely based on local flow conditions as the sub-filter stress term transitions between a modeled Reynolds stress $(\tau_{ij}{}^{RANS})$ and an LES sub-grid stress $(\tau_{ij}{}^{SGS})$.

For the present study and the initial development of the DHRL model, the SST *k-ω* model is used as the RANS component and MILES as the LES component. Recall that MILES does not incorporate a sub-grid stress model. Using Eq. (88), the sub-filter stress and the blending parameter can be expressed as:

$$\tau_{ij} = (1-\alpha)\tau_{ij}{}^{RANS} \tag{91}$$

$$\tau_{ij}{}^{RANS} = \frac{2}{3} k \delta_{ij} - 2\nu_t \overline{S_{ij}} \tag{92}$$

$$\alpha = \overline{u_i^{"} u_j^{"} S_{ij}} \Big/ \tau_{ij}^{RANS} \overline{S_{ij}} \tag{93}$$

since

$$\overline{\tau_{ij}^{SGS}} = 0 \tag{94}$$

and Eq. (83) can be written as,

$$\frac{\partial \hat{u}_i}{\partial t} + \hat{u}_j \frac{\partial \hat{u}_i}{\partial x_j} = -\frac{1}{\rho}\frac{\partial \hat{P}}{\partial x_i} + \frac{\partial}{\partial x_j}\left(\sigma_{ij}\right) - \frac{\partial}{\partial x_j}\left((1-\alpha)\tau_{ij}^{RANS}\right) \tag{95}$$

where the value of α is limited between 1 and 0. For regions with significant levels of resolved turbulent fluctuations, in which the resolved turbulent stress production is larger than the modeled turbulent stress production , i.e., $\overline{u_i^{"} u_j^{"} S_{ij}} \geq \tau_{ij}^{RANS} \overline{S_{ij}}$, the model recovers "pure" LES as $\alpha \to 1$. In regions where the modeled turbulent stress production is larger than resolved turbulent stress production, i.e. $\overline{u_i^{"} u_j^{"} S_{ij}} \ll \tau_{ij}^{RANS} \overline{S_{ij}}$, the model recovers pure RANS as $\alpha \to 0$. In all other regions, the sub-filter stress is represented as a weighted function of resolved and modeled turbulent stress production.

Key improvements of the DHRL modeling framework over traditional hybrid RANS-LES modeling techniques include:

i) since the blending parameter includes only the ratio of resolved to modeled turbulent stress production, any appropriate RANS model with a turbulent stress production term can be coupled with any LES model

ii) the lack of any explicit grid terms in the blending parameter α making the model relatively insensitive to changes in grid resolutions as supported by past studies [14-16].

iii) since the RANS model terms are calculated using the mean (Reynolds Averaged) velocity field, all RANS model terms obtained within the DHRL framework are calculated using the mean, rather than the instantaneous resolved field. Hence, for statistically stationary flows for example, the RANS eddy viscosity does not dampen fluctuations that tend to arise in unstable regions of the flowfield.

7.2.3 New Dynamic Hybrid RANS-LES (DHRL) Model

While the DHRL model has been extensively validated for numerous test cases [13-18], the dependence on the RANS model from RANS-to-LES remains to be a key weakness highlighted in previous studies [46,47,58]. As a consequence, in complex flow regions where the RANS model substantially overpredicts Reynolds stress, the DHRL model will in effect add a non-physical RANS stress component even when the flowfield is sufficiently resolved by the LES model. For example, in pulsating channel flows [46,47], a deviation from mean velocities was observed in the center of the channel as a direct consequence of the model remaining in a RANS biased mode despite the presence of significant turbulent fluctuations.

To address this issue, a new statistical dimensionless variable is introduced to represent regions in the flowfield that are able to be resolved in a purely LES mode. For the velocity field, it is possible to define a scaling variable based on the ratio of the inverse time scale of resolved fluctuations to the large-eddy time-scale, to adequately represent regions that contain sufficient resolved turbulent energy to sustain an LES mode. The new variable ς is defined as:

$$\varsigma = \frac{\overline{\bar{S}_{ij}\bar{S}_{ij}} - \bar{S}_{ij}\bar{S}_{ij}}{\bar{S}_{ij}\bar{S}_{ij}} \tag{96}$$

where S_{ij} is mean rate-of-strain. It is apparent that in regions of numerically steady solution, $\varsigma = \frac{\overline{\bar{S}_{ij}\bar{S}_{ij}} - \bar{S}_{ij}\bar{S}_{ij}}{\bar{S}_{ij}\bar{S}_{ij}} \sim 0$, whereas in regions with highly resolved turbulent fluctuations, $\varsigma = \frac{\overline{\bar{S}_{ij}\bar{S}_{ij}} - \bar{S}_{ij}\bar{S}_{ij}}{\bar{S}_{ij}\bar{S}_{ij}} >> 1$.

The new, alternate parameter proposed to smoothly transition RANS-to-LES in regions of sufficient resolved fluctuations is denoted by γ, with the requirement that $\gamma \to 0$ as $\varsigma \to 0$ and $\gamma \to 1$ as $\varsigma \to \infty$. The initial form of the alternative blending parameter implemented and investigated is given by:

$$\gamma = 1 - \left[1 + \left(\frac{\varsigma}{\varsigma_c}\right)^m\right]^{-1} \tag{97}$$

where m is used to determine the shape of the curve, and ς_c is a constant of calibration used to determine a critical value of ς that dictates where the model shifts to LES mode. Figure 1 shows the behavior of γ plotted against ς for three different values of m.

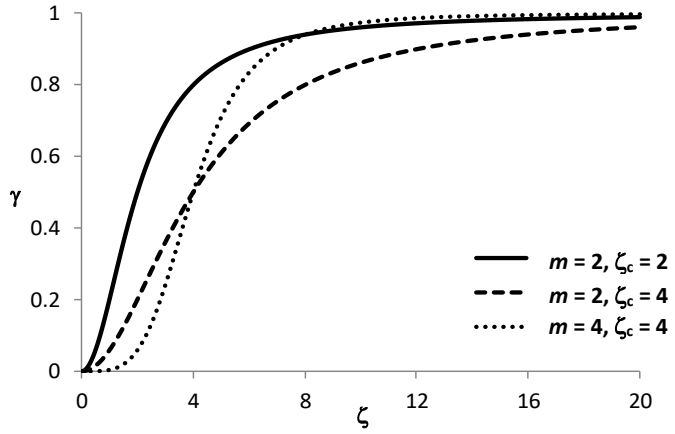

Figure 1. Illustration of new blending function γ using different coefficients

Finally, a new blending parameter can be constructed as the maximum of the original blending parameter (α) and the new parameter (γ) such that:

$$\alpha_{eff} = max(\alpha, \gamma) \tag{98}$$

$$\tau_{ij} = \alpha_{eff}\tau_{ij}^{SGS} + \left(1 - \alpha_{eff}\right)\tau_{ij}^{RANS} \tag{99}$$

where α_{eff} is the new blending parameter and the sub-filter stress term.

Similar to previous studies, the SST *k-ω* model is used as the RANS component and MILES as the LES component. Recall that MILES does not incorporate a sub-grid stress model. Using Eq. (98) and Eq. (99), the sub-filter stress and the blending parameter can be expressed as:

$$\tau_{ij} = (1 - \alpha_{eff})\tau_{ij}{}^{RANS} \tag{100}$$

since

$$\overline{\tau_{ij}^{SGS}} = 0 \tag{101}$$

and Eq. (83) can be written as,

$$\frac{\partial \hat{u}_i}{\partial t} + \hat{u}_j \frac{\partial \hat{u}_i}{\partial x_j} = -\frac{1}{\rho}\frac{\partial \hat{P}}{\partial x_i} + \frac{\partial}{\partial x_j}\left(\sigma_{ij}\right) - \frac{\partial}{\partial x_j}\left((1 - \alpha_{eff})\tau_{ij}{}^{RANS}\right) \tag{102}$$

For highly resolved separated flow regions, the parameter $\gamma \rightarrow 1$ and the simulation operates in a pure LES mode. For attached boundary layers and regions for which the resolved fluctuations are small, $\gamma < 1$ and the simulation operates in the baseline DHRL mode, in which the RANS contribution is governed by the original blending parameter α. The parameters m and ς_c should ideally be selected so that the DHRL model merges smoothly into the LES mode as the wall distance increases for resolved turbulent flow. Initial simulations have been performed for a

turbulent channel flow case. Results using the combination m = 2, ς_c = 2 showed a reasonable delineation of the LES and DHRL regions. Figure 2 shows the predicted values of α and γ for a low Mach number turbulent channel flow at Re_τ=180, for a mesh containing 128^3 hexahedral cells. It is apparent that, in the near wall region, the value of γ tends to zero and the original blending function α will determine the RANS contribution. Near the centerline of the channel ($y/\delta \rightarrow 1$) the new parameter γ dominates and the simulation will operate in a pure LES mode rather than the blended HRL mode as dictated by α in that region. The difference between the original blending function α and the new function α_{eff} is illustrated in Figure 3. Because the mean strain rate is small near the centerline, this difference may not be significant to the overall mean flow results. However, the figure does indicate that, for simulations in which turbulent fluctuations are well resolved, the new parameter can potentially identify LES behavior independent of the details of the RANS model used.

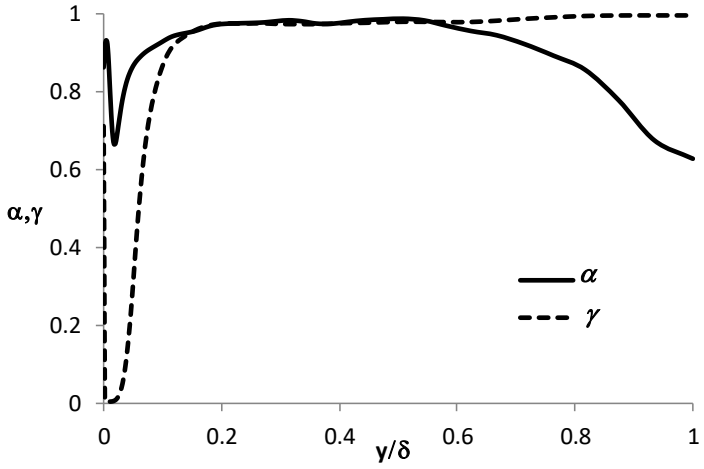

Figure 2. Distribution of original RANS dependent blending function α and the and new RANS independent blending function γ, for turbulent channel flow simulation.

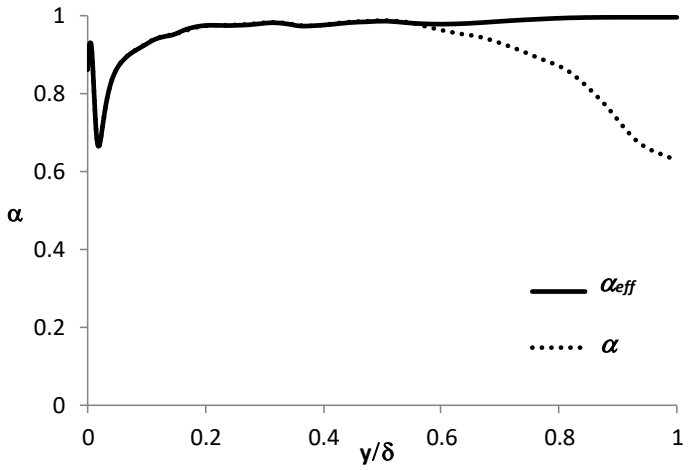

Figure 3. For turbulent channel flow, distribution of original DHRL blending function α and proposed new blending α_{eff} function to be implemented for modified DHRL model.

For the present study, the following combinations of m , ς_c will be investigated for a variety of complex turbulence flows discussed in the following sections.

Table 1. Transition parameter coefficients investigated

Model Variant	m	ς_c
DHRL22	2	2
DHRL24	2	4
DHRL44	4	4

7.3 TEST CASES

The performance of the new DHRL model is validated against the baseline DHRL model, RANS models, hybrid RANS-LES models described in the previous sections for i) fully developed turbulent channel flow at Re_τ =350 and Re_τ = 590, ii) flow over a three-dimensional axisymmetric hill, and iii) non-stationary pulsatile flow in a channel.

7.3.1 Fully Developed Turbulent Channel Flow

Channel flows are perhaps the simplest form of wall-bounded turbulence. These types of flows have provided useful insights about statistical and structural characteristics of flow in the near-wall regions. These flows also have significant relevance to many engineering applications, such as in pipe flows and heat exchangers. Importantly, these flows also serve as canonical test cases for validation and verification of newly developed turbulence models and numerical methods. Two fully developed channel flows are investigated in this study at Re_τ=350 and Re_τ=590, respectively. Performance of RANS, HRL, and DHRL model variants are compared against the DNS study conducted by Scotti et al. [24] for Re_τ=350, and Moser et al. [48] for Re_τ=590 using the same grids used in Chapters V and VI.

7.3.1.2 Results and Discussion

Fully developed flow through a channel was investigated for two Reynolds numbers equal to 350 and 590, based on friction velocity and channel half height. Figure 4 compares the profiles of normalized mean-velocity, $\bar{u}^+$, and figure 5 compares the blending function for the DHRL mode variants at Re_τ = 350. All the models predict the velocity profile with relatively high accuracy except the SST Multiscale model. Since the mesh cells in the near-wall regions are relatively well resolved, the model is in close agreement with DNS however, in the log-layer as the cells get stretched, the model transitions between RANS and LES modes before finally predicting the correct velocity profile in the outer layer. The baseline DHRL model also tends to underpredict velocity in the log-layer due to increased RANS contribution to the sub-filter stress. The new DHRL variants address this issue by accurately resolving the correct LES fluctuations and remaining in LES mode. All the new models however, become partially RANS biased in the center

of the channel due to extremely large grid spacing and the inability of MILES to resolve these fluctuations accurately.

Figure 6 compares the trace of resolved Reynolds stress $\overline{u_i' u_i'}$ and resolved Reynolds shear stress $\overline{u'v'}$ at $Re_\tau = 350$. Since DES operates in RANS mode, this section does not include resolved statistics from DES model. All the DHRL model variants are in general agreement with the data in [24]. All the new DHRL models are similar to MILES as they operate in the LES mode with some disagreement in the log-layer observed which can be attributed to under-resolved LES. Once again, the SST Multiscale model has difficulty accurately resolving the flow because of the grid. Similar to Figure 6, the SST Multiscale performance is significantly improved in the log and outer layer as it correctly switches to LES. In the near-wall regions, the model operates in a pseudo-RANS mode leading to underpredicted stress.

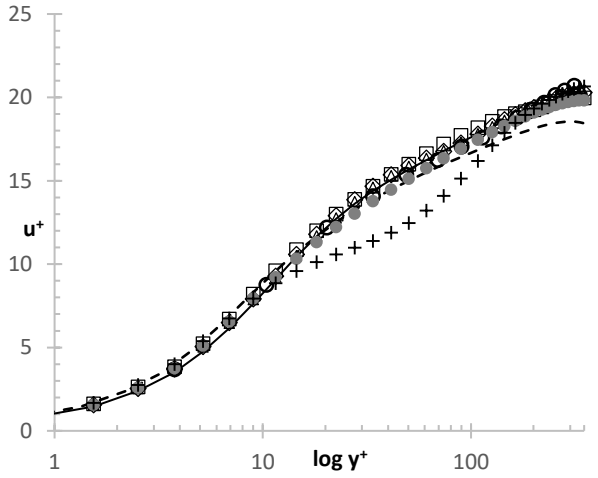

Figure 4. Profiles of normalized mean-velocity for $Re_\tau = 350$. ○ Scotti et al. [24]; —— MILES; ● SST *k*-ω ; SST Multiscale, - - - DHRL; ◇ DHRL22; □ DHRL24; and △ DHRL44

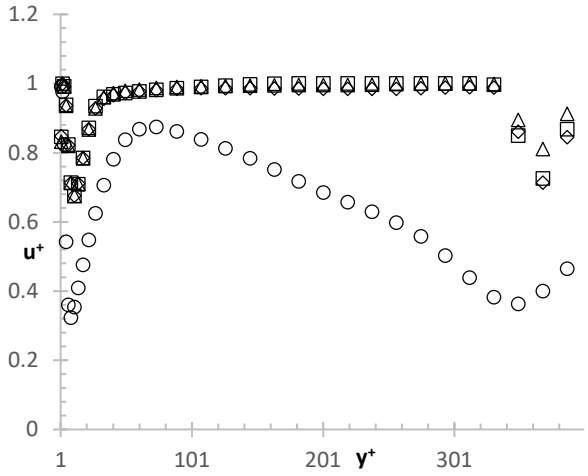

Figure 5. Profiles of blending parameter (α) for Re_τ = 350. ○ DHRL; ◇ DHRL22; □ DHRL24; and △ DHRL44

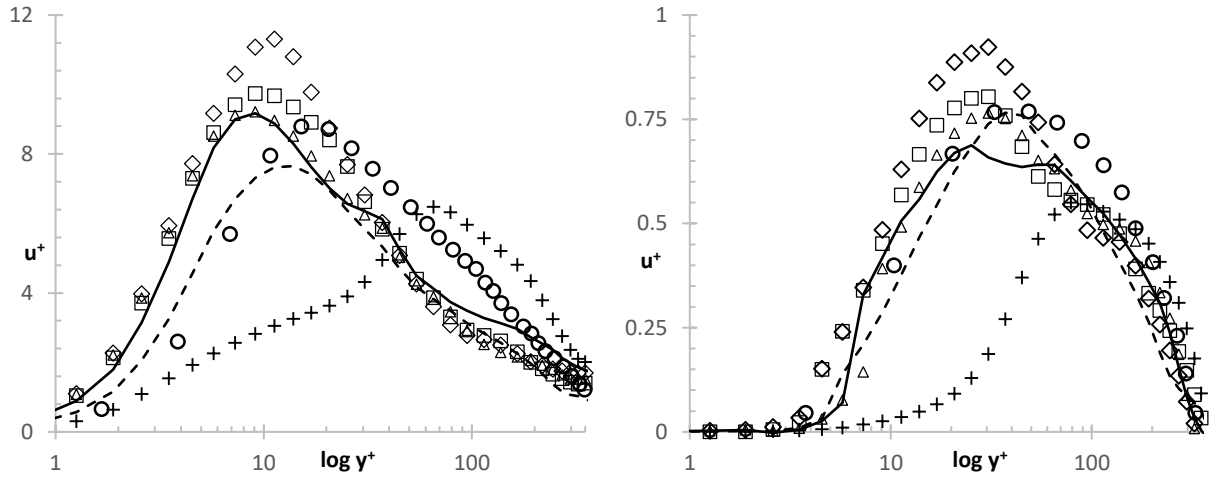

(a) **(b)**

Figure 6. Profiles of resolved (a) $\overline{u_i' u_i'}$, and (c) $\overline{u'v'}$ for Re_τ = 350. ○ Scotti et al. [24]; —— MILES; ● SST k-ω ; + SST Multiscale, - - - DHRL; ◇ DHRL22; □ DHRL24; and △ DHRL44

Figure 7 compares the profiles of normalized mean-velocity $\bar{u}^+$ while figure 8 compares the blending function for the DHRL mode variants at Re_τ = 590. One of the major differences observed for Re_τ = 590 from Re_τ = 350 is the more pronounced log layer with a shorter buffer layer. All the models capture the general trend of DNS with varying degrees of accuracy. MILES significantly overpredicts velocity in the log-layer as it is unable to resolve appreciable levels of turbulence while, the traditional RANS (SST *k*-ω) and HRL (SST Multiscale) model behavior is similar to Re_τ = 350. All the DHRL model variants, once again, resolve the velocity field accurately. The baseline DHRL results are also improved from Re_τ = 350 as the blending parameter is more LES biased as shown in Fig. 7 (b).

Figure 9 compares the resolved normal stresses ($\overline{u'u'}$, $\overline{v'v'}$, $\overline{w'w'}$ **)** and resolved Reynolds shear stress $\overline{u'v'}$ at Re_τ = 590. None of the models accurately capture the streamwise Reynolds stress ($\overline{u'u'}$) accurately. Significant disagreements are observed in the log-layer with all the DHRL model variants and MILES significantly overpredicting stresses. The performance of the new DHRL model variants are a slight improvement over the baseline model and MILES. However, the new DHRL models predict wall-normal, spanwise and Reynolds shear stress profiles with greater accuracy. All the model variants are an improvement over the baseline DHRL model, MILES, and SST Multiscale model.

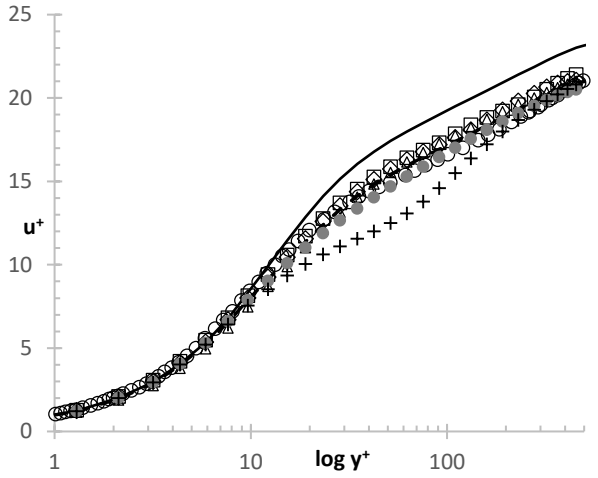

Figure 7. Profiles of normalized mean-velocity for $Re_\tau = 590$. ○ Moser et al. [48]; —— MILES; ● SST k-ω; + SST Multiscale, - - - DHRL; ◇ DHRL22; □ DHRL24; and △ DHRL44

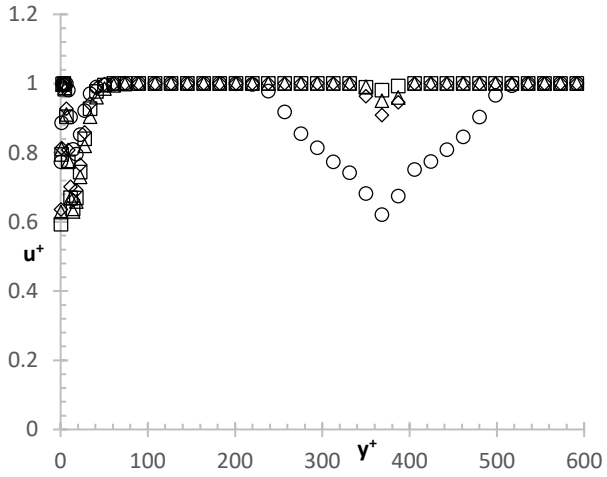

Figure 8. Profiles of blending parameter α for $Re_\tau = 590$. ○ DHRL; ◇ DHRL22; □ DHRL24; and △ DHRL44

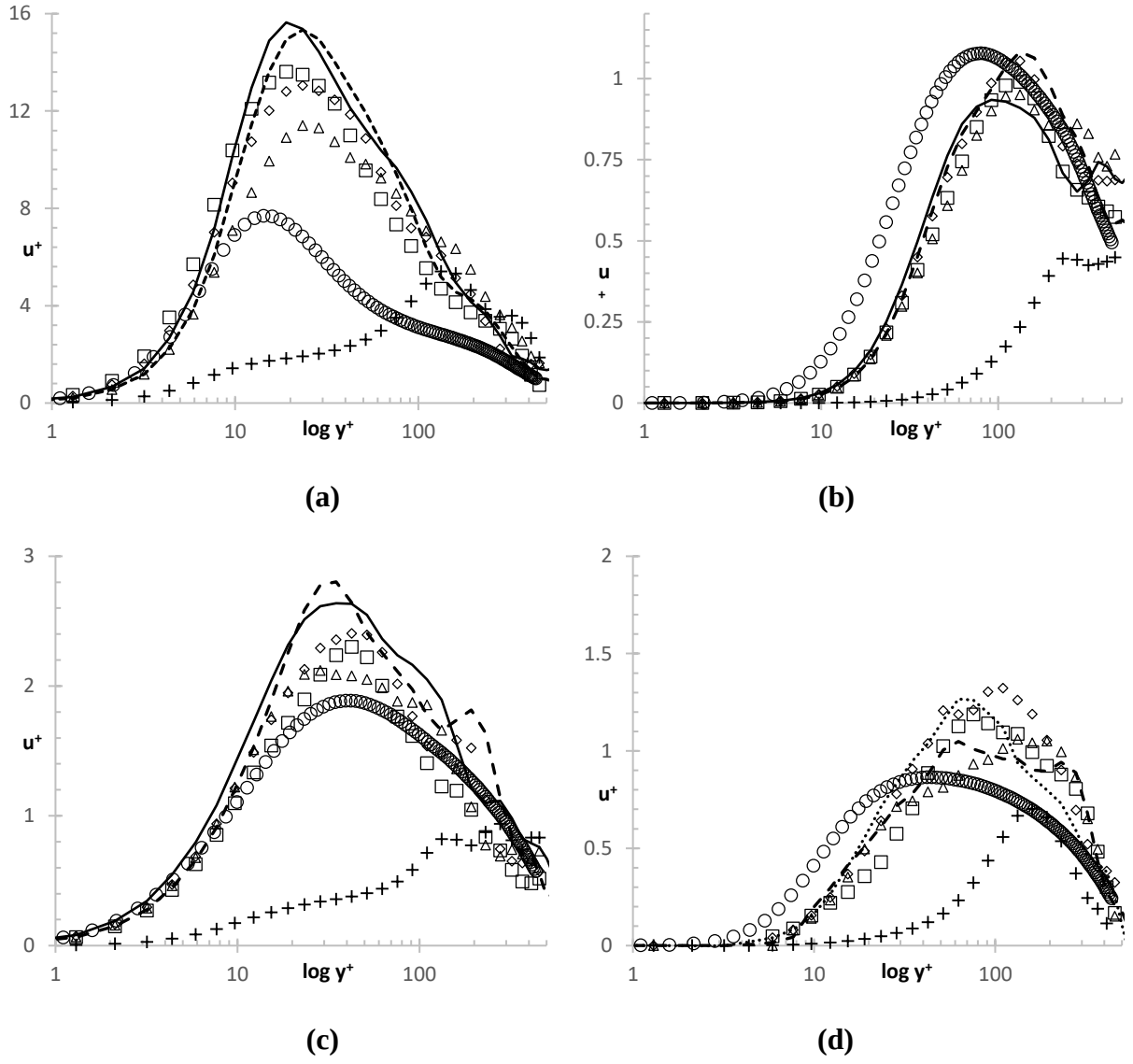

Figure 9. Profiles of (a) mean-velocity, (b) $\overline{u'u'}$, (c) $\overline{v'v'}$, (d) $\overline{w'w'}$, and (e) $\overline{u'v'}$ ○ Moser et al. [48]; —— MILES; ● SST *k*-ω; + SST Multiscale, - - - DHRL; ◇ DHRL22; □ DHRL24; and △ DHRL44

7.3.2 THREE DIMENSIONAL AXISYMMETRIC HILL

Since it was shown that from previous studies that traditional RANS and hybrid RANS models perform poorly for this particular case, while the baseline DHRL model results were in

good agreement with experimental [2,15] and high-resolution LES study [11]. This problem is investigated once again to verify the performance of the new DHRL model variants.

7.3.2.1 Results and Discussion

The performance of the DHRL model variants are evaluated against experimental studies conducted by Simpson et al. [2] and Ma et al. [15], and a high resolution LES study performed by Garcia et al. [11]. Results are compared and contrasted for several different flow metrics.

7.3.2.2 Distribution of Pressure Coefficient on the Centerline z/H = 0

Figure 10 compares the Pressure Coefficient (C_p) distribution on the surface on the hill between experiments and all the DHRL model variants. In the approach region on the windward side, a small recirculation zone at the foot of the hill is formed at approximately at x/H = -2 because of the high-pressure region created due to the geometry of the hill. This recirculation zone represents itself as a small kink in the C_p profiles predicted by the new DHRL model variants. Persson et al. [8] observed the presence of this recirculation zone along with more recent studies by our research group [5,42]. Past the small recirculation zone, C_p values start to decrease as the curvature of the hill slowly changes and flow is accelerated towards the top of the hill. The minimum value of C_p is recovered at the apex of hill, at x/H=0, where the lowest mean pressure is recorded. As flow travels downward into the lee-side of the hill, separation occurs around x/H~0.8 as indicated by the inflection in the plot. Flow reattachment takes place between x/H=1.85 and 2.25.

All the DHRL model variants predict the C_p with close reasonable accuracy and close agreement to one another. As shown in [14], traditional RANS and HRL model predictions for C_p are relatively poor as they tend to over-exaggerate the separation region caused by inaccurate stress

prediction. The new DHRL model variants show slight improvement over the baseline DHRL model in predicting the pressure distribution in the reattachment location slightly more accurately.

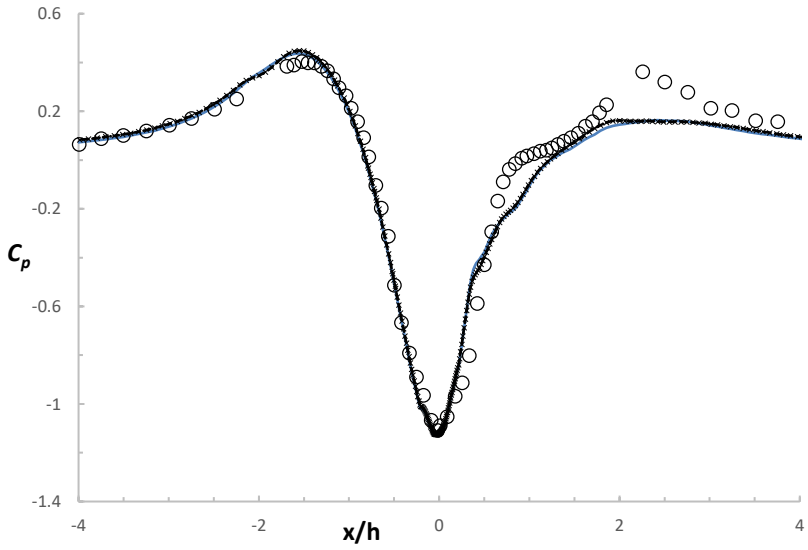

Figure 10. C_P profiles along the centerline z/H = 0. ○ Simpson et al. [2]; ------ baseline DHRL Model; × DHRL22; ------ DHRL24; ····· DHRL44

7.3.2.3 Streamwise and Spanwise Velocity Distribution at x= 3.69H

Normalized streamwise and spanwise velocity profiles in Figure 11 are compared for all the DHRL model variants against experimental data. All model variants predict the velocity distribution with considerable accuracy. The new DHRL models provide an improvement over the baseline DHRL model in the near-hill regions which are dominated by strong downwash and rotation-curvature effects. The discrepancies observed for x/h > 0.5 for z/H ≥ -0.81 can be attributed to under-resolved LES caused by large grid aspect ratio away from the boundary.

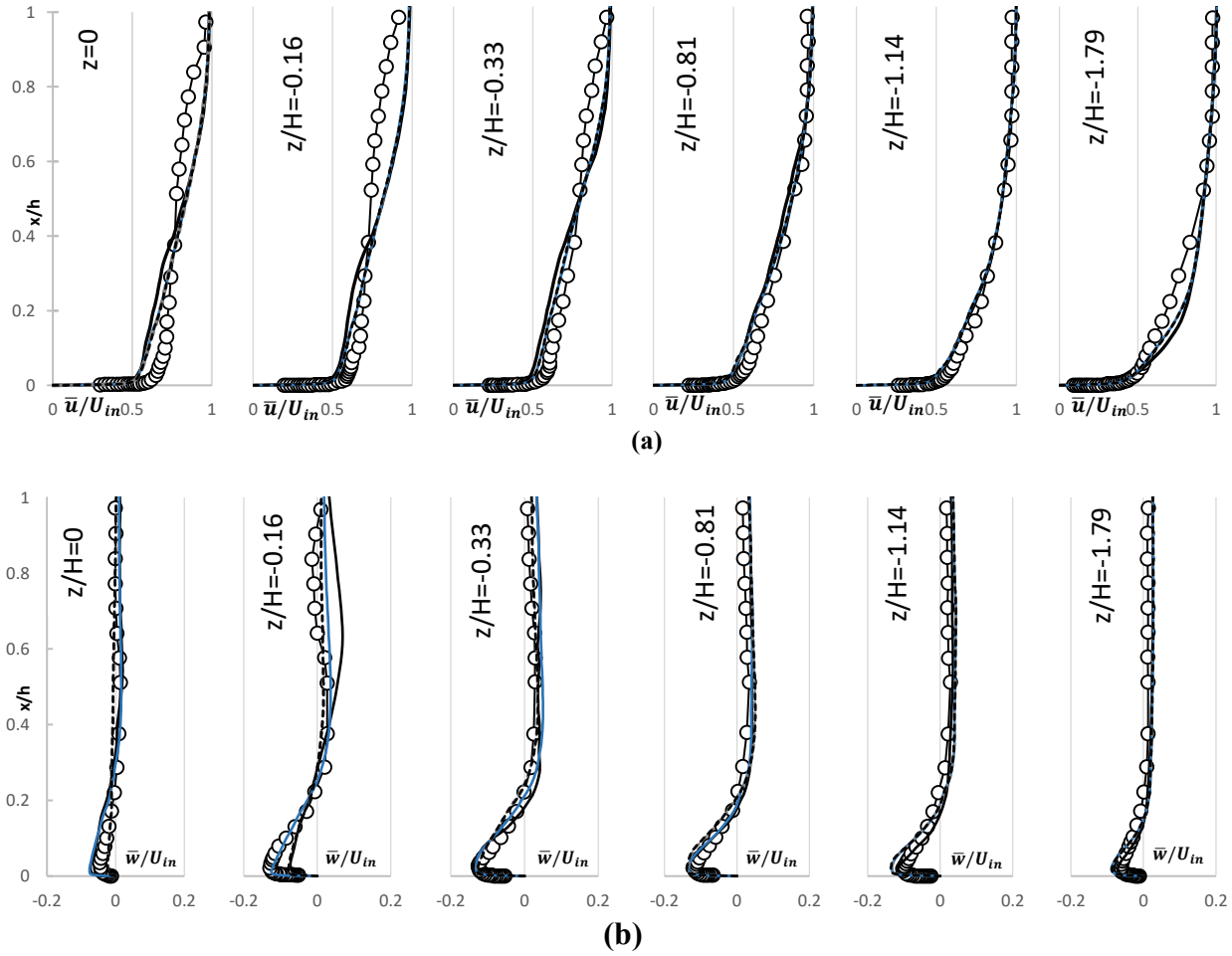

Figure 11. Profiles of (a) $< \bar{u} > /U_{in}$, (b) $< \bar{w} > /U_{in}$ at x= 3.69H. Simpson et al. [2]; baseline DHRL Model; DHRL22; DHRL24; and DHRL44

7.3.2.4 Streamwise and Spanwise Velocity Distribution at x=3.63H

Figure 12 compares streamwise and spanwise velocity distribution at x=3.63H of the DHRL model variants against experimental results by Ma et al. [15] and benchmark numerical simulations by Garcia et al. [11]. All the DHRL model variants underpredict streamwise velocity for z/H ≤ 0.65 however, predictions are improved for z/H ≥ 1.10. The new DHRL models show improved spanwise velocity prediction suggesting that the shape and structured of the wake region

is predicted more accurately. The GVR and LL simulations [30] used grids of approximately 134.5 x10^6 and 36.7x10^6 cells respectively compared to the grid size of 4.5x10^6 cells used in this study. Hence, the general agreement of the DHRL model velocity profiles with the GVR and LL results is a testament to the performance of the DHRL model.

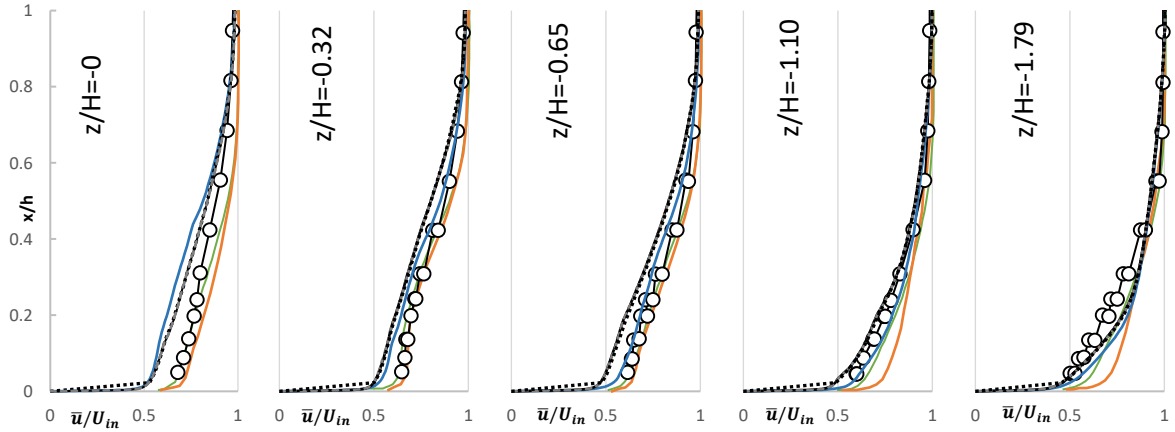

(a)

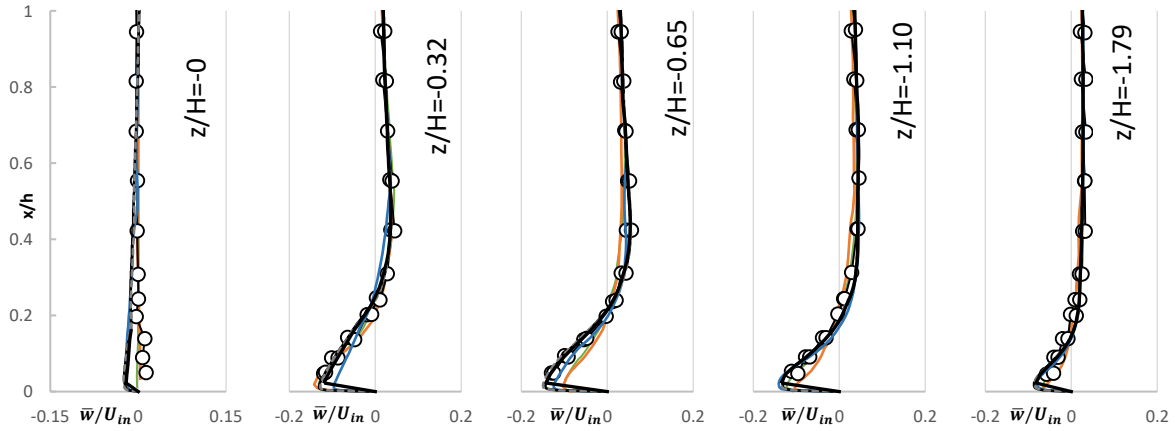

(b)

Figure 12. Plots of (a) $< \bar{u} > /U_{in}$ and (b) $< \bar{w} > /U_{in}$ at x= 3.63H. ○ Ma et al. [15], — LL and — GVR [11], — baseline DHRL Model; × DHRL22; ------ DHRL24; and ····· DHRL44

7.3.2.5 Turbulent Kinetic Energy ($\frac{1}{2}\overline{u'_\iota u'_\iota}$) and Reynolds Shear Stress ($u'v'$) at x=3.63H

Figure 13 compares profiles of resolved Turbulent Kinetic Energy (TKE) and Reynolds Shear Stress at x=3.63H for the DHRL model variants against experimental data [15] and high-resolution LES results [11]. When compared to tradition HRL models, DHRL results are a significant improvement. However, discrepancies can be observed for both TKE and Reynolds shear stress. Resolved TKE is overpredicted away from the centerline due to lack of dissipative scales in the flow in these regions of high aspect ratio cells. The resolved Reynolds stress profiles are also in good agreement with experimental and numerical data. Overall, the new DHRL models provide little to no improvement over the baseline model for resolved TKE and Reynolds shear stress prediction.

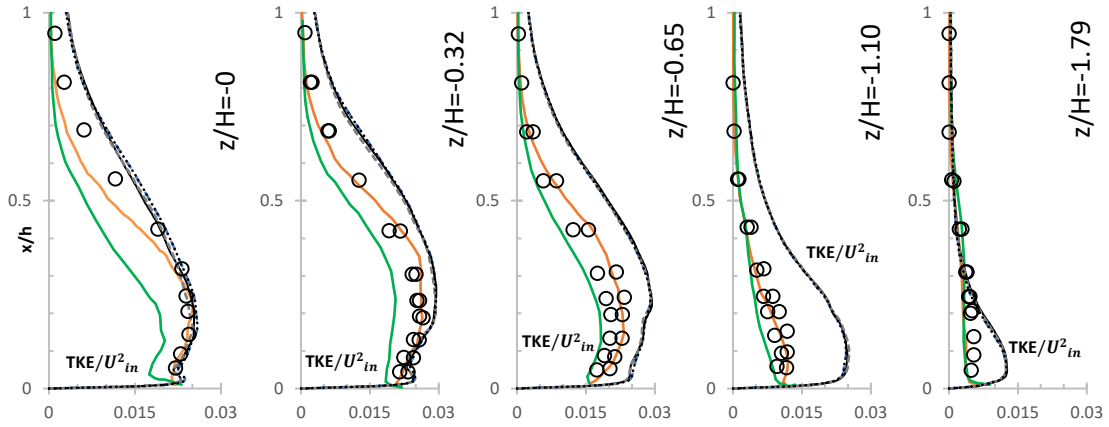

(a)

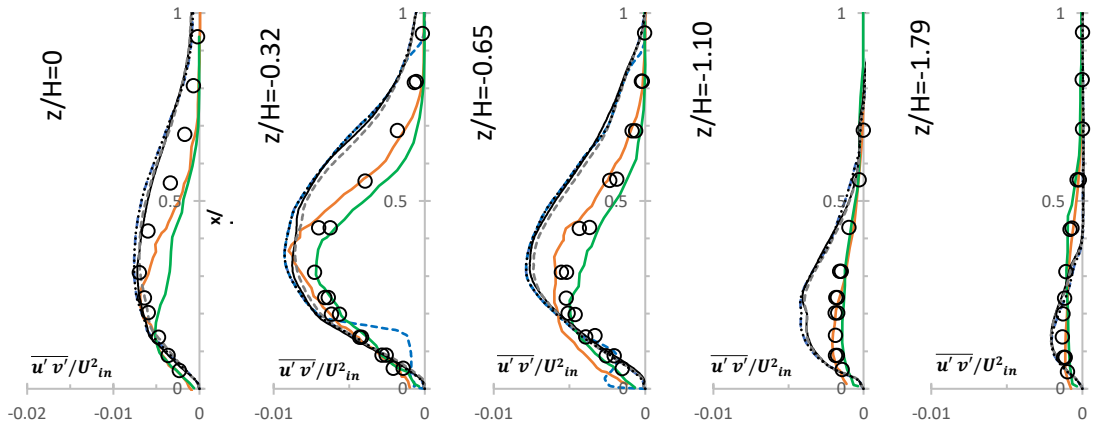

(b)

Figure 13. Plots of (a) Resolved TKE/$U_{in}{}^2$, (b) Resolved Reynolds Stress $(u'v')/U_{in}{}^2$ at x= 3.69H. ○ Ma et al. [15]; — LL and — GVR [11]; - - - DHRL; —— DHRL22; - - - - - DHRL24; and ····· DHRL44

7.3.3 Pulsating Channel

Chapters IV and V highlighted some of the difficulties in accurately predicting turbulence generated in non-stationary pulsatile flows. During parts of the pulsation cycle for low-frequency oscillation, the DHRL model would remain in a RANS-biased mode despite the presence of resolvable turbulence. The implementation of the DTF technique alleviated the issue to a certain degree but a more robust blending parameter was desired. Results from fully developed channel flow at $Re_\tau = 350$ and $Re_\tau = 590$ indicate the effectiveness of the new blending parameter however, because of the complexity of the pulsating channel and the challenge it presents for modern turbulence models, the case is investigated once again to evaluate the performance of the new DHRL model variants.

7.3.3.1 Results and Discussion

Time-varying mean statistic of normalized velocity and Reynolds stresses are discussed in this section. All the DHRL model variants are coupled with the DTF technique discussed in Chapter IV. Similar to past studies, data analysis of all flow statistics is carried out using planar-averaging.

7.3.3.2 Time Varying Mean Velocity

Figures 14, 15, and 16 show the distribution of normalized mean velocity ($\bar{u}^+$) against dimensionless wall distance at (y^+) at 8 equally spaced phases during a pulsation cycle. In each figure, t/T=0.75 and t/T=0.25 mark the beginning of the acceleration and deceleration phases respectively.

One of the interesting features observed for the pulsating channel flow is the change in modulation and structure of the log-layer based on forcing frequency. For the high frequency case,

shown in Figure 14, a distinct log-layer is visible that is modulated upwards and downwards throughout the cycle as the forcing term follows a sinusoidal function. Interestingly however, the outer layer remains intact throughout the cycle. MILES reproduces the general structure of the flow profile qualitatively. Deviations from LES data can be observed in the log-layer where MILES tends to overpredict velocity. The DHRL model variants accurately describe the flow throughout the cycle and no significant disagreements from LES data is observed.

As the forcing is reduced, the physics of the flow is significantly altered, as seen in Figure 15. A major distinction from the high frequency case is the lack of a well-defined log-layer for parts of the cycle. LES data also suggests a strong coupling between log and outer layers in the deceleration phase as a direct consequence of the reduced forcing. Once again, MILES overpredicts the velocity in the log layer with major disagreements with LES data appearing the deceleration phase. This is due to MILES not being able to resolve the dissipative scales appropriately. The DHRL models better predict the time-varying velocity field in the acceleration phase. Some minor deviations are observed in the log-layer but overall, the DHRL model predictions are in good agreement with LES data. In the deceleration phase, the flow behavior is reasonably well described by all the DHRL models.

In past studies [46,47], the accurate description of flow features at low-frequency have proven to be difficult for RANS and HRL models. Similar to the high and medium frequency cases, MILES overpredicts velocity in the log-layer. Discrepancies grow during the deceleration phase due to the lack of dissipative scale resolution in MILES. The DHRL model variants are close to each other and are in good agreement with LES data during the acceleration phase. However, the effects of the alternate blending are evident in the improved RANS-to-LES transition for the all the new DHRL model variants.

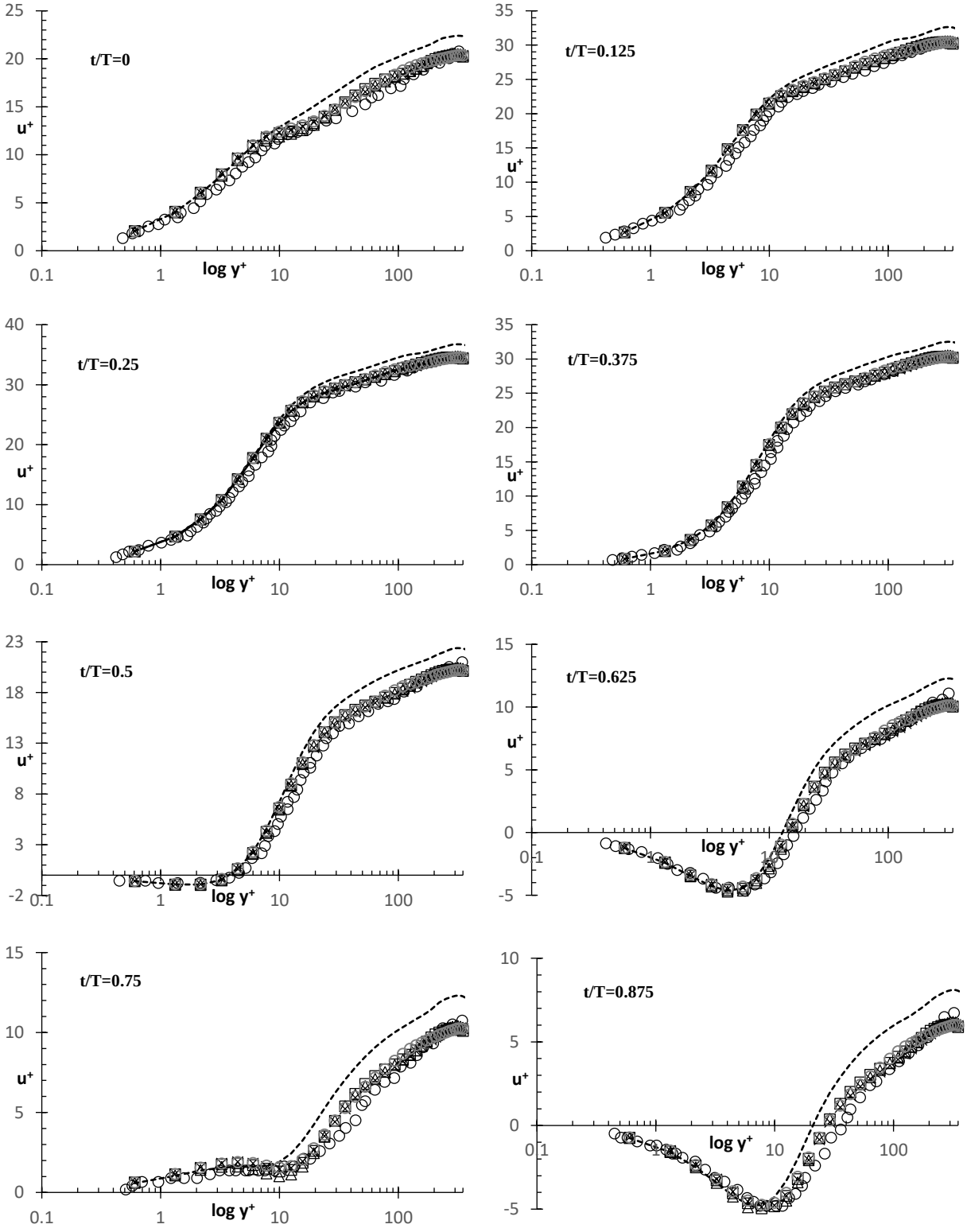

Figure 14. U^+ vs log (Y^+) for high-frequency case. ○ Scotti et al. [24]; --MILES; ○ DHRL DTF; □ DHRL22 DTF, △ DHRL24 DTF, × DHRL44 DTF

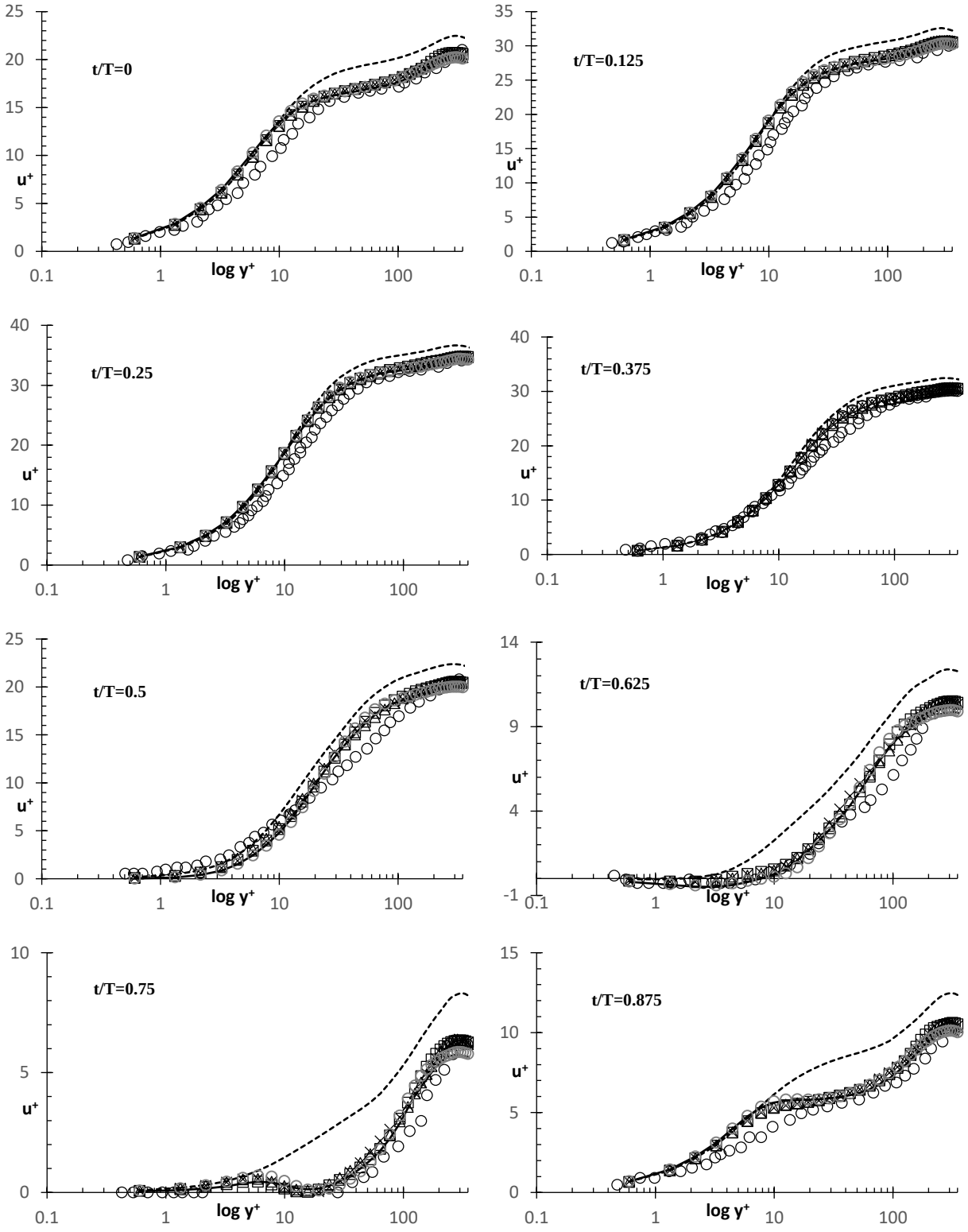

Figure 15. U^+ vs log (Y^+) for medium-frequency case. ○ Scotti et al. [24]; --MILES; ○ DHRL DTF; □ DHRL22 DTF, △ DHRL24 DTF, × DHRL44 DTF

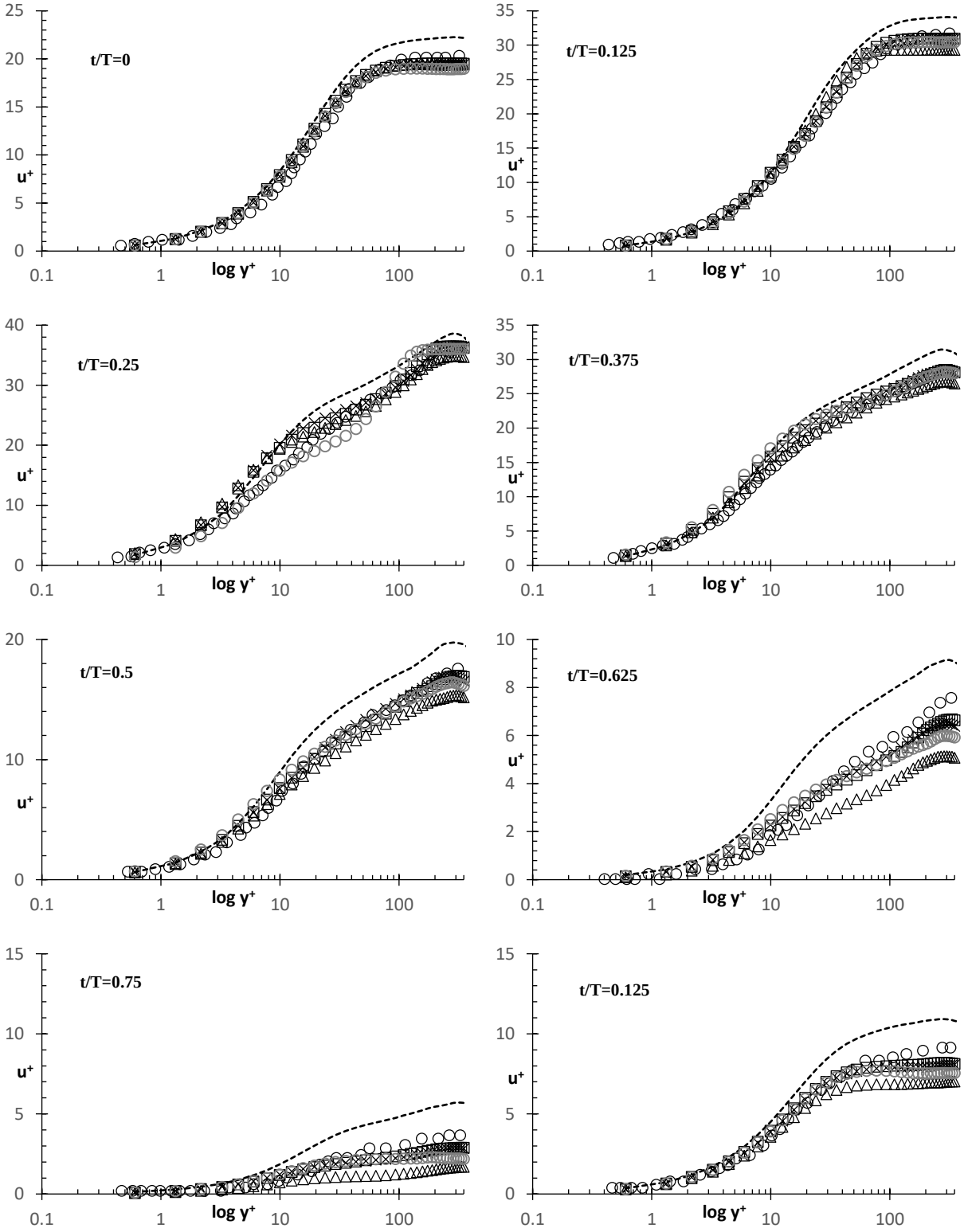

Figure 16. U^+ vs log (Y^+) for low-frequency case. ○ Scotti et al. [24]; --MILES; ○ DHRL DTF; □ DHRL22 DTF, △ DHRL24 DTF, × DHRL44 DTF

7.3.3.3 AC and DC Comparison Reynolds Stresses

Figure 17 compares the alternating and direct, AC and DC, components of resolved Reynolds Stresses of the DHRL model variants against DNS and LES data [24]. All the DHRL model variants are in good agreement with the DC component of Reynolds stress. AC components are however relatively difficult to predict because of the inability of these models to accurately represent flow features a wide range of scales due to grid resolution and numerical dissipation. Overall, the DHRL model results are in fair agreement with DNS and LES results and further improvements can likely be achieved by using a more refined grid.

7.3.3.4 Comparison of $\overline{u_i' u_i'}$

Figures 18-20 compare the trace of resolved Reynolds stresses against LES study conducted by Scotti et al. [24]. The new DHRL model variants predict Reynolds stresses more closely than the MILES model for high and medium-frequency oscillations. The DHRL model also appropriately adjusts RANS contribution to the sub-filter stress in regions where MILES predict inaccurate stresses. For low-frequency oscillations, major discrepancies can be observed during the deceleration phase $t/T>0.5$. This part of the cycle is dominated by enhanced mixing along with flow transition which are difficult to predict. Overall, the new DHRL model variants capture the general trends with reasonable accuracy and are an improvement over the baseline DHRL model.

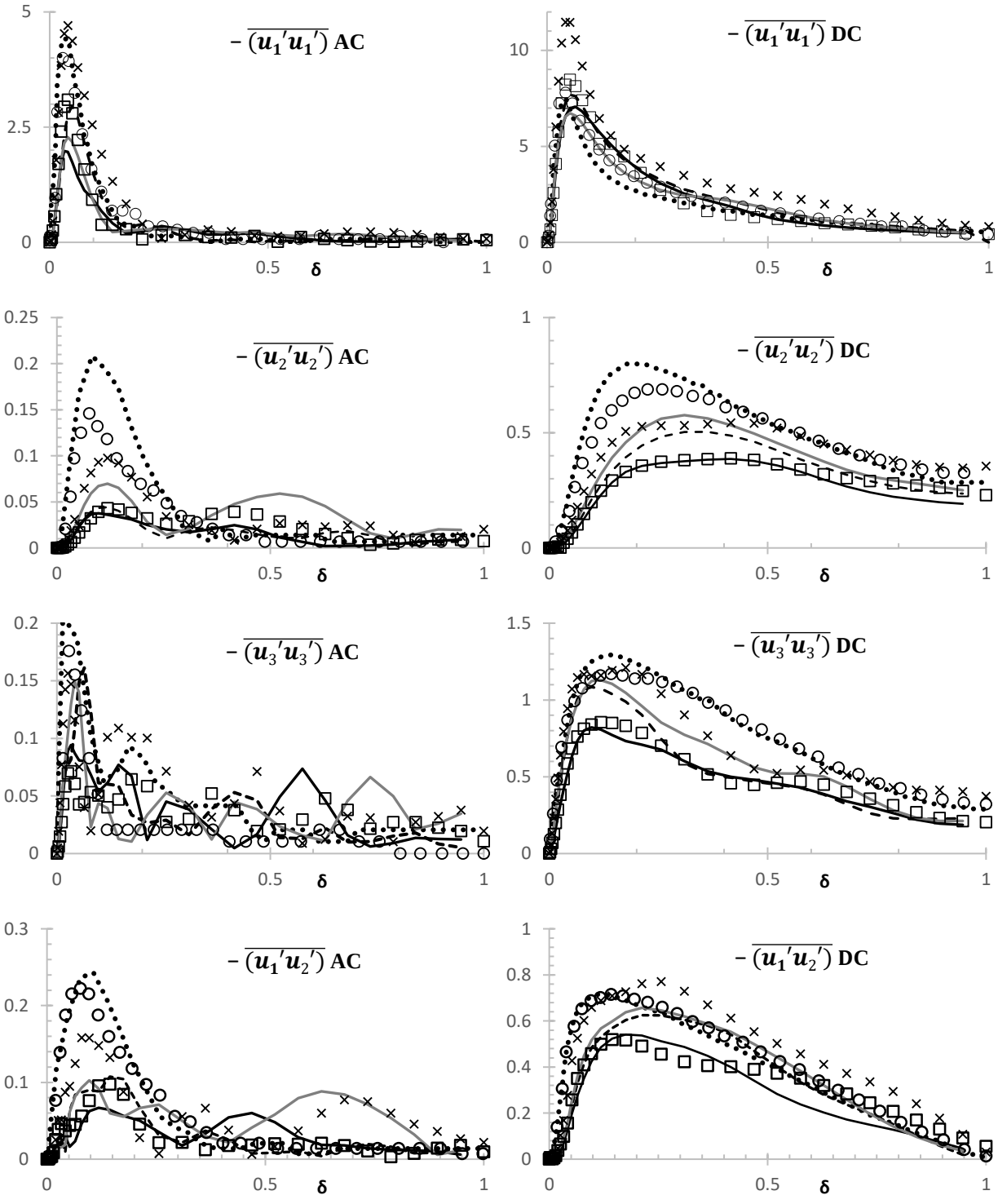

Figure 17. AC and DC Components of resolved Reynolds stresses for high-frequency oscillations. •••DNS and ○LES [24]; × MILES; ▫ DHRL DTF; --- DHRL22; ——DHRL24; and —— DHRL44

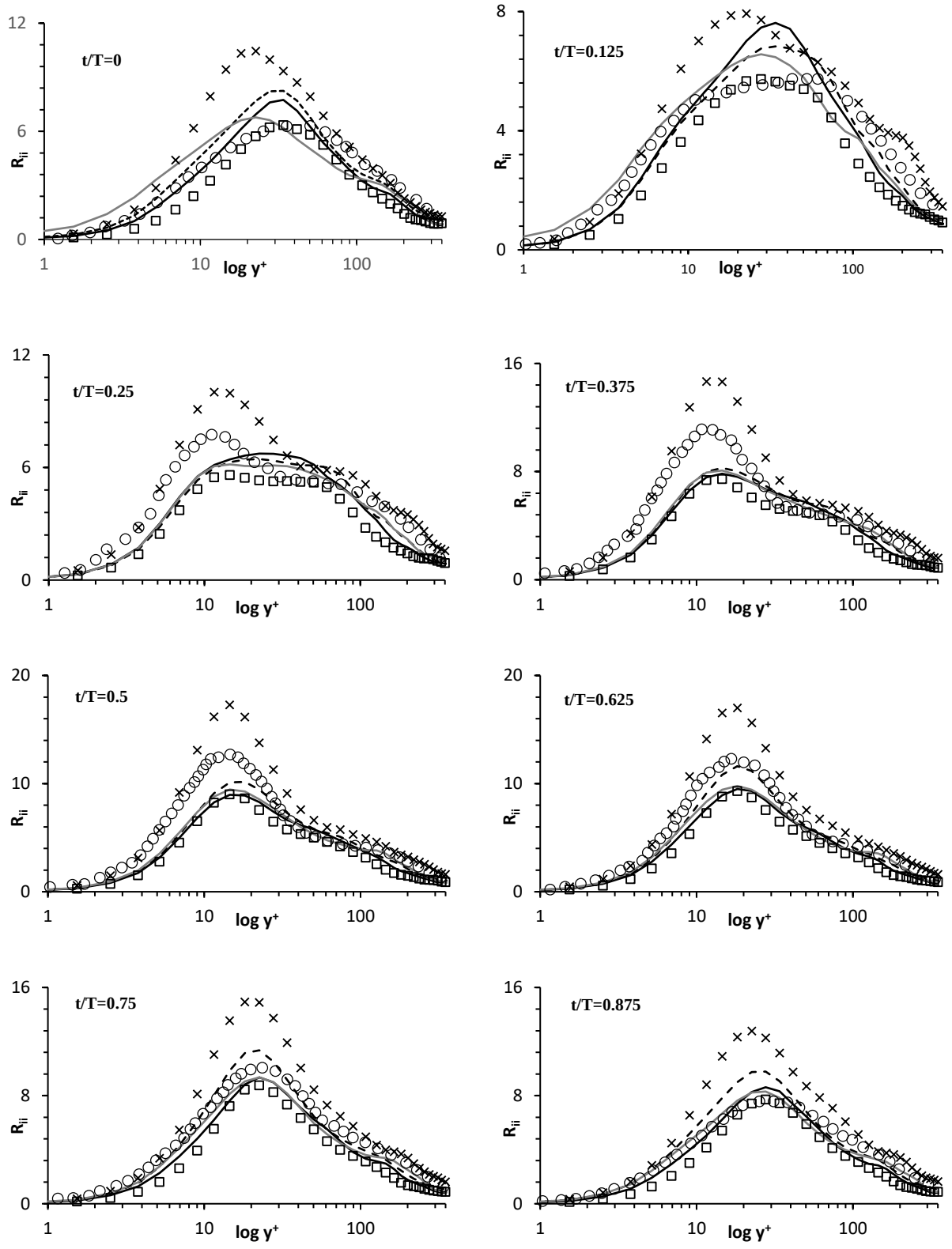

Figure 18. Plots of resolved ($\overline{u_i'u_i'}$) vs y^+ high-frequency oscillations. ○LES [24]; × MILES; □ DHRL DTF; --- DHRL22; —DHRL24; and — DHRL44

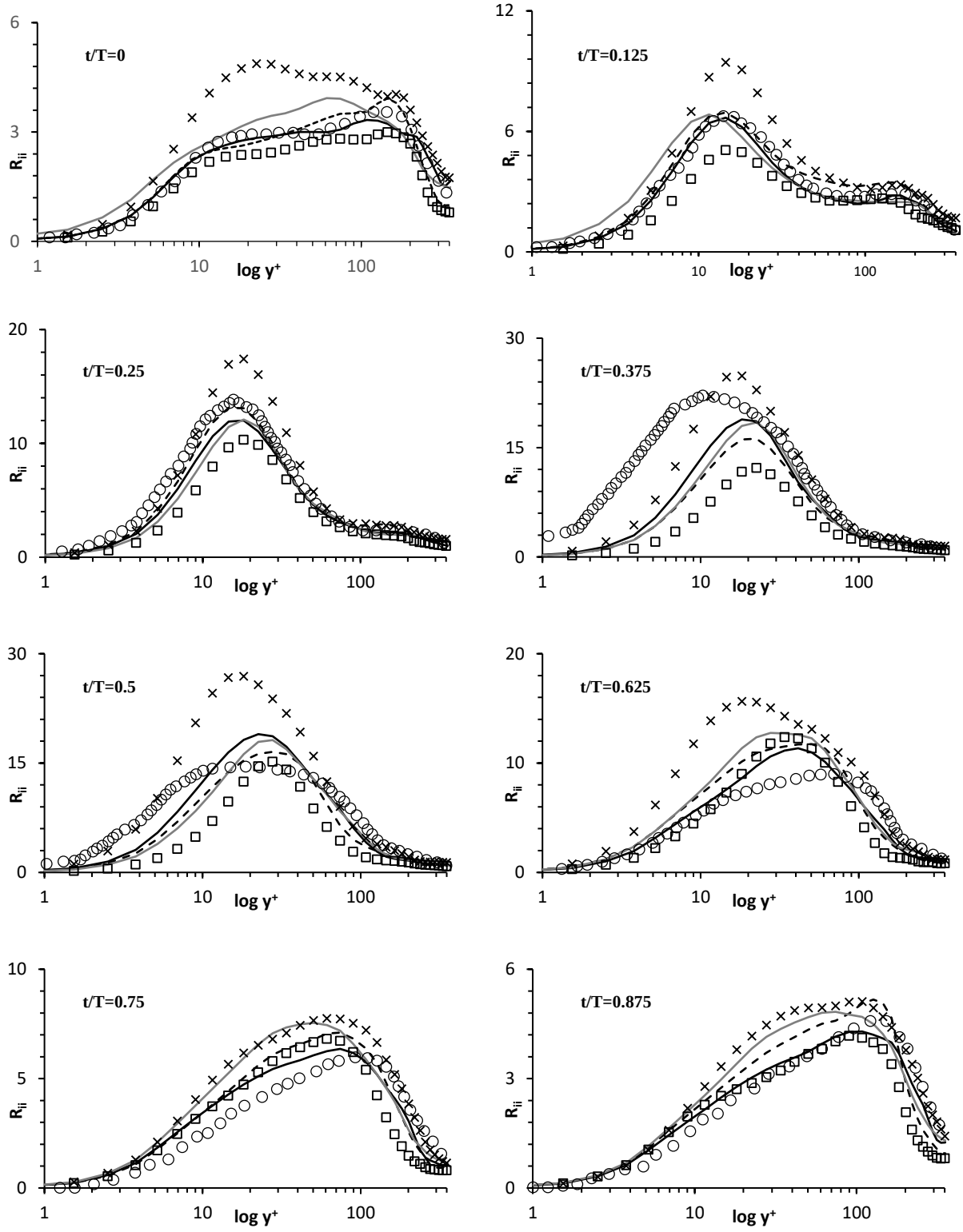

Figure 19. Plots of resolved ($\overline{u_i'u_i'}$) vs y^+ medium-frequency oscillations. ○ LES [24]; x MILES; □ DHRL DTF; --- DHRL22; — DHRL24; and — DHRL44

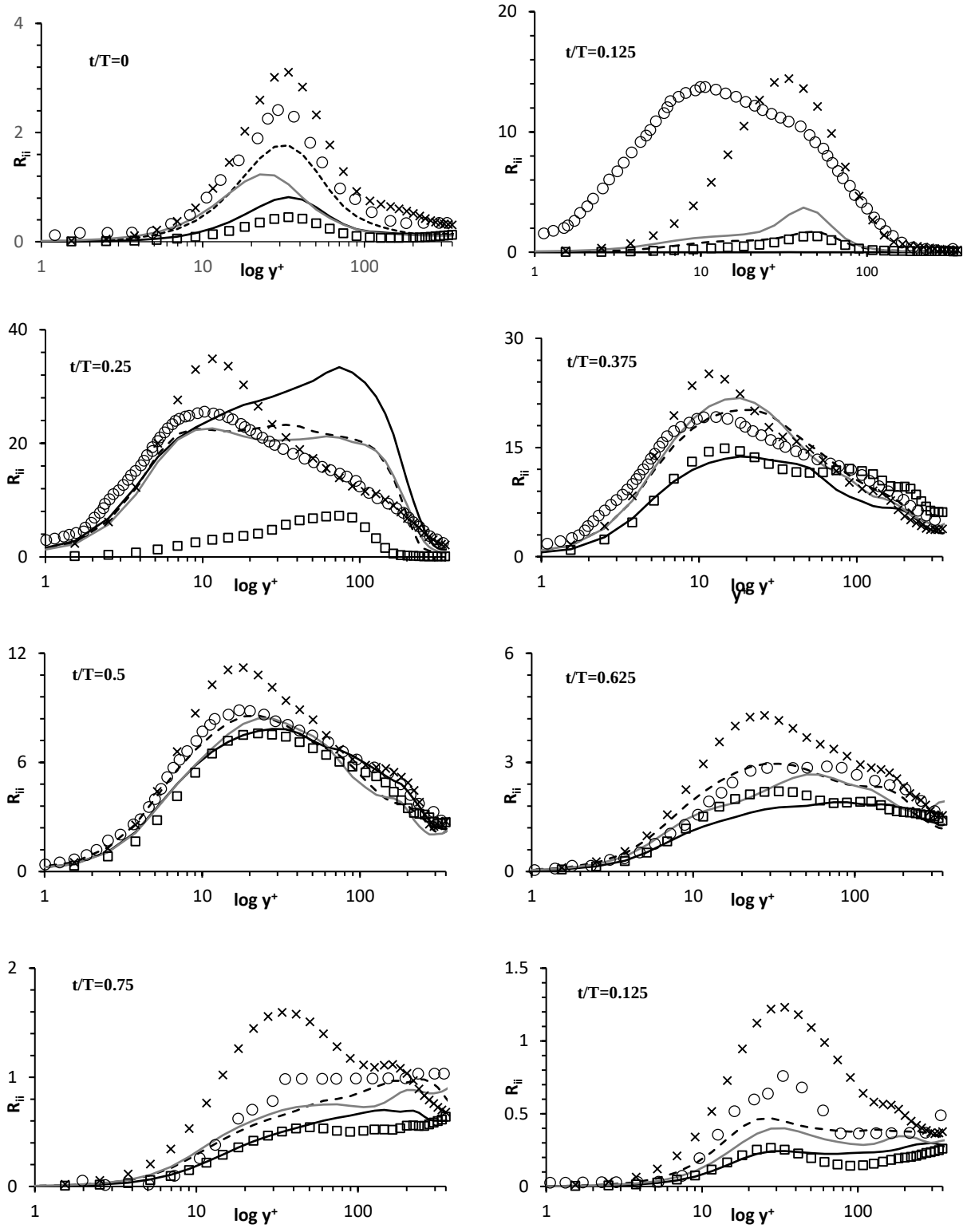

Figure 20. Plots of resolved ($\overline{u_i'u_i'}$) vs y^+ low-frequency oscillations. ○LES [24]; x MILES; □ DHRL DTF; --- DHRL22; —DHRL24; and — DHRL44

7.3.3.5 Comparison of Reynolds Shear Stress ($\overline{u_1'u_2'}$)

Figures 21-23 compare Reynolds shear stress profiles throughout the forcing spectrum. Correlations during the acceleration phase are relatively difficult to predict for traditional HRL models and the baseline DHRL model as it requires an accurate prediction of increased momentum and energy transfer between *u* and *v* components of the velocity. Surprisingly, MILES performance is superior to the baseline DHRL model. During the majority of the flow in medium and low-frequency cases, the RANS stress contribution in the DHRL model is too large. This issue is alleviated by the new DHRL model variants which not only provide improvements over the baseline DHRL model but also show enhanced resolution of flow physics in parts of the flow cycle where MILES tends to inaccurately predict flow statistics by appropriately blending the RANS and LES contribution to the sub-filter stress. Overall, the new blending parameters significantly improve the predictive capability of Reynolds shear stresses for the DHRL model.

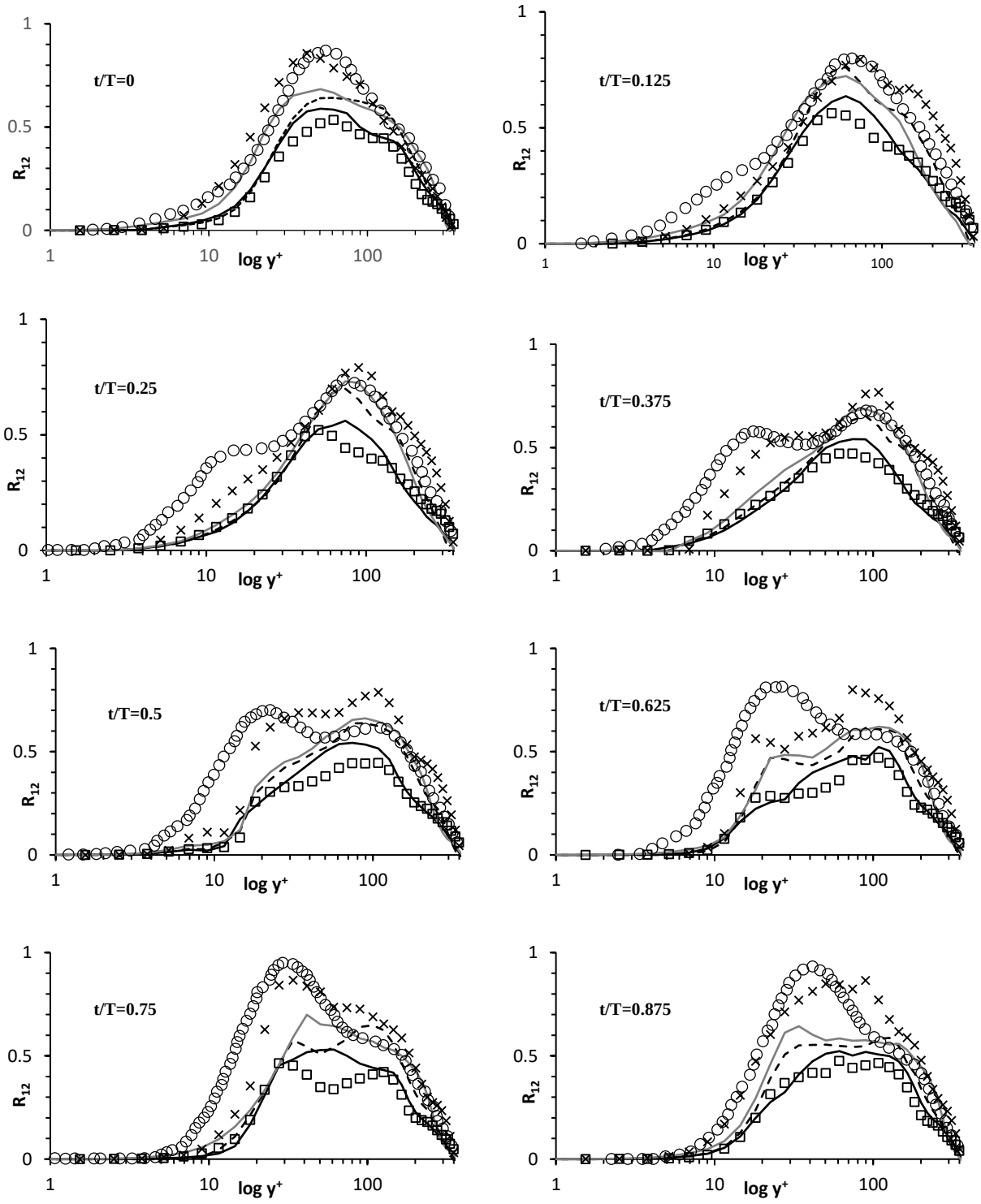

Figure 21. Plots of resolved ($\overline{u_1'u_2'}$) vs y^+ high-frequency oscillations. ○ LES [24]; x MILES; □ DHRL DTF; --- DHRL22; — DHRL24; and — DHRL44

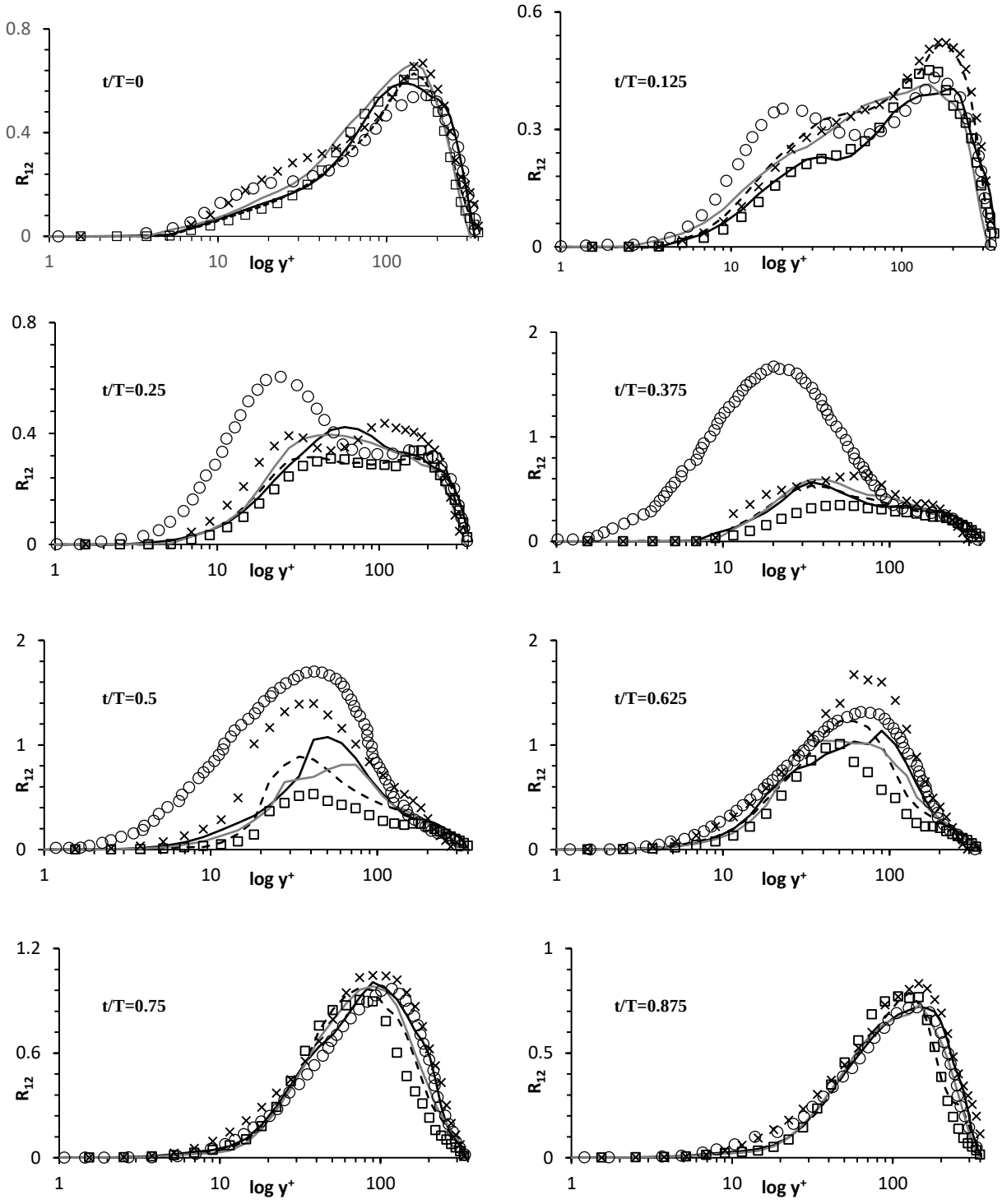

Figure 22. Plots of resolved ($\overline{u_1'u_2'}$) vs y^+ medium-frequency. ○LES [24]; × MILES; □ DHRL DTF; --- DHRL22; —DHRL24; and — DHRL44

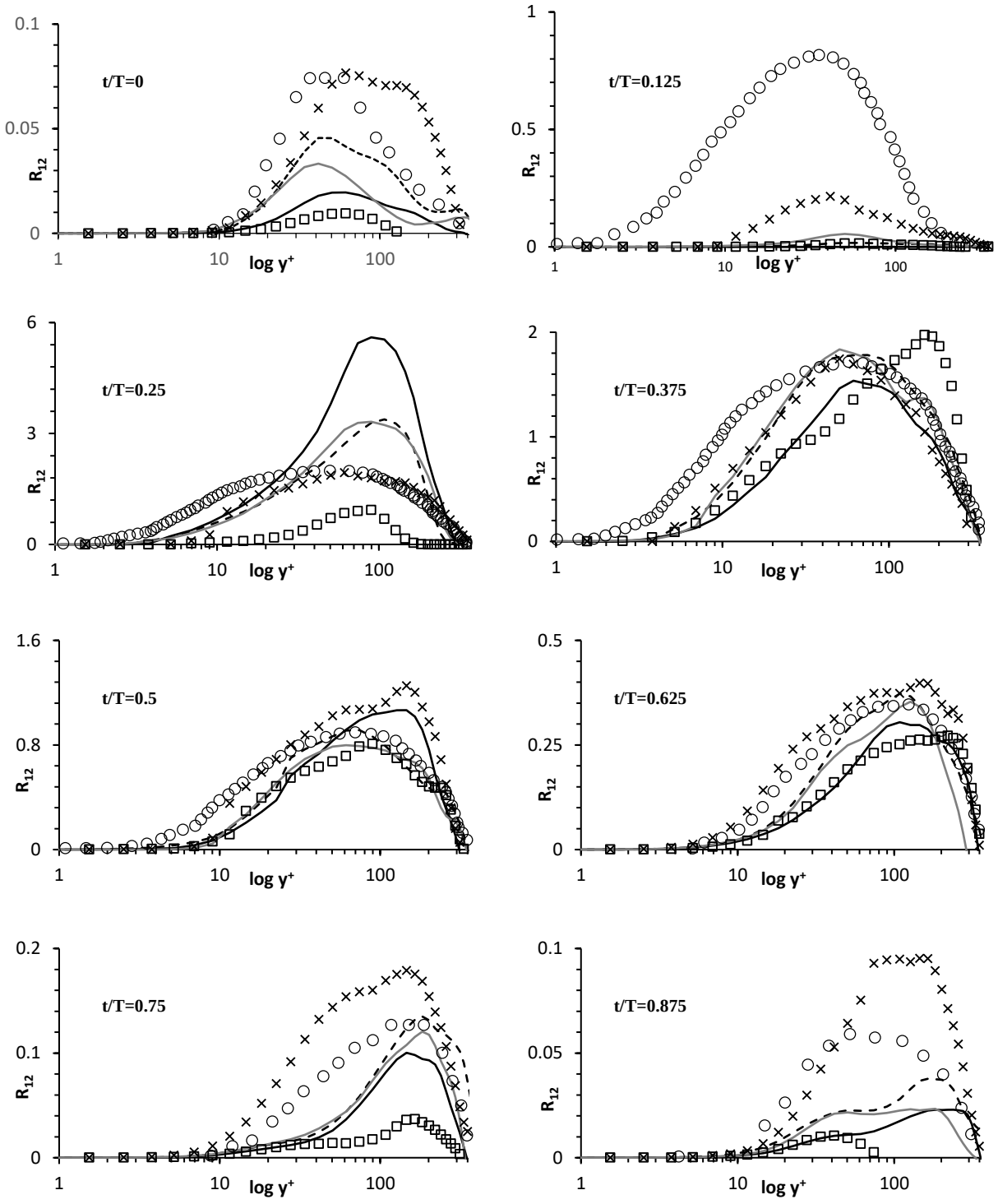

Figure 23. Plots of resolved ($\overline{u_1'u_2'}$) vs y^+ low-frequency. ○LES [24]; x MILES; □ DHRL DTF; --- DHRL22; —DHRL24; and — DHRL44

7.3.3.6 AC and DC component of Blending Parameter

Figure 24 shows the variation of the RANS-to-LES blending parameter for the new DHRL model variants against the baseline DHRL model throughout the forcing frequency spectrum. All the DHRL model variants show similar response to the time-dependent imposed pressure gradient for the high and medium frequency oscillations. The new DHRL model variants show a significant increase in LES content for both, AC and DC, components of the blending parameter which resulted in a significant improvement in Reynolds Stress prediction.

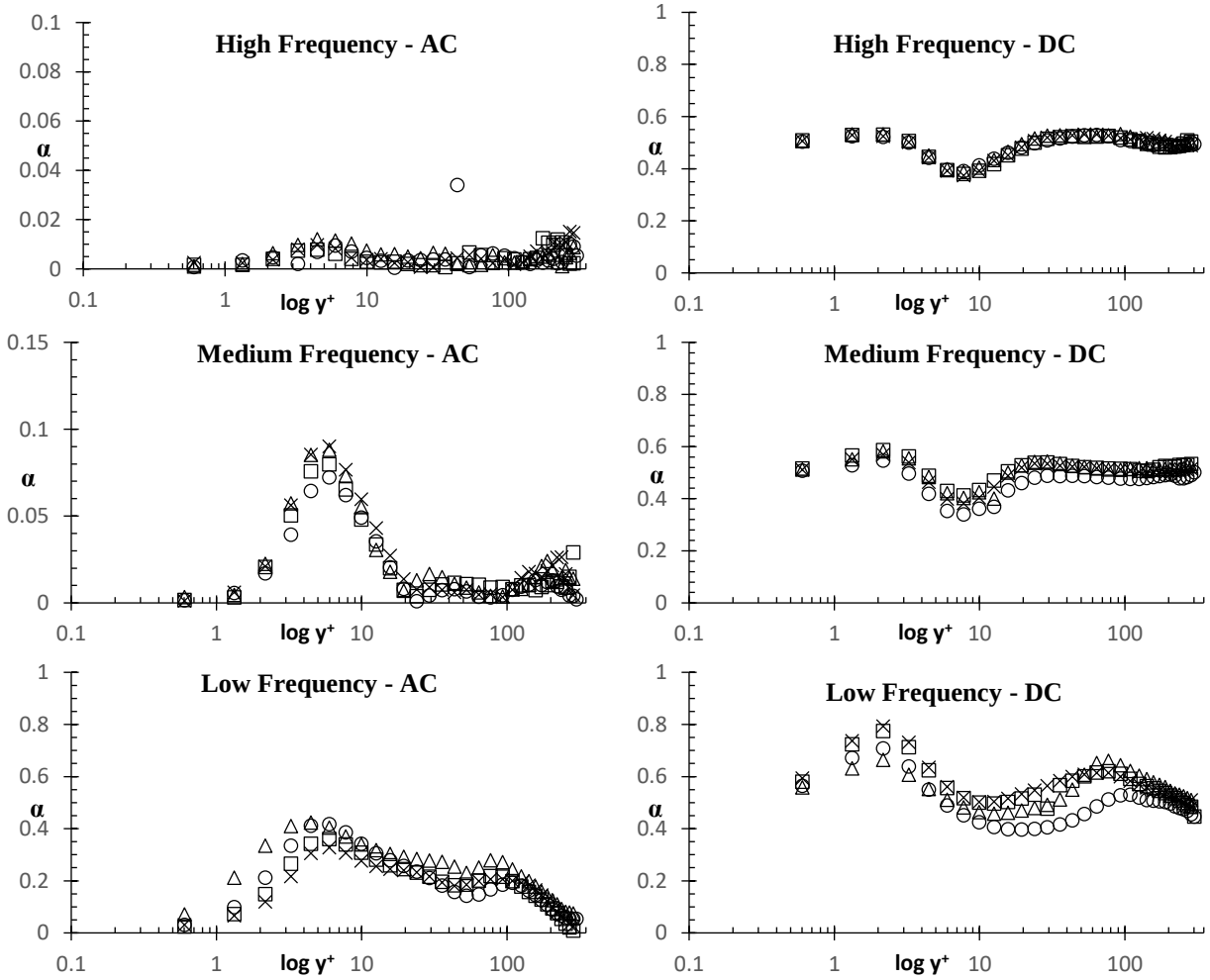

Figure 24. Plots of the blending parameter. ○DHRL DTF; □ DHRL22; △ DHRL24, ✕ DHRL44

7.4 CONCLUSIONS

In this study, an alternate blending parameter is proposed for the Dynamic Hybrid RANS-LES (DHRL) model. The new blending parameter is calculated using a statistical variable based on the ratio of inverse time-scale of resolved fluctuations to large-eddy time scale. This statistical variable is used to identify the presence of resolvable LES content in the flowfield. The variable is incorporated in a blending function that smoothly transitions the model from RANS-to-LES even in regions where RANS stress is significantly overpredicted. Performance of three different variants of the blending parameter is investigated for a flow in a fully developed turbulent channel, flow over a three-dimensional axisymmetric hill, and non-stationary pulsating flow in a channel.

Results from the fully developed channel flow at $Re_\tau = 350$ and $Re_\tau = 590$ suggest that the new DHRL model variants are an improvement over the baseline model. The new variants prevent the model from being RANS-biased and underpredicting the velocity in the log-layer where RANS stresses are overpredicted. The new models also predict second moment statistics with improved accuracy. For flow over a three-dimensional axisymmetric hill, the new model variants tend to behave in a similar fashion to the baseline model with minor improvements observed in C_p and velocity profiles. More substantial improvements in performance can be observed for non-stationary pulsating channel flow. The new model variants significantly improve velocity predictions and second moment statistics especially for low-frequency oscillations, when compared against the baseline DHRL model. Overall it is concluded that the new DHRL model is an improvement over the baseline DHRL model for complex turbulent flows. Results suggest that the blending parameter with optimum performance throughout the spectrum of cases investigated is the DHRL22 with blending coefficients m=2 and ζ_c=2.

Future work will include additional canonical tests cases such as flow over a backward facing step, film-cooling, and flow in a vortex cell. Current work is underway to develop more advanced blending for the DHRL model which is completely independent of the RANS model.

CHAPTER VIII

CONCLUSIONS AND FUTURE WORK

8.1 Conclusions

This Dissertation presents advanced turbulence modeling strategies within the hybrid RANS-LES framework. The performance of the Dynamic Hybrid RANS-LES (DHRL) model is first compared against traditional Reynolds Averaged Navier-Stokes (RANS), Hybrid RANS-LES (HRL), DNS, and experimental data for canonical test cases including stationary and non-stationary flows. Based on results, different modeling techniques are developed and implemented to improve the predictive capabilities of the DHRL model and the cases are reinvestigated.

In Chapter IV of this Dissertation, performance of RANS, HRL and the Dynamic Hybrid RANS-LES (DHRL) are comprehensively studied. Behavior of these models has been cataloged for the canonical case of flow over a three-dimensional axisymmetric hill. The results indicate some of the shortcomings of RANS and traditional HRL models in predicting complex turbulent flows, while highlighting some of the key features of the DHRL modeling technique. Results also show that the HRL models are unable to resolve appreciable levels of turbulent fluctuation energy unless a low-dissipation numerical scheme is used.

In Chapter V, two implementations of the new time filtering techniques are considered: initially a filter width based on imposed oscillation frequency was used to determine a filter width for averaging purposes. For almost all the cases, the filtering method allowed simulation results in

qualitative agreement with experimental data. Next, a dynamic filtering method based on turbulent statistics rather than on imposed frequency was proposed to eliminate the shortcomings of the initial method. The new time filtering technique substantially improved the predictive capability of the Dynamic Hybrid RANS-LES (DHRL) model for non-stationary flows while suffering from minimal detrimental effects when used in stationary flows. In addition, the new method requires less user input than the previously proposed method and dynamically adjusts filter width based on local turbulent statistics.

In Chapter VI, a new variation of the dynamic time filtering is implemented suing double exponential averaging to help the DHRL model predict trends in flows with monotonically changing turbulent statistics. The study also included additional DNS data to supplement the existing DNS database for pulsating channel flow. Following the validation of the DNS data, the newly proposed DDTF technique was validated for pulsating channel and temporally evolving turbulent channel flow. It was observed that the DDTF effectively incorporated trends in its velocity predictions and damped out some of sharp variations in velocity for the low-frequency oscillations in a pulsating channel. However, the model consistently underpredicted velocity in the outer layer. For a temporally evolving turbulent mixing layer, the DHRL-DDTF model was in good agreement with DNS however, temporal evolution of turbulent statistics were not accurately predicted due to differences in initial perturbations from DNS. Future work would involve fine tuning the initial perturbations to help the DHRL-DDTF model predict accurate temporal evolution of the flow.

In Chapter VII, an alternate blending parameter is proposed for the Dynamic Hybrid RANS-LES (DHRL) model. The new blending parameter is calculated using a new statistical variable based on the ratio of inverse time-scale of resolved fluctuations to large-eddy time scale

to identify the presence of sufficient LES content which allows the model to transition from RANS-to-LES even in regions where RANS stress is significantly overpredicted. Performance of three different variants of the blending parameter are investigated for a flow in a fully developed turbulent channel, flow over a three-dimensional axisymmetric hill, and non-stationary pulsating flow in a channel. The new implementation of the DHRL model considered in this study mitigated some of the key deficiencies of the baseline DHRL model such as an improvement in calculation of transition parameters to aid the hybrid models in the RANS to LES transition while improving predictive capabilities of the DHRL model for all cases. Results indicate a significant improvement in predictive capability of the DHRL models with new blending parameters without any additional detrimental effects.

8.2 Future Work

Future work will incorporate more improved RANS models within the DHRL framework. Since traditional RANS models based on Linear Eddy Viscosity framework are unable to resolve flows with system rotation, curvature, and anisotropy with accuracy, work has been ongoing on a newly proposed Algebraic Reynolds Stress Model (ARSM) with an Algebraic Heat Flux Model (AHFM). The model is currently being evaluated for a variety of test cases that include complex flow physics such as buoyancy and spanwise heat transfer typically observed in nuclear reactor cooling applications.

LIST OF REFERENCES

[1] Ishihara, T., & Hibi, K. (2002). Numerical study of turbulent wake flow behind a three-dimensional steep hill. *Wind and Structures, 5*(2_3_4), 317-328. doi:10.12989/was.2002.5.2_3_4.317

[2] Simpson, R. L., Long, C., & Byun, G. (2002). Study of vortical separation from an axisymmetric hill. *International Journal of Heat and Fluid Flow, 23*(5), 582-591. doi:10.1016/s0142-727x(02)00154-6

[3] Probst, A., Wolf, C., Radespiel, R., Knopp, T., & Schwamborn, D. (2010). A Comparison of Detached-Eddy Simulation and Reynolds-Stress Modeling Applied to the Flow over a Backward-Facing Step and an Airfoil at Stall. *48th AIAA Aerospace Sciences Meeting Including the New Horizons Forum and Aerospace Exposition*. doi:10.2514/6.2010-920

[4] Shur, M. L., Spalart, P. R., Strelets, M. K., & Travin, A. K. (2008). A hybrid RANS-LES approach with delayed-DES and wall-modelled LES capabilities. *International Journal of Heat and Fluid Flow, 29*(6), 1638-1649. doi:10.1016/j.ijheatfluidflow.2008.07.001

[5] Chitta, V., Jamal, T., & Walters, D. K. (2018). Computational Fluid Dynamics Study of Separated Flow Over a Three-Dimensional Axisymmetric Hill. *Journal of Fluids Engineering, 141*(1). doi:10.1115/1.4040467

[6] Chitta, V., Dhakal, T. P., & Walters, D. K. (2015). Sensitization of a Transition-Sensitive Linear Eddy-Viscosity Model to Rotation and Curvature Effects. *Journal of Fluids Engineering, 137*(3). doi:10.1115/1.4028627

[7] Temmerman, L., Leschziner, M., & Hanjalic, K. (2002). A-Priori Studies Of A Near-Wall Rans Model Within A Hybrid Les/rans Scheme. *Engineering Turbulence Modelling and Experiments 5*, 317-326. doi:10.1016/b978-008044114-6/50030-2

[8] Persson, T., Liefvendahl, M., Bensow, R. E., & Fureby, C. (2006). Numerical investigation of the flow over an axisymmetric hill using LES, DES, and RANS. *Journal of Turbulence*, *7*. doi:10.1080/14685240500543165

[9] Patel, N., & Menon, S. (2007). Structure of flow separation and reattachment behind an axisymmetric hill. *Journal of Turbulence, 8*. doi:10.1080/14685240701534484

[10] Davidson, L., & Dahlström, S. (2005). Hybrid Les-Rans: Computation of the Flow Around a Three-Dimensional Hill. *Engineering Turbulence Modelling and Experiments 6,* 319-328. doi:10.1016/b978-008044544-1/50030-3

[11] García-Villalba, M., Li, N., Rodi, W., & Leschziner, M. A. (2009). Large-eddy simulation of separated flow over a three-dimensional axisymmetric hill. *Journal of Fluid Mechanics, 627*, 55-96. doi:10.1017/s0022112008005661

[12] Germano, M., Piomelli, U., Moin, P., & Cabot, W. H. (1991). A dynamic subgrid-scale eddy viscosity model. *Physics of Fluids A: Fluid Dynamics, 3*(7), 1760-1765. doi:10.1063/1.857955

[13] Byun, G., Simpson, R. L., & Long, C. H. (2004). Study of Vortical Separation from Three-Dimensional Symmetric Bumps. *AIAA Journal, 42*(4), 754-765. doi:10.2514/1.1829

[14] Byun, G., & Simpson, R. L. (2006). Structure of Three-Dimensional Separated Flow on an Axisymmetric Bump. *AIAA Journal, 44*(5), 999-1008. doi:10.2514/1.17002

[15] Ma, R., Simpson, R. L, (2005) "Characterization of turbulent flow downstream of a three-dimensional axisymmetric bump", Proceedings of the Fourth International Symposium on Turbulence and Shear Flow Phenomena, Williamsburg, Virginia, pp. 1171–1176.

[16] Hino, M., Kashiwayanagi, M., Nakayama, A., & Hara, T. (1983). Experiments on the turbulence statistics and the structure of a reciprocating oscillatory flow. *Journal of Fluid Mechanics, 131*(-1), 363. doi:10.1017/s0022112083001378

[17] Sarpkaya, T. (1993). Coherent structures in oscillatory boundary layers. *Journal of Fluid Mechanics, 253*(-1), 105. doi:10.1017/s0022112093001739

[18] Gundogdu, M. Y., & Carpinlioglu, M. O. (1999). Present State of Art on Pulsatile Flow Theory. Part 1. Laminar and Transitional Flow Regimes. *JSME International Journal Series B, 42*(3), 384-397. doi:10.1299/jsmeb.42.384

[19] Gundogdu, M. Y., & Carpinlioglu, M. O. (1999). Present State of Art on Pulsatile Flow Theory. Part 2. Turbulent Flow Regime. *JSME International Journal Series B, 42*(3), 398-410. doi:10.1299/jsmeb.42.398

[20] Spalart, P. R., & Baldwin, B. S. (1989). Direct Simulation of a Turbulent Oscillating Boundary Layer. *Turbulent Shear Flows 6*, 417-440. doi:10.1007/978-3-642-73948-4_32

[21] Vasilyev, O. V., Lund, T. S., & Moin, P. (1998). A General Class of Commutative Filters for LES in Complex Geometries. *Journal of Computational Physics, 146*(1), 82-104. doi:10.1006/jcph.1998.6060

[22] Lund, T. (2003). The use of explicit filters in large eddy simulation. *Computers & Mathematics with Applications, 46*(4), 603-616. doi:10.1016/s0898-1221(03)90019-8

[23] Scotti, A., & Piomelli, U. (2002). Turbulence models in pulsating flows. *AIAA Journal, 40*, 537-544. doi:10.2514/3.15094

[24] Scotti, A., & Piomelli, U. (2001). Numerical simulation of pulsating turbulent channel flow. *Physics of Fluids, 13*(5), 1367-1384. doi:10.1063/1.1359766

[25] Ansari, A. (1997). Self-similarity and mixing characteristics of turbulent mixing layers starting from laminar initial conditions. *Physics of Fluids, 9*(6), 1714-1728. doi:10.1063/1.869288

[26] Spalart, P., & Allmaras, S. (1992). A one-equation turbulence model for aerodynamic flows. *30th Aerospace Sciences Meeting and Exhibit*. doi:10.2514/6.1992-439

[27] Menter, F. R. (1994). Two-equation eddy-viscosity turbulence models for engineering applications. *AIAA Journal, 32*(8), 1598-1605. doi:10.2514/3.12149

[28] Fureby, C., & Grinstein, F. (2000). Large eddy simulation of high Reynolds-number free and wall-bounded flows. *Fluids 2000 Conference and Exhibit*. doi:10.2514/6.2000-2307

[29] Spalart, P., Jou, W-H., Strelets, M., and Allmaras, S., 1997, “Comments on the Feasibility of LES for Wings, and on a Hybrid RANS/LES Approach,” *Advances in DNS/LES: First AFOSR International Conference on DNS/LES*, C. Liu and Z. Liu, eds. (Greyden, Columbus, OH).

[30 Menter, F. R. (2009). Review of the shear-stress transport turbulence model experience from an industrial perspective. *International Journal of Computational Fluid Dynamics, 23*(4), 305-316. doi:10.1080/10618560902773387

[31] Menter, F.R., Kuntz, M., Langtry, R.B., (2003). “Ten years of Industrial Experience with the SST Turbulence Model,” *4th Internal Symposium, Turbulence, heat and mass transfer; 2003*; Antalya, Turkey.

[32] Spalart, P. R., Deck, S., Shur, M. L., Squires, K. D., Strelets, M. K., & Travin, A. (2006). A New Version of Detached-eddy Simulation, Resistant to Ambiguous Grid Densities. *Theoretical and Computational Fluid Dynamics, 20*(3), 181-195. doi:10.1007/s00162-006-0015-0

[33] Nichols, R.H., Nelson, C.C., (2003). "Application of hybrid RANS/LES turbulence models," AIAA Paper 2003-83.

[34] Nichols, R. (2005). Comparison of Hybrid RANS/LES Turbulence Models on a Circular Cylinder at High Reynolds Number. *43rd AIAA Aerospace Sciences Meeting and Exhibit*. doi:10.2514/6.2005-498

[35] Bhushan, S., Walters, D.K., (2012). "A Dynamic Hybrid RANS/LES Modeling Framework," Physics of Fluids 24, No. 015103.

[36] Walters, D. K., Bhushan, S., Alam, M. F., & Thompson, D. S. (2013). Investigation of a Dynamic Hybrid RANS/LES Modelling Methodology for Finite-Volume CFD Simulations. *Flow, Turbulence and Combustion, 91*(3), 643-667. doi:10.1007/s10494-013-9481-9

[37] Poe, N. M., Walters, D. K., Luke, E. A., & Morris, C. I. (2015). A Low-Dissipation Second-Order Upwind Flux Formulation for Simulation of Complex Turbulent Flows. *Volume 7A: Fluids Engineering Systems and Technologies*. doi:10.1115/imece2015-53725

[38] Jackson, P. S., & Hunt, J. C. (1975). Turbulent wind flow over a low hill. *Quarterly Journal of the Royal Meteorological Society, 101*(430), 929-955. doi:10.1002/qj.49710143015

[39] Luke, E. A., & George, T. (2005). Loci: A rule-based framework for parallel multi-disciplinary simulation synthesis. *Journal of Functional Programming, 15*(3), 477-502. doi:10.1017/s0956796805005514

[40] Luke, E.A., Tong, X., Wu, J., Cinella, P., Chamberlain, R., (2014). "CHEM 3.3: A Finite-Rate Viscous Chemistry Solver – The User Guide". Mississippi State University, MS.

[41] ANSYS Fluent Theory Guide 14.0, ANSYS, Inc., Canonsburg, PA.

[42] Jamal, T., & Walters, D. K. (2016). Simulation of a 3D Axisymmetric Hill: Comparison of RANS and Hybrid RANS-LES Models. *Volume 1B, Symposia: Fluid Mechanics (Fundamental Issues and Perspectives; Industrial and Environmental Applications); Multiphase Flow and Systems (Multiscale Methods; Noninvasive Measurements; Numerical*

Methods; Heat Transfer; Performance); Transport Phenomena (Clean Energy; Mixing; Manufacturing and Materials Processing); Turbulent Flows — Issues and Perspectives; Algorithms and Applications for High Performance CFD Computation; Fluid Power; Fluid Dynamics of Wind Energy; Marine Hydrodynamics. doi:10.1115/fedsm2016-7772

[43] Spalart, P., (2001). "Young-person's guide to detached eddy simulation grids," NASA, Technical Report CR-2001-211032.

[44] Roberts, S. W. (1959). Control Chart Tests Based on Geometric Moving Averages. *Technometrics, 1*(3), 239-250. doi:10.1080/00401706.1959.10489860

[45] Pruett, C. D., Gatski, T. B., Grosch, C. E., & Thacker, W. D. (2003). The temporally filtered Navier–Stokes equations: Properties of the residual stress. *Physics of Fluids, 15*(8), 2127-2140. doi:10.1063/1.1582858

[46] Jamal, T., Wang, H., & Walters, D. K. (2018). LES and Hybrid RANS-LES Simulation of a Pulsating Channel Flow. *Volume 7: Fluids Engineering*. doi:10.1115/imece2018-87990

[47] Jamal, T., & Walters, D. K. (2019). A Dynamic Time Filtering Technique for Hybrid RANS-LES Simulation of Non-Stationary Turbulent Flow. *Volume 2: Computational Fluid Dynamics*. doi:10.1115/ajkfluids2019-4696

[48] Moser, R. D., Kim, J., & Mansour, N. N. (1999). Direct numerical simulation of turbulent channel flow up to Reτ=590. *Physics of Fluids, 11*(4), 943-945. doi:10.1063/1.869966

[49] Bhushan, S., & Walters, D. K. (2014). Development of Parallel Pseudo-Spectral Solver Using Influence Matrix Method and Application to Boundary Layer Transition. *Engineering*

Applications of Computational Fluid Mechanics, 8(1), 158-177. doi:10.1080/19942060.2014.11015505

[50] Bhushan S., S. Muthu, (2019). "Performance and Error Assessment of Parallel Pseudo-Spectra Methods for Direct Numerical Simulations", *Engineering Applications of Computational Fluid Dynamics*, 13 (1): 763-781, 2019.

[51] Mulloy, Patrick G. (1994). "Smoothing data with less lag," *Technical Analysis of Stocks & Commodities*, Volume 12: February.

[52] Ansari, A. (1995). Direct numerical simulation of turbulent mixing layers. *Fluid Dynamics Conference*. doi:10.2514/6.1995-2249

[53] Bell, J., & Mehta, R. (1990). Development of a two-stream mixing layer from tripped and untripped boundary layers. *28th Aerospace Sciences Meeting*. doi:10.2514/6.1990-505

[54] Mahesh, K., Constantinescu, G., Moin, P., (2004). "A new time-accurate finite-volume fractional-step algorithm for prediction of turbulent flows on unstructured hybrid meshes," *Journal of Computational Physics 197*, 215–240.

[55] Walters, D. K., Bhushan, S., Alam, M. F., & Thompson, D. S. (2013). Investigation of a Dynamic Hybrid RANS/LES Modelling Methodology for Finite-Volume CFD Simulations. *Flow, Turbulence and Combustion, 91*(3), 643-667. doi:10.1007/s10494-013-9481-9

[56] Shobayo, O. O., & Walters, D. K. (2018). Evaluation of Performance and Code-to-Code Variation of a Dynamic Hybrid RANS/LES Model for Simulation of Backward-Facing Step Flow. *Volume 1: Flow Manipulation and Active Control; Bio-Inspired Fluid Mechanics;*

Boundary Layer and High-Speed Flows; Fluids Engineering Education; Transport Phenomena in Energy Conversion and Mixing; Turbulent Flows; Vortex Dynamics; DNS/LES and Hybrid RANS/LES Methods; Fluid Structure Interaction; Fluid Dynamics of Wind Energy; Bubble, Droplet, and Aerosol Dynamics. doi:10.1115/fedsm2018-83160

[57] Shobayo, O. O., & Walters, D. K. (2019). Hybrid RANS-LES Simulation of Turbulent Heat Transfer in a Channel Flow With Imposed Spanwise and Streamwise Mean Temperature Gradient. *Volume 2: Computational Fluid Dynamics*. doi:10.1115/ajkfluids2019-4920

[58] Jamal, T., Walters, D. K., & Chitta, V. (2017). 3D Simulation of Flow in a Vortex Cell Using RANS and Hybrid RANS-LES Turbulence Models. *Volume 7: Fluids Engineering*. doi:10.1115/imece2017-70599

[59] Anderson, J., (1997).“A History of Aerodynamics, and Its Impact on Flight Machines”, *Cambridge Aerospace Series, vol. 8,* Cambridge University Press, 1997.

[60] Stokes, G. (2009),.On the Theories of the Internal Friction of Fluids in Motion, and of the Equilibrium and Motion of Elastic Solids. *In Mathematical and Physical Papers (Cambridge Library Collection - Mathematics, pp. 75-129).* Cambridge: Cambridge University Press. doi:10.1017/CBO9780511702242.005